

Quantum Computation and Many-Body Physics with Trapped Ions

Thesis submitted to the
Faculty of Mathematics, Computer Science and Physics
of the Leopold-Franzens University of Innsbruck
in partial fulfillment
of the requirements for the degree of

Doctor of Philosophy
(Physics)

by

Petar Jurcevic

Innsbruck, January 24, 2017

Abstract

Over the last two decades, quantum information science has made significant progress, both theoretically and experimentally, evolving into a prosperous field with potential commercial applications within the next decade. This PhD thesis reports on four different experiments, performed over the last few years, all investigating various aspects of quantum information science. $^{40}\text{Ca}^+$ -ions trapped in a macroscopic, linear Paul trap serve as qubits encoding quantum information that are coherently manipulated with laser light fields.

These four experiments utilise an existing experimental arrangement, adapted to allow coherent manipulation of long ion strings, thus demonstrating the capabilities of the current setup.

Two of the experiments presented in this thesis are focused on *quantum simulations* of interacting many-body systems. In the first experiment, the propagation of entanglement in such a many-body system is experimentally observed for the very first time. Additionally, the system's response is investigated as the spatial range of the interactions is tuned. The following experiment employs a novel spectroscopic method for probing these interacting many-body systems.

The third experiment focuses on quantum computation, specifically the *measurement-based quantum computation* approach. Here, the deterministic generation of cluster states in trapped ions is demonstrated for the first time. Moreover, certain cluster states are used to implement error correction codes of different sizes, granting, to the author's knowledge, the first experimental evidence that larger code words are indeed capable of better protecting quantum information, despite the higher complexity of their preparation.

The fourth and last experiment explores a type of quantum correlation present in mixed states, known as *quantum discord*. The generation of quantum discord via two different, noisy processes - that is, amplitude damping and correlated magnetic field noise - is investigated, and the generated discord is quantified by different measures.

In the last part of this thesis, the limitations of the current setup are presented and, if possible, potential solutions are discussed. Furthermore, open questions encountered in the experimental setup are addressed for future investigations in order to obtain a better understanding of further limitations.

A brief outlook on possible improvements to the experimental setup, as well as ideas for future projects, conclude this manuscript.

Zusammenfassung

In den letzten zwei Dekaden hat sich die Quanteninformationswissenschaft zu einem blühenden Fachgebiet entwickelt, in dem grossartige Fortschritte, von theoretischer und experimenteller Seite her, in Richtung kommerziellen Anwendungen stattgefunden haben. In dieser Dissertationsschrift werden vier Experimente vorgestellt, die sich mit unterschiedlichen Aspekten der Quanteninformationswissenschaft beschäftigen. Als physikalische Plattform um Quanteninformation zu kodieren, dienen $^{40}\text{Ca}^+$ -Ionen, gefangen in einer makroskopischen, linearen Paulfalle, die mit Hilfe von Laserlicht kohärent manipuliert werden können.

Aufbauend auf einem existierenden Experiment, wurden Techniken entwickelt und angewandt um lange Ionenketten kontrolliert zu manipulieren. Hierbei werden die Möglichkeiten des gegenwärtigen Aufbaus aufgezeigt.

Zwei der Experimente, die in dieser Arbeit vorgestellt werden, beschäftigen sich mit der Quantensimulation von wechselwirkenden Vielteilchensystemen. Im ersten der beiden Experimente geht es um die erstmalige Beobachtung wie sich Verschränkung in einem solchen Vielteilchensystem ausbreitet. Des Weiteren wurde die Abhängigkeit dieser Ausbreitung für unterschiedliche Wechselwirkungslängen untersucht. Das nachfolgende Experiment befasst sich mit einer neu-entwickelten spektroskopischen Methode, um ebendiese wechselwirkenden Systeme auf ihre Eigenschaften zu untersuchen.

Der Fokus des dritten Experimentes liegt auf einem spezifischen Model der Quantenrechnung, das sogenannte messbasierte Quantenrechner-Model. Dabei wurden die grundlegenden Bausteine des messbasierten Quantenrechners, sogenannte Cluster-Zustände, erstmalig *deterministisch* erzeugt. Darüber hinaus wurden Cluster-Zustände unterschiedlicher Grösse im Hinblick auf Fehlerkorrekturcodes erzeugt, die, unseres Wissens nach, erstmalig nachweisen, dass längere Codewörter in der Tat Quanteninformation besser beschützen können, trotz der höheren Komplexität bei deren Herstellung.

Das vierte und letzte Experiment erforscht eine grundlegende Art von Quantenkorrelationen in gemischten Zuständen, die man auch als "*Quanten-Zwietracht*" (Quantum discord) kennt. Hier wird die Frage untersucht, wie Quanten-Zwietracht durch unterschiedliches Rauschen erzeugt werden kann, genauer gesagt durch Amplitudenzerfall und korreliertes Magnetfeldrauschen. Hierbei wurde die Quanten-Zwietracht durch unterschiedliche Metriken quantifiziert.

Im letzten Kapitel dieser Arbeit werden die Limitierungen des derzeitigen Aufbaues bezüglich langer Ionen-Ketten erläutert und wenn möglich, werden Lösungen diskutiert. Darüber hinaus werden offene Fragen voergestellt, die in Zukunft untersucht werden müssen, um ein besseres Verständnis der Limitierungen zu erhalten.

Zum Abschluss folgt ein kurzer Ausblick auf mögliche Verbesserungen des experimentellen Aufbaues und Ideen für zukünftige Projekte werden vorgestellt.

Contents

Abstract / Zusammenfassung	i
1. Introduction	1
2. Quantum information science	5
2.1. Quantum Bits	5
2.2. Quantum Correlations	7
2.3. Quantum Computation	10
2.4. Quantum Simulation	15
3. Theoretical framework	19
3.1. Trapped ions	19
3.1.1. Paul trap	19
3.1.2. Quantum harmonic oscillator	21
3.1.3. Normal/collective motional modes	24
3.2. Laser - ion interaction	29
3.2.1. Two level atom - laser interaction	29
3.2.2. Trapped ions - laser Hamiltonian	30
3.3. Entangling Gates and effective spin-spin Hamiltonians	32
3.3.1. Bichromatic light field	32
3.3.2. Mølmer - Sørensen interaction	34
3.3.3. Adiabatic elimination and effective transverse field Ising Hamiltonian	35
3.3.4. Tunable interaction range	37
4. Experimental setup and techniques for long ion strings	39
4.1. $^{40}\text{Ca}^+$ as a qubit/pseudospin	39
4.2. Setup - Overview	40
4.3. Experimental techniques for long ion strings	45
4.3.1. Spatially dependent qubit transition frequencies	49
4.4. Interaction Beam	52
4.4.1. Beam shaping	52
4.4.2. Spatial dependent ac-Stark shift	53
4.5. Trichromatic light field	55
4.5.1. Reasons for compensation failure	56
4.6. Radial Modes	64
4.6.1. Spectrum	65

4.6.2.	Motional mode stabilization	66
4.6.3.	Ground state cooling	71
5.	Quantum simulation of spin models	75
5.1.	Spin models	76
5.1.1.	Transverse Ising and XY -Model	76
5.2.	Lieb-Robinson bounds	80
5.3.	Setting up and calibrating the interactions	82
5.3.1.	Setting up the interactions	82
5.3.2.	Measuring the elements of J_{ij}	86
5.3.3.	Determining the power law decay α	87
5.4.	Spectroscopy of quasiparticles	88
5.4.1.	Spectroscopy of ground state gaps	91
5.4.2.	Spectroscopy of dispersion relations	93
5.4.3.	Spectroscopy of interacting quasiparticles	94
5.5.	Quasiparticle engineering and entanglement propagation	97
5.5.1.	Propagation of entanglement	97
5.5.2.	Tuning the interaction range and Lieb-Robinson bounds	99
5.6.	Discussion and Outlook	102
6.	Measurement-based quantum computation	105
6.1.	Graph and cluster states	105
6.1.1.	Definitions	106
6.2.	Computing via measurement and feedforward	109
6.2.1.	Arbitrary single qubit rotations	111
6.2.2.	Two qubit gates and Clifford gates	111
6.3.	Experimental implementation of cluster and graph states	112
6.3.1.	Box cluster	113
6.3.2.	Linear cluster	116
6.3.3.	Realization of MBQC with a 4-qubit linear cluster state	117
6.3.4.	Error correction	119
6.4.	Conclusion	123
7.	Generation of quantum discord via noise	125
7.1.	Theoretical framework	125
7.1.1.	Quantum discord	126
7.1.2.	Quantum operations and noise	129
7.2.	Discord via local damping	131
7.3.	Discord via correlated noise	135
7.4.	Conclusion	138
8.	Limitations of the current setup and open questions	141

9. Summary and outlook	149
A. List of Publications	153
B. Extended derivations	155
B.1. Derivation of the effective spin-spin Hamiltonian	155
B.1.1. Blue/Red Side Band	156
B.1.2. Time Evolution - Magnus Expansion	157
B.1.3. Second Order	158
B.1.4. Effective Hamiltonian	160
B.2. Temperature estimate from sideband-order index distribution	162
B.3. Coupling strength fluctuations on an addressed ion due to hot axial modes	163
C. Derivation of spectroscopic signals	165
C.1. Spectroscopic signals for single quasiparticle states	165
C.1.1. Absolute quasiparticle energies	167
C.1.2. Relative quasiparticle energies	167
C.2. Spectroscopic signals for two quasiparticle states	168
C.2.1. Mapping spin operators to bosonic operators	168
C.2.2. Perturbative treatment of spin-wave interactions	169
C.2.3. Expected signal	170
C.2.4. Summation of spin-spin correlation measurements	170
C.2.5. Validity of first-order perturbation theory: additional experimental data	171
D. Reconstructed density matrices for MBQC	173
E. Correlated dephasing on two qubits	177
E.1. Separable operations can increase the correlation rank	177
E.2. Correlated dephasing on two qubits	178
E.2.1. Dephasing by fluctuating rotations	179
Correlated dephasing	179
Kraus representation	179
E.2.2. Initial rank-1 states	180
E.2.3. Initial rank-2 states	180
E.2.4. Summary	182
Bibliography	183

1. Introduction

Quantum mechanics, and the advancements it provides, are one of the fundamental pillars of modern day life, guiding and expanding our understanding of nature. Many present-day technological advances, from chemistry to GPS-navigation, rely in one way or another on the understanding of the microscopic world, an understanding gained from quantum physics.

In the early days of quantum mechanics most, if not all, of its founders thought of it as a mere theoretical construction to describe the microscopic world. Despite being fruitful in explaining many experimentally observed phenomena, none of the founding fathers ever dared to dream of observing quantum mechanics on the single particle level, not to mention to fully control them. Or, as to put it into Schrödinger’s famous phrase “[...] we never experiment with just one electron or atom or (small) molecule. In thought-experiments we sometimes assume that we do; this invariably entails ridiculous consequences . . . we are not experimenting with single particles, any more than we can raise Ichthyosauria in the zoo.” [1]. Almost as if it was a prompt to prove Schrödinger wrong, only a year later in 1953, W. Paul suggested trapping charged particles with electric fields [2]¹. Another 25 years had to pass by before Neuhauser, Hohenstatt, Toschek and Dehmelt succeeded in trapping, and laser cooling, a cloud ($N < 50$) of barium ions in a Paul trap [3]². The same team was successful in trapping a *single* barium [5] only two years later in 1980, demonstrating the (once thought ‘unimaginable’) possibility of isolating a single quantum system for the first time. This achievement led into a new era of experimental quantum physics and, six years later, a long lasting question regarding light-matter interactions, namely the existence of quantum jumps, was proven to be true [6–8].

At around the same time experimentalists succeeded in trapping single particles, the concept of quantum computation was introduced by Benioff [9], Manin [10] and Feynman [11]. In contrast to classical computers based on transistors where the information is encoded in distinct values, termed bits, the information in a quantum computer can be in any superposition of two states and is stored in quantum bits (qubits) [12]. However, at the time those ideas emerged it was considered experimentally unrealistic to use single quantum systems, such as atoms, to encode and manipulate information. In one of his lectures in 1986 Feynman said “[...] we are to be even more ridiculous later and consider bits written on one atom instead of the present 10^{11} atoms. Such nonsense is very entertaining to professors like me. I hope you will find it interesting and entertaining also.”

¹Wolfgang Paul and Hans G. Dehmelt received the Nobel prize in 1989 “for the development of the ion trap technique”, and in the same year, Norman F. Ramsey received it “for the invention of the separated oscillatory fields method and its use in the hydrogen maser and other atomic clocks”.

²In the same year, Wineland, Drullinger and Walls, succeeded in laser cooling 5×10^4 Mg-ions stored in a Penning trap [4].

And, once again, a famous Nobel laureate³ was going to be proven wrong.

About 15 years later, Peter Zoller and Ignacio Cirac wrote their seminal paper [13] proposing trapped ions as qubits and using their common motion as a bus system to couple those ions and generate entanglement. With the experimental advances in controlling single ions, such as state preparation and ground state cooling of motional degrees of freedom [14], Monroe *et al.* demonstrated for the first time a quantum logic gate, the so-called controlled-NOT gate or C-NOT, with a single ion⁴ based on the Cirac-Zoller proposal. Over the last two decades, trapped ions have arisen as a prime candidate⁵ for quantum information processing, due to the tremendous control that is available over those systems. On the way towards a fully functional quantum computer, many roadblocks have been overcome with ions, such as high-fidelity two-qubit gates [16, 17] for fault-tolerant computation, error correction [18, 19], entanglement purification [20], creation of large entangled states [21, 22] and the proof of principle implementation of different algorithms, such as the Deutsch-Josza algorithm [23], Grover's search algorithm [24] and Shor's algorithm [25].

Nevertheless, there are still obstacles which need to be overcome before a genuine quantum computer can be achieved; for example, scaling to large numbers of qubits as well as combining all basic building blocks together are but a few of the challenges to be addressed. However, an attractive alternative approach are quantum simulators. Quantum simulations may be able to outperform classical simulations far earlier than quantum computers, due to their lower constraints on system size and the quality of quantum logic gates required.

Over the last decade, many proof of principle experiments have been demonstrated on various platforms⁶. Here in this work, a particular Hamiltonian - namely the transverse field Ising Hamiltonian with tunable spin-spin interaction range - is implemented on up to 15 ions. Moreover, the experiment presented in chapter 5 goes beyond proof of principle, as for the first time it was possible to observe how entanglement spreads out in a many-body interacting system after quenching [26]. The dependence of this spreading on the spin-spin interaction range was investigated and compared to so-called Lieb-Robinson bounds [27], i.e. upper bounds on the speed of correlation propagation in interacting systems. In addition, a spectroscopic technique is demonstrated for probing the low-lying energy states of the Ising Hamiltonian by creating superpositions of its eigenstates [28]. This allows the dispersion relation of the given Hamiltonian to be deduced, revealing information about the dynamical behaviour of the system under consideration. In fact, this spectroscopic method is generic and can be applied to other Hamiltonians that show certain symmetries in their eigenstates.

In the quest to develop a quantum computer, not only experimental progress has been made, but also theoretical developments have led to new insights into quantum information theory over the past two decades. A prominent example is the realization that quantum information can be processed in ways other than in the standard model, or gate model, of quantum computation [12]. In 2001 Raussendorf and Briegel formulated their idea of a measurement-based quantum

³Richard Feynman was awarded the Nobel prize in 1965 jointly with Sin-Itiro Tomonaga and Julian Schwinger "for their fundamental work in quantum electrodynamics, with deep-ploughing consequences for the physics of elementary particles".

⁴The target qubit was encoded in the hyperfine ground state of a $^9\text{Be}^+$ -ion and the control qubit is spanned by the first two states of the harmonic oscillator.

⁵A short overview of different experimental implementations of qubits can be found in [15].

⁶For an incomplete list of the most prominent experiments see 5.

computer (MBQC) [29], where the computation is driven by measurements and feedforward on a large entangled state, specifically a cluster state, instead of quantum gates. From an experimental point of view, it is prudent to test out the various forms of quantum computation - such as the gate model or the MBQC model - as they all possess different advantages and disadvantages. An early proof of principle experiment was demonstrated with photons in the group of Zeilinger in 2005, where the individual building blocks of MBQC - i.e. arbitrary single-qubit rotations and two-qubit gates - were showcased⁷. In this thesis the first implementation of MBQC with trapped ions is demonstrated, where the generation of different cluster states is shown in a deterministic way [30]. In addition to the demonstration of the MBQC-equivalence of a universal set of gates, it was also confirmed that certain graph states⁸ can be used for error correction schemes specifically, in this case for, phase flip errors.

Amongst the quantum information community it is undoubted that the advantage of quantum computers over classical ones originates from quantum correlations, especially entanglement. In their effort to generalise quantum correlations to mixed states, Ollivier & Zurek [31], and independently Henderson & Vedral [32], introduced the notion of quantum discord in 2001. Three years prior to that Knill & Laflamme [33] coined the term ‘power of one bit’, where they proved that a single pure qubit coupled to an arbitrary number of completely mixed qubits can solve certain tasks faster than any known classical counterpart. Later it was realized that such a system has a vanishingly small amount of entanglement, however, it does contain quantum discord [34]. Bearing in mind that quantum discord might be another source to reaching ‘quantum advantage’, it is necessary to investigate it under experimental conditions such as noise. Here in this work it is shown how different types of noise, specifically amplitude damping and correlated dephasing, can generate discord between two qubits, with the discord being quantified with different measures for various initial states.

The structure of the presented thesis is the following:

Chapter 2 provides the reader with an introduction to quantum information science in order to understand the basic theoretical concepts regarding this thesis.

Chapter 3 is a brief summary of the theoretical framework regarding ion trapping, laser-ion interaction and the quantum gates used for the projects presented in later chapters.

Chapter 4 details the original experimental setup, and the subsequent alterations implemented during the course of this PhD work, such as stabilisation of the radial mode frequencies. Additionally, the techniques of most importance for manipulating long strings of ions are presented.

Chapter 5 reports on two experiments regarding quantum simulation of interacting spin models with tunable spin-spin interaction lengths. A theoretical discussion with respect to spin models and Lieb-Robinson bounds allows the reader to understand the physics underpinning

⁷However, in this publication feedforward was not implemented as only certain outcomes that do not require feedforward are post-selected. In addition, with the presented setup, generation of cluster states was only possible in a probabilistic manner.

⁸A more general form of cluster states, see 6.

this aspect of quantum simulation. Furthermore, a following section details the experimental techniques required to setup a quantum simulation with our experimental arrangement.

Chapter 6 showcases our work on measurement-based quantum computation. Additional theoretical and experimental details are presented in order to allow the reader to obtain a more thorough understanding of the subject.

Chapter 7 summarizes the experiment related to discord. A short theoretical overview details the terminology used in this chapter, and the following sections discuss how quantum discord can be generated via amplitude damping and correlated noise.

Chapter 8 outlines the current limitations of the experimental setup with regards to scaling of the number of ions, and discusses possible solutions to these limitations.

Chapter 9 concludes the thesis with a brief summary and outlook for future work.

2. Quantum information science

The term quantum information science (QIS) is often used as a umbrella term covering the theoretical and experimental subgenres, best known as quantum information theory (QIT) and quantum information processing (QIP). While the former is focussed on extending classical information theory to quantum mechanics and developing the fundamental understanding of, for example, quantum bits (qubits), quantum algorithms and quantum computation (QC), to name just a few, the latter is centred around the question of how quantum information is controlled in an experimental system.

As this thesis deals with different aspects of both QIT and QIP the aim of this chapter is to introduce the basic concepts and to bring down the different chapters to a common denominator. Starting from a single qubit, so to say the basic unit in QIS, a brief overview of the most relevant aspects regarding quantum correlations, quantum computation and quantum simulation will be provided [12].

2.1. Quantum Bits

Analogous to classical information theory, where a bit is regarded as the smallest unit of *information*, its quantum counterpart is the quantum bit or *qubit*. In contrast to classical bits, which can take values ‘0’ or ‘1’, a qubit can be in a coherent superposition of both states

$$|\psi\rangle = \alpha|0\rangle + \beta|1\rangle = \alpha|\downarrow\rangle + \beta|\uparrow\rangle, \quad (2.1)$$

where α and β are two complex numbers fulfilling the relation $|\alpha|^2 + |\beta|^2 = 1$ and the probabilities to find respective states are $|\alpha|^2$ and $|\beta|^2$. Throughout this text the notation $|0\rangle / |\downarrow\rangle$, as well as $|1\rangle / |\uparrow\rangle$, will be used equivalently. However, the notation $|0\rangle$ is more common for quantum computation and $|\downarrow\rangle$ is more convenient in the context of quantum simulations, where it is referred to as *pseudo spin*. The ‘Bra-ket’ notation, also known as Dirac-notation, is a short form for a vector $|0\rangle = \begin{pmatrix} 1 \\ 0 \end{pmatrix}$ and $\langle 0| = (1 \ 0)$, $|1\rangle = \begin{pmatrix} 0 \\ 1 \end{pmatrix}$ and $\langle 1| = (0 \ 1)$.

A convenient way to rewrite equation 2.1 is to use spherical coordinates

$$|\psi\rangle = e^{-i\phi_g} \left(\sin\left(\frac{\theta}{2}\right) |0\rangle + \cos\left(\frac{\theta}{2}\right) e^{-i\phi} |1\rangle \right) \quad (2.2)$$

where ϕ_g , θ and ϕ are real numbers. Since the global phase ϕ_g has no absolute reference point it can be set to any arbitrary value, in general $\phi_g = 0$. A visual representation of equation 2.2 is the *Bloch sphere* with angles ϕ and θ as shown in figure 2.1 and it is mostly useful to describe single-qubit (pure and mixed) states.

In order to capture all aspects of a mixed state in multi qubit systems, that is a statistical mixture

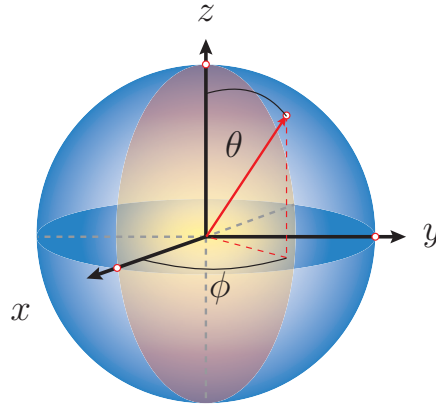


Figure 2.1.: The Bloch sphere, a visual representation of a single-qubit pure state.

of pure states as given by equation 2.1, the *density matrix* formalism provides convenient means. Any quantum state can be expressed as

$$\rho = \sum_i p_i |\psi_i\rangle \langle \psi_i|. \quad (2.3)$$

Here, $|\psi_i\rangle$ is the i^{th} pure state with probability p_i , where the relation $\sum_i p_i = 1$ must hold. The set $\langle p_i |\psi_i\rangle$ is also known as an *ensemble of pure states*.

By choosing a set of orthonormal bases spanning a Hilbert space \mathcal{H} , for example the Pauli group

$$\mathbb{I} = \begin{pmatrix} 1 & 0 \\ 0 & 1 \end{pmatrix}, \quad \sigma_x = \begin{pmatrix} 0 & 1 \\ 1 & 0 \end{pmatrix}, \quad \sigma_y = \begin{pmatrix} 0 & i \\ -i & 0 \end{pmatrix} \text{ and } \sigma_z = \begin{pmatrix} 1 & 0 \\ 0 & -1 \end{pmatrix}, \quad (2.4)$$

has been chosen here for convenience - a pure state as defined by Eq. 2.1 can be written as

$$\rho = (\mathbb{I} + \vec{n} \cdot \vec{\sigma}) \text{ with } \vec{n} = \begin{pmatrix} \langle \sigma_x \rangle \\ \langle \sigma_y \rangle \\ \langle \sigma_z \rangle \end{pmatrix} \text{ and } \vec{\sigma} = \begin{pmatrix} \sigma_x \\ \sigma_y \\ \sigma_z \end{pmatrix}. \quad (2.5)$$

Here, $\langle \sigma_i \rangle$ denotes the i^{th} expectation value given by the trace $\text{Tr}(\sigma_i \rho) = \langle \sigma_i \rangle$. Equations 2.2 and 2.5 are equivalent descriptions in the context of pure states and they will be used interchangeably to best suit the situation.

In order to describe N qubits the total Hilbert space \mathcal{H}_N is expanded by taking the tensor product over all individual Hilbert spaces \mathcal{H}_n

$$\mathcal{H}_N = \bigotimes_{n=1}^N \mathcal{H}_n = \mathcal{H}_n^{\otimes N} = \mathcal{H}_n \otimes \mathcal{H}_{n-1} \otimes \cdots \otimes \mathcal{H}_1, \quad (2.6)$$

where the qubits are counted from left to right in accordance with the computational, binary representation of numbers. The purity $P(\rho) \in \left[1, \frac{1}{2^N}\right]$ is an absolute measure of a quantum state offering information with regards to the amount of mixture. For an N -qubit state it is given by $P(\rho) = \text{Tr}(\rho^2)$ indicating a pure state for $P(\rho) = 1$ and a completely mixed state for $P(\rho) = \frac{1}{2^N}$.

There are many other absolute and relative measures; for a brief overview see [12, 35, and references therein].

2.2. Quantum Correlations

A frequent misconception regarding *quantum speed-up* is that superposition of quantum mechanical states¹ alone is the core resource. However, it has been shown that pure product states [37] and quantum states with ‘little’ entanglement can be simulated efficiently on a classical machine, i.e. the required computational resource increases linearly with the system size [38, 39]. This indicates that entanglement distinguishes between classically computable and classically intractable systems and, hence, it could be thought of as the resource for any quantum algorithm. However, doubts were soon raised that entanglement alone is responsible for quantum speed-up [33] and the notion has been stretched to more general quantum correlations [34, 40].

This section will provide a brief introduction to quantum correlation as a resource for quantum computation, with a main focus on entanglement. The notion of quantum discord [31, 32], as a wider class of correlation, will only be briefly mentioned as chapter 7 [and references therein] provides a detailed introduction.

Classical correlations The concept of correlation is encountered in everyday life; a hot plate and burned hands is a very useful one. However, it is important to note that correlation and causality are not equivalent. The increase of global average temperature is anti-correlated with the decrease of pirates in the Caribbean sea, nevertheless there is no causal chain. Correlations, therefore, are a necessary but not sufficient condition for causal connections.

A formal framework for understanding information and correlations is provided by Shannon’s information theory [41]. Consider two random variables X and Y with two sets of possible outcomes $\{x_i\}$ and $\{y_j\}$, respectively, and the joint probability distribution defined as $P(X = x_i; Y = y_j) \equiv p(x_i; y_j)$ with the individual probabilities $P(X = x_i) \equiv p(x_i) = \sum_j p(x_i; y_j)$ and $P(Y = y_j) \equiv p(y_j) = \sum_i p(x_i; y_j)$ [42]. The uncertainty, or amount of information about X is expressed by the Shannon entropy²

$$S(X) = S(p(x)) = - \sum_i p(x_i) \ln p(x_i) \quad (2.7)$$

and analogously for Y . Regarding correlations between X and Y , the joint probability encodes to what degree they are correlated, and the joint Shannon entropy

$$S(X, Y) = S(p(x, y)) = - \sum_{i,j} p(x, y) \ln p(x, y) \quad (2.8)$$

¹Even though a single qubit can “store an infinite amount of information”, due to the infinite points on the surface of a Bloch sphere, the amount of accessible information is bound by Holevo’s theorem [36]. In fact, n -qubits can maximally carry n classical bits of *retrievable* information.

²Information in Shannon’s information theory is understood as the *unpredictability of information content* or the *surprise value*: Suppose having a ‘fair’ coin with equal probability for head/tail. In such a case we can not predict the outcome of any future coin toss and the uncertainty/entropy has its maximal value (for the example of a coin) of $S(X) = 1$ (here, \log_2 is used which is more common for binomial distributions). Every additional coin toss provides us with the maximal amount of information. On the other hand, a fake coin with only heads is fully predictable, i.e. $S(X) = 0$, and additional coin tosses do not provide any additional information.

quantifies the uncertainty of X having full knowledge about Y , and vice versa. With these definition, one can define the mutual information as

$$\mathcal{I}(X : Y) = S(X) + S(Y) - S(X, Y). \quad (2.9)$$

The mutual information is a quantity that measures ‘how much the knowledge about one random variable tells us about another random variable’. It is zero iff the two random variables X and Y are statistically independent and it reaches a maximum value if the two variables are fully correlated. Imagine having two completely *random*, but equally long, strings of text A & B where reading one of the strings does not reveal anything about the other. In other words, the joint entropy (uncertainty) equals the sum of the individual entropies, $S(X, Y) = S(X) + S(Y)$, and the mutual information is $\mathcal{I}(X : Y) = 0$. However, if they are perfect copies of each other, i.e. perfectly correlated $S(X, Y) = S(X) = S(Y) = \mathcal{I}(X : Y)$, it is enough to possess one string of text in order to have complete knowledge about the other. An important lesson to learn here is that even for perfectly correlated systems, the correlations do not increase the total amount of information contained in both systems individually.

This is quite different for quantum mechanical correlations, especially for entanglement. One of the most important relations in the quantum theory of correlations is the Araki-Lieb inequality [43]

$$S_N(\rho_A) + S_N(\rho_B) \geq S_N(\rho_{AB}) \geq |S_N(\rho_A) - S_N(\rho_B)| \quad (2.10)$$

stating that the uncertainty of a composite system is less (or equal) than the uncertainty of the sum of its two individual subsystems: “The whole is greater than the sum of its parts”. Here, $S_N(\rho) = -\text{Tr}(\rho \ln \rho)$ denotes the von Neumann entropy, ρ_{AB} is the density matrix of the composite system and ρ_A (ρ_B) is the reduced density matrix of subsystem A (B).

Entanglement A composite quantum state, that is a state consisting of more than one subsystem (e.g. qubits), is called *entangled* iff it can not be written in the *separable* form of a *product state* [44]

$$|\psi_N\rangle = |\psi_n\rangle \otimes |\psi_{n-1}\rangle \otimes \cdots \otimes |\psi_1\rangle. \quad (2.11)$$

With regards to the Araki-Lieb inequality, consider a two qubit state

$$|\psi_{AB}\rangle = \cos\left(\frac{\theta}{2}\right) |0_A 0_B\rangle + \sin\left(\frac{\theta}{2}\right) |1_A 1_B\rangle, \quad (2.12)$$

which is entangled for $0 < \theta < \pi$ and separable only for $\theta = \{0, \pi\}$. Calculating the von Neumann entropy $S(\rho_{AB})$, $S(\rho_A)$ and $S(\rho_B)$, indeed reveals that the inequality holds. For a completely separable state the von Neumann entropy of the whole system and the reduced matrices is identical to zero. In contrast, a fully entangled state, that is $\cos(\theta/2) = \sin(\theta/2) = 1/\sqrt{2}$, has still zero uncertainty of the composite system but the reduced states are maximally mixed. This implies even though the whole state might be known with certainty, the individual subsystem can be completely unknown or in the words of Schroedinger “The best possible knowledge of a whole does not include

the best possible knowledge of its parts” [45].

It becomes clearer that entanglement is different from classical correlations when the mutual information of a maximally entangled state $\mathcal{I}(\rho_A, \rho_B : \rho_{AB}) = 2 \ln 2$ is calculated, which is twice the maximum possible mutual information between two classical variables. These stronger-than-classical correlations are generally regarded as the resource for QI. Note that for other values of θ , that is less entangled states, the von Neumann mutual information might not exceed the maximal value of Shannon’s mutual information.

The characterization, classification and measurement of entanglement is a wide field of research with still many open questions [44]. In the following only the most popular classes of entanglement are presented. For a two-qubit system the Bell states are the only maximally entangled states:

$$|\Phi^\pm\rangle = \frac{1}{\sqrt{2}} (|00\rangle \pm |11\rangle), \quad |\Psi^\pm\rangle = \frac{1}{\sqrt{2}} (|01\rangle \pm |10\rangle). \quad (2.13)$$

The classification becomes richer for $N \geq 3$ qubits, with the two most prominent classes of entanglement, *GHZ*-states and *Dicke* states:

$$|\text{GHZ}\rangle = \frac{1}{\sqrt{2}} (|0\rangle^{\otimes N} + |1\rangle^{\otimes N}), \quad |\text{D}^m\rangle = \frac{1}{\sqrt{\binom{N}{m}}} \sum_k P_k |0^{\otimes(N-m)} 1^{\otimes m}\rangle. \quad (2.14)$$

Here, P_k denotes the permutation operator generating all possible permutations of the states $|1_m\rangle$ and $|0_{(N-m)}\rangle$. Important examples of Dicke states are the *W*-states with $m = 1$ such that

$$|\text{W}\rangle = \frac{1}{\sqrt{N}} \left(|10\dots 00\rangle + |01\dots 00\rangle + \dots + |00\dots 10\rangle + |00\dots 01\rangle \right). \quad (2.15)$$

These two classes of states, GHZ-state and W-states, are very distinct not only in terms of their properties, but also in terms of preparing them, as these states can not be transformed into each other by means of local operations and classical communication (LOCC) only [46].

Yet another class of entangled states, *graph* and *cluster* states, will be introduced in the context of measurement-based quantum computation in chapter 6.

So far only pure states have been considered in the discussion. In the case of mixed states, finding criteria for *full separability* [44, 47], that is to answer the question if a mixed state is entangled or not, is a complex task and is beyond the scope of this thesis.

Nevertheless, mixed states bear an interesting extension of quantum correlations beyond entanglement known as **quantum discord** [31, 32, 48]. A brief introduction of quantum discord and its main properties is provided in chapter 7 [and references therein].

2.3. Quantum Computation

A quantum computer is a machine exploiting the laws of quantum mechanics in order to perform certain computational tasks notably³ faster than any classical computer. Instead of using classical bits based on ordinary transistors, the data is encoded by qubits, which can be realized into many different physical systems [see 15, for a comprehensive list]. The field of quantum computation, which is based on the initial work of Benioff [9], Manin [10], Feynman [11] and Deutsch [50] and was, at that time, a mere ‘Gedankenexperiment’, gained a huge boost after the discovery of Shor’s algorithm [51], showing that a quantum computer can indeed factorize a number exponentially faster than any known classical counterpart. Deutsch’s seminal paper in 1985 [50] proved that quantum computation is universal in the sense that the ‘Church-Turing thesis’ is not violated [12, Section 4.5.5 and references therein]. In other words, a quantum computer can solve any algorithm which is solvable on a classical machine, and vice-versa a classical computer can simulate any quantum device, given unlimited resources (energy, time etc.). As an important consequence, undecidable problems, which are in principal not solvable by a Turing-machine can not be solved on a quantum computer either; a famous example is that of the ‘halting-problem’ [52].

The main purpose of this section is to give a brief overview of the different quantum computational models, rather than a thorough introduction into the field of quantum computation which can be found in books [12, 53, 54]. A comprehensive list of known quantum algorithms and their original references can be found here [49].

Regardless of the computational model, a universal quantum computer has to fulfill the so called *DiVincenzo* criteria [55] in order to be functional. These are given as follows:

1. A scalable physical system with well characterized qubits.
2. The ability to initialize the state of the qubits to a fiducial state with high fidelity.
3. Long relevant decoherence times, much longer than the gate operation time.
4. A ‘universal’ set of quantum gates.
5. A qubit-specific measurement capability.

These five criteria are enough for computation alone, however DiVincenzo added two more requirements regarding quantum communication and networks:

6. The ability to interconvert stationary and flying qubits
7. The ability to faithfully transmit flying qubits between specified locations.

Over the past few decades many different models of quantum computation evolved, some of them sharing similarities or being almost identical up to some details, others being conceptually completely distinct. It seems impractical to list and categorize all of the existing theoretical models, nevertheless a few prominent ones shall be quickly summarized.

³The quantum speed-up can range from constant, polynomial, super-polynomial to exponential depending on the compared (classical and quantum) algorithms, see [49].

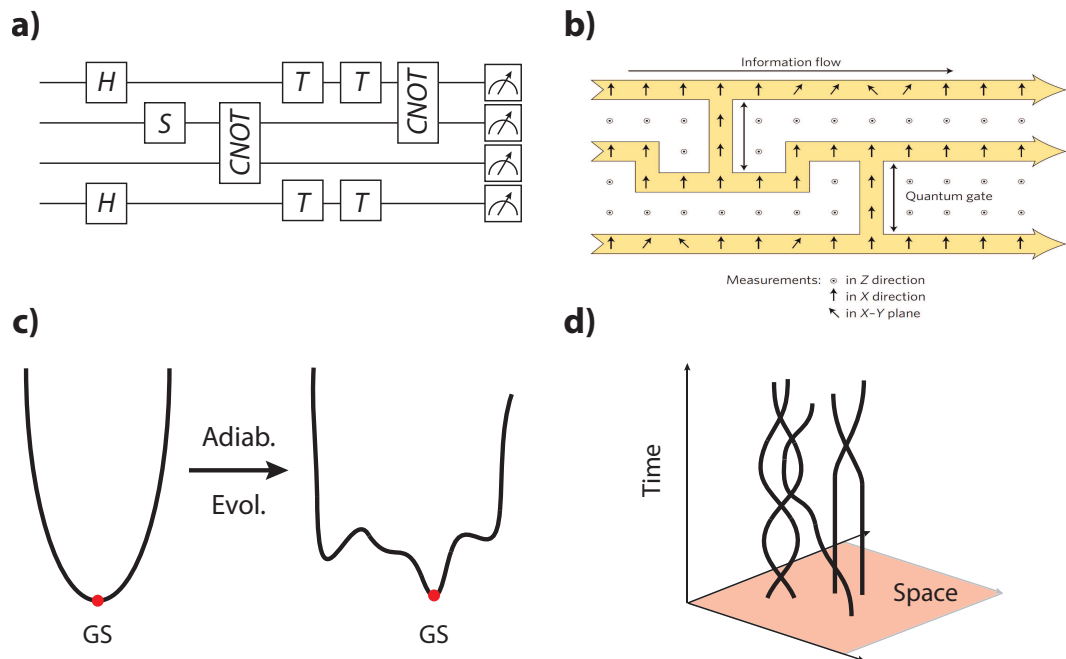


Figure 2.2.: Visual representations of different quantum computation models: **a)** The circuit or gate array model, **b)** the measurement-based or one-way quantum computational model (reprinted from [56, ©Nature Publishing Group]), **c)** the adiabatic and **d)** the topological quantum computational model.

Quantum circuit model The quantum circuit model, also known as the quantum gate array or network model, is the model taught in most classes related to QI. It is the closest model to the classical description of a computer [12, Chapter 4], and is often also referred to as the standard model of quantum computation. In this model, the quantum information is stored in an array of n -qubits called a quantum register, in analogy to a classical n -bit register. At the beginning of a computation the register is initialized into its initial state. A universal set of unitary (reversible) quantum gates acts on the register, or a subspace of the register (e.g. single qubits), and executes the computational steps. Such a set of gates allows for the implementation of all necessary logic gates and thus no other operations are required. The gates are applied in a time-ordered fashion defining a direction of information flow. At the end of the computation the quantum register is read out by performing measurements on the qubits. A visual representation of the circuit model is given in figure 2.2 a).

In contrast to classical computers, where universal computation can be implemented only by a single type of gates (for example a *NAND*, *NOR* or the *Toffoli* gate) its quantum counterpart needs at least one two-qubit gate and a set of single qubit gates to allow arbitrary rotations to be performed. Although the choice of a universal set of gates is not unique, a particular choice allows an optimal set of gates for a given hardware implementation to be chosen. A possible choice is the so called *standard set* [12] consisting of a Hadamard gate H , phase gate S , $\pi/8$ -gate T , and a

controlled-not gate *CNOT*:

$$\begin{aligned}
 H &= \frac{1}{\sqrt{2}} \begin{bmatrix} 1 & 1 \\ 1 & -1 \end{bmatrix} & S &= \begin{bmatrix} 1 & 0 \\ 0 & i \end{bmatrix} \\
 T &= \begin{bmatrix} 1 & 0 \\ 0 & e^{i\pi/4} \end{bmatrix} & \text{CNOT} &= \begin{bmatrix} 1 & 0 & 0 & 0 \\ 0 & 1 & 0 & 0 \\ 0 & 0 & 0 & 1 \\ 0 & 0 & 1 & 0 \end{bmatrix}.
 \end{aligned} \tag{2.16}$$

For quantum computation with trapped ions interacting with laser light fields (see chapter 3.2.1), where the interaction time t and the laser phase ϕ can be precisely controlled, the following set of unitary transformation is much more suitable than the standard set given above:

$$\begin{aligned}
 U(\theta, \phi) &= e^{-i\frac{\theta}{2}\sigma_\phi} = \begin{bmatrix} \cos\left(\frac{\theta}{2}\right) & -ie^{-i\phi}\sin\left(\frac{\theta}{2}\right) \\ -ie^{i\phi}\sin\left(\frac{\theta}{2}\right) & \cos\left(\frac{\theta}{2}\right) \end{bmatrix}, & U_z(\theta) &= e^{-i\frac{\theta}{2}\sigma_z} = \begin{bmatrix} e^{-i\frac{\theta}{2}} & 0 \\ 0 & e^{i\frac{\theta}{2}} \end{bmatrix} \\
 U_x^{MS}\left(\frac{\pi}{2}\right) &= e^{-i\frac{\pi}{4}\sigma_1^x\sigma_2^x} = \frac{1}{\sqrt{2}} \begin{bmatrix} 1 & 0 & 0 & -i \\ 0 & 1 & -i & 0 \\ 0 & -i & 1 & 0 \\ -i & 0 & 0 & 1 \end{bmatrix},
 \end{aligned} \tag{2.17}$$

where $\sigma_\phi = \cos(\phi)\sigma_x + \sin(\phi)\sigma_y$ and $\theta \propto t$ is directly proportional to the pulse length. The *MS*-gate $U_x^{MS}\left(\frac{\pi}{2}\right)$ is a fully entangling gate, see chapter 3.3, and is equivalent to a CNOT-gate up to local unitary transformations.

Measurement-based quantum computation In terms of quantum computation, the measurement-based quantum computation⁴ (MBQC) is a conceptually completely distinct approach, compared to the quantum circuit model described above. For a detailed introduction see chapter 6 and references therein.

In contrast to the previous model, where the initial state is a simple product state and two-qubit gates create entanglement, in the MBQC-framework the initial state is a highly entangled *cluster* or *graph* state [57], which provides the necessary computational resource from the beginning. The computational steps (or gates, to stay in the language of the circuit model) are performed solely by single-qubit measurements in certain bases. The measurements are performed sequentially, and in this way, define the information flow, see fig 2.2 b). Due to the randomness of quantum measurements, the measurement outcomes of each qubit have to be fed forward and the subsequent measurement bases have to be adjusted accordingly in order to guarantee a deterministic quantum gate.

It has been proven that an MBQC-device is equivalent to the circuit approach [58], i.e. it is universal and hence can efficiently simulate, up to a polynomial overhead, any algorithm implementable in the circuit framework and vice-versa. In fact, in some specific instances the MBQC-approach is superior to the gate-based model as it requires less resources [58].

⁴Nowadays set synonymously with the *one-way quantum computer* [29], for more information see Chapter 6.

The most notable difference between the two approaches is the creation of the resource used for the computation, that is entanglement. While in the circuit model, entanglement is created via unitary gates and the creation happens along the line of computation, in the MBQC-approach the initial state is highly entangled and provides the computational resource. The question which model is more feasible depends on the physical system used to implement QC.

There are a few schemes related to the MBQC-approach and the gate model:

- The teleportation-based scheme by Gottesmann [59], where single-rotations and Bell measurements are used to perform the computational steps. This model is a hybrid approach combining the circuit and the MBQC-model.
- Another scheme sharing properties of the two models is proposed in the context of linear optics by Knill, Laflamme and Milburne [60]. They realized that measurements of individual photons are non-linear processes that can be used to efficiently implement universal quantum computation.
- An idea introduced by Nielsen is based on projective (non-destructive) measurements and quantum memory [61] and is closely related to the proposal [29] described in the main text.

Adiabatic quantum computation The idea of an adiabatic quantum computer (AQC) was initially proposed by Farhi *et. al* [62] and relies on the adiabatic theorem. It is closely related to *quantum annealing*, a metaheuristic to find the ground state of a given Hamiltonian by exploiting quantum superposition.

The basic concept of AQC goes as follows: first, a potentially non-trivial Hamiltonian is engineered whose ground state describes the solution to a computationally hard problem of interest. In the next step, a quantum system is initialized in the trivial ground state of a simpler Hamiltonian which allows for an easy implementation. Finally, the simple Hamiltonian is adiabatically transformed into the engineered one and, by the principle of the adiabatic theorem, the system stays in the ground state during the entire evolution, hence yielding the desired solution. For visualization of this process see figure 2.2 c).

A prominent example is the adiabatic evolution of a transverse field Hamiltonian $H_z = B \sum_i \sigma_z^i$, whose ground state is a trivially polarized spin-state along the B-field axis, into a transverse Ising Hamiltonian $H_{\text{Ising}} = \sum_{i,j} J_{ij} \sigma_x^i \sigma_x^j + B \sum_i \sigma_z^i$ with long range coupling J_{ij} . Such a Hamiltonian has a highly non-trivial, entangled ground state exhibiting spin frustration in the case of antiferromagnetic coupling $J_{ij} < 0$ [63], which can not be easily prepared. An experimental demonstration of the adiabatic evolution has been shown by Islam *et al.* [64] in which they started from a H_z Hamiltonian and slowly increased the spin-spin coupling.

An AQC-computer is often thought as a quantum device only capable of finding the solution to an optimization problem rather than as a universal quantum computer. However, it was shown that the AQC-model is polynomially equivalent to the circuit model and thus it is universal [65].

The AQC-model has been recently brought into the spotlight by claims of D-wave having built the first commercially available quantum computer on the market. Although, as of now, it is not

yet clear how much of D-wave's devices is indeed quantum [66], it has been repeatedly shown that it does not outperform classical computers with the best possible algorithms [67].

Topological quantum computer The topological quantum computer (TQC) is yet another intrinsically different concept of computation proposed by Kitaev in 1997 [68]. Compared to the previously introduced models, TQC is the most distinct one, as the quantum information is not stored in physically located or trapped particles but is encoded into quasiparticles, specifically anyons [69, 70].

Anyons are quasiparticles which can only exist confined in a 3-dimensional space-time, that is two spatial dimensions and one time dimension. In contrast to Fermions and Bosons, they do not obey the Fermi-Dirac statistics nor the Bose-Einstein statistics; that is under the exchange of identical anyons the global phase factor is different from $\phi = 0$ (Bosons) and $\phi = \pi$ (Fermions)

$$|\psi_1\psi_2\rangle = e^{i\phi} |\psi_2\psi_1\rangle. \quad (2.18)$$

Nevertheless, anyons behave in a similar way to Fermions, as two identical particles can not occupy the same quantum state; consequently, the world lines of anyons can not cross or merge. However, it is possible to braid the world lines in the 3 dimensional space-time and this allows for implementing a computational circuit. In 2003 it was shown that certain *non-abelian* anyons can make up a complete set of universal gates and hence can simulate any other quantum computer model efficiently [71]. In contrast to abelian anyons, where the global phase factor changes under particle exchange, non-abelian anyons have the additional property that their quantum state also depends on the particle permutation. There is evidence of experimental observation of non-abelian anyons in the 5/2-fractional quantum Hall effect [72, 73], although this is not yet completely conclusive.

The advantage the TQC has over the qubit based models is that the braids are topologically protected, as external noise does not change the topological properties of braids. This makes the TQC-model more resilient against experimental errors and error correction might be less of an issue. However, in certain cases, namely the case of Ising anyons that arise at the end of the so-called Kitaev wire, the topologically protected gates are not sufficient for universal computing. In order to perform the remaining gates, the topologically protected subspace must be left. Once this subspace has been left, the system is subject once again to noise. From this view point, TQC with Ising anyons might be less suitable for computation but for quantum memory.

DQC1 *Deterministic quantum computation with one quantum bit* is not a full scale quantum computational model, as it is not universal and surely less powerful compared to the others, but rather a concept broadening our understanding of quantum information and necessary quantum resources.

Even though the model assumes only one single qubit is available for QC, or equivalently, one pure qubit and n -arbitrary bits in a completely mixed state, it was shown that, for certain tasks, such as spectral density estimation, it outperforms any (known) classical algorithm [33].

Despite the lack of entanglement as a resource, it was soon suggested that these states exhibit quantum discord which delivers the necessary resources [34, 40]. It was the first model to show

that entanglement is not the only useful source of quantum correlations, and the model is often seen as a bridge between classical computation and the ‘standard’ quantum computers.

2.4. Quantum Simulation

For almost a century, quantum mechanics has served as one of *the* most fundamental theories available. Despite its capability to explain an enormous range of phenomena, when it comes down to actually computing a problem, very soon insurmountable limits are reached. This is due to the exponential growth of the Hilbert space as the system size is increased. An ordinary desktop computer might handle 20-30 particles with *only* two degrees of freedom (provided no clever tricks are used) and the worldwide most powerful computer-clusters might manage a few tens more. Compared to the number of particles in actual physics and chemistry (and even biology) problems, where hundreds, thousands, and more is still a low number, one realizes how limited our capabilities are.

With the onset of the quantum computational idea, Feynman soon realized that a quantum computer shows the same exponential growth of the Hilbert space, with desirable consequences: “Let the computer itself be built of quantum mechanical elements which obey quantum mechanical laws” [11]. However, he was not very specific about how such a device could compute or simulate any other quantum system, and it was more than a decade later when Lloyd [74] showed that an universal quantum computer can efficiently solve any arbitrary Hamiltonian with local interactions i.e. interaction strengths decaying fast enough with distance.

Over the past two decades quantum simulation (QS) has been implemented in a variety of systems, and a vast amount of theoretical and experimental literature has been produced; a comprehensive list of implementations and publications (as of 2014) can be found in [75].

A common classification found in literature is to separate quantum simulations into two kinds: analogue quantum simulations (AQS), often also referred to as emulations, and digital quantum simulations (DQS), which are closely related to quantum computation in general.

Analogue quantum simulation The basic principle behind the AQS approach is to use a highly controllable quantum system mimicking (emulating) another quantum system of interest, by directly mapping the system Hamiltonian H_{sys} onto the simulator Hamiltonian H_{sim} [75, 76]

$$H_{\text{sys}} \leftrightarrow H_{\text{sim}}. \quad (2.19)$$

In fact, mapping is nothing else than finding the one-to-one correspondence of the operators in H_{sys} and H_{sim} and equating coefficients if necessary. An example with regards to trapped ion simulators is presented in chapter 5.

The advantage here is that parameters of H_{sim} are precisely controllable, such that H_{sim} can be tuned into regimes which are impossible or impractical to be reached and observed in a real-world system, H_{sys} . Evolving the simulator under $U = e^{-iH_{\text{sim}}t/\hbar}$ yields the dynamics of the system to be investigated. Despite the power of this approach, an AQS is always a special purpose device

designed to solve one specific problem, as the mapping is obviously not universal. Moreover, the accuracy (or fidelity) of the simulation depends strongly on the mapping, since in most instances approximations have to be made; barely any Hamiltonian describing the simulator is identical to a system Hamiltonian. In addition, experimental errors and noise will affect the simulation in a manner which can not be quantified and therefore can not be corrected for (think of error correction in QC). The question really is, as soon as quantum simulators solve classically intractable problems, how can we trust or verify the results? A possible solution to this epistemological problem is to perform cross-checks on different platforms, which are subject to different kinds of errors and mapping. But finding a suitable mapping is not always trivial, sometimes clever schemes involving additional external control fields and an ancillary system to mediate the interaction are required. Nevertheless, even though AQS might suffer from errors diminishing the fidelity, in many instances quantitative results are not required. For questions like, ‘will a certain parameter regime lead to a quantum phase transition?’, a qualitative answer is still of high value and can be obtained despite the errors.

Digital quantum simulation The time evolution of a state under a given Hamiltonian H_{sys} is nothing but a unitary transformation of an initial state. As mentioned in the previous section, any unitary operation can be decomposed into a set of universal gates, that is single-qubit and two-qubit gates, and in principle anything can be simulated. From this perspective, a digital quantum simulator (DQS) is nothing different from a ‘ordinary’ quantum computer, however the term DQS is more common in the context of simulating the time dynamics of a physical system compared to an abstract algorithm solving a purely mathematical problem. It shall be noted that not all unitaries can be efficiently (with polynomial resources) implemented, but only those with local character - that is, a Hamiltonian whose interactions decay quickly enough over distance.

Consider a Hamiltonian $H = \sum_j^m H_j$ written as a sum of local interactions. If the individual terms commute $[H_j, H_i] = 0$ then the unitary time evolution can be written as

$$U(t) = e^{-iHt/\hbar} = e^{-i\sum_j^m H_j t/\hbar} = \prod_j^m e^{-iH_j t/\hbar}. \quad (2.20)$$

In such a case, the decomposition into the universal set of gates is straightforward. However, this is rarely the case as for most interesting Hamiltonians $[H_j, H_i] \neq 0$ holds. The solution to this problem is to break up the evolution into smaller time steps $U(t) = \{\exp(-iH\Delta t/\hbar)\}^{t/\Delta t}$. The exponent can be approximately decomposed into local gates by the first order Trotter approximation [12]

$$U(\Delta t) = e^{-i\sum_j^m H_j \Delta t/\hbar} = \prod_j^m e^{-iH_j \Delta t/\hbar} + \mathcal{O}((\Delta t)^2). \quad (2.21)$$

As $\Delta t \rightarrow 0$ the approximation becomes exact. Unfortunately, the drawback is that the smaller Δt is, the more gates have to be applied to simulate a certain time evolution $U(t)$. Since every experimental gate has a non-vanishing amount of errors, it is always a trade-off between good approximations and low cumulative errors. However, it is possible to find more efficient decompositions in certain instances by taking higher order approximations into account.

One very important advantage of the DQS-approach in comparison to AQS, is the possibility to quantify errors and apply error correction schemes if necessary.

3. Theoretical framework

The experiments presented in this thesis are based upon the interaction between trapped ions and laser fields. It is thus necessary to introduce the theoretical framework regarding ion trapping and atom-light interactions. Many of the subjects discussed in this chapter, such as ion traps, (quantum) harmonic oscillators, and matter-light interactions serve only as a short reminder to the reader as they are treated extensively in a number of books and theses. Others, however, will be presented in more detail, such as the vibrational modes of multi-ion strings modes and tunable spin-spin interaction, since they present key features for the techniques used in this thesis. Even though all derivations presented here can be found in the literature, they are scattered across different publications and the main purpose of this chapter is to provide a coherent overview for the reader. Furthermore, appendix B.1 will supply detailed and extended derivations of the spin-spin interaction specifically for our experiment.

3.1. Trapped ions

In this section, the reader will be briefly reminded of the basic concepts regarding ion trapping with radio frequency (RF) traps. Following this, the notation of the quantum harmonic oscillator is introduced, which accurately describes the motion of the laser-cooled ion in such a trap. An extended part of this section is dedicated to the description and derivation of collective (normal) motional modes, which play an important role in the quantum simulation experiments described in chapter 5.

3.1.1. Paul trap

As most of the following discussion regarding ion trapping has been treated in great detail, see [77–79, and others], only the most important parts will be recapped. In freespace, electrostatic potentials must obey the Laplace equation, $\nabla^2\Phi = 0$, stating that the divergence of electrostatic fields has to add up to zero. In other words, electrostatic fields have to ‘flow’ from a source to a drain. As a consequence, a static quadrupole potential of the form:

$$\Phi(x, y, z) = \sum_{i=x,y,z} \Phi_0 k_i r_i^2 \quad (3.1)$$

has a metastable saddle point, as one of the coefficients k_i must be negative. However, by allowing the potential to be time-varying in one or more directions, it is possible to generate a stable trapping potential¹. The potential Φ can be divided into a dynamical radial part Φ_{rad} and a static axial

¹Wolfgang Paul and Hans Georg Dehmelt received the Nobel prize “for the development of the ion trap technique”.

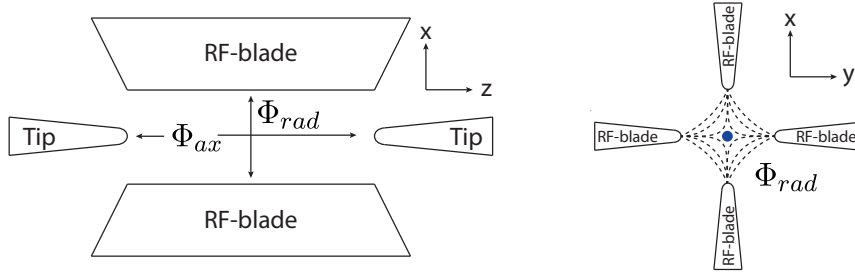


Figure 3.1.: Schematic of a linear radio frequency trap, also known as a Paul trap, shown from two perspectives. The tips create a static quadrupole potential and confine the ions in the *axial* or *z*-direction, and the RF-blades generate a potential confining the ions in the *xy*-plane often referred as the *radial* direction.

part Φ_{ax} [79], see also figure 3.1:

$$\Phi_{rad}(x, y, z, t) = \frac{V_{RF} \cos(\Omega_{RF}t) + U_r}{2} (\alpha_x x^2 + \alpha_y y^2 + \alpha_z z^2) \quad (3.2)$$

$$\Phi_{ax}(x, y, z) = \frac{U_{DC}}{2} (\beta_x x^2 + \beta_y y^2 + \beta_z z^2). \quad (3.3)$$

Here, V_{RF} and Ω_{RF} are the amplitude and the frequency of the RF field, respectively, U_r is a splitting voltage applied to the RF-blades and U_{DC} is the voltage applied to the tips for the axial confinement.

In order to satisfy the Laplace condition at any instant in time, the geometric factors, α_i and β_i , must obey the relation $\sum_i \alpha_i = \sum_i \beta_i = 0$. In a linear Paul trap, this leads to the following relations

$$\alpha_x = -\alpha_y, \quad \alpha_z = 0, \quad (3.4)$$

$$-(\beta_x + \beta_y) = \beta_z > 0. \quad (3.5)$$

The motion of a trapped particle with mass m and charge Q is described by Mathieu's differential equation [79]. Stable solutions can be found for $0 < a_i < q_i < 1$, with the dimensionless parameters given by

$$a_{x,y} = \frac{4\beta_{x,y}QU_{DC}}{mR_{ax}^2\Omega_{RF}^2} = -\frac{1}{2}a_z, \quad q_x = -q_y = \frac{2\alpha_x QV_{RF}}{mR_{rad}^2\Omega_{RF}^2}, \quad q_z = 0, \quad (3.6)$$

where R_{rad} (R_{ax}) corresponds to the ion-blade (ion-tip) distance. Finally, the particle's trajectory can be approximated by

$$r_i(t) \approx \tilde{r}_i \cos(\omega_i t) \left(1 + \frac{q_i}{2} \cos(\Omega_{RF}t) \right), \quad (3.7)$$

consisting of two motions: a harmonic motion with amplitude r_i and frequency ω_i , called *secular motion*, and an additional driven amplitude modulation, with frequency Ω_{RF} , called *micromotion*. The secular frequency is given by

$$\omega_i = \frac{\Omega_{RF}}{2} \sqrt{a_i + \frac{q_i^2}{2}}. \quad (3.8)$$

Using equation 3.6 and 3.8 results in

$$\omega_z = \omega_{ax} = \sqrt{\frac{2\beta_z U_{DC} Q}{mR_{ax}^2}}, \quad \omega_x = \omega_y = \omega_{rad} = \sqrt{\frac{(q_x \Omega_{RF})^2}{8} - \frac{\omega_z}{4}}. \quad (3.9)$$

From equation 3.9 we can directly see how the axial trapping potential influences the radial potential, i.e. increasing the axial confinement lowers the radial frequency.

The secular approximation neglects the micromotion and reinterprets the secular motion as being generated by a harmonic potential $\Psi = \sum_i \frac{1}{2Q} m \omega_i r_i^2$, where Ψ is often referred to as the *pseudopotential*.

3.1.2. Quantum harmonic oscillator

The low temperatures of a trapped ion achievable by laser cooling require a quantum description of the harmonic pseudopotential introduced in the previous section. The quantum equivalent is known as the quantum harmonic oscillator (QHO), one of the most important model systems in quantum mechanics, and is treated in almost every textbook regarding basic quantum mechanics [80–82]. A classical particle of mass m set in a one-dimensional harmonic potential $V(x_c) = \frac{1}{2} m \omega^2 x_c^2$ is described by its position coordinate, x_c , and angular oscillation frequency, ω . A convenient way to describe the periodic oscillation of the particle is to express its motion in the complex phase space plane spanned by the position x_c and momentum coordinate p_c . The particle follows a circular trajectory centred at the origin (Fig. 3.2 a). In order to realise a quantum mechanical description,

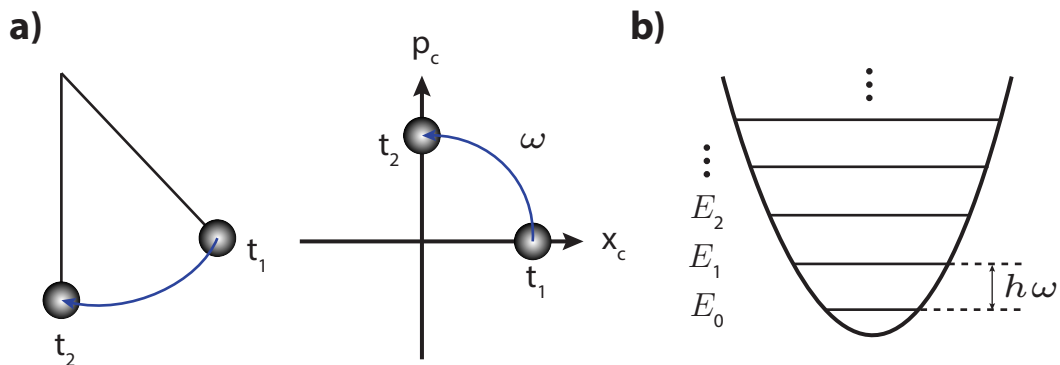


Figure 3.2.: a) A classical particle with mass m swings on a pendulum described by a harmonic potential. The periodic oscillation can be mapped onto the phase space spanned by the position x_c and momentum coordinate p_c . The particle's trajectory follows a circle centred around the origin. b) The quantum mechanical counterpart has a quantized energy with equidistant spacing $E_n = \hbar\omega(n + 1/2)$.

x_c and p_c are replaced by their corresponding operators \hat{x} and $\hat{p} = -i\hbar \frac{\partial}{\partial x}$. These operators are Hermitian and obey the following commutation relation

$$[\hat{x}, \hat{p}] = i\hbar. \quad (3.10)$$

In analogy to the classical case, the energy of the system is described by the Hamiltonian

$$H_{\text{QHO}} = \frac{\hat{p}^2}{2m} + \frac{1}{2} m \hat{x}^2 \omega^2. \quad (3.11)$$

Instead of solving Schrödinger's differential equation, it is more convenient to directly extract the energy eigenvalues with the 'creation/annihilation' operators introduced by Paul Dirac

$$a = \sqrt{\frac{m\omega}{2\hbar}} \left(\hat{x} + \frac{i}{m\omega} \hat{p} \right), \quad a^\dagger = \sqrt{\frac{m\omega}{2\hbar}} \left(\hat{x} - \frac{i}{m\omega} \hat{p} \right). \quad (3.12)$$

By rearranging equation 3.12, \hat{x} and \hat{p} can be expressed as

$$\hat{x} = \sqrt{\frac{\hbar}{2m\omega}} (a^\dagger + a), \quad \hat{p} = i\sqrt{\frac{\hbar m\omega}{2}} (a^\dagger - a). \quad (3.13)$$

Finally, combining Eq. 3.11 and 3.12 we get the familiar form of the QHO Hamiltonian

$$H_{\text{QHO}} = \hbar\omega \left(a^\dagger a + \frac{1}{2} \right) = \hbar\omega \left(\hat{n} + \frac{1}{2} \right), \quad (3.14)$$

where $\hat{n} = a^\dagger a$ is the number operator. The energy spectrum of this Hamiltonian has a ladder-like structure with equidistant spacing $\hbar\omega$, and a zero point energy $E_0 = \frac{1}{2}\hbar\omega$ (Fig. 3.2 b). The eigenstates $|n\rangle$ are called *number states* or *Fock states* and the following relations are valid

$$\begin{aligned} a|0\rangle &= 0, \\ a|n\rangle &= \sqrt{n}|n-1\rangle, \\ a^\dagger|n\rangle &= \sqrt{n+1}|n+1\rangle, \\ \hat{n}|n\rangle &= n|n\rangle. \end{aligned} \quad (3.15)$$

Each Fock state can be generated by applying the creation operator n -times onto the vacuum state $|0\rangle$

$$|n\rangle = \frac{1}{\sqrt{n!}} a^\dagger |n-1\rangle = \frac{1}{\sqrt{n!}} (a^\dagger)^n |0\rangle. \quad (3.16)$$

For a trapped ion, the spatial extent of the ground state wave function, $x_0 = \sqrt{\hbar/2m\omega}$, can range from a few to tens of nm, depending on the choice of secular trapping frequency ω (set by the electrode voltages). When working with the ladder operators it useful to know their commutation relations:

$$[a, a^\dagger] = 1, \quad [\hat{n}, a^\dagger] = a^\dagger \quad \text{and} \quad [\hat{n}, a] = -a. \quad (3.17)$$

Driven QHO Consider an external time-dependent force

$$F_d(t) = A_d \sin(\omega_d t + \phi_d) = \frac{A_d}{2i} \left[e^{i(\omega_d t + \phi_d)} - e^{-i(\omega_d t + \phi_d)} \right] \quad (3.18)$$

of amplitude A_d , frequency ω_d and phase ϕ_d . When such a force is applied to a QHO, the Hamiltonian given in Eq. 3.14 has to be extended by an additional interaction energy $H_d = -\hat{x}F_d(t)$, and the new Hamiltonian becomes $H = H_{\text{QHO}} + H_d(t)$. The effect of the time-dependent perturbation caused by the oscillating force can be best seen in the interaction picture. Here, the transfor-

mation $U = \exp(-iH_{QH}t/\hbar)$ is used to rewrite the state vector $\Psi_I(t) = U\Psi(t)$, the observable $\langle A_I(t) \rangle = \langle U^\dagger A(t) U \rangle$ and the Hamiltonian

$$H_I = U^\dagger H_d U = \left(a e^{-i\omega t} + a^\dagger e^{i\omega t} \right) x_o F(t). \quad (3.19)$$

If the drive frequency is resonant with the secular frequency, $\omega_d = \omega$, a rotating wave approximation (RWA) can be applied and the Hamiltonian reduces to

$$H_I = \frac{A_d x_o}{2i} \left(a e^{-i\phi_d} + a^\dagger e^{i\phi_d} \right). \quad (3.20)$$

The unitary time evolution under this Hamiltonian, $U = \exp(-iH_I t/\hbar)$, can be expressed in terms of the *displacement operator*

$$D(\alpha) = e^{\alpha a^\dagger} - e^{\alpha^* a} \quad (3.21)$$

with a dimensionless amplitude $\alpha = \frac{A_d x_o t}{2\hbar} e^{-i\phi_d}$. The action of the displacement operator on the

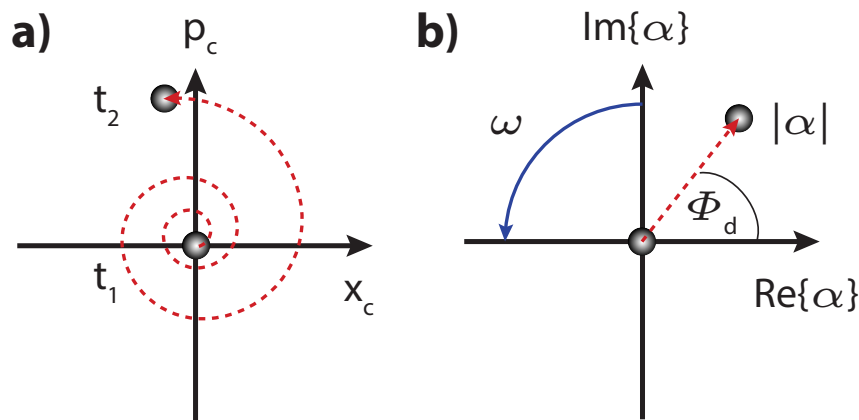


Figure 3.3.: **a)** The effect of a resonant driving force in the classical case. The particle moves on a spiral trajectory with ω starting from the origin at time t_1 , to its final position t_2 , steadily increasing in amplitude. **b)** In the co-rotating frame, the displacement operator $D(\alpha)$ pushes the ground state $|0\rangle$ on a straight line to a coherent state $|\alpha\rangle$. The phase ϕ_d determines the angle of the trajectory.

ground state $|0\rangle$ creates a displaced coherent state $|\alpha\rangle$ (Fig. 3.3 b)

$$D(\alpha) |0\rangle = |\alpha\rangle = e^{-|\alpha|^2/2} \sum_n \frac{\alpha^n}{\sqrt{n!}} |n\rangle. \quad (3.22)$$

The probability to find a certain Fock state $p_\alpha(n) = \frac{\alpha^{2n}}{n!} e^{-|\alpha|^2}$ follows a Poisson distribution with a mean phonon number $\bar{n}_C = |\alpha|^2$ and a variance $\sigma^2 = |\alpha|^2$. A coherent state $|\alpha\rangle$ is the closest analogy to a classical state in a quantum harmonic oscillator, and it obeys the following relations

$$\begin{aligned} a |\alpha\rangle &= \alpha |\alpha\rangle, \\ \langle \alpha | a^\dagger &= \alpha^* \langle \alpha|. \end{aligned} \quad (3.23)$$

In addition to Fock and coherent states, a very important class of states are thermal states. Thermal states are completely mixed and lack any coherence. They arise by coupling the quantum harmonic oscillator to an external thermal reservoir; in the case of trapped ions, this could be electric field noise (see section 4.6.3). For a thermal state, the probability to find a certain Fock state with a mean phonon number \bar{n} is given by a geometrical distribution

$$p_n(\bar{n}) = \frac{\bar{n}^n}{(\bar{n} + 1)^{n+1}} \quad (3.24)$$

with a variance $\sigma^2 = \bar{n}^2 - \bar{n}$. Figure 3.4 compares the distributions of a Fock state $|n\rangle = |10\rangle$ (a), a coherent state $|\alpha\rangle = |\sqrt{10}\rangle$ (b) and a thermal state with $\bar{n} = 10$ (c).

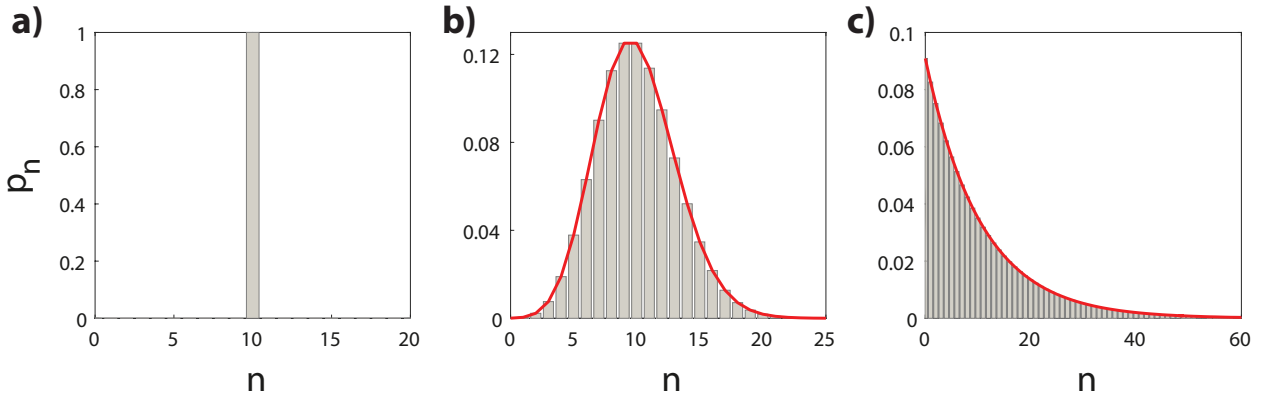


Figure 3.4.: The probability p_n to find a fock state $|n\rangle$ is shown for three different states: **a)** Fock state $|n\rangle = |10\rangle$, **b)** Coherent state $|\alpha\rangle = |\sqrt{10}\rangle$ and **c)** Thermal state with $\bar{n} = 10$

3.1.3. Normal/collective motional modes

Up to now the simple case of a single trapped ion has been treated. However, multiple ions confined in the same trapping potential will influence each other, due to their charged nature. This leads to a set of $3N$ motional modes describing the motion of the ion string in 3 dimensions.

The section is divided into two parts: first, the equilibrium positions of N ions trapped in a harmonic potential are calculated. Once these positions are obtained, they are used to derive the *collective* or *normal* motional modes of motion. The discussion here will go along the lines of [83, 84].

Equilibrium positions Consider a chain of N ions trapped in a linear Paul trap with a highly anisotropic potential, $\omega_{rad} \gg \omega_{ax}$ such that the ions are strongly bound in the transverse direction and form a linear chain in the z -direction (axial). The position of the i th ion is denoted by $z_i(t)$. Due to the Coulomb interaction between charged particles, the motion of each ion will be influenced by its neighbours and the external trapping potential. Hence, the potential energy of the ion chain is given by

$$V = \frac{m\omega_z^2}{2} \sum_{i=1}^N z_i(t)^2 + \frac{(Ze)^2}{8\pi\epsilon_0} \sum_{\substack{j,i=1 \\ n \neq i}}^N \frac{1}{|z_j(t) - z_i(t)|} \quad (3.25)$$

where m is the ion mass, ω_z is the axial trapping frequency, Z is the degree of ionization, e is the electron charge and ε_0 is the permittivity of free space. Assuming that the ions are sufficiently cold, the position $z_i(t)$ can be approximated by

$$z_i(t) \approx z_i^{(0)} + \xi_i(t) \quad (3.26)$$

where $z_i^{(0)}$ is the equilibrium position and $\xi_i(t)$ is a small displacement. After defining the length scale l by

$$l^3 = \frac{(Ze)^2}{4\pi\varepsilon_0 m \omega_z^2}, \quad (3.27)$$

the dimensionless equilibrium position can be expressed as $u_i = z_i^{(0)}/l$. In order to find the equilibrium positions the following equation has to be solved

$$\begin{aligned} \left[\frac{\partial V}{\partial z_i} \right]_{z_i=z_i^{(0)}} = 0 & \iff \\ u_i - \sum_{j=1}^{i-1} \frac{1}{(u_i - u_j)^2} + \sum_{j=i+1}^N \frac{1}{(u_i - u_j)^2} = 0 \end{aligned} \quad (3.28)$$

where $i = (1, 2 \dots N)$. For two and three ions the equation above can be solved analytically leading to equilibrium positions for $N = 2$

$$u_1 = -u_2 = 2^{-\frac{2}{3}}, \quad d_2 = \left(\frac{(Ze)^2}{2\pi\varepsilon m \omega_z^2} \right)^{\frac{1}{3}} \quad (3.29)$$

where d_N denotes the minimum distance, and for $N = 3$

$$u_1 = -u_3 = \left(\frac{4}{5} \right)^{-\frac{1}{3}}, \quad u_2 = 0, \quad d_3 = \left(\frac{5(Ze)^2}{2\pi\varepsilon m \omega_z^2} \right)^{\frac{1}{3}}. \quad (3.30)$$

For $N > 3$ ions, solutions can only be found numerically using solvers for non-linear equations. However, the authors in [85] developed useful empirical formulas for $z_i^{(0)}$

$$\begin{aligned} z_i^{(0)} &= 3.94N^{0.387} \sin \left(\frac{1}{3} \sin^{-1} \left\{ 1.75N^{-0.982} \left[m - \frac{N+1}{2} \right] \right\} \right) l \\ &\approx 2.29 \left(m - N + \frac{1}{2} \right) N^{-0.596} \left(\frac{(Ze)^2}{4\pi\varepsilon m \omega_z^2} \right)^{\frac{1}{3}} \end{aligned} \quad (3.31)$$

where the approximation holds for ions close to the center of the trapping potential. Using equation 3.31 the minimum ion-ion separation d_N can be derived as

$$d_N \approx 2.29N^{-0.596} \left(\frac{(Ze)^2}{4\pi\varepsilon m \omega_z^2} \right)^{\frac{1}{3}}. \quad (3.32)$$

These formulas are especially useful as a rule of thumb estimate regarding single ion addressability and imaging.

Normal motional modes Similar to the section above, the ions' movement in 3 dimensions is described by a small displacement ξ from the equilibrium position $\rho_{i,\lambda}(t) = \rho_{i,\lambda}^{(0)} + \xi_{i,\lambda}(t)$, where the subscript λ denotes the dimension $x, y, z = 1, 2, 3$ and $i = 1, 2 \dots N$ is the ion index. The Lagrangian describing the ion motion is then given by

$$L = T - V = \frac{m}{2} \sum_{\lambda=1}^3 \sum_{i=1}^N \dot{\xi}_{i\lambda}^2 - \frac{m}{2} \sum_{\lambda=1}^3 \sum_{i=1}^N \omega_{\lambda}^2 \left(\rho_{i\lambda}^{(0)} + \xi_{i\lambda} \right)^2 - \frac{Z^2 e^2}{8\pi\epsilon_0} \sum_{\substack{i,j=1 \\ i \neq j}}^N \left\{ \sum_{\lambda=1}^3 \left(\rho_{i\lambda}^{(0)} + \xi_{i\lambda}(t) - \rho_{j\lambda}^{(0)} - \xi_{j\lambda}(t) \right)^2 \right\}^{-\frac{1}{2}}. \quad (3.33)$$

Using a Taylor expansion² around the equilibrium position, and neglecting constant terms as they do not affect the dynamics, leads to

$$L = \frac{m}{2} \sum_{\lambda=1}^3 \sum_{i=1}^N \dot{\xi}_{i,\lambda}^2 - \frac{1}{2} \sum_{\lambda=1}^3 \sum_{i,j=1}^N \omega_{\lambda}^2 \left. \frac{\partial^2 V}{\partial \rho_{i\lambda} \partial \rho_{j\lambda}} \right|_0 \xi_{i\lambda} \xi_{j\lambda} + \mathcal{O} \left[\xi_{i\lambda}^3 \right]. \quad (3.34)$$

In a highly anisotropic trapping potential

$$\left(\frac{\omega_{ax}}{\omega_{rad}} \right)^2 = \left(\frac{\omega_3}{\omega_{1,2}} \right)^2 =: \alpha \ll 1, \quad (3.35)$$

the Lagrangian given in Eq. 3.34, may be approximated [86] and expressed in terms of the axial trapping frequency $\omega_z = \omega_3$ as

$$L \approx \frac{m}{2} \left[\sum_{i=1}^N \dot{\xi}_{i3}^2 - \omega_3^2 \sum_{i,j=1}^N A_{ji} \xi_{i3} \xi_{j3} \right] + \frac{m}{2} \sum_{\lambda=1}^2 \left[\sum_{i=1}^N \dot{\xi}_{i\lambda}^2 - \omega_{\lambda}^2 \sum_{i,j=1}^N B_{ji} \xi_{i\lambda} \xi_{j\lambda} \right]. \quad (3.36)$$

The first term in brackets describes the movement along the axial direction and the second term along the transverse direction. Using the dimensionless equilibrium positions u_i derived in the

²Here, only the first order expansion is relevant. Higher order terms describe mode cross-coupling as described in [86].

previous section, the tensors A_{ji} and B_{ji} can be expressed in terms of the u_i

$$A_{ji} = \begin{cases} 1 + 2 \sum_{\substack{m=1 \\ m \neq i}}^N \frac{1}{|u_i - u_m|^3} & \text{if } i = j \\ \frac{-2}{|u_i - u_j|^3} & \text{if } i \neq j \end{cases} \quad (3.37)$$

$$B_{ji} = \left(\frac{1}{\alpha} + \frac{1}{2} \right) \delta_{ji} - \frac{1}{2} A_{ji} \quad (3.38)$$

where δ_{ji} is the Kronecker delta. Since the matrix A_{ji} is real, symmetric and positive definite, its eigenvalues μ_m must be positive. Thus, the eigenvectors $b_i^{(m)}$ are defined by

$$\sum_{j=1}^N A_{ji} b_j^{(m)} = \mu_m b_i^{(m)}, \quad m = 1, 2, \dots, N \quad (3.39)$$

where the eigenvectors are numbered in order of increasing eigenvalue. The eigenvectors build a complete basis and, if properly normalized, it follows that

$$\sum_{m=1}^N b_j^{(m)} b_i^{(m)} = \delta_{ji}, \quad \sum_{i=1}^N b_i^{(m)} b_i^{(n)} = \delta_{mn}. \quad (3.40)$$

From equation 3.38 it is evident that the transversal modes have the same eigenvectors as the axial modes, but different eigenvalues γ_m , which can be related to the axial eigenvalues by

$$\gamma_m = \frac{1}{2} + \frac{1}{\alpha} - \frac{\mu_m}{2}. \quad (3.41)$$

If the trap anisotropy exceeds a critical value $\alpha_{\text{crit}} = 2/(\mu_N - 1)$, the matrix B_{ji} becomes a non-positive definite, implying unstable transverse oscillations. (Note: using the definition above, the transverse eigenvalues are in order of decreasing eigenvalues).

The *normal* or *collective* motional modes in direction λ can be expressed by the eigenvectors as

$$Q_m^{(\lambda)}(t) = \sum_{i=1}^N b_i^{(m)} \xi_{i\lambda} \quad (3.42)$$

and the *motional frequency* of the m th mode is defined by

$$\omega_m^{(3)} = \sqrt{\mu_m} \omega_3, \quad \omega_m^{(1,2)} = \sqrt{\gamma_m} \omega_{1,2} \quad (3.43)$$

Figure 3.5 shows the mode vectors for a string of 7 ions and the axial/radial mode frequencies for two different anisotropic parameters $\alpha \approx 0.004$ and $\alpha \approx 0.07$. The axial (radial) modes with higher (lower) motional frequencies will be referred to as shorter spatial wavelength modes. It is important to note that the axial and radial modes have an opposite ordering, such that the lowest frequency mode in axial direction is the center of mass (COM) mode, whereas in radial direction this mode has the highest frequency.

Some useful rule of thumb relation can be given for the shorter wavelength modes in the axial direction

$$\omega_2^{\text{ax}} = \sqrt{3}\omega_{\text{COM}}^{\text{ax}}, \quad \omega_3^{\text{ax}} \approx \sqrt{\frac{24}{5}}\omega_{\text{COM}}^{\text{ax}}, \quad \omega_4^{\text{ax}} \approx \sqrt{\frac{47}{5}}\omega_{\text{COM}}^{\text{ax}}, \quad (3.44)$$

where ω_2^{ax} is often referred to as the *stretch* or *breathing* mode. Similarly, for the radial direction

$$\omega_2^{\text{rad}} = \sqrt{(\omega_{\text{COM}}^{\text{rad}})^2 - (\omega_{\text{COM}}^{\text{ax}})^2}, \quad \omega_3^{\text{rad}} \approx \sqrt{(\omega_{\text{COM}}^{\text{rad}})^2 - (\omega_2^{\text{ax}})^2}. \quad (3.45)$$

The mode ω_2^{rad} is also known as the *tilt* mode. In Eq. 3.44 and 3.45 the first two terms are exact expressions independent of system size N , whereas the others yield useful approximations with decreasing validity for very high N [83].

An interesting behaviour that occurs for all even modes m with odd N is that the middle ion doesn't participate in the motion, that is

$$b_{\text{center}}^{(m)} = 0, \quad \text{if } N = \text{odd} \quad \text{and} \quad m = \text{even} \quad (3.46)$$

As a last remark, the Taylor expansion in 3.34 can be extended to higher order terms describing

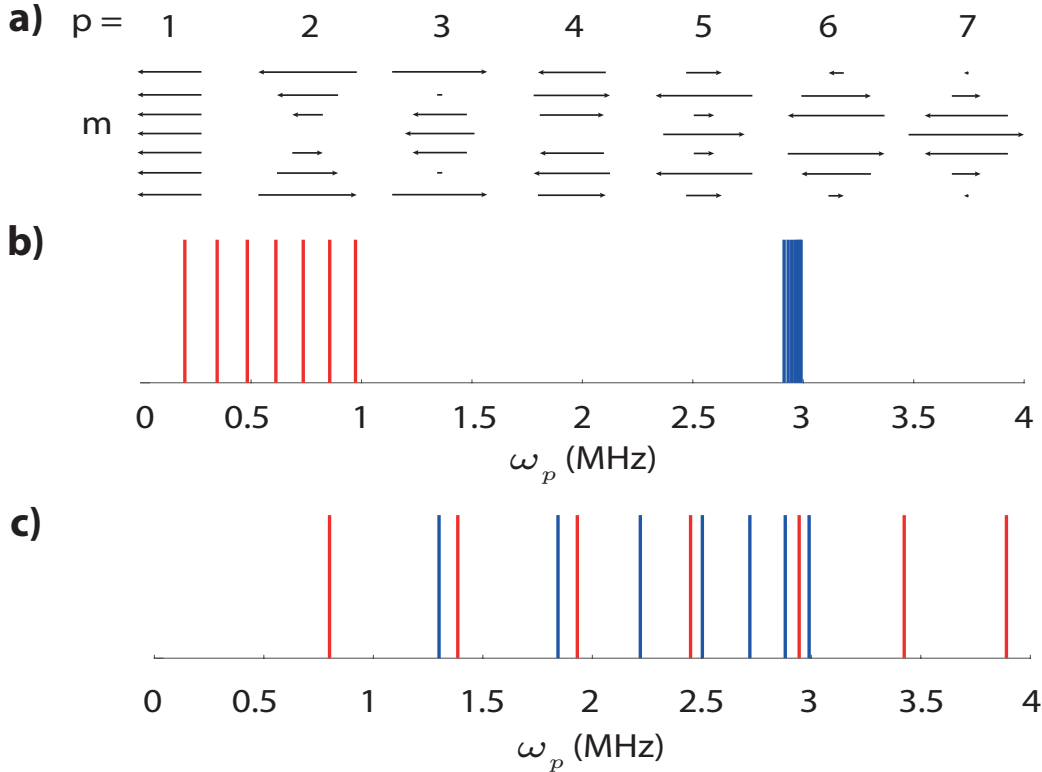


Figure 3.5.: a) The eigenvectors $b_i^{(m)}$ in transverse direction are shown for a string of 7 ions. b) & c) The axial mode frequencies $\omega_m^{(3)}$ (red) and transverse $\omega_m^{(1)} = \omega_m^{(2)}$ (blue) are calculated for two anisotropic parameters $\alpha \approx 0.004$ and $\alpha \approx 0.07$, respectively.

three-mode mixing [86] and higher order cross-coupling. This may lead to additional decoherence of the motional degree of freedom and provides a possible explanation for the observations presented later in this thesis, see table 8.1.

3.2. Laser - ion interaction

This section introduces the theoretical framework of a trapped two-level atom interacting with a coherent light field (laser). First, the interaction of the electronic degrees of freedom with a laser is reviewed. In a second step, the same procedure is applied to the motional degrees of freedom. These two sections are then combined to introduce and derive the Mølmer-Sørensen interaction (MS). This interaction allows us to generate effective interactions between the internal electronic states of ions in a string - which would otherwise not couple at all³. It also provides a tool for entangling gates with the highest observed fidelities [16, 17, 88]. Finally, a different derivation of a ‘detuned’ MS-interaction in the adiabatic limit, which leads to tunable spin-spin interactions, will be given.

3.2.1. Two level atom - laser interaction

A pseudo-spin (or qubit) is encoded in two long-lived⁴ electronic levels of the atom. The natural Hamiltonian of these two levels is given by

$$H_A = \frac{\hbar\omega_0}{2}\sigma_z, \quad (3.47)$$

where σ_z is the z-Pauli operator with eigenstates $|\uparrow\rangle = |+\rangle_z$ and $|\downarrow\rangle = |-\rangle_z$ split by an energy $\hbar\omega_0$. A laser light field with electric field $E = E_0 \cos(\omega_L t + \phi_L)$, frequency ω_L and phase ϕ_L induces a perturbation described by the Hamiltonian

$$H_L = \hbar\Omega\sigma_x \cos(\omega_L t + \phi_L), \quad (3.48)$$

where the coupling strength between the two-level atomic transition and the light field is expressed by the Rabi frequency $\Omega \propto E_0$. Combining the bare atom and perturbation Hamiltonians into a total Hamiltonian, $H_{\text{tot}} = H_A + H_L$, and transforming H_{tot} with $U = \exp(-iH_A t/\hbar)$ into the interaction picture yields

$$H_{Int} = \hbar\frac{\Omega}{2} [\cos(\Delta t + \phi_L)\sigma_x + \sin(\Delta t + \phi_L)\sigma_y]. \quad (3.49)$$

Here, $\Delta = \omega_L - \omega_0$ denotes the detuning of the laser frequency from the bare atomic transition. In the rotating wave approximation (RWA) all terms rotating at the sum frequency $\omega_L + \omega_0$ are neglected, as they average out over the time scale set by Δ , leading to equation 3.49. Introducing the electronic lowering and raising operators $\sigma_{\pm} = (\sigma_x \pm i\sigma_y)/2$, equation 3.49 can be restated as

$$H_{Int} = \hbar\frac{\Omega}{2} [e^{-i(\Delta t + \phi_L)}\sigma_+ + e^{i(\Delta t + \phi_L)}\sigma_-]. \quad (3.50)$$

³There is a tiny dipole-dipole coupling between the internal states which is negligible in our experiments. Nevertheless, these weak couplings were experimentally demonstrated in [87].

⁴The states live for much longer than the time it takes to manipulate and measure them.

A laser on resonance, $\Delta = 0$, induces coherent population exchange between the $|\uparrow\rangle$ and $|\downarrow\rangle$ states by applying the unitary time evolution

$$U = \exp\left(-i\frac{H_{Int}t}{\hbar}\right) = \begin{pmatrix} \cos\frac{\Omega t}{2} & -ie^{i\phi_L}\sin\frac{\Omega t}{2} \\ -ie^{i\phi_L}\sin\frac{\Omega t}{2} & \cos\frac{\Omega t}{2} \end{pmatrix} \quad (3.51)$$

where $\Omega T = \theta$ sets the polar angle on the Bloch sphere. In other words, Ωt determines the probability to find the state $|\uparrow\rangle/|\downarrow\rangle$ and ϕ_L defines the rotation axis (x , y or any other direction on the equatorial plane).

However, if the excitation is non-resonant, $\Delta \neq 0$, the solution of the optical Bloch equations [89, 90] reveals that the probability to find the state $|\uparrow\rangle$

$$p_{\uparrow} = \frac{\Omega^2}{\Omega^2 + \Delta^2} \sin^2\left(\frac{1}{2}\sqrt{\Omega^2 + \Delta^2}t\right) = \frac{\Omega^2}{\Omega_{\text{eff}}^2} \sin^2\left(\frac{1}{2}\Omega_{\text{eff}}t\right) \quad (3.52)$$

oscillates at a higher frequency $\Omega_{\text{eff}} = \sqrt{\Omega^2 + \Delta^2}$ and is reduced in amplitude by $1/\Omega_{\text{eff}}$. In the regime of $\Delta \gg \Omega$, the probability p_{\uparrow} is largely suppressed. Nevertheless, the present oscillating field induces energy shifts of the atomic levels due to the *ac-Stark* effect. In order to see the action of a far detuned light field, it is convenient to change the interaction picture once again. This gives the ac-Stark Hamiltonian

$$H_{AC} = \hbar\frac{\Delta}{2}\sigma_z + \hbar\frac{\Omega}{2}\sigma_x \quad (3.53)$$

with new eigenvalues $\lambda_{\pm} = \pm\frac{1}{2}\sqrt{\Omega^2 + \Delta^2}$. The upper (lower) energy level is shifted by Ω^2/Δ ($-\Omega^2/\Delta$) giving a total ac-Stark shift of

$$\delta_{AC} = 2\frac{\Omega^2}{\Delta}. \quad (3.54)$$

From the Hamiltonian H_{AC} it is evident that the second term becomes negligible for $\Delta \gg \Omega$ and the effective Hamiltonian is consequently proportional to σ_z . This is equivalent to a rotation around the z-axis with an angle of rotation $\phi = \Delta t/2$.

The situation in a real atom is far more complex as there are additional energy levels which can off-resonantly couple to the light field and induce ac-Stark shifts. This issue will be discussed in great detail in section 4.4.2.

3.2.2. Trapped ions - laser Hamiltonian

Combining the previous sections 3.1.2 and 3.2.1 leads to the Hamiltonian describing a bare atom trapped in a harmonic confinement

$$H_0 = \hbar\frac{\omega_0}{2}\sigma_z + \hbar\omega_t\left(a^\dagger a + \frac{1}{2}\right) \quad (3.55)$$

where ω_t is the ion's motional frequency (trapping frequency) and ω_0 is the unperturbed atomic transition frequency. The additional oscillating motion of the trapped ion leads to a frequency modulation of ω_0 which generates motional sidebands either side of the atomic transition at $\omega_0 \pm \omega_t$. In order to take these sidebands into account, equation 3.50 has to be modified to

$$H_L = \hbar \frac{\Omega}{2} (\sigma_+ + \sigma_-) \left[e^{i\eta(a+a^\dagger)} e^{-i(\Delta t + \phi_L)} + e^{-i\eta(a+a^\dagger)} e^{i(\Delta t + \phi_L)} \right]. \quad (3.56)$$

The Lamb-Dicke parameter $\eta = \vec{k} \cdot \vec{e}_\alpha x_0 = \frac{2\pi}{\lambda} \sqrt{\hbar/2m\omega_t} \cos(\theta_k)$ relates the ground state expansion x_0 to the wave vector \vec{k} of the driving field, where \vec{e}_α is the direction of the ion's motion in $\alpha = \{x, y, z\}$. As such, it scales the coupling strength of the laser field driving a motional sideband. A unitary transformation of $H = H_0 + H_L$ with $U = \exp(iH_0 t/\hbar)$ results in the interaction Hamiltonian

$$H_{\text{Int}} = U^\dagger H U = \hbar \frac{\Omega}{2} \left\{ e^{-i(\Delta t - \phi_L)} \sigma_+ \exp \left[i\eta \left(a e^{-i\omega_t t} + a^\dagger e^{i\omega_t t} \right) \right] + h.c. \right\} \quad (3.57)$$

after application of the rotating wave approximation.

In the Lamb-Dicke regime, $\eta^2 (2\bar{n} + 1) \ll 1^5$, equation 3.57 can be further simplified by Taylor expanding

$$\exp \left[i\eta \left(a e^{-i\omega_t t} + a^\dagger e^{i\omega_t t} \right) \right] = 1 + i\eta \left(a e^{-i\omega_t t} + a^\dagger e^{i\omega_t t} \right) + \mathcal{O}(\eta^2) \quad (3.58)$$

and neglecting higher order terms $\mathcal{O}(\eta^2)$, which correspond to changes in the motional quantum number by more than ± 1 . Thus, the trapped ion - laser Hamiltonian simplifies to

$$H_{\text{Int}} = U^\dagger H U = \hbar \frac{\Omega}{2} \left\{ (e^{-i(\Delta t - \phi_L)} \sigma_+ \left[1 + i\eta \left(a e^{-i\omega_t t} + a^\dagger e^{i\omega_t t} \right) \right] + h.c. \right\}. \quad (3.59)$$

In the resolved sideband regime ($\omega_t \gg \Omega$) we can identify three resonant transitions:

- $\Delta = 0$: The laser frequency is in resonance with the bare atomic frequency and the carrier transition $|S, n\rangle \leftrightarrow |D, n\rangle$ is driven. This can be described by the Hamiltonian

$$H_{\text{car}} = \hbar \frac{\Omega_n}{2} \left(\sigma_+ e^{i\phi_L} + \sigma_- e^{-i\phi_L} \right) \quad (3.60)$$

where $\Omega_n = \Omega(1 - \eta^2 n)$ takes the reduction in coupling strength, caused by population of higher Fock states $n > 0$, into consideration (this is a result of taking higher orders into account in Eq. 3.58).

- $\Delta = \omega_t$: The laser frequency is in resonance with the *blue* sideband driving the transition $|S, n\rangle \leftrightarrow |D, n+1\rangle$. The effective Hamiltonian is given by:

$$H_{\text{BSB}} = \hbar \frac{\Omega_{n,n+1}}{2} \left(a^\dagger \sigma_+ e^{i\phi_L} - a \sigma_- e^{-i\phi_L} \right). \quad (3.61)$$

The coupling strength $\Omega_{n,n+1} = \eta \sqrt{n+1} \Omega$ depends on the Lamb-Dicke parameter and the Fock state $|n\rangle$.

⁵Essentially, this ensures the laser does not couple too strongly to the motional state.

- $\Delta = -\omega_t$: The laser frequency is in resonance with the *red* sideband driving the transition $|S, n\rangle \leftrightarrow |D, n-1\rangle$. The effective Hamiltonian is given by:

$$H_{\text{RSB}} = \hbar \frac{\Omega_{n,n-1}}{2} \left(a\sigma_+ e^{i\phi_L} - a^\dagger \sigma_- e^{-i\phi_L} \right) \quad (3.62)$$

and the coupling strength is $\Omega_{n,n-1} = \eta \sqrt{n}\Omega$.

These three resonances allow us to manipulate the ion's internal and external degrees of freedom. As we will see in the following section, this allows coupling to the electronic state of different ions via the motional states, which act as a *bus system* mediating interactions.

3.3. Entangling Gates and effective spin-spin Hamiltonians

All previously established discussions regarding ion trapping, QHOs, normal modes and laser - ion interaction will now be combined to introduce, step wise, the main tools for quantum computations and quantum simulation. After introduction to the notion of a bichromatic laser field consisting of two fields *Bic-* and *Bic+* with different frequencies, this section is divided into three parts:

firstly, the bichromatic light is ‘symmetrically’ detuned from a single normal mode at ω_t by Δ_t as depicted in figure 3.6 a). This will lead to the well known MS-interaction used in chapter 6. Secondly, an ‘asymmetric’ detuning, also called center-line detuning δ_c , will be introduced which off-resonantly drives the MS-interaction (see Fig. 3.6 b). By treating the interaction in the adiabatic limit, the effective transverse field Ising Hamiltonian H_{Ising} and the *XY*-Hamiltonian H_{XY} , depending on δ_c , will be derived. In the last part, the bichromatic light will couple to N -normal modes leading to tunable spin-spin interaction ranges $J_{ij} \propto \frac{1}{|i-j|^\alpha}$ with $0 \leq \alpha \leq 3$. These three cases are depicted in figure 3.6 c).

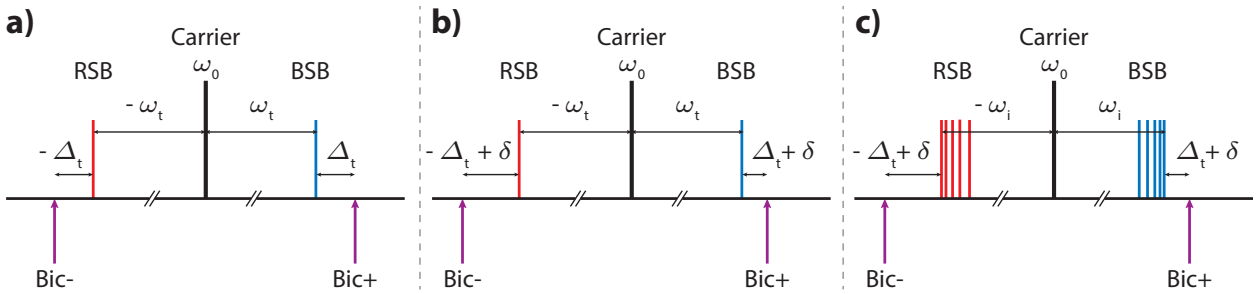


Figure 3.6.: This figure illustrates the interactions described in the following sections. **a)** The bichromatic laser field has a ‘symmetric’ detuning Δ_t from a single normal mode leading to the MS-interaction. **b)** By introducing an additional detuning $\delta_c \ll \Delta_t$ (known as a centre-line detuning) and treating the MS-interaction in the adiabatic limit, the transverse field Ising Hamiltonian and the *XY*-Hamiltonian can be derived. **c)** When N -normal modes couple to the bichromat, the spin-spin interaction range decays approximately according to a power law with distance $J_{ij} \propto \frac{1}{|i-j|^\alpha}$. The interaction range, α , is determined by Δ_t and can have values $0 \leq \alpha \leq 3$.

3.3.1. Bichromatic light field

A bichromatic light field is generated by superimposing two light fields with different frequencies. We define the two fields $E_{\pm}(t) = E_0 \sin[(\omega_0 \pm \Delta_t)t + \phi_{\pm}]$ as being detuned by $\pm\Delta_t$ from a common

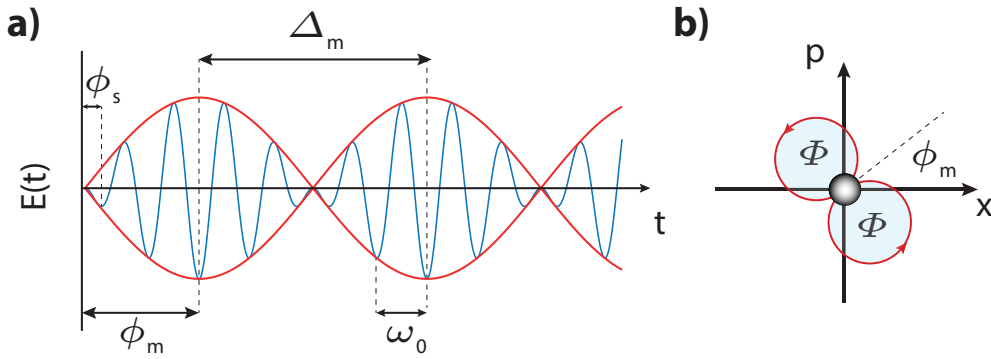


Figure 3.7.: **a)** The two parts of a bichromat induce an amplitude modulated oscillation with carrier frequency ω_0 and envelope frequency Δ_t . The motional phase ϕ_m defines the ‘start’ of the envelope and the spin phase ϕ_s sets the basis of the spin operator $\sigma_\phi = 2(\sigma_x \cos(\phi_s) + \sigma_y \sin(\phi_s))$, **b)** The state-dependent force pushes the two eigenstates $|+\rangle_x$ and $|-\rangle_x$ (of σ_x) on a circular trajectory with the same direction of rotation. Due to this, they pick up a geometric phase Φ with same sign.

frequency ω_0 . Then, the superposition $E(t) = E_+ + E_- = 2E_0 \cos(\omega_0 t + \phi_s) \cos(\Delta_t t + \phi_m)$ is an amplitude modulated oscillation with carrier frequency ω_0 , an envelope frequency Δ_t and two phases $\phi_m = \frac{\phi_+ + \phi_- + \pi}{2}$ and $\phi_s = \frac{\phi_+ - \phi_-}{2}$, as depicted in figure 3.7 a). The spectral power density of such a bichromatic light field consists of two spectral peaks, *Bic+* and *Bic-*, which are detuned by Δ_t from the motional sideband (see Fig. 3.6).

By setting $\Delta = \omega_t \pm \Delta_t$ in equation 3.59 and matching $\Omega_{n,n+1} = \Omega_{n,n-1}$, we derive the bichromatic Hamiltonian

$$H_{\text{Bic}} = H_{\text{Int}}^+ + H_{\text{Int}}^- = \hbar \frac{\eta \Omega}{2} \left(\sigma_+ e^{i\phi_s} + \sigma_- e^{-i\phi_s} \right) \left(a e^{i\Delta_t t} e^{i\phi_m} + a^\dagger e^{-i\Delta_t t} e^{-i\phi_m} \right). \quad (3.63)$$

The phases ϕ_+ and ϕ_- are independent and thus we can set $\phi_m = \phi_s = 0$. This simplifies equation 3.63 to

$$H_{\text{Bic}} = \hbar \eta \Omega \sigma_x \left(a e^{i\Delta_t t} + a^\dagger e^{-i\Delta_t t} \right). \quad (3.64)$$

The action of the bichromatic Hamiltonian can be understood in terms of an off-resonantly driven harmonic oscillator. Instead of linearly displacing the wave function in phase space, such as for a resonant drive, the atomic wave function performs circular motions under the off-resonant bichromatic driving. The wave function periodically overlaps with its origin at times $t = 2\pi/|\Delta_t|$ and the ‘initial’ trajectory is defined by the motional phase ϕ_m , see Fig. 3.7 b).

In contrast to a classical oscillator, in the quantum regime a closed path adds an additional phase Φ to the wave function. This phase is also known as the *geometrical* or *Berry* phase and is proportional to the enclosed area. The spin operators in equation 3.63 and 3.64 cause the driving force to be spin-dependent, i.e. it is conditional on the internal state. This becomes particularly interesting when the bichromatic light acts on more than a single ion, as will be discussed in the upcoming sections. By adjusting the phase ϕ_s one can change the basis of the spin operators by using the relation

$$\sigma_+ e^{i\phi_s} + \sigma_- e^{-i\phi_s} = 2(\sigma_x \cos(\phi_s) + \sigma_y \sin(\phi_s)) =: \sigma_\phi. \quad (3.65)$$

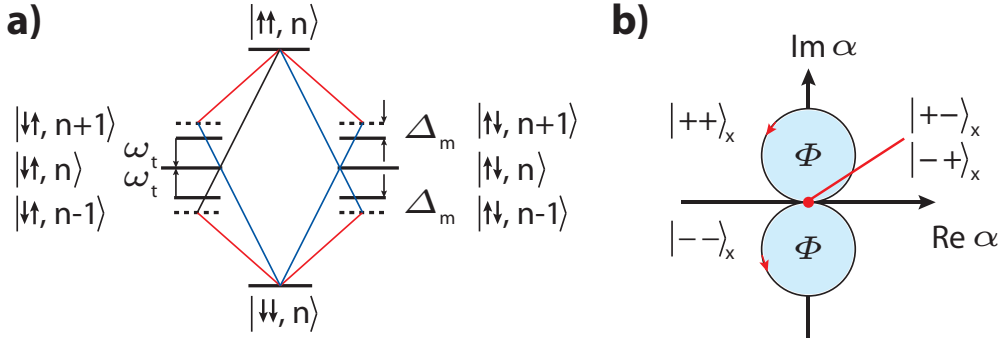


Figure 3.8: **a)** Scheme of Mølmer-Sørensen interaction. The states $|\uparrow\uparrow\rangle \leftrightarrow |\downarrow\downarrow\rangle$ are coupled via constructive interference of the four possible paths created by the bichromatic light. The transient states $|n+1\rangle$ and $|n-1\rangle$ are only virtually populated and the spin-motion gets disentangled after $t = 2\pi/|\Delta_\ell|$. Similarly the states $|\uparrow\downarrow\rangle \leftrightarrow |\downarrow\uparrow\rangle$ can be constructively interfered. **b)** The electronic eigenstates $|++\rangle_x$ and $|--\rangle_x$ experience the same state-dependent force pushing them into a circular trajectory in phase space. After enclosing an area $\propto (\eta\Omega/\Delta_m)^2$, these states pick up a geometrical phase Φ (up to a global phase).

It is worth mentioning that the bichromatic light can also be applied resonantly to the motional mode of a single ion creating macroscopically superposed states also known as *cat states* [91, 92]. Indeed, I was part of the research project during the time of my thesis which exploited such states to enhance spectroscopy at the single atom/photon level [92].

3.3.2. Mølmer - Sørensen interaction

The common motion of trapped ions can be used to entangle the ions with high fidelity [16, 17, 88] by applying the techniques independently proposed by A. Sørensen & K. Mølmer [93, 94], and E. Solano *et al.*[95]. In contrast to the ideas of Cirac and Zoller [13] the MS-interaction is insensitive (to first order) to phonon state preparation [96] and does not require single-ion control with a laser beam.

Here, I will briefly summarize the derivation published in [97, 98] for the simple case of two ions coupled via a bichromatic light field to the COM mode. The MS-interaction induces correlated spin flips between the states $|\uparrow\uparrow\rangle \leftrightarrow |\downarrow\downarrow\rangle$ and $|\uparrow\downarrow\rangle \leftrightarrow |\downarrow\uparrow\rangle$ by constructively interfering the paths generated by the bichromatic light as shown in figure 3.8 a). The interaction is described by an effective spin-spin Hamiltonian $H \propto \sigma_x \otimes \sigma_x$, where the unitary time evolution $U(t = \frac{\pi}{4}) = U^{\text{MS}} = \exp(i\frac{\pi}{4}\sigma_x \otimes \sigma_x)$ creates fully entangled states⁶.

We start with the Hamiltonian given in Eq. 3.64, applying it to two ions, and one of their shared COM vibrational modes

$$H_{\text{MS}} = \hbar\eta\Omega \left(ae^{i\Delta_\ell t} + a^\dagger e^{-i\Delta_\ell t} \right) \left(\sigma_x^{(1)} + \sigma_x^{(2)} \right). \quad (3.66)$$

The Hamiltonian given above is exactly integrable leading to the unitary time evolution

$$U^{\text{MS}}(t) = \hat{D}(\alpha(t)S_x) \exp(i\Phi(t)S_x^2) \quad (3.67)$$

⁶When applied to the initial states $|\uparrow\uparrow\rangle$, $|\uparrow\downarrow\rangle$, $|\downarrow\uparrow\rangle$ or $|\downarrow\downarrow\rangle$.

with the spin operator $S_x = \sigma_x^{(1)} + \sigma_x^{(2)}$, a displacement operator $\hat{D}(\alpha) = e^{\alpha a^\dagger - \alpha^* a}$ with time dependent amplitude $\alpha(t) = \frac{\eta\Omega}{\Delta_t} (e^{i\Delta_t t} - 1)$ and a time-dependent phase $\Phi(t) = \left(\frac{\eta\Omega}{\Delta_t}\right)^2 (\Delta_t t - \sin(\Delta_t t))$. After a time $\tau_{\text{gate}} = 2\pi/\Delta_t$, the displacement operator becomes zero and the wavefunction closes a full circle in phase space, overlapping with its origin. At this point in time, the spin and motion are always factorisable or separable, independent of the initial state. However, the wavefunction picks up a phase

$$\Phi(\tau_{\text{gate}}) = 2\pi \left(\frac{\eta\Omega}{\Delta_t}\right)^2 =: 2\pi J. \quad (3.68)$$

The propagator given in Eq. 3.67 can be then reduced to $U(\tau_{\text{gate}}) = \exp(iJS_x^2)$ and we get an effective Hamiltonian

$$H_{\text{eff}} = -\hbar J \sigma_x \otimes \sigma_x. \quad (3.69)$$

Here, we neglected constant terms in the time evolution which only lead to an off-set energy (global phase). Setting the Rabi frequency to $\Omega = |\Delta_t|/(4\eta)$ creates a maximally entangled state at interaction time τ_{gate} . The derivation can be easily extended to $N > 2$ ions by redefining the spin operator $S_x^N = \sum_i^N \sigma_x^i$ ⁷.

An MS-gate acting on an N ion product state creates GHZ-type states $|\Psi_{\text{GHZ}}\rangle = (|\downarrow\rangle^{\otimes N} + |\uparrow\rangle^{\otimes N})/\sqrt{2}$ [21]. In order to achieve other entangled states such as W-states or cluster states, additional pulses, including single spin rotation and ‘hiding’ pulses, have to be applied - for more details see chapter 6.

An intuitive approach to the MS-interaction is given in figure 3.8 b). The electronic ground state $|\downarrow\rangle_z$ can be rewritten in the basis of σ_x by $|\downarrow\rangle = (|+\rangle_x + |-\rangle_x)/\sqrt{2}$. A bichromatic laser field coupling to the COM mode induces a spin-dependent force, which is only capable of moving the states $|++\rangle_x$ and $|--\rangle_x$. These states pick up a phase Φ , whereas $|+-\rangle_x$ and $|-+\rangle_x$ remain stationary⁸ - this is equivalent to a conditional phase gate, which is capable of entangling pairs of qubits.

3.3.3. Adiabatic elimination and effective transverse field Ising Hamiltonian

Here, I will discuss the case when an additional ‘asymmetric’ detuning δ_c , called centerline detuning, is added to the bichromatic light: $\omega_t \pm \Delta_t + \delta_c$, with $\Delta_t \gg \delta_c$ (see figure 3.6 b)). Similar to the previous sections, the new Hamiltonian is derived by summing Eq. 3.61 and 3.62 and replacing $\Delta = \omega_t \pm \Delta_t + \delta_c$. After applying the rotating wave approximation one finds

$$H_{\text{asymBic}} = \hbar \frac{\eta\Omega}{2} \left(a e^{i\Delta_t t} + a^\dagger e^{-i\Delta_t t} \right) \left(S^+ e^{-i\delta_c t} + S^- e^{i\delta_c t} \right), \quad (3.70)$$

⁷The Hamiltonian contains all spin-spin interactions of all ion pairs. In addition, as the COM-mode is used, all pairs interact with equal strength, regardless of their physical separation distance in the string.

⁸Since the net force on these states cancels to zero for the COM mode (note that the exact opposite is true if the stretch mode is used).

where $S^\pm = \sum_i^N \sigma_i^\pm$ are the collective operators acting on N ions. The phases ϕ_m and ϕ_s are set to zero for simplicity. In order to calculate the time evolution of 3.70 the Magnus expansion is applied

$$U(t) = T \left[e^{-i \int_a^t dt_1 H(t_1)/\hbar} \right] = e^{-(\Omega_1 + \Omega_2 + \Omega_3 \dots)} \quad (3.71)$$

where $\Omega_1(t) = \frac{i}{\hbar} \int_0^t dt_1 H(t_1)$ and $\Omega_2(t) = \frac{1}{2\hbar^2} \int_0^t dt_1 \int_0^{t_1} dt_2 [H(t_1), H(t_2)]$ (a detailed derivation is given appendix B.1).

A key point in the following discussion is that $\eta\Omega \ll \Delta_t$ - i.e. the resonant coupling strength on the sideband is much weaker than the detuning from the sideband. In this *adiabatic limit* or *weak coupling regime*, terms rotating at $\exp\{i(\Delta_t \pm \delta_c)t\}$ average out in the integral 3.71 and can therefore be neglected. More intuitively, the circular trajectory in phase space is small enough such that the wavefunction maintains a high overlap with its original state at all times in the dynamics. As a direct consequence, the spin motion gets only virtually entangled and the system can be described by an effective pure spin-spin Hamiltonian at all times in the dynamics, and not only at τ_{gate} as in the MS-interaction. Moreover, time-independent terms in $\Omega_1(t)$ and $\Omega_2(t)$ give rise only to a global phase which can be neglected. After Taylor expanding the remaining terms in $\Omega_2(t)$ with respect to δ_c/Δ_t and taking the time derivative, the final Hamiltonian can be written as

$$H_{\text{spin-spin}} = \frac{J}{2} \sum_{i,j}^N \left(\sigma_i^+ \sigma_j^+ e^{-2i\delta_c t} + \sigma_i^+ \sigma_j^- + \sigma_i^- \sigma_j^+ + \sigma_i^- \sigma_j^- e^{2i\delta_c t} \right) \quad (3.72)$$

with the effective spin-spin coupling $J = \frac{\Omega\eta}{\Delta_t}$. There are three regimes which can be identified:

- $\delta_c = \mathbf{0}$: This is the simplest case, leading to the same Hamiltonian as in the MS-interaction

$$\begin{aligned} H_{\text{XX}} &= \frac{J}{2} \sum_{i,j}^N \left(\sigma_i^+ \sigma_j^+ + \sigma_i^+ \sigma_j^- + \sigma_i^- \sigma_j^- + \sigma_i^- \sigma_j^+ \right) \\ &= \frac{J}{2} \sum_{i,j}^N \sigma_i^x \sigma_j^x. \end{aligned} \quad (3.73)$$

- $\delta_c \gg \mathbf{J}$: By applying the RWA on the terms oscillating at $e^{\pm 2i\delta_c t}$ the XY-Hamiltonian is derived:

$$H_{\text{XY}} = \frac{J}{2} \sum_{i,j}^N \left(\sigma_i^+ \sigma_j^- + \sigma_i^- \sigma_j^+ \right). \quad (3.74)$$

- $\delta_c \approx \mathbf{J}$: The Hamiltonian 3.72 can be brought into a time-independent form by rewriting it as $H_{\text{spin-spin}} = (H_{\text{spin-spin}} - H_0) + H_0$ and moving to an interaction picture with respect to $H_0 = -\frac{\delta_c}{2} \sum_i \sigma_i^z$

$$\begin{aligned} H_{\text{Ising}} &= U_0^\dagger (H_{\text{spin-spin}} - H_0) U_0 \\ &= \frac{J}{2} \sum_{i,j}^N \sigma_i^x \sigma_j^x + B \sum_i \sigma_i^z. \end{aligned} \quad (3.75)$$

Here, the relation $e^{i\frac{\alpha}{2}\sigma^z}\sigma^\pm e^{i\frac{\alpha}{2}\sigma^z} = e^{i\alpha}\sigma^\pm$ was used for the transformation and H_0 was chosen in order to make H_{Ising} time-independent.

The additional parameter δ_c allows us to tune the interaction into regimes with different effective Hamiltonians. It corresponds to an effective transverse B-field $B = \frac{\delta_c}{2}$.

3.3.4. Tunable interaction range

So far, only the case where the bichromatic light couples to the COM-mode was considered, such that all ions move with the same amplitude and phase, reflected as a single Lamb-Dicke parameter η which is equal for all ions in the string. However, all other modes have a mode structure different from the COM mode resulting in a non-uniform η_i , as described in section 3.1.3. If the bichromatic beam couples to these modes, their structure will be ‘imprinted’ onto the spin-spin coupling matrix J_{ij}^m .

Figure 3.9 shows two different examples of the imprinted J_{ij}^m for each individual mode m and their cumulative sum weighted by the detuning Δ_m . The coupling matrix J_{ij} approximately follows a power law decay with spin-spin distance $|i - j|$ [99–102],

$$J_{ij} \propto \frac{1}{|i - j|^\alpha}. \quad (3.76)$$

By changing Δ_t , the relative contribution of each mode is modified, which leads to a modification of the interaction range α . In the limit of coupling only to the COM mode, an infinite range interaction with $\alpha = 0$ is achieved. However, if all modes are degenerate, such as is the case for free particles, the interaction ranges becomes dipolar with $\alpha = 3$ ⁹.

Exactly as in the previous section, the Hamiltonian is derived by summing Eq. 3.61 and 3.61. However, the contributions of additional modes are now included, leading to

$$H_{\text{Bic}} = \frac{\hbar}{2} \sum_i^N \sum_m^{2N} \eta_{i,m} \Omega_i \left(a_m e^{i\Delta_m t} + a_m^\dagger e^{-i\Delta_m t} \right) \left(\sigma_i^+ e^{-i\delta_c t} + \sigma_j^- e^{i\delta_c t} \right) \quad (3.77)$$

where $\Delta_m = \Delta_t + (\omega_t - \omega_m)$. Applying the same steps as in the previous section results in an effective spin-spin Hamiltonian (Eq. 3.72) with coupling matrix

$$J_{ij} = \frac{\Omega_i \Omega_j}{2} \sum_{i,j}^{2N} \frac{\eta_{i,m} \eta_{j,m}}{\Delta_t + (\omega_t - \omega_m)} \quad (3.78)$$

where the Lamb-Dicke parameter of ion i and mode m is given by

$$\eta_{i,m} = \frac{2\pi}{\lambda} b_{i,m} \sqrt{\hbar/2m\omega_t \cos(\theta_k)}. \quad (3.79)$$

⁹The two limits, $\alpha = 3$ and $\alpha = 0$, are extreme cases which are difficult, if not impossible, to achieve in the lab. For example, to achieve $\alpha = 3$ the detuning has to be so large that the overall coupling strength will decrease to zero. Conversely, $\alpha = 0$ would require the laser frequency to be extremely close to a vibrational mode, and hence violating the adiabatic condition. A possible solution to implement $\alpha = 0$ might be to use the axial modes instead of the radial modes.

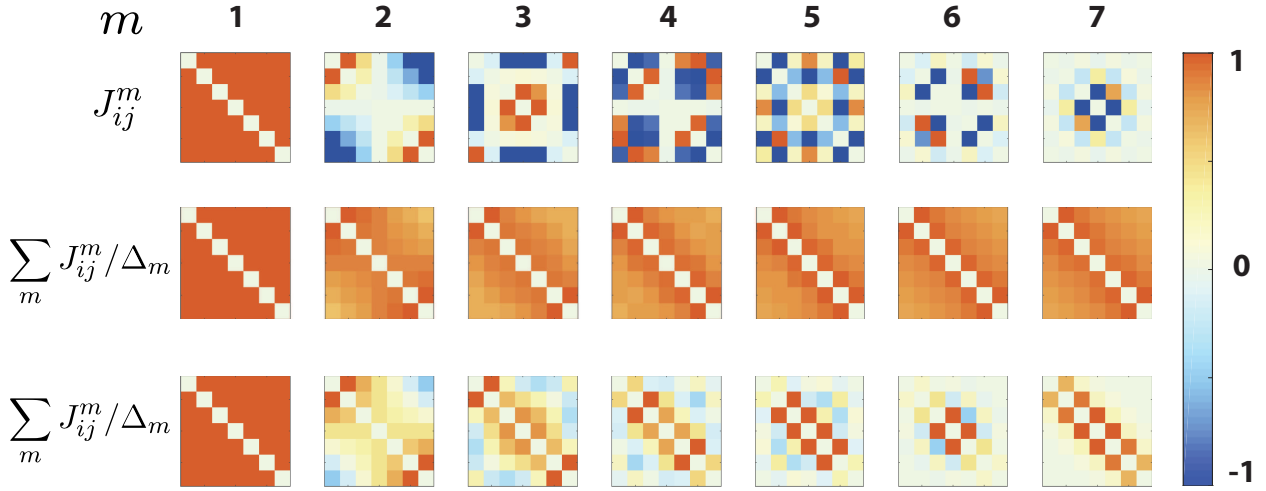


Figure 3.9.: **Top row** The normalized J_{ij}^m correlation matrix induced by mode m of a seven ion string. The trapping frequencies are $\omega_{\text{ax}} = 220$ kHz, $\omega_x = 2.71$ MHz and $\omega_y = 2.68$ MHz and the laser is aligned to couple equally to the two radial directions. **Middle row** The cumulative sum of J_{ij}^m weighted by Δ_m . The detuning from the highest mode is $\Delta_t = 10$ kHz. This gives an interaction range with $\alpha \approx 0$. **Bottom row** Identical to the middle row, however, the detuning from the highest (COM) mode is set to $\Delta_t = 150$ kHz yielding an interaction range $\alpha > 2$.

Here, the mode eigenvector is represented by $b_{i,m}$ and θ_k is the angle between the \vec{k} -vector¹⁰ and the principal axis of the motional modes. Note that for these tunable spin-spin interactions we consider only the radial modes due to their closely spaced dispersion relation. Hence, the summation in Eq. 3.78 runs over $2N$, since there are $2N$ transversal modes overlapping with \vec{k} .

A more elaborate analysis of the spatial decay of J_{ij} [103] reveals that the decay is not a pure power law, but closer to a weighted sum of an exponential and a dipolar decay

$$J_{ij} \propto J_{\text{exp}} e^{-|i-j|/\xi} + \frac{J_{\text{dip}}}{|i-j|^3} \quad (3.80)$$

where the scaling constant ξ and the weights J_{exp} and J_{dip} are non-trivial functions of the trapping frequency ω_t and the overall detuning Δ_t . However, the authors made a crucial approximation by treating the ion-ion separation as equidistant, which is clearly not the case for an harmonic trap.

¹⁰Note that for an optical transition such as it is the case in this thesis, the \vec{k} -vector is in the propagation direction of the laser field and a single photon sufficient to excite the transition. In the case of Raman transitions, the \vec{k} -vector results from the difference between the two Raman beams and the transition is a two-photon process.

4. Experimental setup and techniques for long ion strings

A key topic in this thesis is the coherent manipulation of long strings of ions (with up to 15 ions)¹. In contrast to experiments with either one single ion, or only a few ions, additional experimental challenges arise when multiple ions ($N \gtrsim 10$) are considered, such as the spatial extent or cooling of many motional modes, to name but a few. This chapter presents techniques for coherently controlling long chains of ions and is divided into four main parts. The first section provides a general overview of the $^{40}\text{Ca}^+$ -qubit and introduces our experimental setup. In the second section, key experimental challenges and techniques are specifically discussed with regards to multiple trapped ions. The third section deals with spatially dependent light shifts induced by the entangling beam and methods for compensating them. The fourth section is dedicated to the radial modes, specifically the mode frequency stabilization and ground state cooling, due to their importance for our quantum toolbox regarding quantum simulations.

4.1. $^{40}\text{Ca}^+$ as a qubit/pseudospin

The following section is a short summary of the $^{40}\text{Ca}^+$ -qubit/pseudospin². Further details can be found in [104–107]. ^{40}Ca is an alkaline-earth isotope with zero nuclear spin, which for this reason has no hyperfine structure. In our setup, neutral calcium atoms are evaporated from a calcium filled steel tube resistively heated by currents of 2.7 – 3A. The thermal atoms are ionized via an isotope-selective two-step photoionization process [108, 109]. Another loading technique, laser ablation [110, 111], has been implemented in a neighbouring experiment [112, 113].

The singly charged ^{40}Ca -ion has a simple hydrogen-like electronic energy structure, shown in figure 4.1. The life times τ , the transition wavelengths λ and the corresponding branching ratios are taken from [83, 114–117]. In our experiment, a magnetic field of around $B \approx 4.1$ G is used to lift the degeneracy of the ‘S’ and ‘D’ Zeeman sublevels in order to define a quantization axis of the system. For this field strength, the splittings are $\Delta_{S_{1/2}} \approx 11.5$ MHz and $\Delta_{D_{5/2}} \approx 6.9$ MHz. The qubit is encoded in two Zeeman levels of the $|S_{1/2}, m_j\rangle \leftrightarrow |D_{5/2}, m'_j\rangle$ transition. Given the selection rules for this quadrupole transition, here are a total of 2×5 possibilities to encode a qubit, see figure 4.1 b). The most relevant encodings used in this theses are $|1\rangle = |\downarrow\rangle = |S_{1/2}, m_j = 1/2\rangle \leftrightarrow |0\rangle =$

¹At the time of writing this thesis, we perform experiments with 20 ions

²The two terms are equivalent, but ‘qubit’ is more common in the context of quantum computation and ‘pseudospin’ is used in quantum simulations.

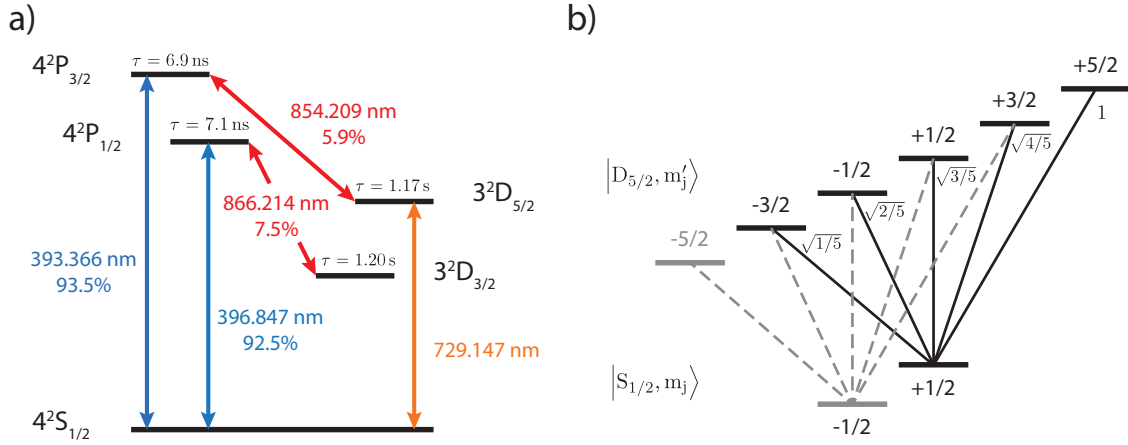


Figure 4.1.: a) A schematic level scheme showing the relevant levels and transition wavelengths of $^{40}\text{Ca}^+$ with regards to the experiments in this thesis. The fast cycling $S_{1/2} \leftrightarrow P_{1/2}$ transition serves for Doppler cooling, optical pumping and state detection. Light at 854 nm and 866 nm pumps out the metastable D-states. The qubit itself is encoded in two Zeeman sublevels of the $S_{1/2} \leftrightarrow D_{5/2}$ transition and is manipulated with 729 nm light. b) A magnetic field of a few Gauss lifts the degeneracy of Zeeman manifolds and defines the quantization axis, giving 2×5 possibilities to encode the qubit. In our setup, the qubit state $|1\rangle$ is encoded in $|S_{1/2}, m_j = 1/2\rangle$, and $|0\rangle$ in $|D_{5/2}, m_j = 3/2\rangle$ or $|D_{5/2}, m_j = 5/2\rangle$, although any of the $m'_j = [-3/2, \dots, 5/2]$ can be used. The Clebsch-Gordan coefficients are given for the relevant transitions.

$|\uparrow\rangle = |D_{5/2}, m_j = 3/2\rangle$ and $|1\rangle = |\downarrow\rangle = |S_{1/2}, m_j = 1/2\rangle \leftrightarrow |0\rangle = |\uparrow\rangle = |D_{5/2}, m_j = 5/2\rangle^3$.

Detection of the qubit state is done by means of electron shelving [118]. Here, 397 nm laser light is shone onto the $S_{1/2} \leftrightarrow P_{1/2}$ transition. If the valence electron is in the $S_{1/2}$ -state, photons are scattered and collected with a photonmultiplier tube (PMT) and/or a CCD camera, whereas if the $D_{5/2}$ -state is occupied, no photons are scattered. The binary information bright or dark ($|1\rangle$ or $|0\rangle$) is interpreted as a projective measurement of the quantum state onto σ_z^i of each individual qubit/pseudospin. A thorough analysis of state discrimination and PMT/CCD performances can be found in C. Hempel's thesis [119].

Further, Doppler cooling of the ions and optical pumping into the $S_{1/2}$ -state are realized on the fast-cycling $S_{1/2} \leftrightarrow P_{1/2}$ transition with the help of 866 nm light for repumping. Additionally, an 854 nm laser is used to quench the metastable $D_{5/2}$ state in the process of sideband cooling [14, 120, and section 4.6.3], 729 nm-optical pumping [119, and references therein] and state re-initialization.

4.2. Setup - Overview

The ion trap, vacuum setup and laser system used in this theses are described by my predecessors in great detail [98, 119, 121, 122]. Here I will give a condensed overview of the current setup to establish a common terminology and describe new extensions of the setup, which haven't yet been described.

The ion trap is a macroscopic linear Paul trap with a blade design based on [23], including modifications such as a reduced blade-to-blade distance (1.13 mm) and tip electrodes (4.5 mm separation)

³The $|D_{5/2}, m_j = 3/2\rangle$ -level has the advantage of longer coherence times as it is less prone to B-field noise compared to the $|D_{5/2}, m_j = 5/2\rangle$ -state. However, the $|D_{5/2}, m_j = 5/2\rangle$ -state is a so called stretched state which can be directly used for sideband cooling as described in section 4.6.3.

with bore holes ($d = 0.5$ mm) for direct optical access along the ion string, Fig. 4.2 a). A detailed trap simulation and characterization is provided in [119]. The operational trapping frequencies used in this thesis span a wide range depending on the experimental requirements, as discussed in the appropriate chapters: $\omega_z = \omega_{ax} \approx 2\pi \times 0.2 - 1.2$ MHz and $\omega_{x,y} = \omega_{rad} \approx 2\pi \times 1.5 - 3.8$ MHz, where the degeneracy of radial modes can be split by applying a DC-offset to the ground blades giving $\Delta_{split} \approx 2\pi \times 0 - 500$ kHz.

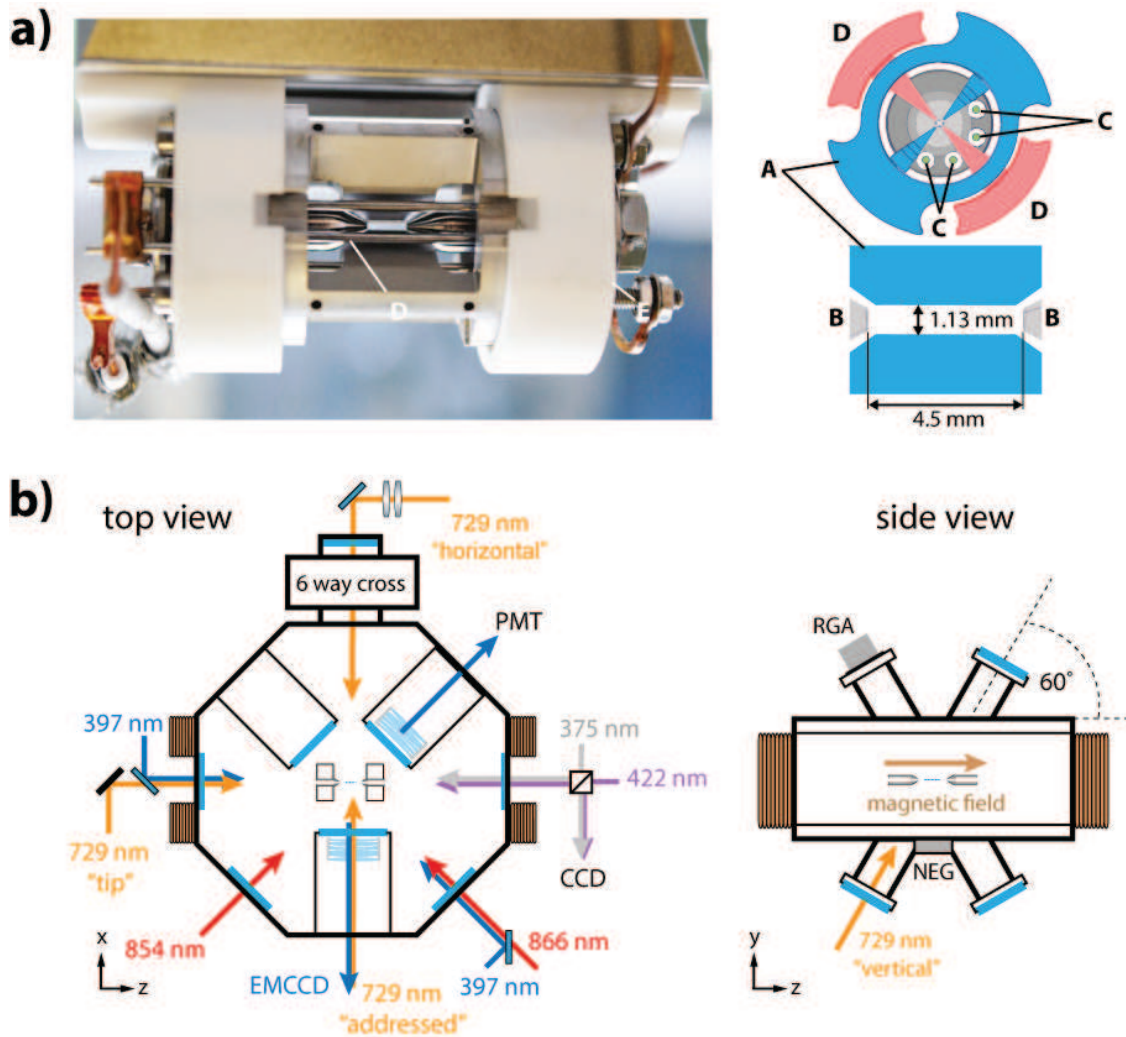


Figure 4.2.: Figures taken from C. Hempel’s Thesis [119] and slightly modified. **a)** A picture and a schematic drawing of the linear Paul trap showing (A) RF blades and (D) ground blades, (B) tip electrodes and (C) compensation electrodes. **b)** Two schematic drawings from top (left) and side (right) view showing the vacuum vessel with the trap in the middle and the different laser and imaging directions.

Figure 4.2 b) illustrates the optical access points of the vacuum vessel and describes the different beam paths. The ‘tip’ beam illuminates the ions along the crystal axis allowing for a homogeneous intensity distribution across the ion string (Rayleigh length $z_r \approx 8$ mm, beam waist $w_0 \approx 43$ μ m) and exclusively coupling to the axial motional modes. Due to selection rules only $\Delta m = 1$ transitions can be driven [123] by the ‘tip’ beam. Since the current sideband cooling scheme requires the stretched state $|D_{5/2}, m_j = 5/2\rangle$ for closed cycling [119], this beam cannot be used for ground

state cooling⁴.

The ‘horizontal’ beam is perpendicular with respect to the string of ions, and thus its overlap with the radial modes is maximal. Therefore, it is used for experiments with variable range spin-spin couplings see chapters 3.3.3 & 5. According to the quadrupole selection rules, $\Delta m = 1$ or $\Delta m = 2$ transitions provide the largest coupling strength when the appropriate polarization is chosen, see section 4.5.1 for more details. The major challenge here is the Gaussian intensity distribution leading to spatially inhomogeneous Rabi frequencies Ω_i across the linear ion string. A way around this is to perform beam shaping, see section 4.4.1.

The ‘addressed’ port is used for single ion addressing by tightly focussing the laser beam close to the diffraction limit with a beam diameter of $d_0 < 2 \mu\text{m}$. An acousto-optical deflector (AOD)⁵ is used to steer the beam across the ion string. A detailed description of the single-ion addressing setup and its characterization is given in the thesis of C. Hempel [119, Chapter 3.5].

The ‘vertical’ beam is an all-purpose beam. It is the only beam able to drive all Δm transitions and overlaps with both the axial and the radial modes, allowing for sideband cooling of all motional modes. However, its rather large beam diameter ($300 \mu\text{m}$) results in lower coupling strengths compared to the other beams⁶.

The setup, as described in the thesis of Hempel, has since been extended in several ways that will be now described. In summary, a tapered amplifier (TA) and a fiber AOM (FAOM), both for 729 nm were installed to enhance power and performance, as described in the following paragraphs. Furthermore, a stabilizing circuit for the RF voltage across the blades was installed, this is described later in section 4.6.2.

Tapered amplifier The tapered amplifier (TA)⁷ is used to feed the horizontal beam path, as shown in figure 4.3 a). The TA provides sufficient laser intensity for the driven spin-spin interactions, as some of the 729 nm light from the TiSa is shared with Lab2 and used for a beat measurement with the university lab. Since our pulse box contains only two direct digital synthesizers (DDS), one (DDS1) driving the double-pass AOM 1 (DP AOM 1) and the other (DDS2) driving the addressing AOD, the only means to drive the DP AOM 2 of the TA path is to split the RF of DDS1. Because of this, DP AOM 1 & 2 are switched simultaneously. Note that even though the fiber AOM is turned off when other ports are used, some light is scattered into the fiber, with a suppression of -47 dB . For most purposes the suppression is strong enough, however for precision spectroscopy, the scattered light ($\approx 500 \text{ nW}$) is enough to cause ac-Stark shifts of several Hz. Figures 4.3 b) & c) show the measured performance curves of the TA as a function of drive current and seed power, respectively. It is important that $I_{\text{drive}}^{\text{max}} = 1.050 \text{ A}$ and $P_{\text{seed}}^{\text{max}} = 39 \text{ mW}$ are not exceeded. Further, the TA should not be running without being seeded nor should it be seeded without any applied current, as the amplifier might degrade. In order to perform high fidelity gates it is crucial that

⁴However, one could implement a bichromatic cooling scheme, where one frequency drives the red sideband transition for cooling and the other repumps populations trapped in the $|S_{1/2}, m_j = -1/2\rangle$ state back to the cooling transition.

⁵Gooch & Housego: 45070-5-6.5DEG-633

⁶Tight focusing typically requires regular maintenance and here we wanted a beam which is always aligned, for instance to measure the clock transitions, for more information on locking the clock see [119, Chapter 4.8.1].

⁷Toptica Photonics, BoostA pro, S/N:07011, $I_{\text{max}} = 1050 \text{ mA}$, $T_{\text{set}} = 20.0 \text{ }^\circ\text{C}$. NEVER exceed 39 mW injection power!

the TA does not introduce additional phase noise to the laser light. A meaningful way to check this is to measure the coherence decay [124] with a Ramsey type experiment [125] and to compare it with the coherence decay using laser light directly from the Ti:Sa, without TA amplification. Figure 4.3 d) shows such a side-by-side comparison, without any significant difference. With a more elaborate spin echo sequence, one could use the ion as a spectrum analyser to determine the spectral noise density in a certain range, as shown by [126, 127].

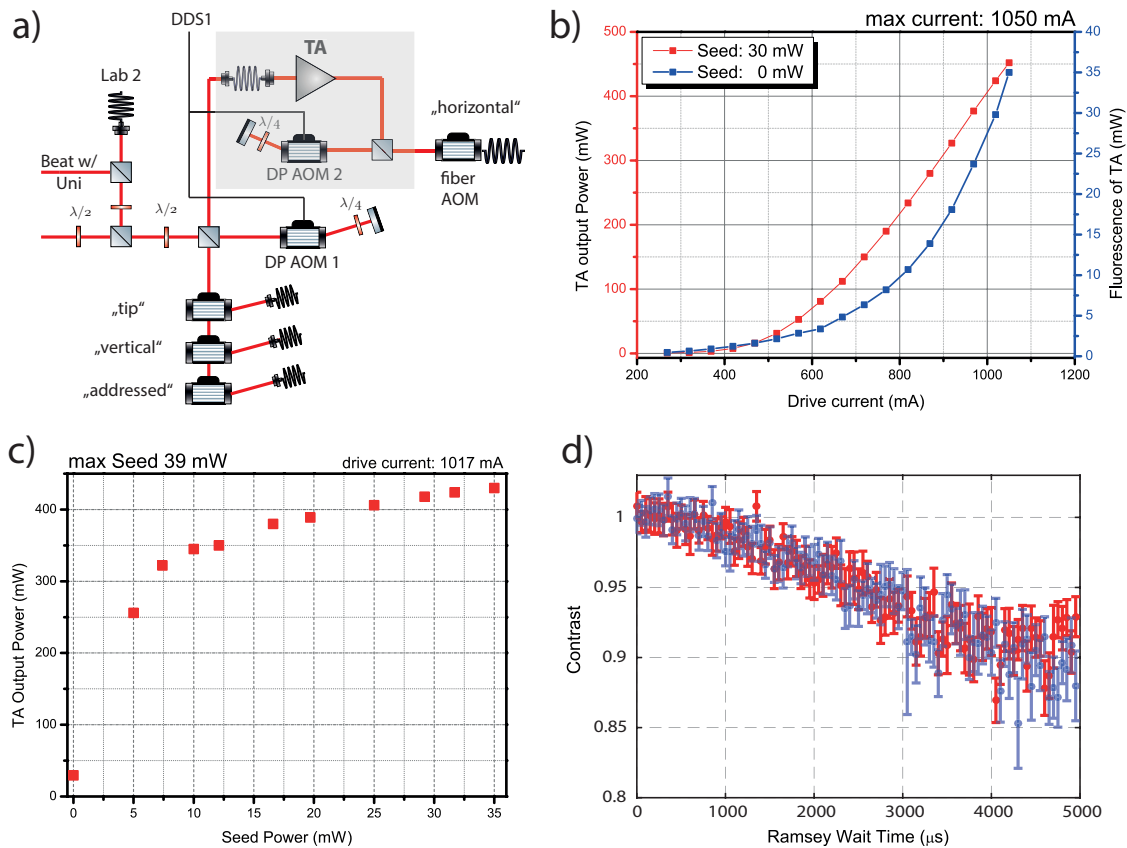


Figure 4.3.: a) An overview of the current setup of the 729nm ‘qubit’ laser optical path with the additional TA path. b) The TA output power is measured as a function of the drive current when seeded with 30 mW (red) and without seed (blue), n.b. the latter leads only to fluorescence light. Do not exceed $I^{\text{max}} = 1.05 \text{ A}$ c) The TA output power is measured dependent on the seed power. d) The coherence on the $1/2 \leftrightarrow 3/2$ transition is measured and compared between the ‘horizontal’ port (red, TA path) and the ‘vertical’ port (transparent blue), showing no difference between the TA path and the ‘old’ path. Error bars are calculated from the covariance matrix of the fit.

Fiber AOM In order to drive a Mølmer-Sørensen type interaction, either for entangling gates or tunable spin-spin couplings, a bichromatic light field with relative phase stability needs to be applied. A successful way to achieve this is to drive an AOM with two frequencies f_1 & f_2 simultaneously and couple the light into a single mode fiber. This generates two light fields with the same spatial mode and a relative phase which is determined by the phases of the two RF frequencies. However, the two light fields generated by f_1 & f_2 have two different Bragg angles and are therefore spatially separated. In order to couple both fields into a single mode fiber, the fiber mode is set to have an equal overlap with both light fields such that their intensities are equal. As a consequence

neither light field couples with maximum efficiency. This issue becomes more pronounced when $\Delta = f_1 - f_2$ becomes larger, as the diffraction angle difference increases correspondingly. Due to the larger misalignment the coupling efficiency decreases and intensity fluctuations increase. To

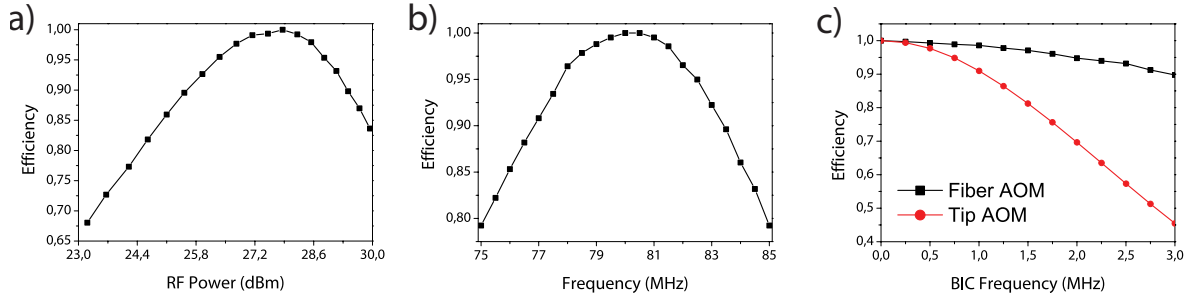


Figure 4.4.: **a)** The relative efficiency of the fiber AOM (FAOM) is measured as a function of the input RF power with a peak efficiency at 27.86 dB = 610 mW measured at the center frequency $f_c = 80$ MHz. The maximum power of 30 dB = 1 W should not be exceeded. **b)** Efficiency measured as a function of the applied RF frequency. **c)** A comparison between the FAOM and the tip AOM (free space and then coupled into a single mode fiber) bichromatic efficiency when the frequency of the bichromat is changed.

overcome these problems we use a fiber AOM (FAOM)⁸ where input/output fibers are as close as possible to the AOM crystal, thereby minimizing the spatial mode separation. Figures 4.4 a) & b) show the efficiency of the FAOM as a function of the RF power and the frequency applied. A comparison between the fiber AOM and the AOM of the ‘tip’ port is given in Fig. 4.4 c). At frequencies relevant for our experiments ($f_1 = 2.75$ kHz = $-f_2$) the FAOM efficiency is $> 90\%$ whereas the efficiency in the tip setup drops to only 50%.

However, there is a major drawback of the FAOM: due to manufacturing it is not possible to align the two PM-fibers perfectly with respect to each other. This reduces the overall polarization extinction ratio (PER) from > 30 dB for a single PM-fiber to < 20 dB for the total system. Since the qubit transitions are polarization sensitive, the low PER will cause polarization fluctuations which are perceived as variations in coupling. To circumvent this issue, we simply removed the input fiber restoring a PER of 30 dB. Unfortunately, the coupling into the FAOM is now prone to beam pointing instabilities⁹, which induce common mode (both light fields) and relative (between the two light fields) fluctuations. Common mode fluctuations are less severe as only the overall Rabi coupling changes. When the relative intensities vary, however, additional ac-Stark shifts will corrupt the time dynamics and lead to decoherence.

In order to characterize intensity fluctuations due to fluctuations of coupling into the output fiber, the light power is recorded for 2 min¹⁰ at the output of the output fiber, and the fluctuations are given as one standard deviation normalized by the mean value. Table 4.1 compares fluctuations for different settings: optimal coupling into a fiber for a single light field (‘Carrier’) driven at the center frequency of the FAOM/tip AOM, balanced coupling into output fiber for a bichromatic light field (‘Bic’) and single light fields of the bichromatic beam (‘Bic \pm ’) coupled as in the case of ‘Bic’.

⁸Gooch & Housego: MM080-1C2V14-5-F2SH-B, ($f_c = 80$ MHz, $P_{\text{RF}}^{\text{max}} = 30$ dBm = 1 W, $t_{\text{rise}} < 50$ ns)

⁹Beam pointing here refers to spatial changes in the laser beam path, for instance caused by temperature changes in the lab.

¹⁰Measured with Newport power meter: 1918-C, head: 918-UV-OD3, S/N 10676.

	Carrier	1.2 MHz			2.7 MHz		
		Bic	Bic-	Bic+	Bic	Bic-	Bic+
FAOM	0.32%	0.26%	0.3%	0.32%	0.27%	0.36%	0.41%
Tip AOM	0.11%	0.1%	0.72%	0.5%	0.15%	0.78%	0.79%

Table 4.1.: A comparison of the intensity fluctuations between the FAOM and the AOM setup for different settings at the end of the output fiber. ‘Carrier’ corresponds to driving the FAOM/AOM at the center frequency and light mode is optimally aligned with the fiber mode. ‘Bic’ represents the case of a bichromatic light field driven at two frequencies, 1.2 MHz and 2.7 MHz, respectively, where both light modes are equally coupled into the output fiber. ‘Bic-’ and ‘Bic+’ are the single frequency components of the ‘Bic’, where the coupling into the fiber is set as in the case of ‘Bic’, however, the RF-drives of ‘Bic+’ (‘Bic-’) is turned off. The light power is recorded for 2 min and the fluctuations are expressed as one standard deviation normalized by the mean value.

The table suggests that the overall fluctuations are bigger in the FAOM. The periscope in this path induces larger beam pointing fluctuations and additional telescope lenses enlarge these effects. On the other hand, the fluctuations for a single light field, ‘Bic \pm ’, show that the relative variations are smaller in the FAOM due to better mode overlap between fiber and laser light. In conclusion there is some room to improve the FAOM path by getting rid of the periscope and shortening the laser path lengths. Further, the relative fluctuations in the tip AOM could be improved by reducing the spot size and thus reducing the number of resolvable spots [119].

An alternative approach would be to use imaging such as $2f - 2f$, where the point of divergence in the AOM crystal is mapped onto the core of a light collection fiber. However, a quick test setup did not show significant improvements and might need more careful investigations.

4.3. Experimental techniques for long ion strings

The focus of this sections is on the main challenges and issues when trapping and coherently manipulating long strings of ions in our linear Paul trap.

Linear and zig-zag configuration When trapped ions are sufficiently cold, they will form a Wigner crystal [128], a remarkable example of self-organized matter. The driving force behind this self-organization is the interplay between the Coulomb repulsion and the confining trap potential: at the equilibrium position of the ions these two forces are balanced. In a linear Paul trap with highly anisotropic trapping potentials, i.e. $\omega_{\text{ax}}/\omega_{\text{rad}} \ll 1$, the ions condense into a one-dimensional Coulomb crystal at sufficiently low temperatures. Figure 4.5 a) shows such a Coulomb crystal with 30 ions confined in our trap. However, at $\beta = (\omega_{\text{ax}}/\omega_{\text{rad}})^2 \approx \beta_{\text{crit}}$, the crystal will undergo a second order phase transition [129, 130] into a zig-zag configuration (Fig. 4.5 b)). The value of β_{crit} depends on the number of ions N . Several theoretical (Schiffer [129]) and theoretical/experimental (Enzer et. al [131]) analyses reveal a power law scaling with the number of ions $\beta_{\text{crit}}(N) = cN^{-\gamma}$, where c and γ are constants. While Schiffer and Enzer base their findings on the analysis of the radial mode spectrum, Dubin [132] follows a different approach by analysing the equilibrium crystalline configuration, which reveals a different scaling $\beta_{\text{crit}}(N) = c_1 N^{-2} * (\ln(c_2 N) + 1)$. Nevertheless, Dubin’s scaling matches the power law scaling extremely well for $N > 4$, as shown in figure 4.5 c). The interpretation of this phase transition can be given as follows: when $\beta \rightarrow \beta_{\text{crit}}(N)$ the frequency

of the lowest radial mode $\omega_{\text{rad}}^{\text{lowest}} \rightarrow 0$, beyond this point the radial oscillations become unstable and so does the linear configuration of the string, for more details see sections 3.1.3 and 4.6.

Recently, the linear to zig-zag phase transition has received much theoretical and experimental attention. Theoretical studies suggest that the phase transition is driven by quantum fluctuations at zero temperature, thus being a quantum phase transition [133, 134]. Furthermore, the formation of defects has been linked to the Kibble-Zurek mechanism [135, 136] and extensively studied both theoretically [137–139] and experimentally [140–143].

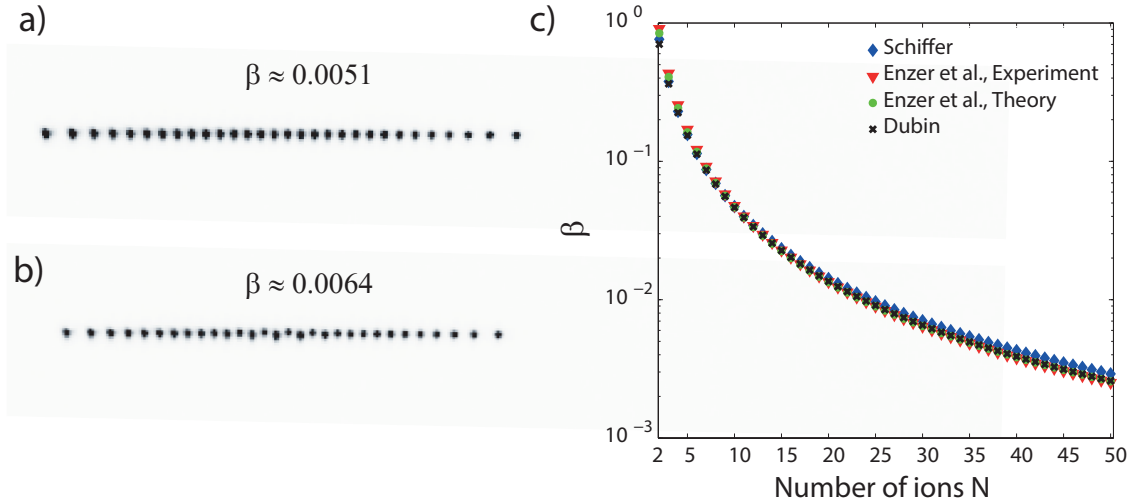


Figure 4.5.: a) A linear Coulomb crystal of 30 trapped ions, with $\omega_{\text{rad}} = 2\pi \times 3.5$ MHz and $\omega_{\text{ax}} = 2\pi \times 0.249$ MHz. b) The axial confinement is squeezed to $\omega_{\text{ax}} = 2\pi \times 0.279$ MHz and the ion crystal undergoes a phase transition into the zig-zag configuration. c) A comparison between the different scaling laws of $\beta_{\text{crit}}(N) = cN^\gamma$, with $c = 2.53, 3.23, 2.94$ and $\gamma = -1.73, -1.83, -1.8$ for Schiffer, Enzer (exp.) resp. Enzer (theor.). Dubin has a different approach, where $\beta_{\text{crit}}(N) = c_1 N^{-2} * (\ln(c_2 N) + 1)$, with $c_1 = 1.14$ and $c_2 = 2.22$. For $N > 4$ all four scaling laws match closely and the values for 30 ions are in very good agreement with our observation, $\beta_{\text{crit}}(30) \approx 0.0065$.

Despite all the interesting physics behind the zig-zag phase transition, the experiments presented in this thesis were all carried out in a regime where the ion string has a stable, one-dimensional configuration for the following reasons:

- (1) The micromotion cannot be compensated, at least not for the ions being pushed out of the string axis.
- (2) There exist different zig-zag configurations, ‘zig-zag-zig’, ‘zag-zig-zag’, kinked, doubly kinked, with defects etc. [143] making it difficult to repeatably address single ions, as collisions with background gas can cause transitions from one configuration to another.
- (3) Beyond the phase transition, the ion crystal loses its one-dimensionality and the vibrational modes cannot be treated as decoupled¹¹, such as in section 3.1.3.

Depending on the number of trapped ions and the experimental procedure, the trapping frequency can significantly vary. A selection of the most common parameters used for the different experi-

¹¹Regarding spin-spin simulations (Chapter 5) it would be interesting to see what the mode vectors, frequencies and finally the effective spin-spin couplings would look like. However, it remains unclear how motional coherence and motional heating rates are influenced, as we have seen unexpected heating rate behaviour close to β_{crit} (see Chapter 8).

ments presented in this thesis are listed here:

Chapter 5: 7 and 15 ions - $\omega_{\text{ax}} = 2\pi \times 220$ kHz, $\omega_{\text{rad}} \approx 2\pi \times 2.7$ MHz.

Chapter 6: 4 ions - $\omega_{\text{ax}} = 2\pi \times 1.23$ MHz, $\omega_{\text{rad}} \approx 2\pi \times 3.5$ MHz; 3 & 5 & 7 ions - $\omega_{\text{ax}} = 2\pi \times 1$ MHz, $\omega_{\text{rad}} \approx 2\pi \times 3.5$ MHz.

Chapter 7: 2 ions - $\omega_{\text{ax}} = 2\pi \times 1.23$ MHz, $\omega_{\text{rad}} \approx 2\pi \times 3.5$ MHz.

Restrictions on trapping parameters, and consequentially, limitations on the number of ions which can be meaningfully trapped, will be discussed in chapter 8.

Coherent Rabi oscillations with long ion strings An indispensable tool when working with long ion strings is the EMCCD¹² camera¹³. A comparison between the atomic fluorescence measured with the PMT (photomultiplier tube) and the camera is presented in figure 4.6 a) and b). Here, resonant Rabi oscillations (‘carrier’) on 5 ions are driven from the ‘horizontal’ port (perpendicular to the string axis). The signal measured with the PMT in 4.6 a) decays within the first few oscillation periods, which can be easily confused with ‘extremely hot’¹⁴ ions or laser fluctuations¹⁵. However, a revival is observable after 3 oscillations ruling out incoherent processes. Measuring the Rabi oscillations with the camera, where the fluorescence is detectable for each ion individually, reveals that the coupling strength varies from ion to ion. This indicates a potential misalignment of the beam. After centering the beam with respect to the ion string, the oscillations on the PMT (Fig. 4.6 c)) are comparable to the resolved single-ion oscillations on the camera (Fig. 4.6 d)). The remaining damping on the PMT signal (no damping observable on the camera) is due to the Gaussian intensity distribution of the laser beam, for more details on this topic and the resulting experimental consequences see section 4.4.

Micromotion An ion which is not exactly located on the RF null (RF nodal line) experiences an extra driven motion, in addition to the secular motion, due to the oscillating electric field gradient at the RF drive frequency Ω_{RF} . This *excess micromotion* causes Doppler shifts and can be treated [144] in the rest frame of the ion as a modulation of the laser’s electric field $E(t) = E_0 e^{-i\omega_L t}$:

$$\begin{aligned} E(t) &= E_0 e^{-i\omega_L t} e^{i\beta \sin(\Omega_{\text{RF}} t)} \\ &= E_0 e^{-i\omega_L t} \sum_{n=-\infty}^{\infty} J_n(\beta) e^{in\Omega_{\text{RF}} t}. \end{aligned} \quad (4.1)$$

Here, $J_n(\beta)$ is the n^{th} -order Bessel function and β is the modulation index directly related to the amplitude of the micromotion. The carrier coupling strength Ω_{carrier} is proportional to $J_0(\beta)$ and the coupling strength on the first order micromotional sideband Ω_{mm} is proportional to $J_1(\beta)$. A

¹²Electron-multiplying charge-coupled device

¹³Andor iXon “blue” DU-897-DCS-BBB, a detailed description on our camera detection is given in [119, Chapter 3.4].

¹⁴A single ion with mean phonon number $\bar{n} > 40$ and typical Lamb-Dicke parameter $\eta = 0.06$ shows a similar decay.

¹⁵A similar decay could be observed on a single, ground state cooled ion with intensity fluctuations $> 10\%$.

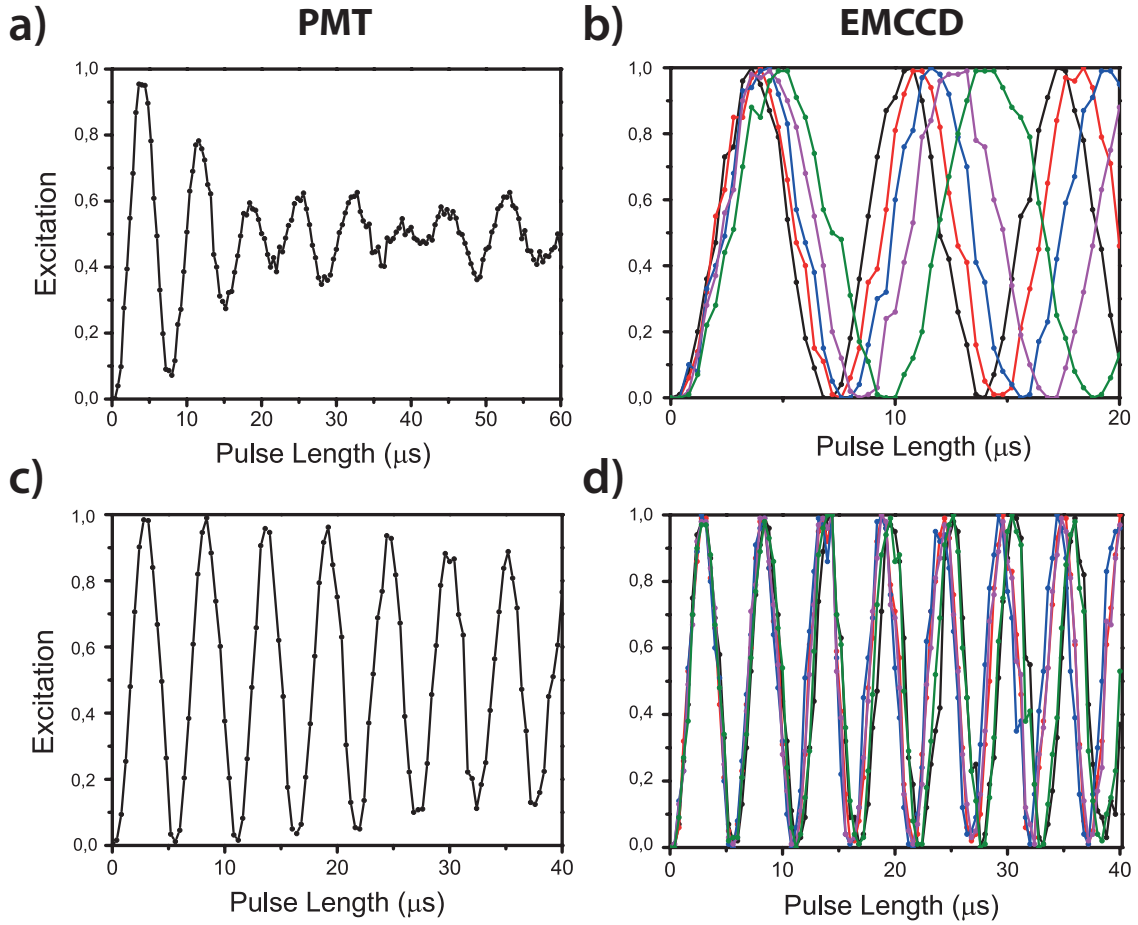


Figure 4.6.: a) & b) Comparison between Rabi oscillations measured with the PMT (a)) and the CCD-camera (b)) for a deliberately misaligned beam. While on the PMT the oscillations seem to damp out very quickly; the camera reveals Rabi oscillations with full amplitude, but different Rabi frequencies, for each ion due to beam misalignment. Black, red, blue, purple and green represent ions 1 – 5. c) & d) Rabi oscillations after realigning and centering the beam. The remaining damping seen on the PMT (c)) is due to the Gaussian beam shape, as the camera (d)) indicates a nearly perfect symmetric coupling distribution across the string.

Taylor expansion of the Bessel function $J_0(\beta)$ around $\beta = 0$ up to second order leads to

$$\Omega_{\text{carrier}}^{\text{eff}} \propto 1 - \frac{\beta^2}{4} = 1 - \left(\frac{\Omega_{mm}}{\Omega_{\text{carrier}}} \right)^2. \quad (4.2)$$

This approximation holds as long as $\beta \ll 1$ and can be used to quantify the micromotional amplitude by measuring the coupling strengths in Eq. 4.2.

Any stray electric field exerts a force on the ions, displacing them out of the RF null and thus inducing micromotion. These stray electric fields can be compensated by applying DC voltages to additional electrodes parallel to the RF blades, pushing the ions back onto the RF nodal line. Nevertheless, an unavoidable micromotion will remain as the secular motion moves the ion back and forth through the nodal line. In the case of a single ion, the micromotion can be well compensated to $\beta < 0.01$. However, this is no longer necessarily true for long ion strings as the stray field amplitudes may not be constant over the entire ion crystal.

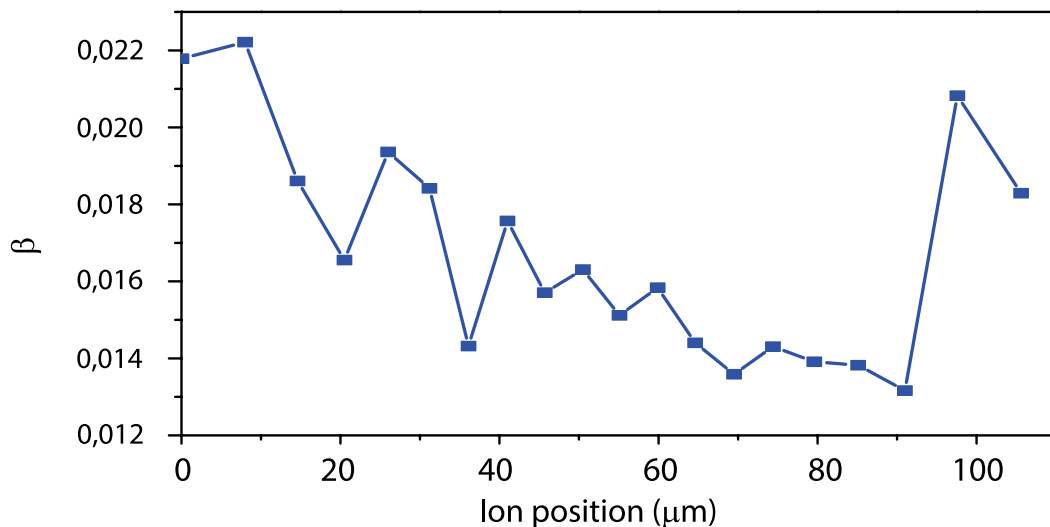


Figure 4.7.: The horizontal micromotion of a 20 ion string ($\omega_{\text{ax}} = 2\pi \times 220$ kHz) is measured using the relation Eq. 4.2. Due to this low axial confinement / high axial temperature it is not possible to measure the vertical micromotion. The horizontal micromotion is well compensated, $\beta < 0.03$, even though there is quite some scatter over the chain.

Figure 4.7 shows the ‘horizontal’ micromotion distribution of a 20 ion string¹⁶. In general, the micromotion can be well compensated to values of $\beta < 0.03$ for a multi-ion string ($N \approx 20$). Nevertheless, the micromotion strength shows some scatter with $\beta_{\text{max}}/\beta_{\text{min}} \approx 2$. This scatter might cause trouble when the micromotion is not compensated (for details see section 4.5.1).

4.3.1. Spatially dependent qubit transition frequencies

For long strings of ions, inhomogeneities in the magnetic field B and electric field gradients ∇E will cause the atomic transition frequency to change as a function of the ion position. These frequency shifts can be in the order of tens of Hz, thus negligible for many experiments. However, for precise clock experiments, high fidelity entangling gates, and quantum simulations with low spin-spin couplings, these shifts have a high impact on the performance and fidelity of the experiments. This section will focus on spatially dependent shifts caused by B-field gradients and inhomogeneous quadrupole shifts due to electric field gradients. Shifts caused by inhomogeneous ac-stark shifts are extensively discussed in section 4.4.2.

B-field gradient Since the qubits are encoded into Zeeman sublevels of the $S_{1/2} \leftrightarrow D_{5/2}$ transition, their frequencies depend linearly on the B-field¹⁷. In order to lift the degeneracy of the Zeeman levels and to define a quantization axis two magnetic field coils are aligned such that the resulting \vec{B} is along the string axis. Each coil has $N = 350$ windings with an inner radius $R = 57.5$ mm and a coil-to-coil distance $L = 300$ mm. Such an arrangement does not fulfill the Helmholtz criterion

¹⁶In order to keep a string of 20 ions linear the axial trapping frequency is set to $\omega_{\text{ax}} = 2\pi \times 220$ kHz. At this ‘low’ axial confinement, the temperature of the axial modes is very high, $\bar{n} > 250$ (see Chapter 8). This prohibits us from driving Rabi flops on the carrier or micromotional sideband with the ‘vertical’ port due to substantial \vec{k} -vector overlap (30°) with the hot axial modes. Not a single Rabi oscillation is observable due to immediate decoherence.

¹⁷The higher order contributions are negligible at a B-field of $B \approx 4.1$ G.

($L = R$), but it is imposed by spatial restrictions given by the vacuum chamber. As a result, the B-field along the string axis has a quadratic dependency. Figure 4.8 a) shows the calculated B-field strength along the coil-axis. Any misalignment between the trap center and the center of the two coils will give rise to a linear (to first order) dependency of the transition frequency shift¹⁸. Using the camera for detection, it is possible to measure the frequency offset of each ion compared to the laser frequency with a Ramsey type experiment [125]. In contrast to clock experiments we care only about relative frequency shifts between the qubits. As such, the interrogation time can go beyond > 100 ms reducing the contrast to zero. The relative phase information is then gained from two-point correlation functions, e.g. $\langle \sigma_i^z(t) \sigma_j^z(t) \rangle$ [145].

For a string of 20 ions trapped at $\omega_{\text{ax}} = 2\pi \times 220$ kHz (string size ~ 105 μm) a frequency difference of 250 Hz is measured from edge-to-edge (see Fig. 4.8 b)). Given the B-field sensitivity 2.798 MHz G^{-1} on the $|S_{1/2}, m_j = 1/2\rangle \leftrightarrow |D_{5/2}, m_j = 5/2\rangle$ transition a gradient of 0.85 $\mu\text{G}/\mu\text{m}$ is measured. A second pair of coils arranged in a quadrupole configuration generates a linear B-field gradient (18.89 G/Am) to counteract the frequency shift by applying a current of 45 mA.

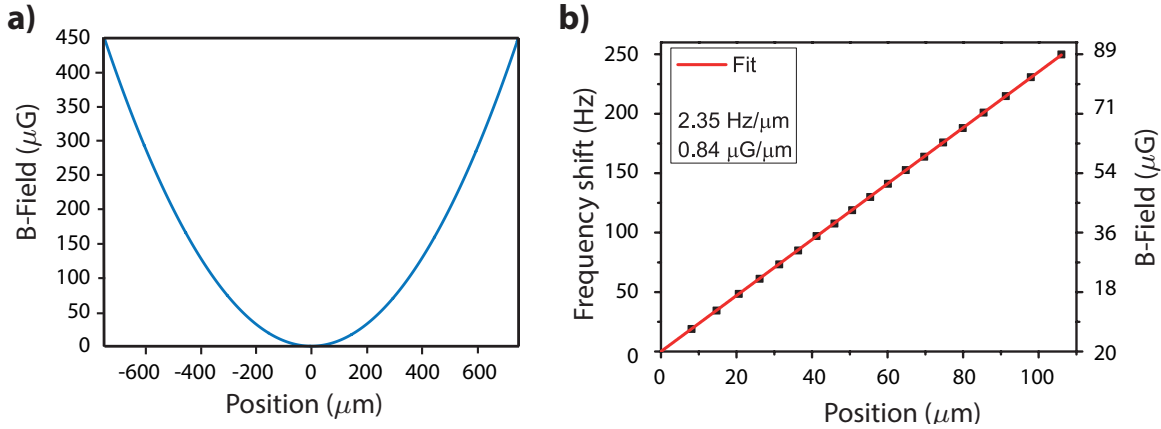


Figure 4.8: **a)** The B-field strength is calculated along the axis of the coils for the current arrangement (blue). A constant offset $B_{\text{offset}} = 4.105$ G is subtracted for better readability. **b)** The frequency shifts for 20 ions are measured with a Ramsey experiment revealing ~ 250 Hz difference from edge-to-edge. Using the B-field sensitivity of 2.798 MHz G^{-1} a gradient of 0.85 $\mu\text{G}/\mu\text{m}$ is calculated. Using a second pair of coils (18.89 G/Am) the gradient is compensated by applying 45 mA.

Quadrupole shifts On top of the magnetic field dependency, the quadrupole moment Q of the D -states couples to any E-field gradient by $H = Q \cdot \nabla E$, determining the atomic quadrupole transition frequency. In contrast to spherical Paul traps, the static trapping potential applied to the tips in linear Paul traps gives rise to an electric field gradient along the z-direction $dE_z/dz = m\omega_{\text{ax}}^2/e$, where m is the ion's mass, ω_{ax} is the frequency of the axial COM and e is the elementary charge. Assuming any additional E-field gradients from patch potentials are negligible compared to dE_z/dz of the trap potential, the trap's rotationally symmetric field gradient shifts the transition frequency

¹⁸Other sources for residual B-field gradients could be stray fields, for instance from the getter pump or current carrying wires.

$S_{1/2} \leftrightarrow D_{5/2}$ by [146]

$$\Delta\omega = \frac{1}{4} \frac{dE}{dz} \Theta(D, J) \frac{J(J+1) - 3m_j^2}{J(2J-1)} \left[\frac{3 \cos^2(\beta) - 1}{4\hbar} \right]. \quad (4.3)$$

Here, dE_z/dz denotes the E-field gradient along the principal trap axis, $\Theta(D, J)$ is the quadrupole moment of the D levels with a total angular momentum J , and β is the angle between the quantization axis and the principal axis of the trap. The quadrupole moment was measured to be $\Theta(D, 5/2) = 1.83(1)ea_0^2$ [147]. As the E-field gradient is constant, all ions experience a uniform frequency shift of $\Delta\omega \approx -2\pi \times 0.5$ Hz for $m_j = 5/2$ at a trapping frequency $\omega_{\text{ax}} = 2\pi \times 200$ kHz, which is negligible for the experiments presented here.

However, in a multi-ion string, each ion generates an additional E-field gradient for its neighbours. In the simple case of two ions, the E-field gradient is doubled $dE_z/dz = 2m\omega_{\text{ax}}^2/e$ [148], since the inter-ion distance is $\Delta z = (e^2/(2\pi m\epsilon_0\omega_{\text{ax}}))^{1/3}$. For more than two ions, the gradient can only be calculated numerically. First, the ion positions z_i are calculated as described in section 3.1.3. The E-field gradient at position z_i is then given by:

$$\frac{dE_i}{dz} = \frac{m\omega_{\text{ax}}^2}{e} + \sum_j^{N-i} \frac{e}{2\pi\epsilon_0} \frac{1}{|z_i - z_j|^3} \quad (4.4)$$

The first term in Eq. 4.4 is the uniform gradient from the trapping potential, whereas the second takes the gradient generated by the neighbouring ions into account. Due to the non-equidistant spacing between the ions and the various number of close neighbours in an open ion chain, each ion experiences a different E-field gradient.

In Fig. 4.9 a) & b) quadrupole shifts for five ions are calculated and compared for three different transitions $|S_{1/2}, m_j = 1/2\rangle \leftrightarrow |D_{5/2}, m_j\rangle$ at two trapping potentials, 220 kHz and 900 kHz. When the ions are far apart, such as in the shallow potential, the frequency shifts become negligible for all the transitions. This is no longer true when the ions are squeezed together by ramping up the trapping potential or by increasing the ion number. Figure 4.9 c) compares the theoretical relative quadrupole shifts with the relative shifts measured after the linear B-field gradient is compensated. The shifts are measured with the same Ramsey type experiment as in the previous paragraph. There is a significant difference between the theoretical and the experimental values, which could be explained by the quadratic form of the B-field.

There are several ways to circumvent the quadrupole shift, if necessary. If absolute frequency measurements are the goal, one can average over all possible m_j -states, as the sum over all possible m_j in Eq. 4.3 adds to zero [149]. This, however, is not suitable for the experiments presented in this thesis¹⁹. The straightforward approach is to use the $|D_{5/2}, m_j = 3/2\rangle$ level, as this one is least prone to the quadrupole shift, with some disadvantages regarding sideband cooling in our setup (for details see section 4.6.3). A more laborious solution is to make use of the angle dependency β in equation 4.3. By changing the B-field direction with respect to the traps principal axis, the quadrupole shifts become zero for $\beta \approx \pi/3.3$, given there are no spurious E-field gradients from

¹⁹We encode the qubit/pseudospin in to a single transition, and thus cannot average over all transitions.

other directions.

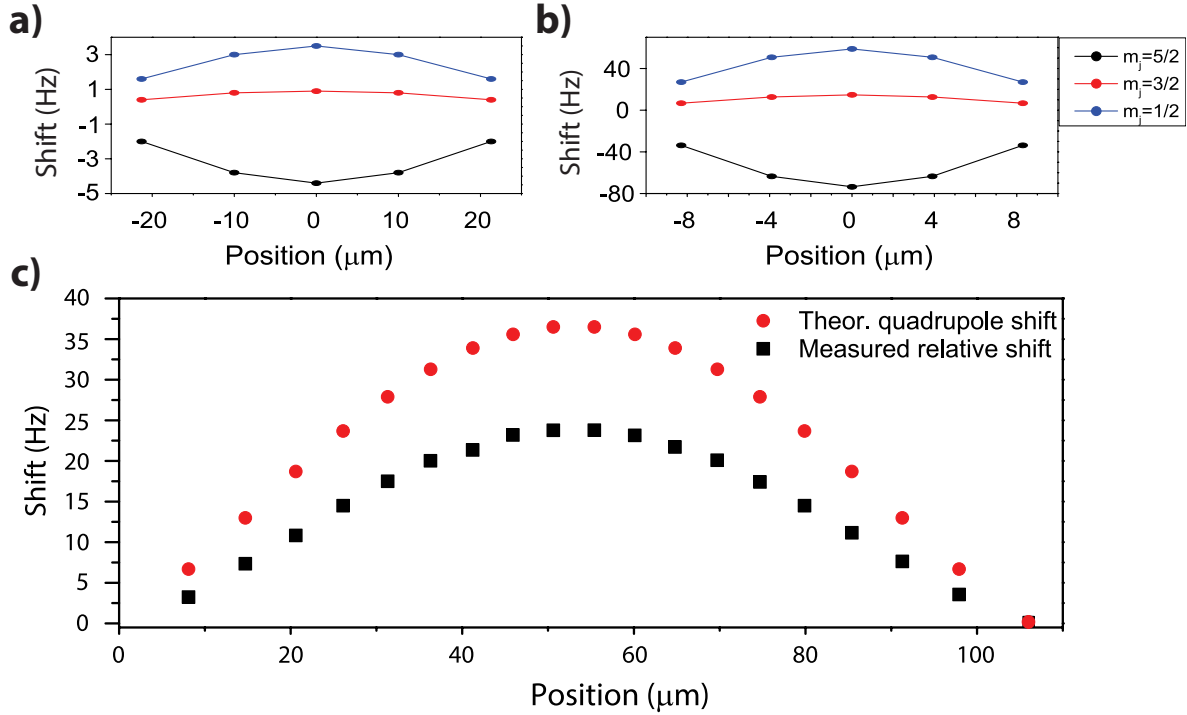


Figure 4.9.: a) & b) Theoretical calculation of the quadrupole shifts on different $|D_{5/2}, m_j = [5/2, 3/2, 1/2]\rangle$ transitions for 5 ions trapped at 220 kHz (a)) and 900 kHz (b)). c) A Ramsey experiment with $\tau_{\text{wait}} = 4$ ms performed on the $|D_{5/2}, m_j = 5/2\rangle$ -transition (black squares) and compared to the theoretical values (red dots) shows hardly any difference in transition frequency. The measurements reveal a frequency difference of 23 Hz between the edge and the middle ion. The theoretical value of the quadrupole shift alone is 37 Hz.

4.4. Interaction Beam

In order to achieve a high coupling strength on the radial modes, i.e. a strong effective spin-spin interaction, the driving laser field has to overlap with the direction of motion. Optimally, the \vec{k} -vector is perpendicular to the ion string. For long ion strings, this has some undesired consequences due to the Gaussian intensity distribution i.e. ions in the center experience a higher coupling than those closer to the edge.

This section deals with the implications of an inhomogeneous coupling strength distribution and its experimental consequences.

4.4.1. Beam shaping

Simply expanding the beam size is suboptimal, since light is ‘wasted’, hence, the overall intensity is decreased. An obvious way to improve the situation is by beam shaping and there are several ways to influence the Gaussian shape, all with their own advantages and disadvantages.

In this thesis we implemented beam shaping by using cylindrical lenses as depicted in Fig 4.10 a). By combining two cylindrical lenses oriented orthogonally with respect to each other, it is possible to independently change the main axis of the elliptical beam, see Fig 4.10 b). Here, we place the two

lenses, $f = 700 \text{ mm}$ ²⁰ and $f = 500 \text{ mm}$ ²¹ on individual translation stages²² and, by separately moving the focal planes, it allows us to control the ellipticity at the ion crystal plane. The beam is launched by a fiber coupler²³ with a collimated beam diameter specified as $D \approx 22.5 \text{ mm}$. However, the real diameter depends on the wavelength and the fiber NA and could not be measured appropriately, since its size exceeds the dimensions of any measurement device at hand.

Given the specified beam diameter D and the focal lengths f , one can estimate the Gaussian waist diameter, i.e. $1/e^2$, at the focal plane by using Gaussian beam optics $2w_0 = \left(\frac{4\lambda}{\pi}\right) \left(\frac{f}{D}\right)$. The beam waists are estimated to be $w_0^y \approx 10.3 \mu\text{m}$ and $w_0^z \approx 14.4 \mu\text{m}$. In contrast, the measured values are $w_0^y \approx 16.5 \mu\text{m}$ and $w_0^z \approx 22.5 \mu\text{m}$, respectively. This discrepancy can be explained by the unknown diameter D and additional aberrations. By displacing the 700 mm - lens such that its focal plane does not coincide with the ion crystal plane, an elliptical beam with $w^y \approx 16.5 \mu\text{m}$ and $w^z \approx 190 \mu\text{m}$ is achieved, see Fig 4.10 c). For a string of 20 ions ($108 \mu\text{m}$ at $\omega_{ax} = 2\pi \times 214 \text{ kHz}$) this results in a Rabi frequency $\Omega_{\text{center}} \approx 2\pi \times 180 \text{ kHz}$ and a variation of $\approx 15\%$ from the center to the outermost ion, as depicted in Fig. 4.10 d).

The approach described above has a crucial advantage in that it is straightforward to set up and can be implemented within a day. However, there always remains a trade-off between a flat intensity distribution and high intensity at the ion crystal plane. The residual intensity inhomogeneity has some severe consequences, such as a spatially dependent ac-Stark shift, which will be discussed in detail in the following section. Preferably, the Gaussian intensity distribution is transformed into a flat distribution with sharp edges, called a top hat function. This can be achieved by customized diffractive optical elements (DOE). These DOE are special purpose devices, i.e. once specifically designed for a given setup there is no flexibility in terms of input beam size, working distance, and spot size. A critical drawback is that a uniform top hat is only achievable at specific working distance within a very small tolerance ($< 50\%$ spot size) with a typical uniformity of only $\pm 5\%$ [150]. Furthermore, the attainable top hat spot size is, as a rule of thumb, 3 to 5 times larger than the diffraction limited spot size, i.e. large input beam diameters D and oversize optics are needed to obtain decent spot sizes.

A more advanced and flexible way for beam shaping is to use spatial light modulators (SLM) as described in the master thesis of Sebastian Schunke [151].

4.4.2. Spatial dependent ac-Stark shift

As a consequence of the remaining non-uniform, though flattened, intensity distribution one has to cope with spatially dependent ac-Stark shifts in addition to non-uniform Rabi frequencies. In an ideal two-level atom system, driven resonantly, there is no ac-Stark shift present. However, real atoms have many additional energy levels. Even though the qubit is driven resonantly, the light field couples off-resonantly to other available transitions and thus induces light shifts on the qubit transition, see Fig 4.11 a). In $^{40}\text{Ca}^+$ the main contributions come from the off-resonant dipole coupling $S_{1/2} \leftrightarrow P_{1/2}$, $S_{1/2} \leftrightarrow P_{3/2}$ and $D_{5/2} \leftrightarrow P_{3/2}$ as well as from the off-resonant quadrupole

²⁰Thorlabs: LJ1836L1-B

²¹Thorlabs: LJ1144L2-B

²²Thorlabs: LT3

²³Schäfter + Kirchhoff: 60FC-L-4-M125-54

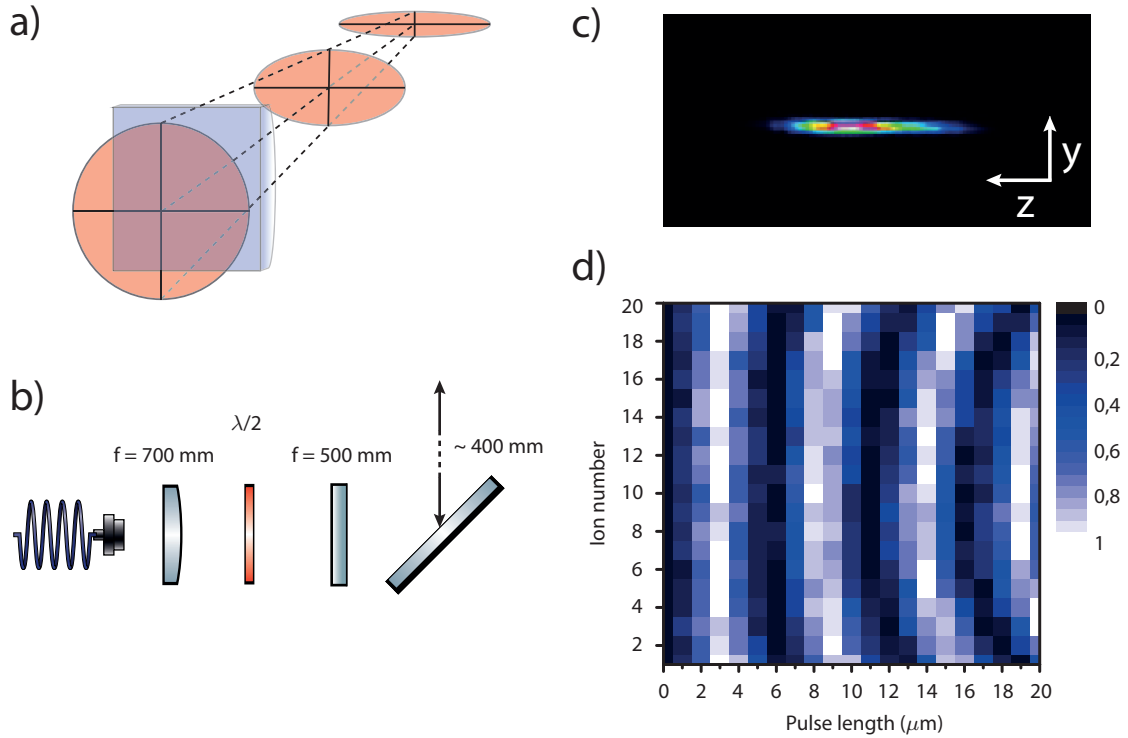


Figure 4.10.: **a)** A sketch showing the effect of a cylindrical lens transforming a collimated, round Gaussian beam into a partly collimated ellipse, where the non-transformed axis stays collimated. **b)** Schematic drawing of the cylindrical lens setup, consisting of a 60FC-L-4-M125-54 fiber collimator from Schäfter + Kirchhoff, two cylindrical lenses ($f = 700$ mm and $f = 500$ mm, resp.) placed on individual translation stages, a 2" $\lambda/2$ wave plate and a 2" mirror mounted on a mirror holder with Newport NSA12 actuators for precise control. The mirror mount center is roughly 400 mm placed from the trap center. The uncertainty comes from the nescience of the viewport thickness. **c)** Intensity distribution of the beam taken with a beam profiler. Here, the $f = 700$ mm - lens was moved out of focus to expand the beam to $w^y \approx 16.5 \mu\text{m}$ and $w^z \approx 190 \mu\text{m}$. **d)** Rabi flops on 20 ions with $\Omega_{\text{center}} \approx 2\pi \times 170$ kHz and a variation of $\Omega_{\text{edge}}/\Omega_{\text{center}} \approx 1.15$, trapped at $\omega_{a,x} = 2\pi \times 214$ kHz.

coupling to the other transitions within the $S_{1/2} \leftrightarrow D_{5/2}$ -Zeeman manifold. The induced ac-Stark shifts are measured with a Ramsey type experiment on a single ion as described in [152]. First, the system is prepared in its ground state ($|S\rangle$) followed by a $\pi/2$ pulse to create an equal superposition $|\Psi\rangle = (|S\rangle + |D\rangle) / \sqrt{2}$, see inset Fig 4.11 b). An off-resonant pulse induces an ac-Stark shift for a duration τ . The accumulated phase information $|\Psi\rangle = (|S\rangle + e^{-i\delta_{ac}\tau} |D\rangle) / \sqrt{2}$ is then mapped to the population and detected with a projective measurement. For a systematic investigation, the separation between the two Ramsey pulses is kept constant with an additional waiting time t_w such that $\tau + t_w = \text{const}$, where τ is the interrogation time. The frequency of the Ramsey pattern allows us to directly infer the induced ac-Stark shift for a given detuning Δ from the carrier transition. By repeating the experiment with different detunings Δ , the summed contributions from all transitions but the carrier can be extracted. In figure 4.11 b) such measurements are presented, where $|S_{1/2, m_j = 1/2}\rangle$ and $|D_{5/2, m'_j = 3/2}\rangle$ are chosen as the qubit levels. The Rabi frequency is set to $\Omega = 2\pi \times 162.3$ kHz ($t^\pi = 6.16 \mu\text{s}$). Fitting the data with $y = a/\Delta + b$ yields an ac-Stark shift $\delta_{ac} = 2\pi \times 2.07$ kHz.

It is a perfectly justified question to ask why the ac-Stark shift should cause any trouble, since

in general it is taken care of by changing the laser frequency to the shifted transition frequency. However, as soon as there are several ions illuminated by a non-uniform light field, there will be a spatially dependent ac-Stark shift (Fig. 4.11 c)), which cannot be compensated by simply adjusting the laser frequency. To see why this is troublesome, let us do a back-of-the-envelope calculation: we assume a bichromatic light field, each component inducing a shift $\delta_{ac} \approx 2\pi \times 2$ kHz thus $\delta_{ac} \approx 2\pi \times 4$ kHz, and we further assume a coupling distribution of $\Omega_{\text{edge}}/\Omega_{\text{center}} \approx 1.1$. Following Eq. 3.54 the difference in transition frequency between the center and the edge qubit is $\approx 2\pi \times 800$ Hz. Comparing this value to a typical effective spin-spin coupling $\max\{J_{ij}\} \approx 2\pi \times 50$ Hz (detuning from the sidebands $\Delta = 2\pi \times 40$ kHz), it is obvious that the spatially dependent ac-Stark shift will cause unwanted effects (a detailed discussion of these effects in the context of quantum simulations is presented in chapter 5).

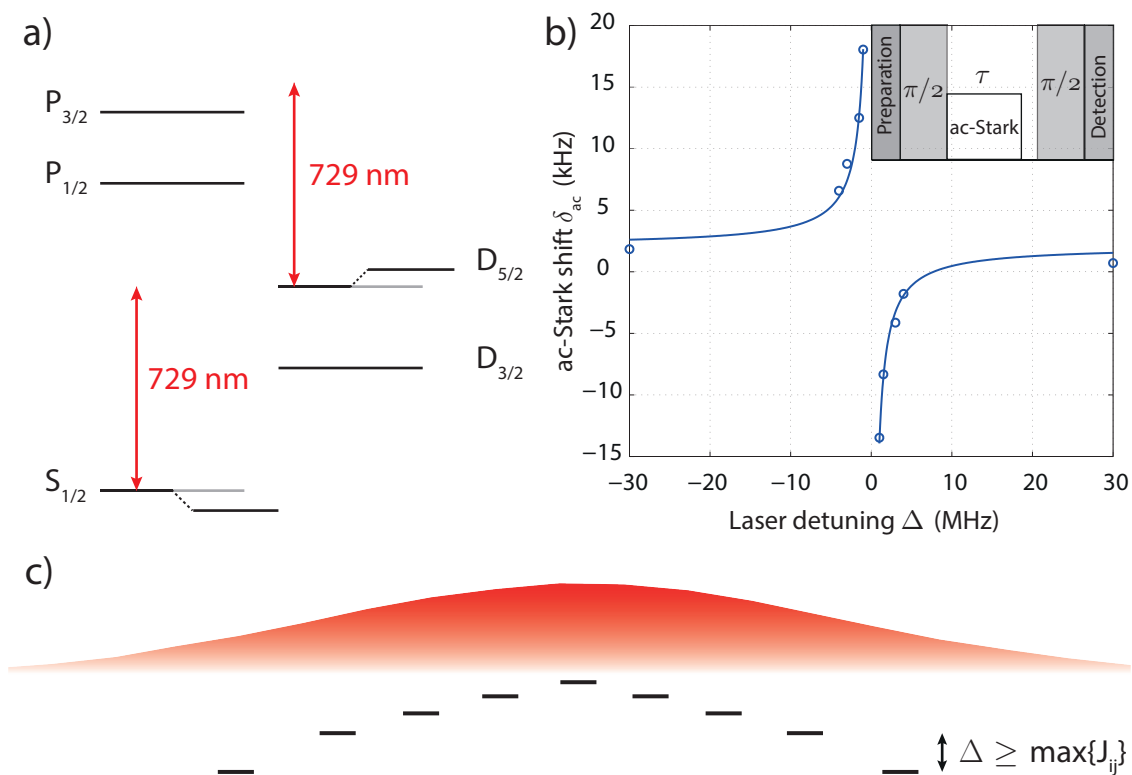


Figure 4.11.: a) A schematic energy diagram of $^{40}\text{Ca}^+$ when the qubit transition is driven resonantly. Due to additional dipole and quadrupole (not shown) transitions, other than the qubit transition, coupling to the light field, the qubit levels experience an ac-Stark shift. b) The ac-Stark shift measured as a function of the detuning Δ to the carrier transition $|S_{1/2}, m_j = 1/2\rangle \leftrightarrow |D_{1/2}, m'_j = 3/2\rangle$ with a Rabi frequency $\Omega = 2\pi \times 162.3$ kHz. Circles: Data, line: Fit ($y = a/\Delta + b$). The resulting ac-Stark shift from all transitions except the carrier is $\delta_{ac} = 2\pi \times 2.07$ kHz. c) Due to the Gaussian intensity profile of the light field, qubits experience a spatially dependent ac-Stark shift, which is of the order of the effective spin-spin coupling.

4.5. Trichromatic light field

Any ac-Stark shift can be nulled by adding a second, off-resonant light field counteracting the light shift [153]. In our setup the shaped beam is mainly used to drive effective spin-spin interaction, and

therefore a bichromatic light field is illuminating the ions. Due to the symmetric detuning from the carrier, these two light fields cancel exactly any ac-Stark shift induced by the carrier itself. However, the ac-Stark shift due to the additional transitions remains. The standard tricks to compensate for this shift in the Mølmer-Sørensen gate operation, center-line detuning or bichromatic imbalancing [98], do not work in this case: the method of center-line detuning, i.e. an additional detuning δ_{cl} of both laser fields $\Delta_b = \Delta + \delta_{cl}$ and $\Delta_r = -\Delta + \delta_{cl}$, fails due to the spatial dependency of the qubit transitions. The alternative, bichromatic imbalancing, where the Rabi frequencies of the blue-detuned $\Omega_b = \Omega(1 + \varepsilon)$ and red-detuned component $\Omega_r = \Omega(1 - \varepsilon)$ are unequal, is inapt because of the large detuning $\Delta > 2\pi \times 2.7$ MHz. In order to compensate for the light shift, the imbalancing has to be $\varepsilon \approx 0.5$, which is too large for proper operation of the gate, where $\varepsilon \ll 1$ has to hold [154].

It is not very demanding to add a third light field for compensation. All that is needed is an additional RF-source²⁴ and a splitter/combiner²⁵, as depicted in figure 4.12 a). All three radio frequencies are sent to a fiber AOM²⁶. It has to be mentioned that the blue/red Rabi frequencies Ω_b and Ω_r are influenced by the RF power sent in for the compensation field, i.e. while the coupling Ω_{comp} of the compensation field is increased, Ω_b and Ω_r become weaker, see figure 4.12 b).

Since all light fields are combined within the same fiber, their spatial modes are identical and as such the compensation field can cancel the spatially dependent light shift. The frequency of the compensation field is set to a positive detuning, e.g. $\Delta_{\text{comp}} = 2\pi \times 1$ MHz, and the power is chosen such that it exactly nulls the remaining ac Stark shift. Figure 4.12 c) shows from left to right: Rabi flops on 8 ions with $\Omega_{\text{max}} = 2\pi \times 221$ kHz and $\Omega_{\text{max}}/\Omega_{\text{min}} = 1.113$; ac Stark flops induced with a detuned light field $\Delta = 2\pi \times 3$ MHz yielding $\delta_{ac}^{\text{max}} = 2\pi \times 5.1$ kHz and $\delta_{ac}^{\text{max}}/\delta_{ac}^{\text{min}} = 1.23$; and finally a fully compensated ac Stark shift using a third light field at $\Delta_{\text{comp}} = 2\pi \times 1$ MHz and $\Omega_{\text{comp}} = 2\pi \times 92.1$ kHz.

There are two main methods to properly set up the compensation. The first one is to off resonantly drive the carrier transition and to measure the cumulative ac Stark shift in a Ramsey like fashion, as described in section 4.4.2. For a given frequency of the compensation field, one has to tune the RF power of the compensation such that the frequency of the ac-Stark flops becomes lower. A more convenient way is to use the spin-spin interaction itself to calibrate the compensation. This method will be described in chapter 5.

4.5.1. Reasons for compensation failure

There are several effects which can corrupt a proper compensation of the induced light shifts. Some of these effects are severe, others are negligible. Nevertheless, a complete list with the corresponding explanations will be given in this section. The order in the following list is somewhat according to their severity on the compensation:

- a) Reflections
- b) trichromat: higher order beat frequencies

²⁴Rohde & Schwarz: SML01

²⁵Mini-Circuits: ZSC-2-1W

²⁶Gooch & Housego, model MM080 1C2V14 5 F2SH B

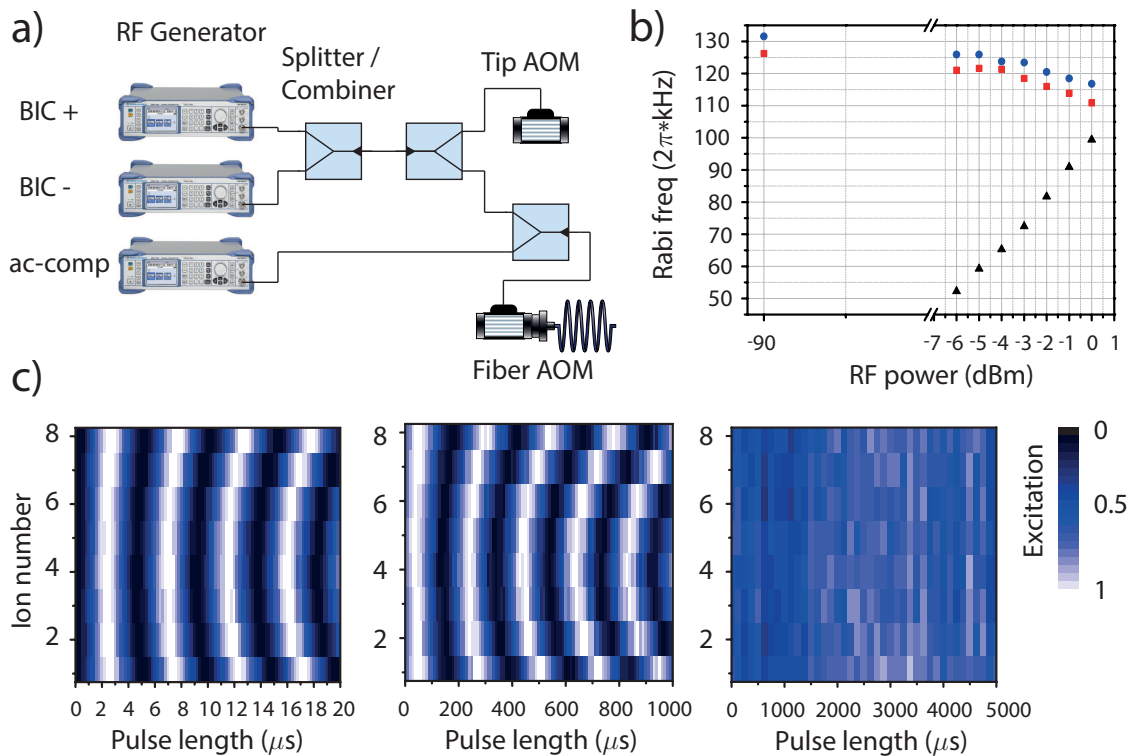


Figure 4.12.: **a)** Setup to generate a trichromatic light field. The three RF frequencies are individually produced by separate RF-sources²⁴, combined²⁵ and sent to a fiber AOM²⁶ as depicted above. **b)** The three light fields share a common input light field and, as the RF power of one of the components is changed, it will influence the others. Here, the effect is shown on the individual coupling to the ion, as the RF power of the compensation component is increased. **c)** (from left to right) Rabi flops on eight ions, where the coupling distribution is clearly visible. The resulting cumulative ac-Stark shift, when the bichromatic field is set to a detuning $\delta = \pm 3$ MHz from the carrier. The ac-Stark flops are measured with the Ramsey type method described in the chapter above. In the last plot, the compensation field is set to compensate for the ac-Stark shifts, resulting in a remaining ac-Stark shift which is hardly measurable.

- c) Mode structure and temperature
- d) Micromotion
- e) Polarization and k-vector gradients
- f) Transverse E-field gradient

a) Reflections The strongest effect regarding unwanted ac-Stark shifts is caused by the interaction beam being reflected off the opposite inverted viewport and the optics behind, such as lenses, wave plates and the fiber coupler of the addressed beam. In contrast to the spatially dependent qubit transition caused by the Gaussian beam shape, B-field gradient, and differential quadrupole shift, the reflections are not stationary and vary over time, as beam pointing variations play a large role.

One might be inclined to think that the reflected pattern of the bichromatic light fields and the compensation field have the same spatial distribution, hence, the compensation should be straightforward. However, the compensation fails and the reason for this is not obvious. The following arguments are rather educated guesses than definitive answers. Small amounts of back

reflected light can interfere with the strong primary beam, resulting in a standing wave structure that gives rise to ac-Stark shifts which vary on a sub-micrometer scale²⁷.

The failure in compensation most likely results from the different couplings of the dipole and the quadrupole transitions. The ac-Stark shift caused by the dipole transition is proportional to the light field intensity, $\delta_{ac}^{dp} \propto I$, whereas the quadrupole ac-Stark shift, and as such the compensation field, are proportional to the gradient of the light field, $\delta_{ac}^{qp} \propto \nabla I$. Further, it is rather implausible to assume that all ions sit at similar positions in the standing wave, some might be close to a node and others to an antinode. While ions in the nodes experience no dipole ac-Stark shift from the backreflection, the quadrupole ac-Stark shift is the strongest, and ions at the antinodes feel the strongest δ_{ac}^{dp} and no δ_{ac}^{qp} induced by the backreflection. Hence, depending on the ions' position, the compensation field will under or over compensate the ac-Stark shifts.

On top of that, additional effects might play a role. It is quite likely that the back reflections show aberrations and have no perfect planar wavefront, as the light has to pass many optical elements²⁸, twice, before reaching the ions. This may result in a spatially dependent k-vector and even in polarization gradients, leading to different couplings of the dipole and quadrupole ac-Stark shifts. A more detailed discussion regarding polarization/k-vector is given in the last paragraphs of this section.

The solution to avoid reflections in our setup is to lift the last mirror in the interaction beam path by ≈ 2 cm such that the beam comes in at an angle of a few degrees. This is enough to guide the reflections below the trap blades.

b) Higher order beat frequencies Even though splitters/combiners are used to add up the three frequency components of the trichromat, due to non-linearities in the combiners additional frequencies can be observed in the RF-Spectrum sent to the AOM, as shown in figure 4.13 a) - c). These additional, unwanted frequency components correspond to frequencies $f = 2f_{1(2)} - f_{2(1)}$ and are transduced to the optical spectrum. In figure 4.13 d) - f) optical beat frequencies are presented, where the light after the fiber AOM is beat with the light before the double pass AOM, giving a center beat frequency at $f_{\text{beat}} \approx 476 \text{ MHz} + 80 \text{ MHz}$. In the bichromatic case the number of frequencies is quite manageable (Fig 4.13 b & e), whereas in the trichromatic case it becomes rather messy (Fig 4.13 c & f). Although the amplitude of the unwanted frequency components is at least 15 dB lower compared to the desired ones, caution is recommended especially when working with many ions. One of the many unwanted frequency components might lie close to a motional mode and disturb the time dynamics in the quantum simulation. It is straightforward to calculate the frequency spectrum and to compare it with the motional spectrum. Should one of the frequencies be suspiciously close to a motional mode, there are several options to adjust the situation. By modifying the frequency of the compensation field or the bichromat frequency, it is possible to shift certain frequency components. Another way is to change the axial or the radial confinement, although this is less preferable, as usually at this point in the experimental procedure sideband

²⁷Here, we assume that all three frequency components generate standing waves with the same phase $\phi = 0$, given that they only differ by $\Delta f \approx 2 \text{ MHz}$ the path length difference required for them to be out of phase $\phi = 180$ is $\Delta l \approx 100 \text{ m}$.

²⁸It seems most reflections are caused by the addressing optics outside the vacuum chamber such as the objective, collimator and the fiber coupler.

cooling is already set up.

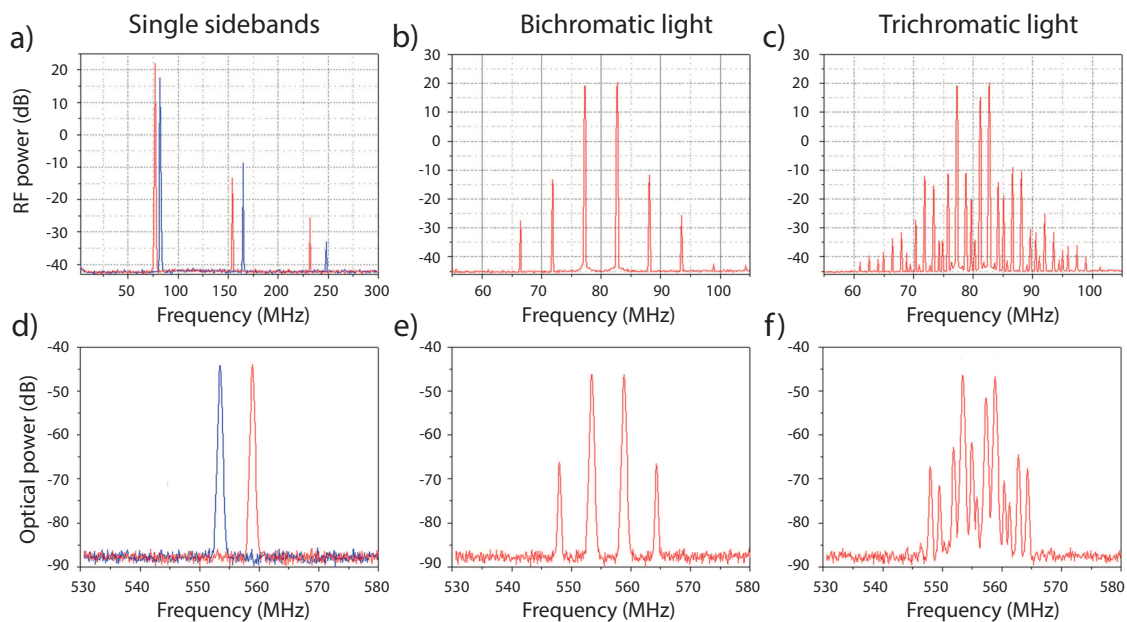


Figure 4.13.: **a)-c)** The RF spectrum sent to the fiber AOM and measured with a spectrum analyser for **a)** individual frequencies, **b)** bichromatic light and **c)** trichromatic light. **d)-f)** is the corresponding optical spectrum, where the light before the double pass AOM ($f_{DP} = 476$ MHz) is beaten with the light after the fiber AOM. **a)** & **d)** The individual sideband frequencies at $f_r = 77.3$ MHz and $f_b = 82.7$ MHz are applied to the fiber AOM. Higher order frequencies, due to non-linearities, are clearly visible in the RF Spectrum (not shown in the optical spectrum). **b)** & **e)** When both frequencies f_b and f_r are applied simultaneously, higher order frequencies appear in their vicinity at $f_1 = 2f_b - f_r$ and $f_2 = 2f_r - f_b$. In the optical spectrum these unwanted frequencies are suppressed by 20 dB. **b)** & **e)** In addition a third frequency $f_{comp} = 81.2$ MHz is added at -5 dB lower power. The resulting beat frequencies are mainly of the type $f_{beat} = 2f_1 - f_2$ and at least -15 dB lower.

c) Mode structure and temperature The structure of the motional modes and their temperatures have two distinct, non-negligible effects altering the ac-Stark compensation. On the one hand, there is an additional ac-Stark shift coming from the off-resonant driving of the motional sidebands, imprinting the mode's spatial structure onto the ions. This cannot be compensated by a simple Gaussian beam shape. On the other hand, thermally populated motional modes reduce the coupling strength on the carrier in an inhomogeneous way, i.e. distorting the ac-Stark compensation.

First, we consider the off-resonant coupling to the sidebands by examining a seven-ion string. Given the operational trapping parameters $\omega_z = 2\pi \times 220$ kHz, $\omega_x = 2\pi \times 2.70$ MHz and $\omega_y = 2\pi \times 2.35$ MHz, the eigenmode matrix $b_{i,m}$ and the eigenfrequencies ω_m^λ , we calculate the Lamb-Dicke parameter $\eta_{i,m}^\lambda$ for each ion i and mode m in the direction $\lambda = \{x, y\}$:

$$\eta_{i,m}^\lambda = kb_{i,m} \sqrt{\frac{\hbar}{2m_{Ca}\omega_m^\lambda}} \cos(\theta) \quad (4.5)$$

A representative example in the x -direction is given by:

$$\eta_{i,m}^x = \begin{pmatrix} -0.07 & 0.26 & -0.64 & -1.18 & -1.67 & -1.73 & 1.12 \\ 0.52 & -1.24 & 1.72 & 1.33 & 0.09 & -1.08 & 1.12 \\ -1.48 & 1.72 & -0.36 & 1.14 & 0.96 & -0.52 & 1.12 \\ 2.06 & 0.00 & -1.43 & 0.00 & 1.23 & 0.00 & 1.12 \\ -1.48 & -1.72 & -0.36 & -1.14 & 0.96 & 0.52 & 1.12 \\ 0.25 & 1.24 & 1.72 & -1.33 & 0.09 & 1.08 & 1.12 \\ -0.07 & -0.26 & -0.64 & 1.18 & -1.67 & 1.73 & 1.12 \end{pmatrix} \times 10^{-2} \quad (4.6)$$

Here, the modes are sorted from lowest frequency (left) to highest frequency (right), which in the case of the radial modes is the COM-mode. From the matrix in Eq. 4.6, it is evident that not all ions are equally affected. An obvious example is the second highest mode, where the edge ions have a high amplitude and the middle ion doesn't participate in the motion. Since the sidebands are driven off-resonantly for the spin-spin interactions, we need to calculate the ac-Stark effects resulting from the blue and red sidebands:

$$\delta_i^{ac} = \sum_{m,\lambda} \left(\frac{\left(\eta_{i,m}^\lambda \sqrt{n_m^\lambda + 1} \Omega \right)^2}{2(\Delta_m + \delta^{cl})} + \frac{\left(\eta_{i,m}^\lambda \sqrt{n_m^\lambda} \Omega \right)^2}{2(\Delta_m - \delta^{cl})} \right) \quad (4.7)$$

where the sum goes over all m -modes in both directions $\lambda = \{x, y\}$, n_m^λ is the number of phonons for a given mode, Δ_m is the laser detuning from the m th sidebands and δ^{cl} is the centerline detuning²⁹.

In the following discussion, we are mainly interested in the difference of the qubit transition between neighbouring ions and therefore we define:

$$\delta_{i,i+1}^{ac} = |\delta_i^{ac} - \delta_{i+1}^{ac}| \quad (4.8)$$

Since the absolute value of $\delta_{i,i+1}^{ac}$ depends strongly on Δ_m and ω_m^λ , it is sensible to normalize it by the nearest neighbour spin-spin coupling, $J_{i,i+1}$, in order to have a fair comparison between different parameter regimes.

Experimentally, the most interesting case is when all modes are ground state cooled, i.e. $n_m^\lambda = 0$. In this case, the coupling on the red sidebands is zero, and Eq. 4.7 simplifies to

$$\delta_i^{ac} = \sum_{m,\lambda} \frac{\left(\eta_{i,m}^\lambda \Omega \right)^2}{2(\Delta_m + \delta^{cl})}. \quad (4.9)$$

Interestingly, these are exactly the diagonal elements of the J_{ij} -matrix and can be interpreted as a *self-coupling* of the spins. In figure 4.14 a) the normalized $\delta_{i,i+1}^{ac} = \delta_i^{ac} - \delta_{i+1}^{ac}$ are shown for different numbers of ions, with $\Delta_{\text{COM}}^x = \Delta_{\text{COM}} = 2\pi \times 40$ kHz and $\delta^{cl} = 0$. Quite surprisingly, the effects are rather strong on the edges of the string, where the differences can exceed the nearest neighbour

²⁹Here we neglect the fact that the 'blue' ('red') part of the bichromatic light field also couples to the red (blue) sideband. This coupling is far off-resonant, ≈ 5 MHz, and therefore negligible.

coupling $J_{i,i+1}$. This has to be taken into account when running simulations of spin-spin dynamics, since the time evolution gets slightly distorted depending on the interaction range.

When the detuning from the sidebands changes, also the relative contribution of each mode changes, as shown in figure 4.14 b). The closer the laser frequency to the center of mass mode, the smaller $\delta_{i,i+1}^{ac}$ becomes, as the COM-mode imprints a homogeneous ac-Stark shift. However, as Δ_{COM} becomes larger the normalized differences, $\delta_{i,i+1}^{ac}/J_{i,i+1}$, approach fixed values, rather than approaching zero as intuitively expected for Δ_{COM} . In the limit of $\lim_{\Delta_{\text{COM}} \rightarrow \infty} \delta_{i,i+1}^{ac} = 0$, all ω_m^λ become degenerate compared to Δ_{COM} , such that each mode has the same weight in the sum 4.7. With the constraint $\sum_m b_{i,m}^2 = 1$ ³⁰, one would intuitively guess a spatially homogeneous shift. The only explanation I have for the time being is that the $J_{i,i+1}$'s approach fixed values for large Δ_{COM} as well, as simulations indicate.

When dealing with thermally populated modes, for instance after Doppler cooling, each of the ω_m^λ modes is randomly sampled over a thermal distribution with probability p_n^m to find n phonons [89]

$$p_n^m(\bar{n}_m) = \frac{1}{\bar{n}_m + 1} \left(\frac{\bar{n}_m}{\bar{n}_m + 1} \right)^n, \quad (4.10)$$

where \bar{n}_m is the mean phonon number of mode m . In the symmetric case, that is $\delta^{cl} = 0$, all phonon number dependent terms in Eq. 4.7 cancel each other. However, this is not the case anymore as soon as the red and the blue sideband are not equally weighted, i.e. $|\delta^{cl}| \neq 0$. Here, we make the sensible approximation that all modes have the same mean phonon number after Doppler cooling $\bar{n}_m = \bar{n}$ ³¹. In figure 4.14 c) the normalized mean and standard deviation of $|\delta_{i,i+1}^{ac}|$ are shown as a function of \bar{n} for the different pairs of a seven ion string. Interestingly, the mean $|\delta_{i,i+1}^{ac}|$ of the edge pair can be reduced by having hotter modes, such that the red sideband can counteract the blue one. Nevertheless, increasing the temperature is undesirable, since fluctuations of $|\delta_{i,i+1}^{ac}|$ become rather large due to the thermal distribution.

These ac-Stark shifts described above, cannot be compensated with the Gaussian third light field. More elaborate schemes, such as a spatial light modulator, can mimic the spatial distribution of ac-Stark shifts induced by the motional modes and null the mean shift, but not the fluctuations.

The last part examines the effect of the mode temperatures on the reduction of the carrier coupling strength in the Lamb-Dicke regime. The ratios between the unperturbed coupling strengths Ω_i on the carrier of ion i , and the thermal ones $\Omega_i^{\text{thermal}}$ are approximated by [123]:

$$\frac{\Omega_i^{\text{thermal}}}{\Omega_i} = \prod_m \left(1 - \eta_{i,m}^2 \bar{n}_m \right). \quad (4.11)$$

As shown in figure 4.14 d), the mean reduction and the associated standard deviation on the edge and the middle ion (7 ions) are similar because, here, all modes are equally weighted, under the

³⁰What this means is that the sum of all Lamb-Dicke factors over all modes m is the same for all ions, given that the mode frequencies ω_m^λ are the same.

³¹ $\bar{n}_{\text{Doppler}} = \frac{\Gamma}{2\omega_m} \approx \frac{\Gamma}{2\omega_{\text{COM}}}$, as $|\omega_m - \omega_{\text{COM}}| \ll \omega_{\text{COM}}$.

assumption of $\bar{n}_m = \bar{n}$. However, from shot to shot the carrier coupling strengths on different ions might be significantly different, i.e. affecting the ac-Stark compensation. For $\bar{n} \approx 2$, the coupling variation from ion to ion can be up to $\approx 2\%$, resulting in $\approx 4\%$ variation of the ac-Stark compensation and in such a case $|\delta_{i,i+1}^{ac}| > J_{i,i+1}$.

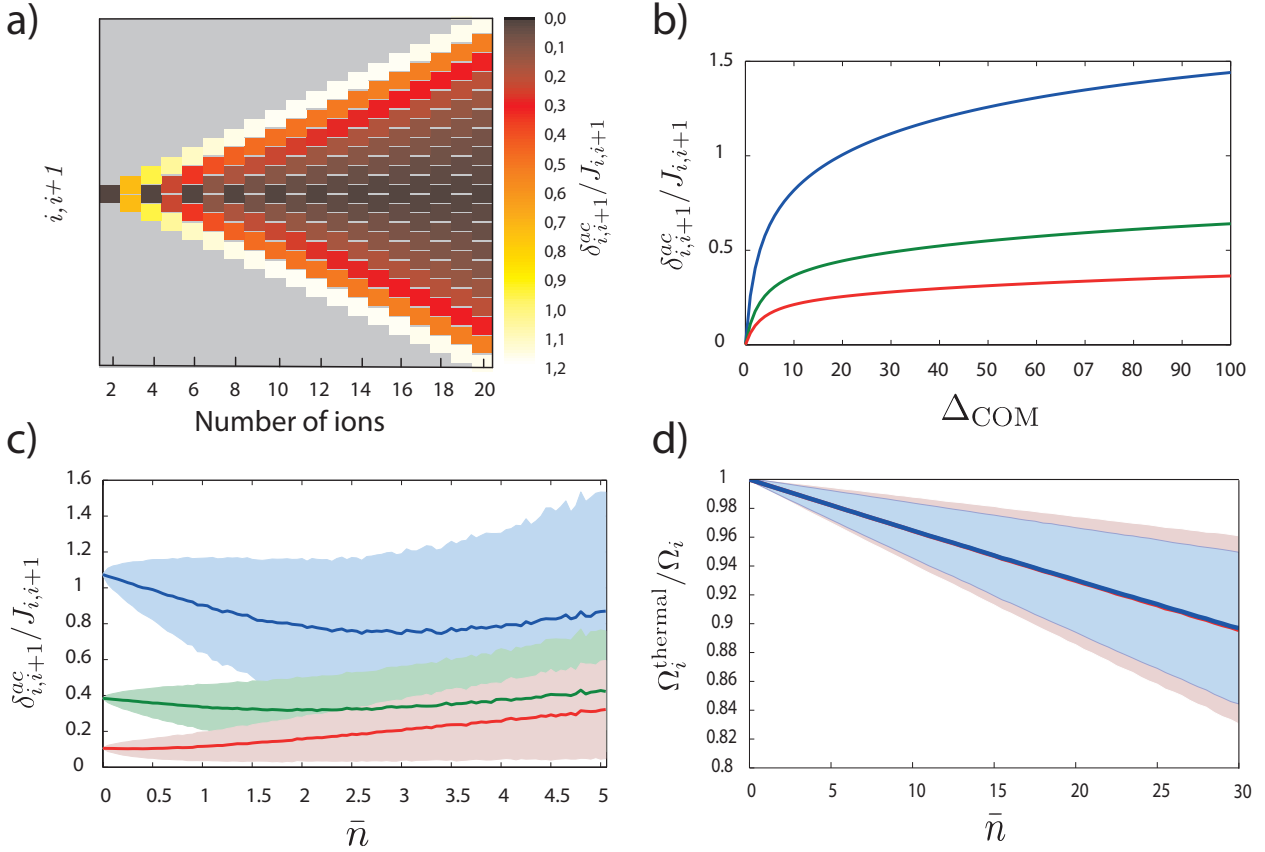


Figure 4.14.: All graphs are calculated for the following trapping frequencies: $\omega_{\text{ax}} = 2\pi \times 220$ kHz and $\omega_{\text{radial}} = 2\pi \times 2.65$ MHz. **a)** The normalized differential ac-Stark shift $\delta_{i,i+1}^{ac}/J_{i,i+1} = |\delta_i^{ac} - \delta_{i+1}^{ac}|/J_{i,i+1}$ is calculated for a common detuning $\Delta_{\text{COM}} = 2\pi \times 40$ kHz, where δ_i^{ac} is the induced ac-Stark shift on ion i and $J_{i,i+1}$ is the next neighbour spin-spin coupling between ions i and $i+1$. This differential ac-Stark shift is a result of the eigenmode matrix $b_{i,m}$, the lifted degeneracy of the eigenmode frequencies ω_m^λ and the laser only coupling to the blue sideband due to ground state cooling. The effect is most pronounced at the string edges and can exceed the spin-spin coupling. **b)** The normalized differential ac-Stark shift is calculated for 7 ions as a function of the detuning Δ_{COM} . Blue are ions 1 & 2 resp. 6 & 7; green are ions 2 & 3 resp. 5 & 6; and red 3 & 4 resp. 4 & 5. **c)** $\delta_{i,i+1}^{ac}/J_{i,i+1}$ is sampled over a thermal distribution with a mean phonon number \bar{n} for $\Delta_{\text{COM}} = 2\pi \times 40$ kHz and $\delta^{cl} = 3$ kHz. Bold lines represent the mean value and the shaded region is one standard deviation. **d)** The reduction in the carrier coupling is calculated as a function of \bar{n} , where Ω_i is the unperturbed ($\bar{n} = 0$) Rabi frequency of ion i .

d) Micromotion The effect of the micromotion is that it generates sidebands which ‘steal’ coupling strength from the carrier transition. For a single ion the micromotion can be efficiently compensated to $\beta < 0.01$, as described in section 4.3. However, in long ion strings it is not necessarily true that the micromotion compensation is perfect on each ion. Such an inhomogeneous compensation will cause the carrier coupling strength to differ and might corrupt the ac-Stark compensation.

	Ion 1	Ion 2	Ion 3	Ion 4	Ion 5	Ion 6	Ion 7
$\Omega_{3/2}/\Omega_{5/2}$	27.5	27.9	27.6	28.5	28.5	29.7	29.7
$\Omega_{3/2}/\Omega_{1/2}$	15.8	12.7	12.8	10.0	8.9	6.9	5.7

Table 4.2.: Normalized Rabi frequencies for different Δm -transitions of a 7 ion string. Ω'_m is a short cut notation of the Rabi frequency for a given transition $|S_{1/2}, m_j = 1/2\rangle \leftrightarrow |D_{5/2}, m'_j\rangle$, with $m'_j = \{\frac{1}{2}, \frac{3}{2}, \frac{5}{2}\}$. The Rabi frequencies are normalized with respect to the main quadrupole transition $\Omega_{3/2}$ used at that time. $\Omega_{3/2}/\Omega_{5/2}$ shows little variation across the ion string, whereas the variation of $\Omega_{3/2}/\Omega_{1/2}$ is more pronounced. This allows us to conclude that there is a slight \vec{k} -vector gradient due to the astigmatic focussing.

The effective carrier coupling is given by

$$\Omega_{\text{carrier}}^{\text{eff}} \propto 1 - \frac{\beta^2}{4}. \quad (4.12)$$

The measured modulation index does indeed vary from ion to ion (Fig. 4.7) giving $\beta_{\text{max}}/\beta_{\text{min}} \approx 2$ in the case of 20 ions. Following eq. 4.12, we find that the maximal coupling strength variation is of the order of 10^{-4} . Nevertheless, it is advisable to check the micromotion for the different settings of axial/radial potentials and radial splitting voltages, as the modulation index can easily exceed $\beta > 0.1$.

e) Polarization and k-vector gradients The Rabi frequency on the different carrier Zeeman levels is not only proportional to the \vec{E} -field gradient but also depends on a geometrical factor $g_{\Delta m_j}$ [83, 123], incorporating the angle ϕ between the laser beam and the \vec{B} -field axis, as well as the polarization angle γ , shown in Fig. 4.15 a). If a trichromatic beam has a \vec{k} -gradient or polarization gradient along the ion string axis, the compensation of the ac-Stark shifts might be corrupted, due to different selection rules for dipole and quadrupole transitions. A possible \vec{k} -gradient could arise from a non-planar wavefront being the case for a focussed beam outside the Rayleigh range. Aberrations also distort the wavefront and imperfect optical elements, such as lenses, mirrors and view ports, could cause polarization gradients. One way to measure \vec{k} - and polarization gradients is to use the ions as a sensor by driving and comparing different $|S_{1/2}, m_j = 1/2\rangle \leftrightarrow |D_{5/2}, m'_j\rangle$ transitions, where $m'_j = \{\frac{1}{2}, \frac{3}{2}, \frac{5}{2}\}$.

In figure 4.15 b) the dependency on ϕ and γ is shown for different $\Delta m = m'_j - m_j$. At the time of these measurements (Nov. 2013), the interaction beam was optimized to drive the $|S_{1/2}, m_j = 1/2\rangle \leftrightarrow |D_{5/2}, m'_j = 3/2\rangle$ transition, i.e. $\phi \approx 90^\circ$ and $\gamma \approx 0^\circ$. Due to slight alignment imperfections it is possible to feebly drive the other two Δm -transitions. Table 4.2 shows the coupling strengths of the different transitions $\Delta = \{0, 2\}$ normalized by the main transition $\Delta m = 1$ for a string of 7 ions. The observed weak couplings strengths on $\Delta m = 0$ can be explained by a small tilt of the \vec{k} -vector by 0.3° , and to couple to the $\Delta m = 2$ transition it is sufficient to rotate the polarization by $\approx 1.5^\circ$. From the coupling strength ratios given in the table one can infer that there is mainly a \vec{k} -vector gradient due to the astigmatic focussing, and any polarization gradient is negligible.

Any coupling to other unwanted quadrupole transitions will ‘steal’ coupling strength from the compensation. However, these unwanted couplings are well suppressed and the effects are below 10^{-3} of the overall ac-Stark compensation.

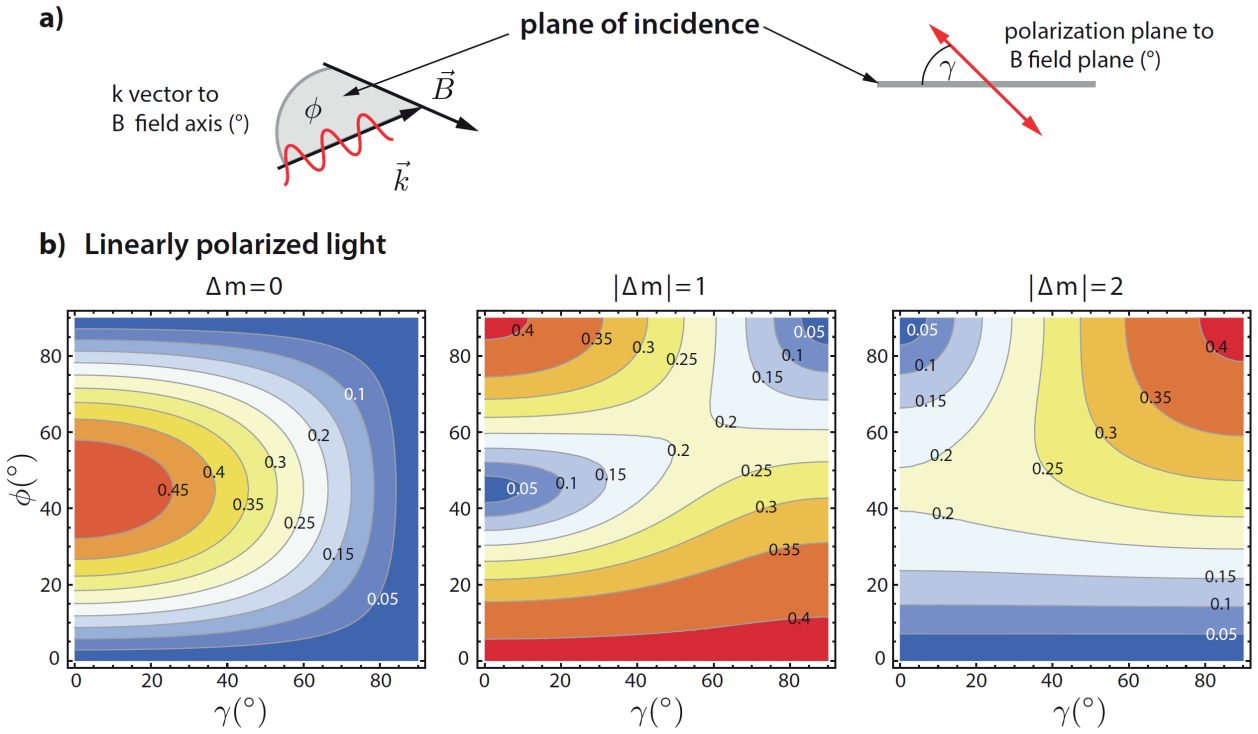


Figure 4.15.: Figure taken from C. Hempel thesis. The coupling of the quadrupole transitions depend on a geometrical factor $g_{\Delta m_j}$, which takes the \vec{k} -vector and the polarization into account. **a)** The angle ϕ is defined by the \vec{B} -field quantization axis and the incoming \vec{k} -vector, spanning a plane of incidence. Linearly polarized light can be in plane or rotated out of plane by γ . **b)** Calculated values of $g_{\Delta m_j}$ as a function of ϕ and γ for different Δm -transitions.

f) Transverse E-field gradient A spatial \vec{E} -field gradient, resulting from the Gaussian beam shape, can also induce a coupling to the quadrupole transition, where the coupling strength depends on the ion's position. This effect is minor, however, it might come into play when the beam is tightly focussed. In order to estimate the size of this effect we compare the relevant length scales, where the intensity varies from maximum to zero. Along the \vec{k} -vector this length scale is $\lambda/4$. In the transverse direction of the beam profile, this length scale is roughly half the beam waist ω_0 . For a beam waist $\omega_0 \approx 200 \mu\text{m}$ at a wavelength of $\lambda = 729 \text{ nm}$ we can estimate the coupling strength variation due to the transverse gradient to be smaller than $\lambda/2\omega_0 \approx 2 * 10^{-3}$. This is sufficiently low and can therefore be neglected.

4.6. Radial Modes

The motional sidebands are a versatile and important tool in trapped ion experiments since they are used to mediate the spin-spin coupling between different ions, frequently referred to as the bus system in ion traps. While axial sidebands are often used for Mølmer-Sørensen entangling gates, due to their 'clear' frequency separation and intrinsic stability, radial/transverse modes hold the possibility for far more versatile and complex spin-spin interactions. However, due to their closeness in the spectrum (bunching), all of the modes need to be ground state cooled in to order assure proper time evolution of the gates. Further, stabilizing the radial frequency is more complex, since

the RF-voltage across the RF-blades needs to be measured and controlled. Here, these experimental issues concerning the radial modes will be addressed.

4.6.1. Spectrum

The calculation of the radial spectrum for more than two ions needs to be solved numerically as described in chapter 3.1.3. However, the spectrum can be easily measured and resolved as shown in Fig. 4.16 a).

Here, five ions are trapped at $\omega_{ax} = 2\pi \times 220$ kHz and the red sideband spectrum is recorded with a PMT, where 9 out of 10 peaks are resolved (5^{th}_x and 3^{rd}_y modes overlap). Judging solely from the PMT data, it is not obvious which spectral peak belongs to which mode, since both x- and y-modes are excited. One can calculate the radial spectrum given the three COM-mode frequencies and assign the different spectral features accordingly. A neater way is to use the camera for detection (Fig. 4.16 b)). The camera reveals that not all ions are excited with the same amplitude, in fact the amplitudes are proportional to the Lamb-Dicke factors $\eta_{i,m}^\lambda = b_{i,m} k x_0$, where $b_{i,m}$ are the eigenmode vectors in the direction $\lambda = \{x, y\}$. Figure 4.16 c) shows three close-ups of the spectrum taken with the camera and indeed, the mode structure is directly visible in the amplitudes of the ions.

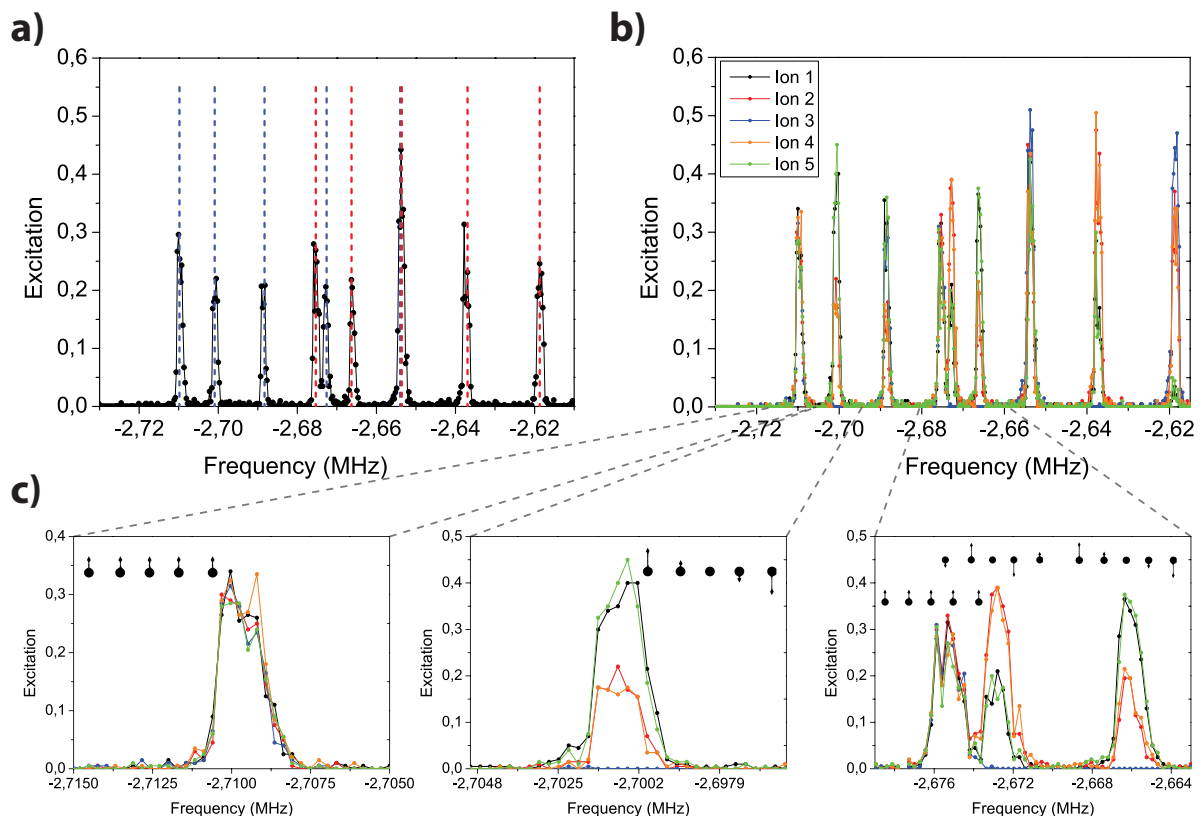


Figure 4.16.: a) The radial spectrum taken with the PMT for 5 ions trapped at $\omega_{ax} = 2\pi \times 220$ kHz & $\omega_{rad} = 2\pi \times 2.713$ MHz. The dashed lines show the calculated spectrum for the x-modes (blue) and y-modes (red). b) The same spectrum as before, however, the camera is used for detection. The close up c) reveals the mode structure in terms of excitation amplitude of each individual ion.

4.6.2. Motional mode stabilization

In order to use the radial modes for quantum information processing protocols, they need to be stable in frequency ($\ll \Delta_m$) on slow (seconds to hours) and fast (< 20 ms) time scales. The slow drifts are mainly caused by changes in the RF voltage V_{RF} , due to fluctuations in the amplification circuit (RF amplifier and helical resonator). In addition, thermal variations of the trap itself [119] can change the ion-to-blade distance r slightly. This will affect the radial trapping frequency as

$$\omega_{\text{rad}} \propto \frac{V_{\text{RF}}}{r^2 \Omega_{\text{RF}}}. \quad (4.13)$$

Regarding the frequency stability, fluctuations of the drive frequency $\Omega_{\text{RF}} = 2\pi \times 28.829$ MHz can be ruled out, since the generated frequency is extremely stable ($\ll 1$ Hz)³². Hence, the following

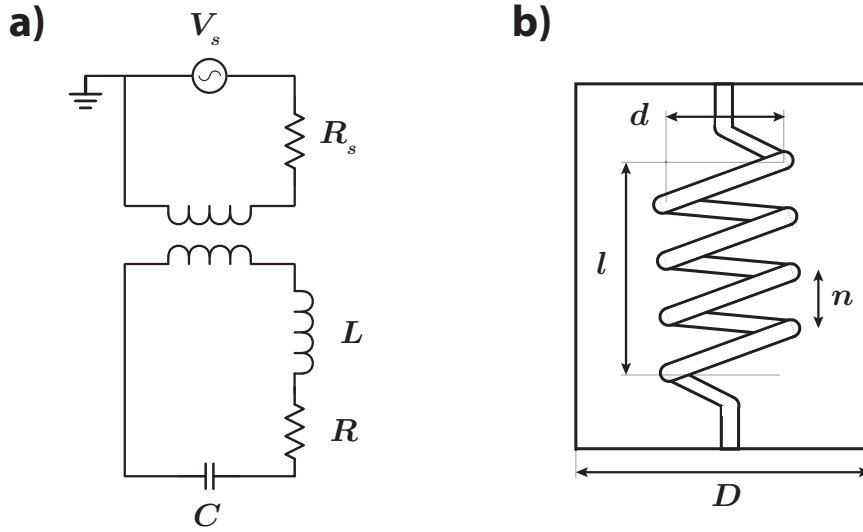


Figure 4.17.: a) A schematic drawing of the LCR circuit matching the resonator's resistance R on resonance to the source impedance R_s of the voltage source V_s . b) An outline design of the helical resonator with length $l = 182$ mm, inner diameter $d = 38$ mm, wire thickness $b = 5$ mm and $n = 0.1 \text{ mm}^{-1}$ windings. The resonator is inside of a conductive shield with inner diameter $D = 80$ mm.

discussion will focus on the radio frequency voltage V_{RF} and the amplification circuit used to generate it.

In our setup, $V_{\text{RF}} > 1000$ V are applied to generate a deep trapping potential, which is desirable for long trapping times. In order to reach these high voltages the Rf signal is first amplified³³ to 5 W – 8 W and then coupled into a helical resonator [155–157] amplifying the voltage. The combined resonator - ion trap circuit can be represented as an effective LCR circuit with the main purpose of impedance matching between the RF source and the trap [158], see Fig.4.17 a). The resonance frequency is given by $\omega_0 = 1/\sqrt{LC}$ with the quality factor $Q = \frac{1}{R} \sqrt{\frac{L}{C}}$. When the capacitance of the trap dominates the overall capacitance, the voltage across the trap will be approximately equal to the voltage over the capacitor C . Moreover, at resonance the peak voltage over the capacitor C

³²Rohde & Schwarz SML01, SSB phase noise < -122 dBc/Hz (at $f = 1$ GHz, $\Delta f = 20$ kHz)

³³Mini Circuits LZY -22+ (Gain ≈ 44.4 dB, max output = 30 W, noise figure ≈ 8.3 dB)

is equal to the peak voltage over the inductor L . Thus, the voltage over an inductor is given by

$$V(t) = \frac{dI_{\text{peak}}}{dt} \sin(\omega_0 t) = \omega_0 L I_{\text{peak}} \cos(\omega_0 t) \quad (4.14)$$

where I_{peak} is the peak current in the resonator. At times τ , where $\cos(\omega_0 \tau) = 1$, the peak voltage over the trap can be written as:

$$V_{\text{peak}} \approx \omega_0 L I_{\text{peak}} \quad (4.15)$$

Since the resonator circuit is not loss-free, power is dissipated through the resistance R :

$$P = \frac{1}{2} R I_{\text{peak}}^2 = R I_{\text{rms}}^2 \quad (4.16)$$

where $I_{\text{rms}} = I_{\text{peak}}/\sqrt{2}$ is the root mean square current. Combining equations 4.15 & 4.16 with the definition of Q we can rewrite

$$V_{\text{rms}} \approx \left(\frac{L}{C}\right)^{1/4} \sqrt{PQ}. \quad (4.17)$$

Equation 4.17 shows directly the parameters influencing the RF voltage and thus the trapping potential. In a helical resonator the inductance L is a function of the dimensions of the resonator, such as the coil length l , the coil inner diameter d , the turns per unit length n and the shield diameter D (for details see figure 4.17 b)). Macalpine et al. [156] give an empirical formula for the case $l > d$:

$$L = l \times 0.98425 n^2 d^2 \left[1 - \left(\frac{d}{D}\right)^2 \right] 10^{-6} \mu\text{H}. \quad (4.18)$$

The quality factor Q depends not only on the parameters described above but also on the resistance R which in turn depends on material properties such as resistivity ρ . Due to the skin effect ac-currents do not penetrate the whole bulk material, hence the current density is highest close to the surface. For copper the skin depth δ is calculated to be $\sim 30 \mu\text{m}$ at $\Omega_{\text{RF}} = 2\pi \times 30 \text{ MHz}$. This circumstance makes Q not only dependent on temperature but also on surface chemistry such as oxidation. Further, the resonator has a self-capacitance which also varies with dimensional changes.

All the issues mentioned above have a non-trivial temperature dependency and lead to a shift of the radial mode frequency. A passive stabilization of the resonator circuit by stabilizing the temperature turned out to be insufficient. However, following equation 4.17 the radial mode frequency can be manipulated by varying the RF power. And, if the RF voltage over the trap is measurable, one can build a feedback loop controlling the RF power. Figure 4.18 shows schematic diagrams of the final RF stabilization circuit, after many iterations, used in this thesis.

The RF signal is split³⁴ into two paths, one unaffected and the other one attenuated by -20 dB ³⁵ and by a voltage variable attenuator (VVA³⁶). The control voltage of the VVA is set by a PID

³⁴Mini Circuits: ZSC-2-1+ (insertion Loss $\approx 3 \text{ dB}$, insulation $\approx 28 \text{ dB}$)

³⁵Mini Circuits: HAT-20+

³⁶Mini Circuits: ZX73-2500-S+ (attenuation $\approx -41 \text{ dB}$ (0 V) to -5 dB (10 V))

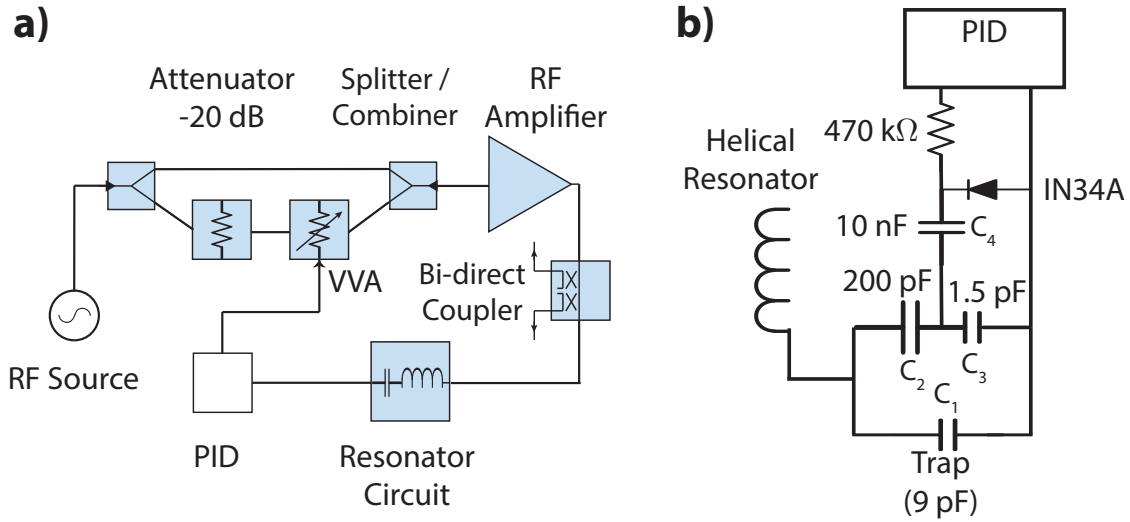


Figure 4.18: a) A schematic drawing of the stabilization circuit used to stabilize the RF voltage V_{RF} over the trap by controlling the RF power sent to the resonator-trap circuit. b) The RF voltage is measured with a capacitive divider and the oscillation signal is converted to DC with a half wave rectifier and then measured with the PID controller.

controller³⁷, thus controlling the RF power. At the end these two RF paths are recombined and amplified³³. With a bi-directional coupler³⁸ the forward and the reflected power can be monitored if needed.

The voltage over the trap is measured with a capacitive divider picking off a small amount of voltage ($\sim 1 : 133$), which is then rectified and measured with the PID controller, see Fig.4.18 b). In order to keep the trap capacitance $C_1 = 9 \text{ nF}$ ³⁹ the dominant one, the capacitors of the divider $C_2 = 200 \text{ pF}$ & $C_3 = 1.5 \text{ pF}$ are chosen such that

$$C_{\text{tot}} = C_1 + \frac{C_2 C_3}{C_2 + C_3} = 10.5 \text{ pF} \approx C_1 \quad (4.19)$$

Here, the self-capacitance of the helical resonator is neglected. The picked-up RF voltage is rectified over a Germanium diode⁴⁰, since they possess the lowest forward current. This setup is also known as a half wave rectifier, as only half of the oscillation period can pass the diode. The additional capacitances of the diode and the smoothing capacitor $C_4 = 10 \text{ nF}$ hardly modify C_{tot} . However, C_3 is changed to 2.3 pF giving a new value for the divider ($\sim 1 : 87$).

The calibration of the total control path is shown in figure 4.19. The voltage divider and the rectifier read 1.57 mV/kHz and the radial COM-mode frequency moves by 17.8 kHz/V as a function of the applied control voltage on the VVA.

In figure 4.20 a), the intrinsic radial frequency stability is shown by repeatedly scanning over the COM-mode frequency and tracking its peak frequency over two hours. The frequency peak drifts over many kHz within less than an hour. In fact, without stabilization the frequency changes

³⁷SRS: SIM960 (BW = 100 kHz, input impedance = 1 MΩ, input/out range = $\pm 10 \text{ V}$)

³⁸ZFBDC20-61HP-S+ (coupling $\approx 20 \text{ dB}$, directivity coupling $\approx 30 \text{ dB}$)

³⁹The capacitances are measured with: Iso Tech LCR-821 at 100 kHz

⁴⁰IN34A, forward voltage drop $\approx 0.3 \text{ V}$, $C_{\text{diode}} \approx 0.8 \text{ pF}$

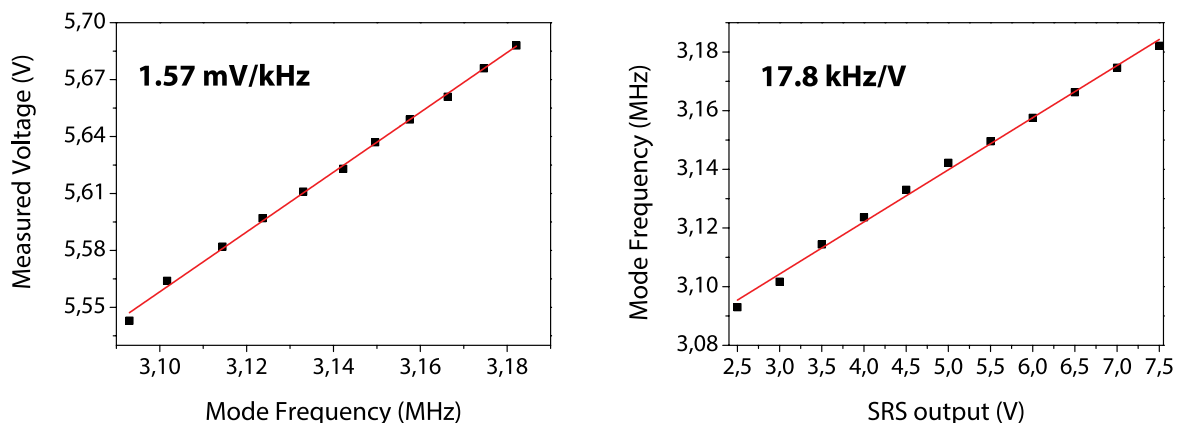


Figure 4.19.: The sensitivity of the divider and rectifier are measured as a function of the COM-mode frequency (left) as well as the dependency of the COM-mode frequency on the control voltage.

are so large, that spectral scans were the only reasonable method to monitor the frequency drifts. By implementing the previously described stabilization circuit, it is possible to coherently drive a blue sideband over a long period of time (hours). With this, it is possible to perform a motional Ramsey experiment [159] in order to measure the frequency deviation of the COM-mode from the laser frequency. For this purpose the electronic superposition $(|S\rangle + e^{i\phi_e}|D\rangle) \otimes |0\rangle$ is mapped onto the motional superposition $|D\rangle \otimes (|0\rangle + e^{i\phi_m}|1\rangle)$ by transferring the ground state population $|S\rangle \otimes |0\rangle$ to $|D\rangle \otimes |1\rangle$ with a π -pulse on the blue sideband (BSB). After an interrogation time τ_{wait} the phase ϕ_m is mapped back onto the electronic states by reversing the pulse sequence, as shown in figure 4.20 b). Due to the η -times smaller coupling on the BSB the time for a π -pulse does not necessarily fulfill the condition $\tau_{\text{BSB}}^\pi \ll \tau_{\text{wait}}$. In such a case an effective waiting time is given by $\tau_{\text{wait}}^{\text{eff}} \approx \tau_{\text{wait}} + 4\tau_{\text{BSB}}^\pi/\pi$ [122]. Performing many sequential Ramsey experiments we can monitor the COM-mode frequency stability over long times. Not only the frequency deviation can be extracted, but also Bloch vector lengths which offer information regarding fast noise (> 50 Hz).

Figure 4.20 b) shows such measurements tracking the mode frequency and the Bloch vector length over the period of one hour. A histogram of all measurements reveals a stability of ~ 180 Hz (one standard deviation) with a mean Bloch vector length of 0.72 ± 0.12 for a $\tau_{\text{wait}}^{\text{eff}} \approx 500$ ms. At the time of writing this thesis, a new stabilization circuit has been developed by Matthias Brandl and Gerhard Hendl. In this new generation everything is integrated on a single PCB board consisting of two independent VVA's, one for very slow drifts and the other for fast noise. Moreover, instead of using a half wave rectifier, a temperature stabilized RF power meter is being implemented. First preliminary data show a stability better than ~ 10 Hz and a mean Bloch vector length > 0.85 for $\tau_{\text{wait}}^{\text{eff}} \approx 4000$ ms, which looks very promising.

Limitations regarding the frequency stability of motional modes can arise from a few different sources. The most obvious one is the temperature dependency of the capacitive voltage divider. However, this can be solved by having a temperature sensor attached to the divider and a carefully calibrated temperature-capacitance curve. Less obvious are changes in the ion-to-blade distance by thermal expansion. A rough estimate gives ~ 1 kHz K^{-1} for steel blades (length $l_0 \approx 1$ cm) with a

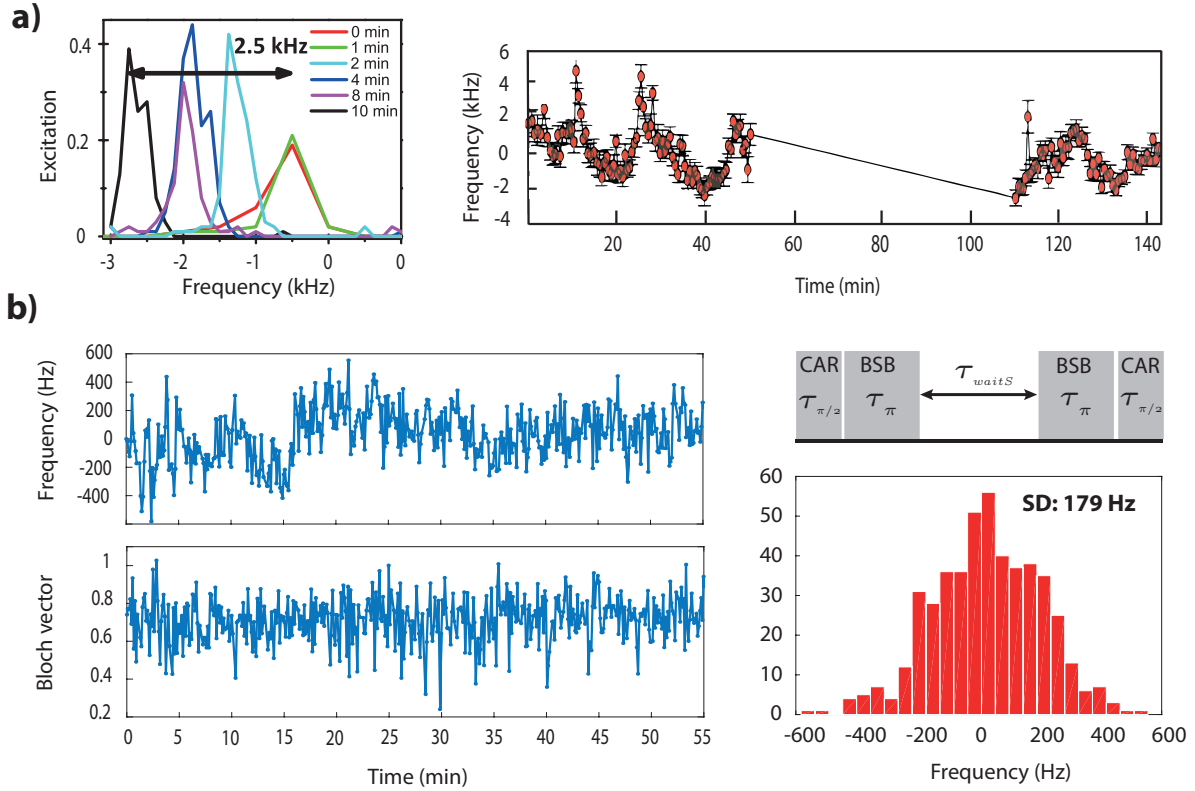


Figure 4.20.: **a)** (left) A few spectral traces of one radial COM-mode taken over the course of 10 min without any stabilization (right). The spectral traces are fitted and the peak frequency is plotted as a function of time. Error bars correspond to the FWHM. The radial frequency drifts over many kHz in less than an hour. **b)** Here, the stabilization circuit is implemented as previously described. (left) Subsequent motional Ramsey experiments are performed to measure the frequency deviation and the Bloch vector length. Since $\tau_{\text{BSB}}^{\pi} = 108 \mu\text{s} \ll \tau_{\text{wait}} = 350 \mu\text{s}$, an effective interrogation time is given by $\tau_{\text{wait}}^{\text{eff}} = 488 \mu\text{s}$. (right) A histogram of the frequency deviation shows a Gaussian distribution of the frequencies with a standard deviation = 179 Hz.

thermal expansion coefficient $\alpha \approx 12 \times 10^{-6} \text{ K}^{-1}$, ion-blade distance $r = 565 \mu\text{m}$ and a trapping frequency $\omega = 2\pi \times 3 \text{ MHz}$ ⁴¹. Since only the voltage over the trap is stabilized and not the electric field amplitude at the ions' position, the mode frequency will change when the trap temperature changes.

So far, the effects and dependencies of the radial trapping potential are discussed, but when it comes to more than a single ion, additional effects need to be considered. In a multi-ion string the shorter wavelength modes experience a dispersive coupling between the axial and the radial modes. It is a non-linear, non-resonant Kerr-type coupling [160] which arises from the Coulomb interaction and depends on the phonon states and frequencies of each mode. The intuitive picture for two ions is as follows: in the radial tilt mode the two ions experience the lowest Coulomb repulsion at the turning points (distance is maximal) and the highest repulsion when they are crossing the center (closest distance). When the axial potential is increased and the ions get closer together, the tilt mode frequency increases due to the higher repulsion. Further, in the axial stretch mode the ions swing with opposite phase but the same amplitude, where the ion-ion distance changes over one

⁴¹ $\omega = A/r^2$, where A depends on voltage, drive frequency, charge, mass etc. Then, $\Delta\omega = (\omega r^2 / (r - \Delta l)^2) - \omega$, where $\Delta l = \alpha \Delta T l_0$ and α is the thermal expansion coefficient.

period. The amplitude depends on the Fock state and scales with $\sim \sqrt{n}$ which in turn shifts the frequency of the radial tilt mode as a function of the axial stretch mode Fock state population and vice versa. If the modes are thermally occupied, such as the axial modes in our experiment, it will cause motional decoherence on the radial modes.

In [159] Roos et al. derive the dispersive cross-Kerr coupling χ for a two ion crystal and measure the frequency shift of the stretch mode per phonon in the tilt mode $\delta\omega_s/\delta_t$ at different axial trapping potentials. At $\omega_{\text{ax}} = 2\pi \times 1.716$ MHz ($\omega_{\text{rad}} = 2\pi \times 4$ MHz) the shift was measured to be $\delta\omega_s/\delta_t = 20.5$ Hz/phonon with an empirical power law $\delta\omega_s/\delta_t \propto \omega_{\text{ax}}^\beta$, where $\beta = 3.25$. Even though the coupling becomes negligible for confinements of $\omega_{\text{ax}} = 2\pi \times 220$ kHz in the case of two ions, it remains an open question as to how the Kerr coupling is influenced when additional modes (more ions) participate. Given the high thermal distribution of the axial mode, as shown in section 8, the shorter wavelength modes might be considerably broadened. Further dedicated experiments are needed to investigate these limitations of the mode frequency stability.

Additionally, if the trapping anisotropy is beyond a certain threshold, see section 3.1.3 and [86], resonant three-mode mixing between the axial and radial modes might occur and introduce further decoherence.

4.6.3. Ground state cooling

In addition to decoherence induced by frequency fluctuations and mode mixing, the thermal distribution of the radial modes causes fluctuations in coupling strength and in ac-Stark shifts (see section 4.5.1). These fluctuations can be reduced by ground state cooling each mode. When performing Mølmer-Sørensen gates on the axial modes, it is usually sufficient to cool the modes closest in frequency to the bichromatic laser beam detunings, since all other modes are far away in frequency space. This is quite different, when the radial modes are used, since their frequency spreading is much smaller. Therefore, all $2N$ radial modes must be ground state cooled in order to make the effective spin-spin interaction work.

Sideband cooling (SBC) is a technique to ground state cool [14, 120, 161] the normal modes of trapped ions. The cooling rate Γ_C depends on the coupling strength Ω on the $S_{1/2} \leftrightarrow D_{5/2}$ transition and the effective decay rate Γ' of the quenched system ($S_{1/2} \leftrightarrow P_{3/2} \leftrightarrow D_{5/2}$):

$$\Gamma_C = \frac{(\eta\Omega)^2}{\Gamma'^2 + 2(\eta\Omega)^2} \Gamma', \text{ with } \Gamma' = \frac{\Omega_{\text{aux}}^2}{\Gamma_{\text{aux}}^2 + 4\Delta_{\text{aux}}^2} \Gamma_{\text{aux}} \quad (4.20)$$

Here, Ω_{aux} is the coupling strength on the $D_{5/2} \leftrightarrow P_{3/2}$ transition, Δ_{aux} is the detuning of the 854 nm quenching light and Γ_{aux} is the decay rate of the $P_{3/2}$ -state. The cooling rate can be influenced by adjusting Ω and Ω_{aux} . Figure 4.21 a) compares the cooling speed⁴² of the ‘vertical’ and ‘horizontal’ beam with Rabi frequencies $\Omega \approx 2\pi \times 35$ kHz resp. $\Omega \approx 2\pi \times 300$ kHz. (Note: the ‘tip’ beam can’t be used for SBC as the selection rules allow it to only to drive $\Delta m = \pm 1$ transitions.) In addition to the lower coupling strength of the ‘vertical’ port, its \vec{k} is not optimally

⁴²The cooling speed is quantified by a probe pulse on the red-sideband transition with a coupling strength proportional to \sqrt{n} . In order to measure the cooling rate in terms of phonons, one could use the technique described in section 8.

aligned with the radial modes (60°), resulting in a lower Lamb-Dicke factor $\eta \approx 0.053$ compared to $\eta \approx 0.061$ of the ‘horizontal’ beam. The higher cooling speed of the ‘horizontal’ beam leads also to a wider spectral feature, as shown in Fig. 4.21 b) and 4.21 c). Here, the residual population in $n > 0$ after SBC is checked with a weak probe pulse on the red sideband as a function of 729 nm-shift from the $|S, n + 1\rangle \leftrightarrow |D, n\rangle$ transition. In contrast to the narrow spectral feature of the ‘vertical’ port, the large FWHM ≈ 260 kHz of the ‘horizontal’ beam allows simultaneous cooling of multiple, frequency-separated modes. As such, 38 radial modes can be cooled with less than 4 SBC-cycles⁴³, see figure 4.22. This, however, is impractical to do with the ‘vertical’ port, since it takes too many individual cooling pulses.

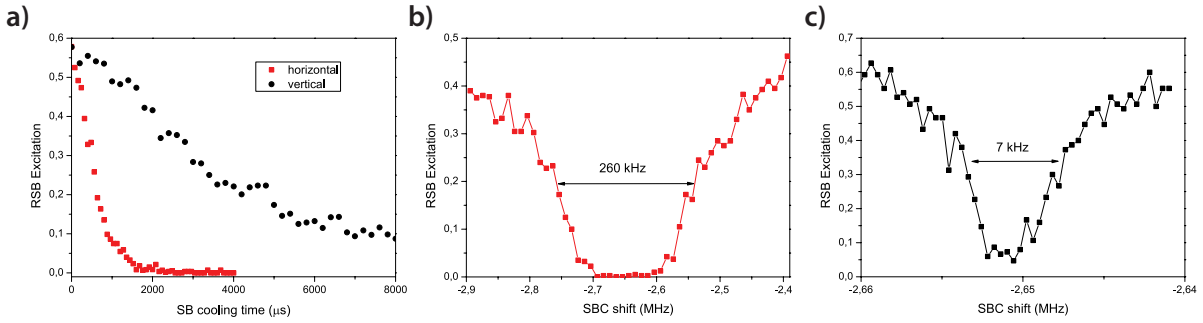


Figure 4.21.: a) Comparison of the red-sideband excitation between the ‘vertical’ and the ‘horizontal’ beam as a function of the sideband cooling time. For a cooling time of $\tau_{\text{cool}} \approx 2.2$ ms the coupling on the RSB is reduced to zero, which means the mean phonon number $\bar{n} \approx 0$. In order to achieve the same mean phonon number with ‘vertical’ cooling, $\tau_{\text{cool}} > 8$ ms is required. b) & c) The red-sideband excitation is measured as the laser frequency of the sideband cooling pulse is shifted. Due to the higher Rabi frequency and higher Lamb-Dicke parameter, the spectral feature of the ‘horizontal’ beam is much wider with a FWHM ≈ 260 kHz compared to a FWHM ≈ 7 kHz in the ‘vertical’ beam. The wide spectral feature allows ground state cooling of many modes simultaneously.

Another method to cool to the motional ground state is electromagnetically induced transparency (EIT) cooling. Due to the Fano type spectral feature, it has been proposed [162] for ground state cooling and has been experimentally demonstrated for cooling a single ion [163, 164]. Its broad spectral width is suited to cool many frequency-separated modes simultaneously [165, 166] with a considerably larger cooling rate. However, in the current setup, EIT cooling leads to additional heating of the axial motional modes, impairing the addressing even more (see 8). This might be related to the already high axial temperature (low confinement) which lifts the axial motion above the Lamb-Dicke regime leading to additional light scattering [166].

⁴³An SBC-cycle is a collection of different pulses (see [119, Chapter 3.8]) for one setting of the sideband cooling frequency.

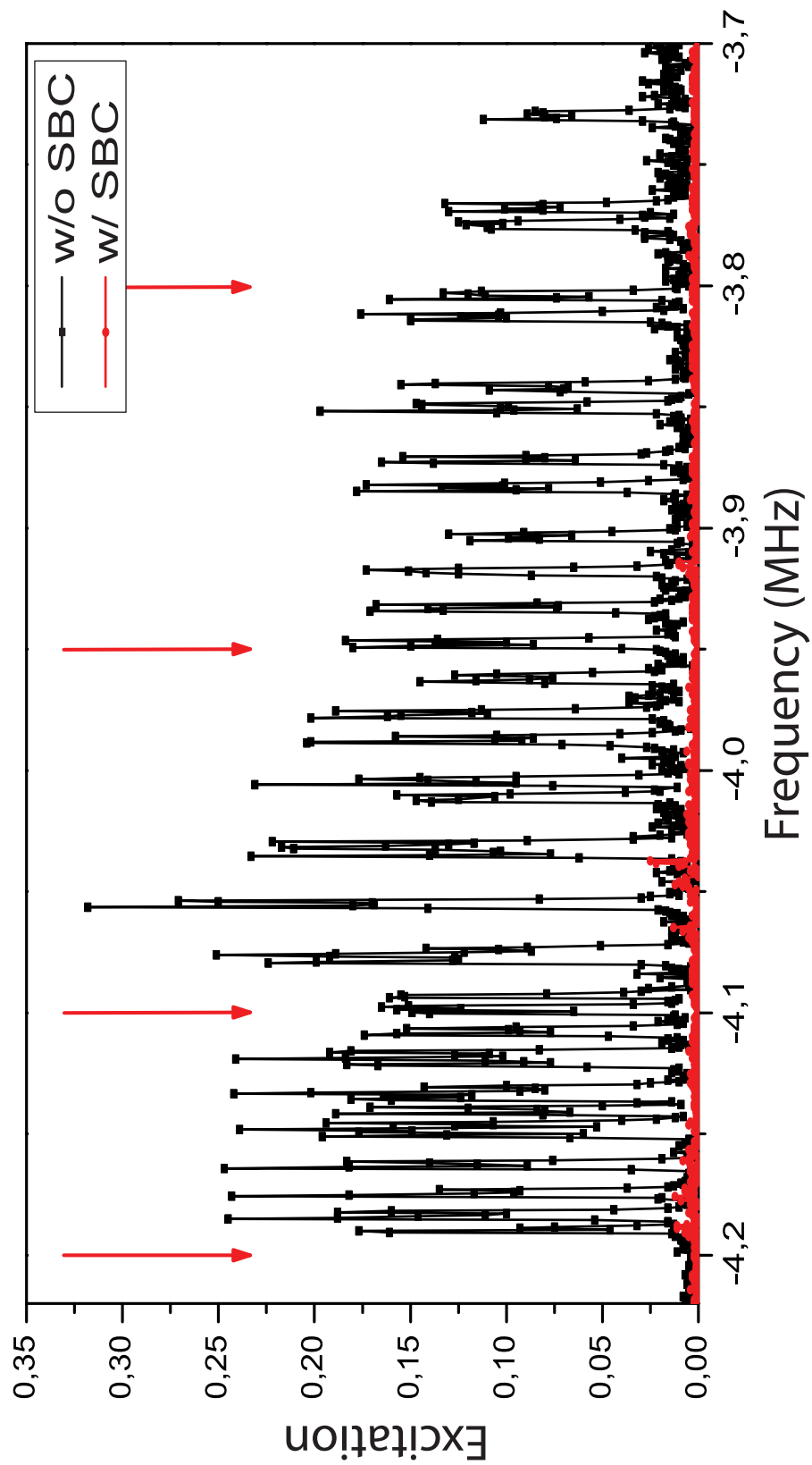


Figure 4.22.: A frequency spectrum of the radial motional modes of 19 ions is shown without sideband cooling (black) and with sideband cooling. The red arrows indicate the frequency of the 729 nm-sideband pulses. The ions are trapped at $\omega_{\text{ax}} = 0.219$ MHz, $\omega_{\text{rad}}^x = 4.19$ MHz and $\omega_{\text{rad}}^y = 4.16$ MHz.

5. Quantum simulation of spin models

The purpose of a quantum simulator is to study quantum systems that are inaccessible to classical supercomputers or difficult to study in the laboratory, due to limited experimental access of parameters, e.g. lattice constants in a solid or interactions between particles to name a few. The basic concept is to use a highly controllable quantum system that is described by the same mathematical model as the system of interest. Over the past decade the experimental controllability over quantum systems has led to a variety of engineered quantum many-body interaction, implemented into different physical platforms, such as in NMR [167–170], optical lattices [171–175], photons [176, 177], ions [64, 178–184] and solid-state circuits [185–189]¹. Up to now, trapped ions remain unrivalled in terms of controllability down to the single-particle level. This allows us to precisely prepare, manipulate and read out the quantum state, fulfilling all basic requirements for a functional quantum simulator. In fact, trapped ions, along with neutral atoms in optical lattices, are at the moment the most promising candidates for a full-fledged quantum simulator².

This chapter presents a trapped ion quantum simulator, specifically for the implementation of interacting spin models. The first section, 5.1, is concerned with the theoretical background regarding those spin models, namely the transverse Ising model and the XY -model. It provides the reader with the necessary understanding for the following sections and offers additional information for completeness. The second section, 5.2, will briefly summarize the physics of Lieb-Robinson bounds³, first in general and then specifically for power law decaying interaction, preparing the reader for the discussion of section 5.5. A central subject in 5.2 is the dispersion relation, which provides intuitive understanding for the physical behaviour of different power law regimes. The third section of this chapter, 5.3, is a step-by-step guide on to how to set up and calibrate the effective spin-spin couplings. In addition, techniques are discussed how the J_{ij} -coupling matrix can be measured. Furthermore, a method is presented for extracting the power law exponent α , which relies on the discussion of the dispersion relation in section 5.2. In the fourth section, 5.4, additional experimental details and observations regarding the experiment ‘*Spectroscopy of Interacting Quasiparticles in Trapped Ions*’ [28] are presented. This section showcases methods for spectroscopically probing the engineered interactions by preparing superpositions of eigenstates and analysing the time evolution of the system. The fifth and last section, 5.5, treats the experiment published in ‘*Quasiparticle engineering and entanglement propagation in a quantum many-body system*’ [26]. Here, the first experimental observation on propagation of entanglement is reported.

¹This reference list outlines the rapid progress in the field, and is far from being complete.

²In some sense ions and atoms pursue orthogonal approaches. While the ‘ion-approach’ is more a bottom-up process, that is from highly controllable single particles to large systems, neutral atoms follow a top-down approach, starting from large-scale system trying to obtain single-atom control.

³These are the upper bounds to the velocity at which information and correlations can propagate in an interacting many-body system.

Moreover, the tunability of the engineered interactions is used to investigate Lieb-Robinson bounds in different regimes.

5.1. Spin models

The term spin models is a smorgasbord of mathematical models, primarily explaining the physics behind magnetic phenomena, and includes classical and quantum mechanical descriptions of interactions between particles. This section will briefly introduce two special instances of the so called n -vector models⁴: *transverse Ising*-model with $n = 1$ and *XY*-model with $n = 2$.

5.1.1. Transverse Ising and XY-Model

The Ising model, introduced by Wilhelm Lenz in 1920 and handed down as a problem to his student Ernst Ising⁵, is one of the most well-known *toy* models in physics.

The model consist of a Hamiltonian with two parts :

$$H_{\text{Ising}} = H_I + H_B = - \sum_{i,j}^N J_{ij} \sigma_i^x \sigma_j^x - \sum_i^N B_i \sigma_i^z \quad (5.1)$$

where H_I describes a spin-spin interaction along one axis and H_B is an interaction with an external B-field in a transversal direction. The spin-spin coupling strength is defined by the coupling matrix J_{ij} and in the simplest form of the model, J_{ij} is homogeneous, time-independent and contains only nearest-neighbour interactions. The nearest-neighbour case is often denoted by $\langle i, j \rangle$ in the sum ‘ $\sum_{\langle i, j \rangle}$ ’⁶. In order to distinguish models with a transverse field $|B_i| > 0$ from those without ($B_i = 0$), the former ones are often referred to as *transverse Ising* models, where in most cases the external field is assumed to be time-independent and homogeneous over all spins, i.e. $B_i = B$. Depending on the sign of J_{ij} and the sign convention given in equation 5.1, the spin-spin interaction is divided into three classes:

Ferromagnetic (FM) for $J_{ij} > 0$

Anti-ferromagnetic (AFM) for $J_{ij} < 0$

Non-interacting for $J_{ij} = 0$

The Ising model becomes highly non-trivial for spin-spin interactions beyond nearest-neighbours (NN) couplings. An early extension of the NN-model were the so called ANNNI (axial next-nearest-neighbour interactions) models [190, 191] describing the interaction of nearest and next-nearest spins along one of the crystallographic axes of the lattice. Despite their simplicity, these models

⁴Here, n denotes the dimensionality of the interaction. The case $n = 3$ is known as the Heisenberg model and $n = 4$ is a toy model used in the standard model of particle physics.

⁵Ising solved it for the first time in his PhD thesis. He specifically solved the one-dimensional problem with nearest-neighbour $\sigma_i^x \sigma_j^x$ interactions and, without a transverse field, analytically and was able to show that there is *no* phase transition in this case. It took more than 20 years until Lars Onsager (1944) solved the model for a 2 dimensional square-lattice showing that in higher dimensions phase transitions can indeed exist.

⁶Some authors use ‘ $\sum_{i,i+1}$ ’ for one dimensional systems.

are still capable of explaining some experimental observations in solid-state physics[192]. However, almost no interactions found in nature have strict zero coupling beyond their close neighbours as most interactions decay polynomially in strength over distance⁷. To model such interactions, the Ising interaction strength can be written as

$$J_{ij} = \frac{J_0}{|i - j|^\alpha} \quad (5.2)$$

with a power law decay α , $J_0 = \max\{J_{ij}\}$ as an overall scaling factor and $|i - j|$ denoting the distance between spin i and j . With regards to trapped-ion quantum simulators, the decay can be approximated by Eq. 5.2 with $0 \leq \alpha \leq 3$ (chapter 3.3.4).

For the remaining discussion only one-dimensional strings of spins will be considered. The ground state energy and its properties strongly depend on the competing terms H_I and H_B , and their relative strengths. In the zero field regime, $B = 0$, the ground states solely depend on the sign of the interaction and the interaction range. For an FM-coupling one finds a two-fold degenerate ground state consisting of a symmetric and an antisymmetric superposition $|\uparrow\uparrow \dots \uparrow\uparrow\rangle_x \pm |\downarrow\downarrow \dots \downarrow\downarrow\rangle_x$, independent of the interaction range. In the case of NN-AFM-coupling, the ground state is also two-fold degenerate, where the spins show a Neel ordering $|\uparrow\downarrow\uparrow \dots \downarrow\uparrow\downarrow\rangle_x \pm |\downarrow\uparrow\downarrow \dots \uparrow\downarrow\uparrow\rangle_x$, see inset figure 5.1 a). However, as the AFM-interactions become longer ranged, a phenomenon known as spin frustration emerges⁸. The spins try to anti-align with respect to each other, which is not possible as soon as the interactions are beyond nearest-neighbour couplings. Different spin orientations compete against each other, as visualized in the inset of figure 5.1 b) that leads to a highly degenerate ground state compared to the case with short range interactions.

As we implement only AFM-couplings only those will be considered in the forthcoming sections and discussions of this thesis⁹.

On the other hand, the ground state in the high B-field regime ($|B| \gg |J_0|$) is a fully polarized spin state $|\uparrow\uparrow \dots \uparrow\uparrow\rangle_z$ along the B-field axis (z) and shows a paramagnetic ordering along the z -direction. The energy spectrum splits up into $N + 1$ subspaces (see Fig. 5.1), where N is the number of spins. These subspaces can be identified as the number of excited spins l (or spins anti-aligned with the B-field)¹⁰. In fact, the eigenstates can be written as entangled states in the form of Dicke states (see chapter 2.2) with non-uniform coefficients. For example, eigenstates in the one-excitation subspace with $N = 5$ are of the form

$$|\psi\rangle = c_1 |\uparrow\downarrow\downarrow\downarrow\downarrow\rangle + c_2 |\downarrow\uparrow\downarrow\downarrow\downarrow\rangle + c_3 |\downarrow\downarrow\uparrow\downarrow\downarrow\rangle + c_4 |\downarrow\downarrow\downarrow\uparrow\downarrow\rangle + c_5 |\downarrow\downarrow\downarrow\downarrow\uparrow\rangle \quad (5.3)$$

where the exact coefficients depend on the k^{th} -eigenstate and α (see Eq. 5.2) as will be discussed in section 5.4.

⁷Coulomb interaction $\sim 1/r^2$, dipole-dipole interaction $\sim 1/r^3$, London dispersion $\sim 1/r^6$. There are also exponentially decaying interactions such as screening. One could count engineered systems such as neutral atoms in an optical lattice as an example of strict NN-interaction.

⁸In systems with more than one dimension, spin frustration can also occur with NN-interactions.

⁹As the FM-couplings only differ by the sign of the coupling matrix, J_{ij} , the Hamiltonian spectrum is an inversion of the AFM-Hamiltonian spectrum, e.g. the AFM-ground state is the highest excited state in the FM-Hamiltonian.

¹⁰For example the ground state has zero excitations, the next subspace has states containing one delocalized excitation and so on.

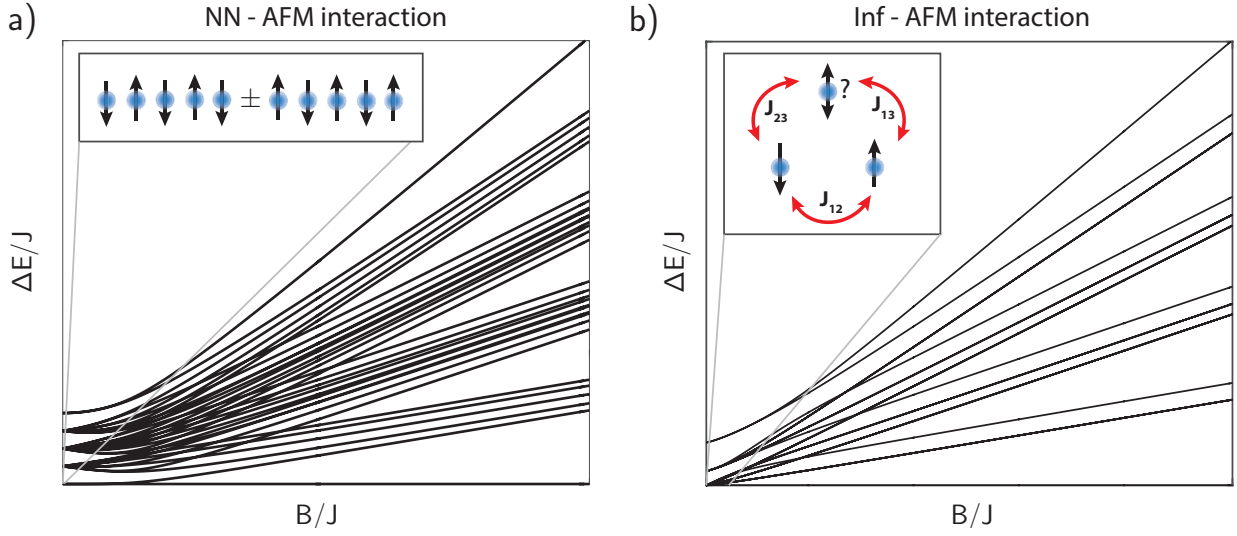


Figure 5.1.: Ising Hamiltonian energy spectra of a five spin system as a function of the transverse B-field strength for **a)** nearest-neighbour AFM-coupling ($\alpha \rightarrow \infty$) and **b)** infinite range AFM-interactions ($\alpha \rightarrow 0$). The inset of **a)** shows the two-fold degenerate ground state at $B = 0$ and the inset of **b)** visualizes spin frustration emerging from the long range coupling, resulting in a highly degenerate ground state at $B = 0$. The high field regime $B \gg J$ can be described by an H_{XY} -Hamiltonian.

When the transverse B-field goes to infinity, $B \rightarrow \infty$, the subspaces become completely separate and uncoupled, since connecting subspaces involves additional spin flips that are energetically unfavourable. In such a case, the physics of a single subspace can be described by the XY-Hamiltonian (cf. section 3.3.3)

$$H_{XY} = \sum_{i,j} J_{ij} (\sigma_i^x \sigma_j^x + \sigma_i^y \sigma_j^y) = \sum_{i,j} J_{ij} (\sigma_i^+ \sigma_j^- + \sigma_i^- \sigma_j^+), \quad (5.4)$$

where $\sigma_i \pm = \sigma_i^x \pm i\sigma_i^y$ are the spin creation and annihilation operators, respectively. The terms ' $\sigma_i^+ \sigma_j^- + \sigma_i^- \sigma_j^+$ ' are also known as flip-flop operations, destroying a spin excitation at site j and creating one at site i and vice versa. Hence these operations (and therefore H_{XY}) are excitation conserving. Only states with equal spin excitations couple to each other via J_{ij} and, as a result, the degeneracy of each manifold is lifted into $\binom{N}{l}$ -levels which shall be labelled as E_k^l , where k defines the eigenstate of manifold l . In the case of $\alpha > 1$ ¹¹, the total splitting of the one-excitation manifold¹², that is the difference between the lowest and the highest eigenstate, is very well approximated by $\frac{2}{N} \sum_{i,j} J_{ij}$ and becomes exact in the thermodynamic limit of the NN-coupling.

The high field eigenstates E_k^1 with one excitation¹² take on the form of spin waves as visualized in figure 5.2 a). An intuitive argument as to why spin waves are formed goes as follows: the transverse field wants to align all spins along the z -direction, however, the perturbatively weak spin-spin interaction tries to anti-align the spins in the x -direction. As a consequence the spins will slightly move out of the z -direction and form standing waves in one plane due to the open boundary conditions of the spin string¹³. The state with lowest energy has the shortest wavelength¹⁴.

¹¹The case $\alpha = 0$ is not as relevant in the prospect of this thesis, but shall be briefly mentioned at the end.

¹²As well as the $l = N - 1$ manifold due to symmetry.

¹³In the case of periodic boundary conditions, the spin wave would have a helical structure.

¹⁴This is the closest state to a Neel-ordering; for FM-coupling it is the longest wavelength state.

Interestingly, even though the exact c_i 's depend on the interaction range, the main features such as the spin wave nodes and anti-nodes remain the same, as long as $\alpha > 0$. Figure 5.2 b) compares these coefficients for different α 's, showing that indeed the spin waves retain their wave like structure, only slightly deformed. The most distinctive modification happens to the longest wavelength state, where the edges start to flatten out.

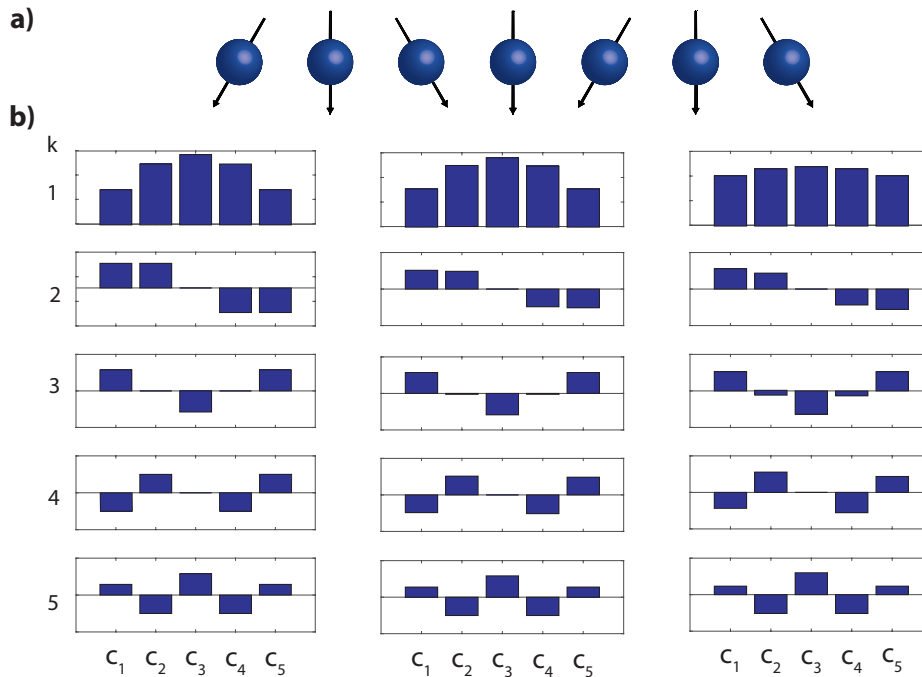


Figure 5.2.: a) A visual example of a spin wave with $N = 7$ and $k = 4$. Due to the open boundary condition, the spins are deflected in a plane. b) Comparison of the exact coefficients for all k -modes for different α . From left to right $\alpha \rightarrow \infty$, $\alpha = 3$ and $\alpha = 0.5$. The overall structure doesn't change, only the amplitudes differ slightly.

Due to the clear energy separation of these eigenstates, the spin waves can be interpreted as quasiparticles, collective excitations of an interacting many-body system¹⁵ with a dispersion relation. In fact, the dispersion relation contains all relevant physical informations about a single quasiparticle, for example its effective mass. More information about dispersion relations and their relevance to propagation of information and Lieb-Robinson bounds can be found in section 5.2.

Creation and annihilation operators of quasiparticles are a useful method of describing an interacting many-body system, especially with regards to the experiments presented in section 5.4. The k^{th} -spin wave mode is created from the vacuum state (ground state) by $|k\rangle = \sigma_k^+ |0\rangle$, with the creation operator $\sigma_k^+ = \sum_j c_j^k \sigma_j^+$ ($\sigma_k^- = \sum_j c_j^k \sigma_j^-$ is the annihilation operator). By means of these operators, the Hamiltonian describing the single-excitation subspace (containing a single quasiparticle) can be mapped to $H = \sum_k \varepsilon_k \sigma_k^+ \sigma_k^-$. The dispersion relation ε_k is then obtained by diagonalizing the J_{ij} coupling matrix¹⁶. As a consequence the dispersion relation depends directly

¹⁵Quasiparticles are an emergent phenomenon and they can not exist in free space, however, they show particle-like properties such as effective mass, energy and momentum. Amongst the long list of quasiparticles, some of the most prominent ones are Phonons, Excitons, Plasmons and Cooper pairs.

¹⁶This doesn't hold any more for the higher excitation subspaces, except for the second highest subspace, which contains also $l = N$ energy levels. The diagonalization of a $N \times N$ matrix yields maximally N eigenvalues.

on the interactions and their spatial decay. One can identify three distinct regimes of α where the dispersion relation shows a qualitatively different behaviour [193] as will be shown in section 5.2.

5.2. Lieb-Robinson bounds

A central question in physics is: “What is cause and what is effect?”, well known under the term *causality*.

According to the theory of relativity, the concept of causality is well defined: the speed of light sets an ultimate upper limit on the speed of how fast information and/or correlations can propagate. However, none of the five postulates in quantum mechanics ensures causality in non-relativistic quantum mechanics. In fact, causality emerges due to the locality of interactions, i.e. interactions act only on a finite spatial extent. In 1972 Lieb and Robinson mathematically proved the existence of an upper bound, nowadays known as the *Lieb-Robinson* bound [27]. This bound predicts a finite velocity, known as Lieb-Robinson velocity, with which correlations/information can propagate in an interacting system with finite range interactions¹⁷. In contrast to relativity, the Lieb-Robinson velocity is not universal, but depends on the underlying interactions. As an important implication, distant parts of a physical system can be viewed and treated independently for dynamics shorter than the time it takes to ‘connect’ those parts, independently on the quantum state. Introduction and reviews regarding Lieb-Robinson bounds can be found in [194–196].

Consider two operators, \mathcal{O}_A and $\mathcal{O}_B(t)$, which at time $t = 0$ act on two disjoint regions A and B separated by a distance L . The Lieb-Robinson bound can be expressed as a bound of the time-dependent commutator [194, 195]

$$\|[\mathcal{O}_A, \mathcal{O}_B(t)]\| \leq \|\mathcal{O}_A\| \|\mathcal{O}_B\| g(L) \frac{vt}{L}, \quad (5.5)$$

where $g(L)$ is an exponentially decaying function with L and v is the Lieb-Robinson velocity, both depend on the Hamiltonian under consideration. The operator norm $\|\mathcal{O}\|$ of a hermitian operator \mathcal{O} is defined as the absolute value of the largest eigenvalue of \mathcal{O} . In a formal way, an arbitrary operator norm can be written as

$$\|\mathcal{O}\| = \max_{\psi, |\psi|=1} |\mathcal{O}\psi|, \quad (5.6)$$

where the maximum is taken over vectors ψ with norm 1 and $|\mathcal{O}\psi|$ denotes the norm of the vector $\mathcal{O}\psi$ [194]. Originally the Lieb-Robinson bounds were formulated for local interactions such as nearest-neighbour interactions, but were soon after generalized to exponentially decaying interactions [197]. In both case, NN and exponentially decaying interactions, one can define a light cone in the space time diagram, where all correlations are bound within a causal region and are exponentially suppressed [198, 199] beyond this light cone¹⁸, see figure 5.3 a).

More recently, bounds were formulated for interactions decaying with a power law over distance [193, 200–202]. However, as the interaction grow in range, the strict light cone picture becomes

¹⁷The original proof only considered nearest-neighbour interactions.

¹⁸Note: Some authors use here the term sound cone or wavefront. We will make equivalent use of light cone and wavefront.

less of a valid description. With decreasing α (Eq. 5.2), the boundary of the causal region starts to ‘soften’, as the correlations outside the regions become only algebraically suppressed $\sim r^{-\alpha}$. In addition, the light cone ‘deforms’ from exhibiting a linear character in space time to a polynomial character [201].

Figure 5.3 b) shows numerical simulations of the magnetization, $m_i(t) = \langle \sigma_i^z(t) \rangle$, of a locally quenched H_{XY} -Hamiltonian for three different values of α [193]. One can qualitatively identify three distinct regimes of dynamical behaviour, corresponding to three distinct ranges of alpha, where the bounds exhibit different behaviour. For $\alpha > 2$ the excitation (quench) is light-cone-like bound as in NN-range models (as well as for exponentially decaying models). In an intermediate regime, $2 > \alpha > 1$, there is no well-defined light cone, but the excitation needs a finite time to expand. Finally, for $\alpha < 1$, the propagation speed of an excitation becomes faster for larger systems, as it will be discussed later.

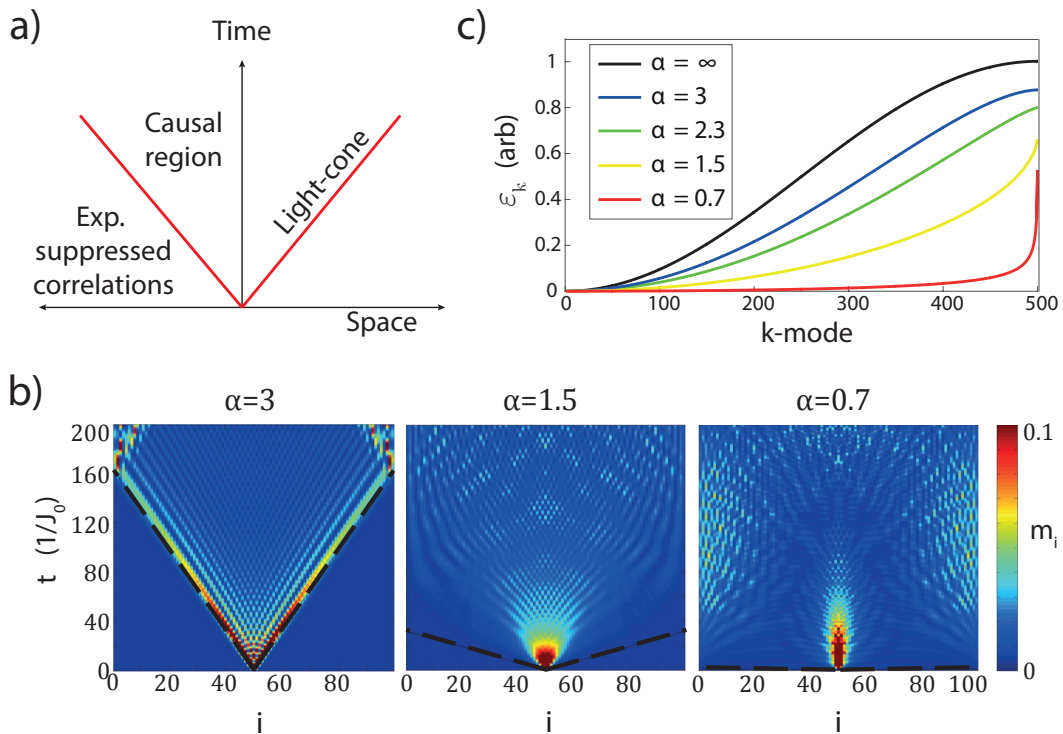


Figure 5.3.: **a)** A schematic diagram of a light cone. The part within the light cone is known and no (significant amount) of information can travel faster than the light cone. This means that all correlations generated between the parts of the system outside the light cone, and the parts inside the light cone are exponentially suppressed. **b)** Numerical simulation of a locally quenched H_{XY} Hamiltonian with 100 spins simulated for 3 different α 's (reprinted from [193], ©APS). The spin on site 50 is excited and the single site magnetization m_i is shown as a color plot for various times in the dynamics. One can identify 3 regimes: $\alpha > 2$, where the light cone picture is valid; $2 > \alpha > 1$, no light cone, but correlations have a finite velocity and $\alpha < 1$, where correlations spread out instantaneously. **c)** The observed behaviour regarding light cones can be explained by examining the dispersion relation, here calculated for a system of 500 spins. In the short range interaction regime and for $\alpha > 2$, the dispersion shows a cosine like structure and most k -modes have the same finite group velocity $v_g = \partial \epsilon_k / \partial k$. In the intermediate regime, $2 > \alpha > 1$, the dispersion relation flattens for lower k -modes, but shows a cusp at higher k resulting in a large maximal velocity v_{\max} . For truly long range interactions, i.e. $\alpha < 1$, the group velocity is nearly zero for most k -modes except for a few, where the maximal velocity v_{\max} diverges.

This behaviour can be intuitively understood by the quasiparticle picture of the single excitation subspace introduced in section 5.1.1. By examining the dispersion relation one finds again three qualitatively distinct regimes, as shown in figure 5.3 c). Given the dispersion relation, one can directly calculate the group velocity $v_g = \partial\varepsilon_k/\partial k$ of each quasiparticle k -mode¹⁹. For short range regimes, that is $\infty > \alpha > 2$, the dispersion relation has a cosine-like shape and the maximal group velocity barely depends on α . Most of the quasiparticle modes have similar group velocities, except those towards the ends of the spectrum ($\min \varepsilon_k, \max \varepsilon_k$) where $v_g \rightarrow 0$. Hence a clear wavefront can be observed in this regime as the wavepacket barely disperses. In the case of $\alpha < 2$, the dispersion relation develops a cusp at one end that becomes sharper with decreasing α and at the other end the curve becomes flatter. This leads to the effect that most modes have a rather low group velocity and the excitation stays localized for a long time. The maximal group velocity diverges with the system size N as $v_{\max} \propto (1/N)^{\alpha-2}$. Furthermore, the time for the fastest quasiparticle to reach the boundary scales as $t_b \propto N/v_{\max} = N^{\alpha-1}$ and increases for larger systems [193]. As the interaction range increases further to $0 < \alpha < 1$, the maximal group velocity diverges even stronger, $v_{\max} \propto (1/N)^{(\alpha-3)/2}$. In this case, the time to reach the system boundaries decreases with system size, $t_b \propto N^{(\alpha-1)/2}$. In the extreme case $\alpha = 0$, all modes have a group velocity $v_g = 0$ except for one that has $v_g = \infty$. A detailed, theoretical analysis can be found in [193].

The experimental demonstration of how to measure the dispersion relation is the subject of section 5.4.2 and the experimental investigation into the Lieb-Robinson bounds in an engineered quantum many-body system is presented in section 5.5.

5.3. Setting up and calibrating the interactions

This section briefly summarizes the procedures and experimental tricks for setting up the Ising and the XY -interactions in the lab. Further, techniques will be discussed on how to characterize those interactions, specifically how to measure individual elements of the J_{ij} -matrix. In fact, the very same technique can be used for error diagnostics and debugging the experimental setup. The next sections will present further methods to directly measure the ground state gaps, the dispersion relation and the interactions between quasiparticles. These latter methods are published in ‘*Spectroscopy of interacting quasiparticles in trapped ions*’ [28].

5.3.1. Setting up the interactions

This section shall serve as a step-by-step guide for setting up the effective spin-spin interactions in our setup. Clearly there might be different strategies for the individual steps, some of them ‘quick and dirty’, others more elaborate, but here the most common instructions will be presented. Since the laser-ion interaction is an MS-interaction (see sections 3.3), except for coupling to many radial modes, the procedure is quite similar to setting up entangling gates, with a few distinct features pointed out in this section.

First, the two components of the bichromatic light field have to be balanced, i.e. the FAOM (section 4.2) needs some tweaking such that both light intensities at the output are as equal as

¹⁹If information is carried by a quasiparticle, the group velocity tells how fast the information propagates.

possible. This is usually done by repeatedly switching between one of the RF-sources being off and the other running and vice versa. The single-frequency light field intensities are measured with a photodiode at the end of the optical path and, by adjusting the angle FAOM in the horizontal plane, the two intensities can be equalized. After this course alignment, a more accurate calibration is done using the ion. Specifically, the bichromat is detuned such that one of the components drives the carrier resonantly²⁰, while the other is turned off, and the Rabi frequency is measured. This step is then repeated with the other component set on resonance and the two Rabi frequencies are compared. If they are not equal within 0.4 – 0.6%, the individual RF-powers have to be adjusted accordingly²¹. As soon as the Rabi frequencies are within the margin, the entire bichromatic light field is shifted in frequency such that the blue and red part are symmetric around the carrier frequency and detuned from the radial trapping frequency by $\pm\Delta_t$, respectively.

Important note: The relation $\Delta_t \gg \eta\Omega$ must hold in order to be in the adiabatic limit²², see 3.3.3. If very long range interactions are desired, $\alpha \approx 0$, a better strategy might be to set up the gates along the principle string axis and drive the axial COM-mode²³, as this allows to keep a large enough Δ_t and not to violate the adiabatic condition.

The next step is to reduce the induced ac-Stark shifts by means of a third light field. This section will make extensive use of the discussion presented in sections 4.4.2 and 4.5. Here, a technique is presented which directly uses the bichromat to measure the induced light shifts. When $|B| \gg J_0$, we operate in the regime of the XY -Hamiltonian. Preparing the ground state $|\downarrow\downarrow \dots \downarrow\rangle = |S_{1/2}S_{1/2} \dots S_{1/2}\rangle$ ²⁴ and evolving it under H_{XY} won't change the excitation of the ions, as this state is well separated in energy to other states. When scanning the centerline detuning $\delta_c \equiv 2 * B$, one will finally reach a point where the separation of the ground state and next excited states is $\sim J_{ij}$. At this point, the ground state will couple to other states and one can observe correlated spin flips, i.e. pairs of spins flip together; past this point the coupling is again suppressed and all ions stay in $S_{1/2}$, as shown in figure 5.4 a). The center of the peak reveals the ac-Stark shift to be compensated and the width is somewhat proportional to J_{ij} ²⁵. The third light field is then switched on with a certain frequency and RF-power, in order to compensate for the ac-Stark shifts. Care must be taken when choosing the frequency, as higher order beat frequencies might (near-)resonantly drive unwanted transitions (section 4.5.1). A common trichromat frequency in our experiment is 1.2 MHz for $\omega_{\text{rad}} = 2.7$ MHz and $\omega_{\text{ax}} = 0.22$ MHz. After setting $\delta_c = 0$, the trichromat RF-power is scanned and the ion excitation is monitored. The RF-power for which a peak excitation (of correlated spin flips) is observed, is chosen for the final setting. This can be also rechecked by again scanning the transverse field, i.e. δ_c , and the peak center should now be at

²⁰In general the bichromat has to be detuned by $\pm\omega_{\text{rad}} + \Delta_t$, where ω_{rad} is the radial trapping frequency and Δ_t is the detuning from the sideband. At this point the third light field is turned off and the centerline detuning δ_c is set to zero.

²¹These are typical values which have been used over the years.

²²Such that entanglement between spin and motion is negligible.

²³Remember, the smaller Δ_t the smaller α , see section 3.3.4. How well such axial gates will work depends on the number of ions, trapping parameter, and SBC and has to be checked first.

²⁴It works equivalently with $|\uparrow\uparrow \dots \uparrow\rangle = |D_m D_m \dots D_m\rangle$.

²⁵There isn't an exact relation between the peak width and J_0 , since it depends as well on α . The smaller α the more elements in J_{ij} contribute to the width. Further, the width also depends on the differential ac-Stark shift, which hasn't been compensated at this point.

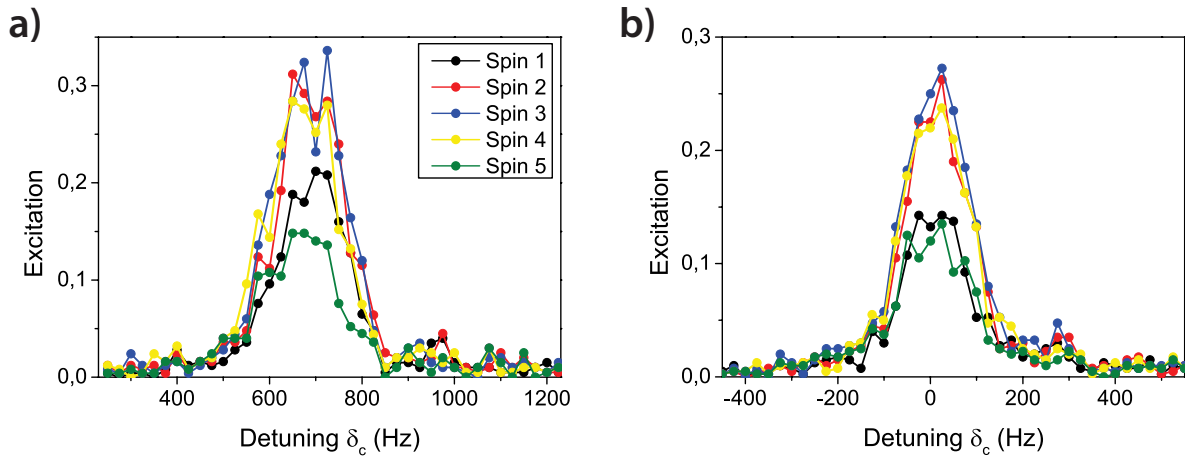


Figure 5.4.: A scan of the center-line detuning $\delta_c \equiv 2B$ for a string of five spin when the third compensation light field is **a)** switched off and **b)** switched on with right parameters, that is RF-power and frequency such that all ac-Stark shifts are compensated. The observed peak positions are proportional to the induced ac-Stark shifts. As soon as $B \approx J_{ij}$ correlated spin flips are no longer suppressed resulting in the observed spin excitation when starting with an initial state $|\downarrow\downarrow\downarrow\downarrow\rangle$.

$\delta_c = 0$, see figure 5.4 b). The required RF-power depends on the bichromat Rabi frequencies and on the chosen trichromat frequency²⁶.

These steps might need some iterations, since changing the RF-power of the third light field slightly influences the RF-power bichromatic light fields and vice versa. Nevertheless, once the interactions are setup properly the re-establishment on a follow-up day is straightforward.

Something which hasn't been mentioned yet is for how long the H_{XY} -interaction is turned on. This is a tricky question, since the optimum T depends on the bichromat Rabi frequency and the detuning Δ_t , hence on the J_{ij} -matrix. If T is too short, then hardly any excitation is observable. On the other hand, if T is too long, the dynamics will 'overflow' and couple to many other states producing artificial structures such as asymmetric peaks and multi-peaks. As a rule of thumb, a reliable duration T_{opt} is the time it takes a quenched spin in the middle, i.e. $|\downarrow\downarrow \dots \uparrow \dots \downarrow\downarrow\rangle$ to be at 0.5 excitation, see figure 5.5 a).

Finally, an efficient but less quantitative check of how well the interaction is set up, is to compare the time dynamics between experiment and numerical simulation of a local quench, or in lab jargon 'single-ion walk'²⁷. Here, the middle spin is flipped with the addressing beam and the system is evolved under the H_{XY} -Hamiltonian for several ms, depending on J_{ij} -coupling strength. The single-ion excitation, which corresponds to the single-spin magnetization σ_i^z ²⁸, is measured with the camera at different time points in the dynamics, as shown in figure 5.5 a).

Comparing the arrival times and amplitudes of the single-ion excitations (σ_i^z) allows us to infer valuable information. First of all, one can check that the experiment works as expected, that is if

²⁶To a lesser degree on the bichromat frequency, as this influences the coupling into the FOAM and thus the Rabi frequency. The change in the induced ac-Stark due to frequency change is negligible.

²⁷What sounds like a mere calibration technique that is routinely used, is in fact one of the biggest results achieved during this PhD work.

²⁸However, with a different normalization, $m_i = 2 * p_i - 1$, where m_i is the magnetization of spin i and p_i is the measured excitation probability.

all experimental parameters are properly calibrated, e.g. Rabi frequencies, and if all ac-Stark shifts are well compensated. However, one important note has to be made: even though the bichromatic Rabi frequencies can be precisely measured, the values in the numerical simulation differ by a few percent from the experimentally obtained values - in order to match the simulation to the data. It is not clear why this is the case and further investigations are needed to clarify the discrepancy between experimental calibration and simulation. In any case, this Rabi frequency is the only parameter that requires some adjusting (from measured values) in order to produce the theory plots throughout this chapter.

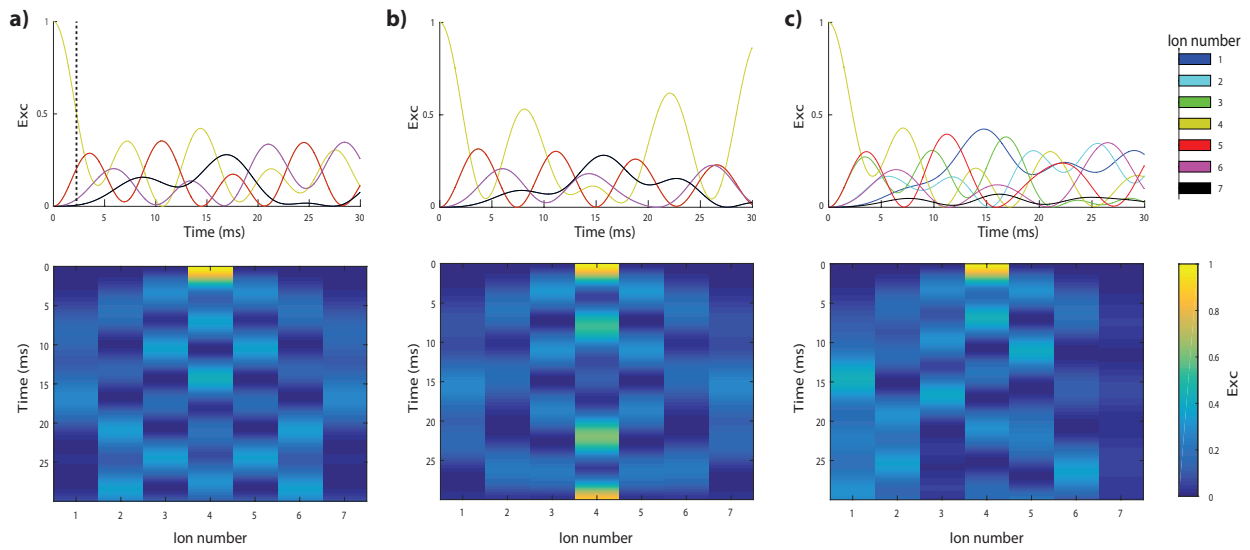


Figure 5.5.: Simulated time evolutions where the middle spin is quenched for three different cases. **(top)** Shows individual traces of the single-ion excitation (corresponding to single-spin magnetization σ_i^z) and **(bottom)** shows the same dynamics but in a different visualization style giving a better overview of the dynamics. **a)** Ideal time evolution. T_{opt} indicates the optimal time of the interaction for measuring correlated spin flips, as described in the text and figure 5.4. **b)** Time evolution without compensation of differential ac-Stark shifts which arise from the Gaussian beam profile. **c)** Time evolution with random but static ac-Stark shifts imprinting a potential landscape which randomly distorts the evolution.

Due to the qualitative nature of these checks, error syndromes are not unambiguous, nevertheless two common examples shall be explained. Figures 5.5 b) and c) show time evolutions with the same settings, Rabi frequencies, detunings etc, except that the ac-Stark shifts are not compensated in the right way. An overall light shift that is equal on all ions is irrelevant, but frequency differences between spins can be understood as additional local fields, B_i , modifying the potential landscape. Since the B_i 's tune the spins out of resonance, the flip-flop terms $\sigma_i^+ \sigma_j^- + h.c.$ become attenuated. In figure 5.5 b), the trichromatic compensatory field is turned off and the B_i 's follow a Gaussian distribution due to the beam profile. The quench becomes more localized in the middle as it can be seen by the revivals of the middle spin, but the evolution in general is symmetric with respect to the quench site.

However, if the trichromat is turned on and additional ac-Stark shifts, arising for example from reflections of the viewport, act randomly upon the ions the whole time evolution becomes distorted, as shown in Fig. 5.5 c). A strong indication for reflections of the trichromatic beam is when repeatedly taking time evolutions and they change over a few minutes time scale. An comprehensive list of

various effects which are capable of corrupting the ac-Stark compensation is given in section 4.5.1.

A more elaborate and quantitative method to measure differential light shifts is presented in the following section.

5.3.2. Measuring the elements of J_{ij}

The time evolution observed in single-site quench experiments allows us to calibrate the Rabi frequencies in the theoretical simulation. The calibrated theoretical simulation then provides an J_{ij} -matrix. However, it is possible to directly measure each individual element of the coupling matrix. This can be done by exploiting the single-ion addressing with the following protocol. First, the interactions are set up as previously described. Second, to measure the ij -th element of the matrix all ions except i and j are hidden in a different Zeeman level (for details about hiding see 6.3.2 and references therein). Next, spins i and j are prepared in a $|\uparrow_i\downarrow_j\rangle$ or $|\downarrow_i\uparrow_j\rangle$ state and can be coupled by the effective spin-spin Hamiltonian, while ensuring that the effective transverse B-field is large enough, $\delta_c \gg J_0$, in order to operate in the H_{XY} -regime. This ensures that only the transition $|\uparrow_i\downarrow_j\rangle \leftrightarrow |\downarrow_i\uparrow_j\rangle$ is driven²⁹ and the Rabi frequency $\Omega_{ij}^{\uparrow\downarrow}$ is exactly the coupling strength element J_{ij} between those two spins, as shown with experimental data in figure 5.6 a). By repeating the procedure for all $(N^2 - N)/2$ pairs, one can map out the complete coupling matrix as shown in figure 5.6 b).

Remarkably, the coherent flopping can be observed beyond 100 ms, which is a direct consequence of the decoupled subspaces with different spin excitations. Each of these subspaces is a decoherence-free subspace (DFS) [203, 204] with respect to external B-field and laser frequency fluctuations, as the energy of each state in such a subspace is influenced in the same way. Despite the DFS, there is an ultimate limit due to the finite lifetime of the excited $D_{5/2}$ -state (~ 1 s). As can be seen in Fig. 5.6 b) the elements J_{16} , J_{17} and J_{27} could not be measured as they are of the order of 1 Hz or less.

Moreover, not only the frequency can be measured but also the amplitude. Similar to an off-resonantly driven two-level atom, the oscillation changes its frequency and amplitude with the detuning Δ from the resonance frequency, as shown in equation 3.52. Hence, the very same protocol allows us to measure the transition frequency difference between ion i and j . In fact, only the absolute value of the difference is directly measurable, nevertheless by combining different spin-pairs it is possible to infer the signs too. Measuring all combinations of spin-pairs allows one to map out any residual or uncompensated effects, which inhomogeneously shift the transition frequency of the ions in the string, as described in chapter 4.3.1 and 4.4.

Although the protocol is tedious for large spin-chains, it is the most accurate experimental protocol to infer the J_{ij} -matrix. Other protocols indirectly deduce J_{ij} by measuring the energy spectrum of the Hamiltonian, for example, selectively exciting eigenstates of the Hamiltonian, as will be shown in the forthcoming section ‘*Spectroscopy of quasiparticles*’. A slightly different approach was pursued in [205], where the system is ‘shaken’ in order to excite many eigenstates, which then can be spectroscopically resolved.

²⁹A large δ_c pushes the states $|\downarrow\downarrow_j\rangle$ and $|\uparrow\uparrow_j\rangle$ out of resonance, since they have different numbers of excitations.

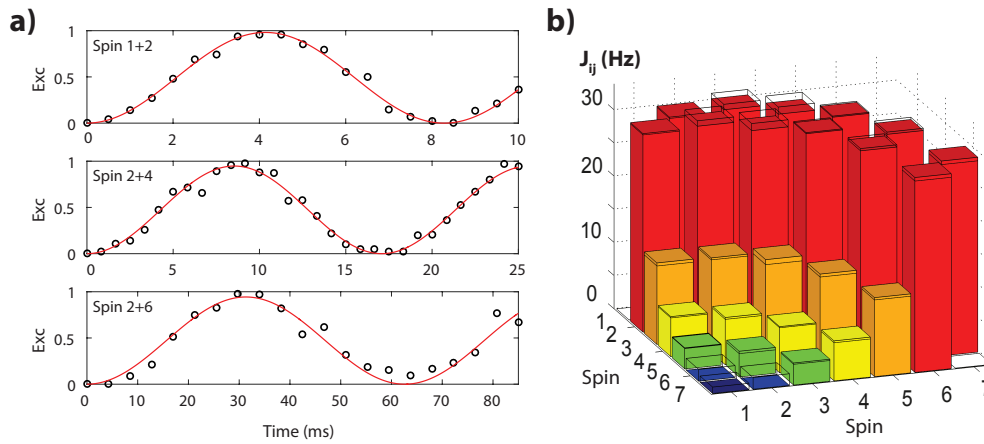


Figure 5.6.: a) An effective H_{XY} interaction drives the transition $|\uparrow_i\downarrow_j\rangle \leftrightarrow |\downarrow_i\uparrow_j\rangle$ for three different spin pairs. The measured Rabi frequency $\Omega_{ij}^{\uparrow\downarrow}$ (black circles: data, red line: fit) directly correspond to the coupling element in the matrix J_{ij} . The long coherence times of more than 100 ms are result of the decoherence-free subspace. b) By measuring all $(N^2 - N)/2$ combinations of spin-pairs, it is possible to map out the complete coupling matrix. This is an measured example of a J_{ij} -matrix for parameters $\omega_z = 220$ kHz, $\omega_x = 2.69$ MHz, $\omega_y = 2.66$ MHz and $\Delta_t = 40$ kHz. The theoretically calculated J_{ij} -matrix is overlaid with transparent bars.

5.3.3. Determining the power law decay α

The determination of α in equation 5.2 is not trivial, since the power law decay over distance is just an approximation, see equation 3.80. The actual decay can deviate significantly from a pure power law depending on the trapping parameters and detunings [103]. Figure 5.7 a) shows simulated spin-spin coupling strength decays over distance for a few different combinations of parameters. As shown, none of the calculated values follow a power law decay; the question is how to assign an α that most accurately approximates the real physical system.

A possible method is to only take the first few interactions into account, such as the nearest and next-nearest neighbours - since the longer the spin-spin separation, the less the interactions contribute to the Hamiltonian - and fit a power law to those ‘accountable’ interactions. However, this doesn’t seem right since it will always neglect exactly those long range interactions of interest. Another method is to assign an $\alpha_{|i-j|}$ to all pairs of spins starting from spin $i = 1$ and average over all $\sum_j^{N-2} \alpha_{|1-j|}/(N - 2)$. However, this approach has its flaws as explained later.

Here, we present a method which indeed tries to capture the relevant physics behind the long-range interactions. As described in the previous section, the dispersion relation defines many physical properties of the system, such as its dynamical time scales, and it also strongly depends on the interaction range. Hence, we use the dispersion relation itself as a measure to find the best fitting α . The experimental coupling matrix J_{ij} can be easily obtained³⁰ and, by diagonalizing the matrix, one gets directly the dispersion relation $\varepsilon_k^{\text{exp}}$ ³¹. The very same can be done with a theoretical J_{ij} that decays with a power law α yielding $\varepsilon_k^{\text{theor}}(\alpha)$. By simply minimizing the distance $|\varepsilon_k^{\text{exp}} - \varepsilon_k^{\text{theor}}(\alpha)|$ one can find an α that describes the experimental system as close as

³⁰Either by measuring all individual elements or by running the simulation with physical parameters, as we usually do.

³¹In order to compare the dispersion relation to other experimental parameters, the J_{ij} matrix is normalized by the nearest-neighbour couplings $J_{(i,j)}$.

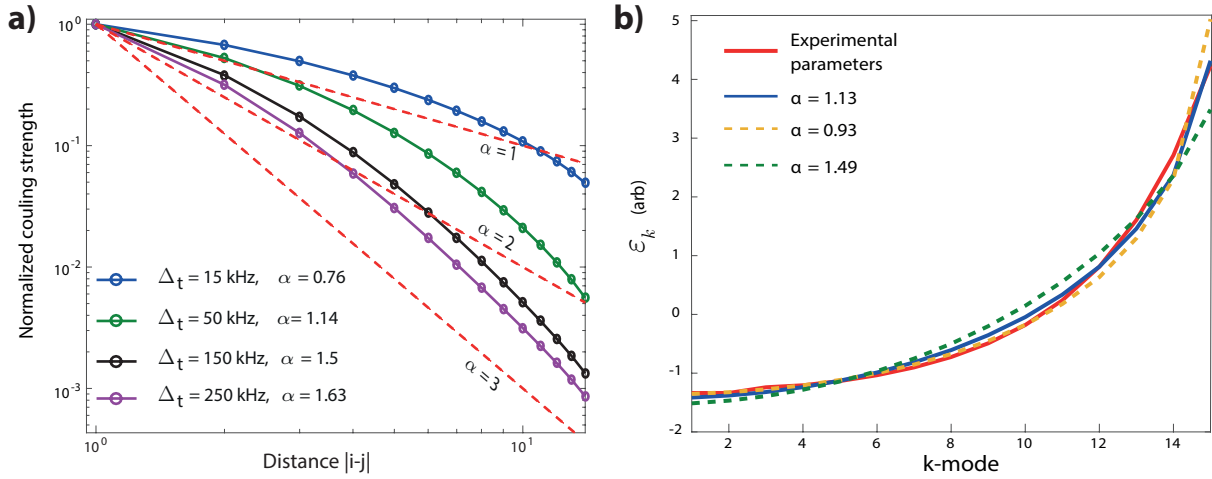


Figure 5.7.: **a)** Deviation from a pure power law decay $J_{ij} \propto 1/|i-j|^\alpha$. The coupling matrix is calculated for different Δ_t , see legend, each with the same trapping frequencies parameters $\omega_{ax} = 219$ kHz, $\omega_x = 2.710$ MHz and $\omega_x = 2.68$ MHz. The coupling strengths are normalized by the NN-coupling. Dashed red lines show the power law decays $\alpha = 1, 2, 3$. **b)** Comparison between the dispersion relation $\varepsilon_k^{\text{exp}}$ obtained from experimental parameters and the dispersion relations $\varepsilon_k^{\text{theor}}(\alpha)$ from a pure power law decay, where α is obtained by 3 different methods: $\alpha = 1.13$ is obtained by minimizing the distance $|\varepsilon_k^{\text{exp}} - \varepsilon_k^{\text{theor}}(\alpha)|$, $\alpha = 0.93$ results by comparing NN and NNN-couplings and $\alpha = 1.49$ by averaging over all decays $\alpha_{|1-j|}$, see text. The minimization method seems to be best suited to capture the relevant physical properties, such as the (non-) diverging behaviour for higher k -modes.

possible.

Figure 5.7 b) compares the experimental dispersion relation with the ones for α obtained by the three different methods. Although at first glance all dispersion relations seem to fit quite well, only the one obtained by distance minimization of the dispersion relations describes the long range behaviour properly and captures the right (non-) diverging behaviour, whereas the other two methods either over or underestimate the curvature, respectively.

5.4. Spectroscopy of quasiparticles

Spectroscopy in general is one of the most established and reliable techniques to measure energies of systems across all fields of physics, due to its broad applicability. The core principal is always the same: a physical system of interest is excited usually by means of electromagnetic waves³² and the system's energy-resolved response is observed.

Here, a spectroscopic technique is applied to an engineered quantum many-body system by controllably exciting specific eigenstates of a many-body Hamiltonian, which then yields information about the energy spectrum of the Hamiltonian. The basic concept of the spectroscopic procedure is related to Ramsey spectroscopy, where a superposition of two states of interest is created and its time evolution is investigated. As a consequence of the energy difference between those two states, a beat note is observable with a frequency proportional to the energy separation. The particularity of this technique is that the states prepared into a superposition are the many-body 'quasiparticle'

³²Not only restricted to em-waves, but acoustic waves, mechanical waves in solids and even particles such as electrons and neutrons, due to their de Broglie-wavelength, are used for spectroscopy.

modes of the interacting system. For this, techniques had to be developed to address and excite individual fundamental modes of the system.

In order to establish a common terminology, Fig. 5.8 sums up the most important subjects. Figure 5.8 a) shows a schematic energy spectrum of a Ising-Hamiltonian in the high B-field regime, depicting the relevant energy subspaces. The structure of the corresponding energy eigenstates of the one-excitation subspace are schematically showcased in figure 5.8 b). The experimental parameters

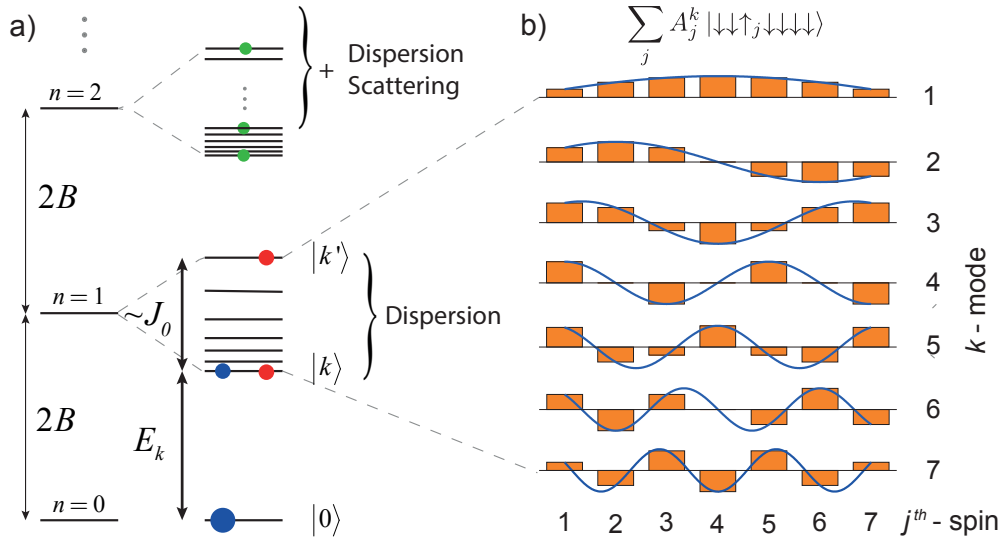


Figure 5.8.: a) The energy spectrum of a $N = 7$ -spin H_{XY} -Hamiltonian, where each excitation subspace, containing exactly l spin excitations, is separated by $2B$. Due to the large transverse field $B \gg J_0$, those subspaces do not couple to each other. The degeneracy of each subspace is lifted by the spin-spin coupling into $\binom{N}{l}$ -levels. The coloured dots show the different superpositions presented in the three sections: superposition between the ground state and a one-excitation state (blue) probing the ground state gap and the sign of J_{ij} , superposition of two one-excitation states used to measure the dispersion relation (red) and superposition of two-excitation states probing the quasiparticle interactions (green). b) Calculated coefficients A_j^k of all k -spin wave modes for a string of 7 spins (orange). The blue spline serves as a guide-to-the-eye to visualize the spin wave structure of the coefficients.

for all the spectroscopy experiments presented in this section are the same, if not stated otherwise:

- $\omega_{\text{ax}} = 2\pi \times 219 \text{ kHz}$, $\omega_x = 2\pi \times 2.7106 \text{ MHz}$ and $\omega_y = 2\pi \times 2.68 \text{ MHz}$
- $N = 7$, $\Omega_{\text{bic}} \approx 2\pi \times 110 \text{ kHz}$, $\Delta_t = 2\pi \times 20 \text{ kHz}$ and $\delta_c = 2\pi \times 2 \text{ kHz}$
- $J_0 \approx 2\pi \times 50 \text{ Hz}$, $B \approx 2\pi \times 640 \text{ Hz}$, $\alpha \approx 1.08$ and H_{XY} -regime (Eq. 5.4)

There are two crucial approximations underpinning the spectroscopic method presented here. The first one is concerned with the coefficients c_j^k of the spin waves (Eq. 5.3), where j denotes the flipped j^{th} -spin and k is the k^{th} -mode. In order to prepare such a spin wave mode, or superpositions of two, one must know the coefficients. However, knowing exactly those coefficients would in some way render the idea of spectroscopy unnecessary, as knowing them implies having already solved the Hamiltonian. The question is, can the exact coefficients $c_j^k(\alpha)$, which depend on α , be approximated by generic coefficients and how good is the approximation? Since the spin chain has non-cyclic,

open boundary conditions an educated guess for approximating the exact c_j^k is given by generic one-dimensional standing waves

$$A_j^k = \sqrt{\frac{2}{N+1}} \sin\left(\frac{kj\pi}{N+1}\right), \quad (5.7)$$

where we use A_j^k for the generic coefficients³³ to contrast them from the exact ones, c_j^k . The approximation is exact for the NN-coupling case, that is $A_j^k = c_j^k(\alpha \rightarrow \infty)$. In order to check its validity for longer range interactions, one can calculate the overlap probability (OP) between the exact eigenvectors for a given J_{ij} , denoted as ψ_c^k , and the approximated ones denoted as ψ_A^k . The overlap probability is then given by $|\langle \psi_c^{k'} | \psi_A^k \rangle|^2 \approx \delta_{k'k}$ as long as $A_j^k \approx c_j^k$ holds, where $\delta_{k'k}$ is the Kronecker-Delta.

Figure 5.9 a) shows $|\langle \psi_c^{k'} | \psi_A^{k=1} \rangle|^2$ ³⁴ for different k' as a function of α . As expected, states with opposite inversion symmetry (spatial anti-/symmetric wavefunction) show zero OP, whereas for states with the same symmetry a non-zero overlap is observable. However, even for those states the overlap probability is vanishingly small as long as $\alpha > 2$ and beyond that regime only states with a number of ‘nodes’ close to that of the state of interest show a significantly observable overlap. Nevertheless, for our purposes with an experimental $\alpha \approx 1.08$, any such overlap probability is sufficiently small and can be neglected, as confirmed by numerical simulations³⁵.

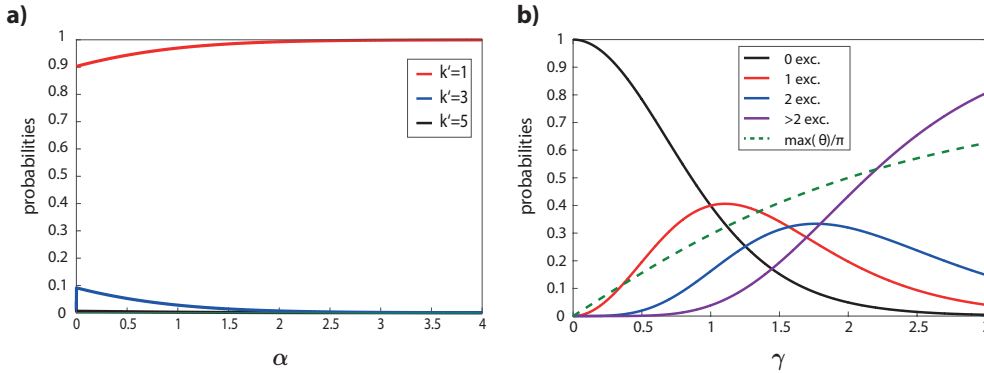


Figure 5.9.: **a)** As the generic spin wave coefficients $A_j^k = c_j^k(\alpha \rightarrow \infty)$ are only an approximation to the exact coefficients $c_j^k(\alpha < \infty)$, one might expect to excite additional eigenstates. Here, the overlap probabilities $|\langle \psi_c^{k'} | \psi_A^{k=1} \rangle|^2$ are calculated to find eigenstates other than $k' = 1$ as a function of α . The generic coefficients only deviate significantly from the exact ones for $\alpha < 2$. Even for the extreme case $\alpha = 0$ the probability of finding the state $k = 1$ is $p_1 \sim 0.9\%$ and only the state $k = 3$ gets excited with $p_3 \sim 0.1$. Hence, the approximation seems to be reasonable. **b)** The probability to project into different excitation subspaces as a function of the parameter γ , since we prepare product states as described in the text.

The other approximation is concerned with the experimental preparation of such spin waves. As mentioned earlier, the spin wave states are closely related to entangled W-states and the creation of such W-states [206] is costly in terms of experimental resources (laser pulses). Moreover, in

³³If we had cyclic boundary conditions, such as in a closed, circular chain, the k -modes would be planar waves with $A_j^k = 1/\sqrt{N} \exp(ikj\pi/(N+1))$.

³⁴It basically tells us, if we prepared a generic spin wave $k = 1$ -mode, what is the probability to excite other states due to the approximation.

³⁵Any additional state with sufficiently large probability will be in a superposition with the desired state, which will create a beat note in the time evolution.

contrast to W-states, spin waves have non-uniform coefficients A_j^k making the preparation even more challenging. Instead of preparing entangled states with a vast number of laser pulses and thus, possibly lower fidelities, one can prepare product states that are easily achievable with our quantum toolbox. By rotating each spin j into the state

$$|\theta_j\rangle = \cos(\theta_j)|\downarrow_j\rangle + \sin(\theta_j)|\uparrow_j\rangle, \quad (5.8)$$

where the angle of rotation is $\theta_j = \arctan(\gamma A_j^k)$, the resulting state can be written as a product state

$$|\psi_k\rangle \propto \bigotimes_{j=1}^N (|\downarrow_j\rangle + \gamma A_j^k |\uparrow_j\rangle) = |0\rangle + \gamma |k\rangle + \mathcal{O}(\gamma^2). \quad (5.9)$$

Here, the parameter γ is an overall excitation and determines the probability to find the desired spin wave state $|k\rangle$. In figure 5.9 b), various probabilities to project into a state with zero, one, two and more excitations are shown. Depending on the desired experimental protocol, as will be explained in the forthcoming sections, γ is chosen accordingly to fit the situation.

5.4.1. Spectroscopy of ground state gaps

In order to measure the energy E_k between the ground state $|0\rangle$ and a spin wave mode $|k\rangle$, we prepare a superposed product state $|\psi_k\rangle$ as described by equations 5.8 and 5.9. By exploiting the single ion addressability, each of the spins can be rotated individually by the right amount θ_j . First all ions are rotated by $\pi/2$ around the x -axis of the Bloch-sphere, then the addressing beam sequentially imposes an ac-Stark shift resulting in individual rotations around the z -axis. A final $-\pi/2$ pulse around x brings the spins into the state $|\psi_k\rangle$. However, since the rotation angle θ might be positive or negative depending on the sign of A_j^k and the ac-Stark rotation direction is fixed, we apply the following procedure: instead of ‘over-rotating’ all negative angles by $2\pi - \theta_j$ around z , we rotate all spins by $\tilde{\theta}_j = \theta + \delta\theta$, where $\delta\theta = \min \theta_j$ is the most negative rotational angle. After the final $-\pi/2$ pulse around x , the spin wave is slightly ‘tilted’ and an additional pulse around the y -axis with angle $-\delta\theta$ creates the desired state ψ_k . Figure 5.10 a) shows schematically the pulse sequence just described.

The overall excitation $\gamma = 0.4$ is chosen such that most of the population is in the ground state (probability $p_0 = 0.74$) and in the desired k -mode of the one excitation subspace ($p_1 = 0.24$)³⁶.

The prepared state $|\psi_k\rangle$ is evolved under the XY-Hamiltonian to $|\psi(t)\rangle = \exp(-iH_{XY}t/\hbar)|\psi_k\rangle$ and the magnetization of each spin is measured in the xy -plane of the Bloch-sphere by performing a resonant $\pi/2$ -pulse around x or y , respectively. This corresponds to measurements of $\sigma_j^{x(y)}$ in the reference frame of the Mølmer-Sørensen Hamiltonian and has to be transformed accordingly into the rotating frame of the H_{XY} -Hamiltonian³⁷. After the transformation, the resulting new bases are $\sigma^{\tilde{x}} = \cos(2B)\sigma^x - \sin(2B)\sigma^y$ and $\sigma^{\tilde{y}} = \sin(2B)\sigma^x + \cos(2B)\sigma^y$. Then, the time-dependent

³⁶This ensures that the strongest Fourier component in the beat note is related to ε_k , as will be explained later.

³⁷ $\sigma^{\tilde{\beta}} = e^{iBt\sigma^z} \sigma^{\beta} e^{-iBt\sigma^z}$, with $\beta = \{x, y, z\}$ and $B = \frac{\delta c}{2}$, see also appendix B.1.4.

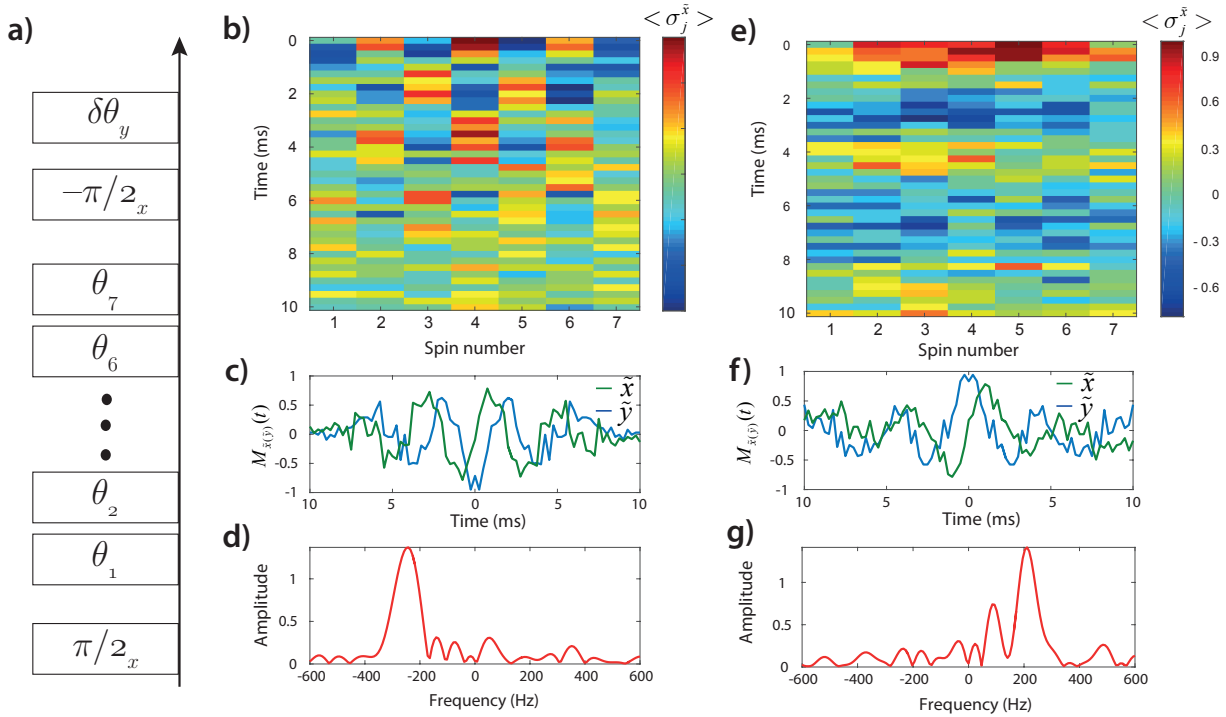


Figure 5.10.: **a)** Schematic of the pulse sequence for preparing a spin wave mode. **b) - c)** Spectroscopic signal and its analysis for initial states $|0\rangle + |k=1\rangle$ and **e) - f)** $|0\rangle + |k=7\rangle$. **b) & e)** Time evolution of the single-spin magnetization $\langle \sigma_j^{\tilde{x}(\tilde{y})}(t) \rangle$. **c) & f)** The single-spin signals summed $M_{\tilde{x}(\tilde{y})}$ in order to increase the signal to noise ratio. **d) & g)** A Fourier transformation of the signal $M_{\tilde{x}(\tilde{y})}$ yields the energy splitting between the ground state and the k -mode.

expectation value is given by

$$\langle \sigma_j^{\tilde{x}(\tilde{y})}(t) \rangle = \langle \psi(t) | \sigma_j^{\tilde{x}(\tilde{y})} | \psi(t) \rangle = 2\gamma \operatorname{Re} \left(e^{-i\frac{\varepsilon_k t}{\hbar}} \langle 0 | \sigma_j^{\tilde{x}(\tilde{y})} | k \rangle \right) + \mathcal{O}(\gamma^3), \quad (5.10)$$

where $\varepsilon_k = E_k - 2B$ is the energy shift of the k^{th} -mode caused by the spin-spin interactions. From equation 5.10 it is evident that the expectation values will oscillate at a frequency proportional to ε_k as shown in figure 5.10 b) & e) for the two spin wave modes $k=7$ and $k=1$, respectively and a Fourier transform directly yields ε_k . In order to minimize transformation artefacts, the signals are mirrored to negative times and the signal-to-noise ratio is increased by summing the single-spin values to

$$M_{\tilde{x}(\tilde{y})}(t) = \sum_j^N A_j^k \langle \sigma_j^{\tilde{x}(\tilde{y})}(t) \rangle. \quad (5.11)$$

In figure 5.10 c) & f), $M_{\tilde{x}(\tilde{y})}$ is shown for $k=7$ and $k=1$, respectively. Finally the signal $M(t) = M_{\tilde{x}} + iM_{\tilde{y}}$ is Fourier transformed yielding a distinct peak presented in 5.10 d) & g). In the case of $k=7$ a Gaussian fit reveals a peak position at $\varepsilon_7/\hbar = -249 \text{ Hz} \pm 77 \text{ Hz}$ ³⁸ and for $k=1$ the peak is centred at $\varepsilon_1/\hbar = 213 \text{ Hz} \pm 53 \text{ Hz}$.

The first thing we can learn from the two peaks is the sign of the spin-spin coupling J_{ij} . As the shortest wavelength mode $k=7$ is shifted to lower energies and the longest wavelength mode to

³⁸The error is defined as the FWHM.

higher ones, one can imply that the spin-spin coupling must be *anti-ferromagnetic*. Unfortunately, as the superposition $|0\rangle + |k\rangle$ is outside the decoherence-free subspace the signal $M(t)$ decays rapidly within a few oscillation periods due to ambient magnetic field fluctuations and laser frequency noise limits the resolution of this approach. The signal decay leads also to artefacts in the Fourier transform, such as the peak at 90 Hz visible in figure 5.10 g).

Despite these limitations, the method discloses valuable information regarding the spin-spin coupling and, in addition, the approximations prove to be valid as there are hardly any spurious frequency components in the transformed signal.

5.4.2. Spectroscopy of dispersion relations

In a similar fashion as before, a superposition of two k -modes separated by $\Delta E_{kk'} = E_k - E_{k'}$ can be created. The advantage now is that both spin waves are in the same subspace, decoupled from other subspaces, and as a result the relative phase between the two states $|k\rangle$ and $|k'\rangle$ is insensitive to ambient magnetic field noise or laser frequency fluctuations.

Here, the initial state is prepared by individually rotating each spin j by

$$\theta_j = \arctan \left[\gamma \left(A_j^k + A_j^{k'} \right) \right] \quad (5.12)$$

resulting in

$$|\psi_{kk'}\rangle = |0\rangle + \gamma (|k\rangle + |k'\rangle) + \mathcal{O}(\gamma^2). \quad (5.13)$$

We choose the overall rotation to be $\gamma = 0.7$ resulting in a much higher probability to project into the one-excitation subspace $p_1 = 0.42$ ($p_0 = 0.43$). The state is time-evolved under H_{XY} and the signal is measured in the z -basis. Since the measurement of σ_j^z commutes with H_{XY} , it is permissible to post-select the signal by retaining only data with a single excitation. In this way, only $|k\rangle + |k'\rangle$ contributes to the time-dependent magnetization signal

$$M_1(t) = \sum_j^N \kappa_j \langle \sigma_j^z(t) \rangle = \cos \left(\frac{\Delta E_{kk'} t}{\hbar} \right) \sum_j^N \kappa_j \langle k | \sigma_j^z | k \rangle, \quad (5.14)$$

where $\kappa_j = \text{sign} \left(A_j^k A_j^{k'} \right)$ ensures a constructive summation. A Fourier transform of $M_1(t)$ yields the energy difference between the spin wave modes $|k\rangle$ and $|k'\rangle$.

Figure 5.11 a) - c) shows spectroscopic signals of a superposition $|k = 1\rangle + |k' = 7\rangle$, specifically the time-dependent spin-resolved magnetization $\langle \sigma_j^z(t) \rangle$, the summed signal $M_1(t)$ and its Fourier transformation. The first observation standing out is the extraordinarily long coherence time compared to the measurements presented before, allowing us to record many oscillation periods and hence increase the resolution substantially. The Fourier transformed peak in Fig. 5.11 c) is at $383 \text{ Hz} \pm 13 \text{ Hz}$, at least a factor of five narrower than in the previous method. The achievable resolution allows us to now superpose various states and measure their relative energy splitting, thus resolving small energy differences such as in the dispersion relation. Figure 5.11 c) shows the dispersion relation measured relative to $|k = 1\rangle$ and the observed peaks coincide very well with the theoretically calculated dispersion relation. Moreover, the measurements reproduce the divergent

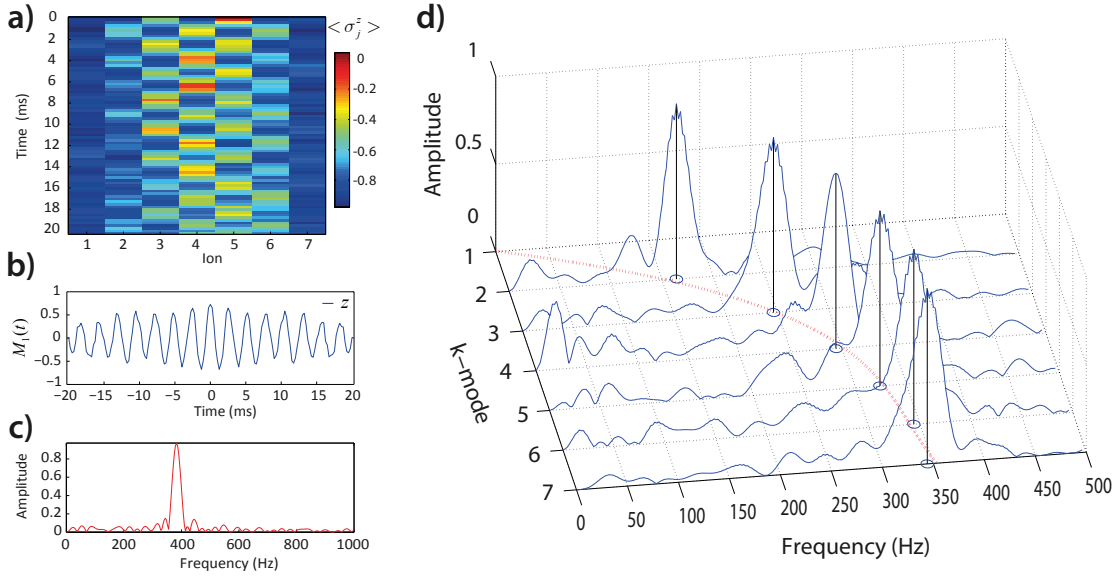


Figure 5.11.: **a) - c)** Spectroscopic signals of the superposition $|k = 1\rangle + |k' = 7\rangle$, where **a)** is the single-spin resolved magnetization $\langle \sigma_j^z(t) \rangle$, **b)** is the summed signal $M_1(t)$ mirrored to negative times in order to minimize transformation artefacts and **c)** is the Fourier transformation of $M_1(t)$ yielding a single peak at 383 Hz with FWHM of 13 Hz **d)** Spectroscopically measuring different initial superposition states $|k = 1\rangle + |k'\rangle$ with $k' = 2 \dots 7$ (blue traces) allows to reconstruct the dispersion relation. The blue circles are a projection onto the plane and mark the position which closely matches the theory curve (red line).

group velocity $v_g = \partial E_k / \partial k$ at $k = 1$ for long range interactions $\alpha < 2$, as discussed in section 5.2. Using the method described in section 5.3.3 we get a power law exponent $\alpha \approx 1.08$.

A closer look at the Fourier transformed signals reveals a single dominant peak affirming the validity of our approximation of generic coefficients, even for long range interactions.

5.4.3. Spectroscopy of interacting quasiparticles

In the previous sections only single excitations, that is single quasiparticles dynamics, were probed. What will happen if two quasiparticles are excited in the system, do they interact and if so, is there an observable signature of these interactions? In order to investigate this, we follow the same procedure as for measuring the dispersion relation, however, the overall excitation is increased to $\gamma = 1.4$ resulting in a probability $p_2 = 0.41$ of finding two excitations in the system ($p_0 = 0.08$ and $p_1 = 0.33$). The initial state $|\psi_{kk'}\rangle$ is of the same form as in equation 5.13 with the next order contribution

$$|\psi_{kk'}^{(2)}\rangle = \gamma^2 \left(\sum_j^N (A_j^k + A_j^{k'}) \sigma_j^+ \right)^2 \equiv \gamma^2 (|kk\rangle + 2|k'k\rangle + |k'k'\rangle) \quad (5.15)$$

becoming relevant. The initial state is time-evolved under the same Hamiltonian as before and the expectation values $\langle \sigma_j^z(t) \rangle$ are measured. In contrast to before, the measurements with two excitations are post-selected instead of one and the observable

$$\mathcal{P}_{ij}^z = \frac{1}{4} \langle (1 + \sigma_i^z) + (1 + \sigma_j^z) \rangle \quad (5.16)$$

is computed. Once again the signal is summed to

$$M_{2a(b)}(t) = \sum_{i \neq j} \kappa_{ij}^{a(b)} \mathcal{P}_{ij}^z(t) \quad (5.17)$$

in order to increase the signal-to-noise ratio. The weighting factors κ_{ij}^a and κ_{ij}^b enhance and suppress different parts of the signal, as shown later (a detailed derivation can be found in appendix C), and are given by:

$$\kappa_{ij}^a = \text{sign} \left(A_j^k A_i^k A_j^{k'} A_i^{k'} \right) \quad \kappa_{ij}^b = \text{sign} \left(A_j^k A_i^{k'} \right) + \text{sign} \left(A_j^{k'} A_i^k \right). \quad (5.18)$$

In addition, single-excitation outcomes are post-selected in order to obtain the energy splitting $|\Delta E_{kk'}|/h$ as a reference.

If the interaction between quasiparticles was zero, all the higher excitation states would be a simple combination of the single-quasiparticle states. For instance, the higher order contribution $|\psi_{kk'}^{(2)}\rangle$ would generate two beat notes proportional to $2\Delta E_{kk'}$ and $\Delta E_{kk'}$, respectively³⁹.

On the other hand, if the quasiparticles are interacting, the energy levels would experience an interaction shift and, as a consequence, one would observe three beat notes, depicted as $h\nu_a$, $h\nu_b$ and $h\nu_c$ in figure 5.12 a). Indeed, the measured frequency spectrum of $|\psi_{k=1, k'=7}^2\rangle$ shows a peak at $665 \text{ Hz} \pm 14 \text{ Hz}$ which is significantly lower than $765 \text{ Hz} \pm 28 \text{ Hz} = 2|\Delta E_{kk'}|/h$ (dark green line), expected for non-interacting bosonic (NIB) quasiparticles, as shown in figure 5.12 b). Here, the observable \mathcal{P}_{ij}^z is summed with the weighting factors κ_{ij}^a which results in enhancing $h\nu_c$ and suppressing $h\nu_a$ & $h\nu_b$. If the quasiparticles, on the other hand, were non-interacting fermions (NIF) one would expect a beat note at $|E_{k=7} + E_{k=6} - E_{k=1} - E_{k=2}|/h = 585 \text{ Hz} \pm 21 \text{ Hz}$ (light green line), due to the Pauli-exclusion principle. From these observations it is already possible to infer that the quasiparticles of the underlying system cannot be described by free, non-interacting particles. A NIF-description would be only accurate for $\alpha \rightarrow \infty$, that is for strictly nearest-neighbour interactions [207].

In figure 5.12 c) the Fourier transformed signal of $M_{2b}(t)$ is shown where the weighting factors κ_{ij}^b are used. This allows us to enhance peaks proportional to $h\nu_a$ and $h\nu_b$, but suppresses the beat note due to $h\nu_c$. The observed peaks are located at $304 \text{ Hz} \pm 14 \text{ Hz}$ and $368 \text{ Hz} \pm 15 \text{ Hz}$.

A qualitative understanding of the two-quasiparticle spectra can be gained from a perturbation theory approach, where a detailed derivation can be found in Appendix C.2.2. First, the spin creation (annihilation) operators σ_i^+ (σ_i^-) are mapped to hardcore bosonic creation (annihilation) operators $\sigma_i^+ \rightarrow b_j^\dagger$ ($\sigma_i^- \rightarrow b_j$) via the Holstein-Primakoff transformation⁴⁰ [208]. A quasiparticle mode $|k\rangle$ is then created from the vacuum state by $|k\rangle = b_k^\dagger |0\rangle = \sum_j A_j^k b_j^\dagger |0\rangle$ and the two-quasiparticle subspace can be excited by $|kk'\rangle = b_k^\dagger b_{k'}^\dagger |0\rangle$ ⁴¹, see the schematic energy diagram in figure 5.12 a).

³⁹ $(|kk\rangle + |k'k'\rangle)$ would beat at $2|\Delta E_{kk'}|/h$, $(|kk\rangle + |k'k'\rangle)$ and $(|k'k\rangle + |kk'\rangle)$ at $|\Delta E_{kk'}|/h$.

⁴⁰The transformation preserves the bosonic commutation relation $[\sigma_i^+, \sigma_j^-] = 0$ for $i \neq j$, but introduces the hardcore constraint $\sigma_j^+ \sigma_j^+ = 0$, which is a consequence of the spin-1/2 system, that is per lattice site (spin position) maximally a spin-1/2 can be excited.

⁴¹Note: the two-quasiparticle state $|kk'\rangle = b_k^\dagger b_{k'}^\dagger |0\rangle$, where $k(k') = 1 \dots N$, is not exactly an eigenstate of the $l = 2$ -subspace, since there should be $N(N+1)/2$ different kk' -modes. However, the $l = 2$ -subspace in our system counts only $N(N-1)/2$ eigenstates due to the hardcore constraint. Nevertheless, for small perturbations, i.e. $N \gg l = 2$, there should be significant overlap between $|kk'\rangle$ and the proper eigenstates.

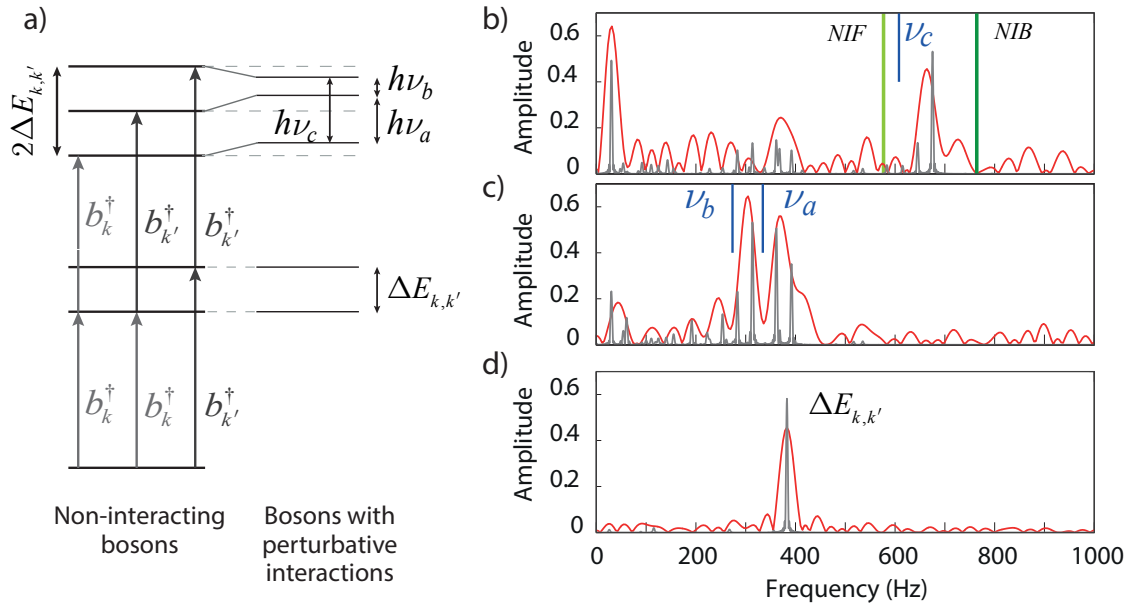


Figure 5.12.: a) Schematic energy diagram for non-interacting quasiparticles (left side) and for interacting quasiparticles (right side). b) Fourier transformation of M_{2a} where κ_{ij}^a 's are used as weighting factors. In this way the beat note due to ν_c is enhanced and beat notes due to ν_a and ν_b are suppressed. If the quasiparticles were non-interacting bosons (NIB) the beat note coincides with the dark green line and for non-interacting fermions (NIF) it would be the light green line. The blue line shows the position of the peak predicted by first order perturbation theory. c) Fourier transformation of M_{2b} with κ_{ij}^b as the weighting factors, which enhance ν_a and ν_b and suppress ν_c . d) Fourier transformation of the single-excitation subspace signal $M_1(t)$ as a reference.

Secondly, a first order perturbation theory predicts interaction shifts $V_{kk'}$ of the states $|kk'\rangle$. As a consequence, there are three beat notes to be expected, one at $\nu_a = |\Delta E_{kk'} + V_{kk} - V_{kk'}|/h$, one at $\nu_b = |\Delta E_{kk'} - V_{k'k'} + V_{kk'}|/h$ and another one at $\nu_c = \nu_a + \nu_b$, shown as blue lines in figure 5.12 b) and c), respectively. In terms of number of peaks and signs of the interaction shift, the predictions resulting from a perturbative approach prove to be qualitatively correct. However, in comparison to the measured data, perturbation theory overestimates the effects. In addition, perturbation theory fails to predict the peak observed at $33 \text{ Hz} \pm 20 \text{ Hz}$, which can be explained by studying the exact eigenstates of this manifold. Indeed, one finds that the initial state has substantial overlap with a fourth eigenstate generating additional beat notes not predicted by first order perturbation theory. This discrepancy can be explained by considering the magnitude of the perturbation, that is the quasiparticle density $l/N = 2/7$, which is not sufficiently low in order to treat the hardcore interaction as a small perturbation. However, with increasing system size the density $l/N \rightarrow 0$ is sufficiently small such that the perturbation theory eventually provides quantitatively valid results, as the states $|k'k\rangle$ come closer to the true eigenstates of the two-excitation manifold.

As these results show, the developed spectroscopy method allows us to obtain information about the generated Hamiltonian, including its quasiparticle spectrum and quasiparticle interactions. Such techniques will be indispensable for characterizing and validating engineered Hamiltonians in quantum simulation. The method is applicable to Hamiltonians, where isolated eigenstates and superpositions of such states can be prepared in a controllable manner.

5.5. Quasiparticle engineering and entanglement propagation

In the light of quantum information processing, a fundamental question is how fast does information propagate in an interacting many-body system⁴². As introduced in section 5.2 the spread of correlations is bound by a light cone for short range interacting systems, where any correlations outside the causal region are suppressed by the Lieb-Robinson bound, see Eq. 5.5. An important question is whether the two opposite sides of the wavefront (for a 1D system) are correlated and whether those correlations are classical or quantum. Theoretically it is expected that an excited, interacting quantum many-body system will generate entanglement which spreads out bound by the wavefront [209]. However, experimental evidences for Lieb-Robinson bounds in general have not been shown until 2012, when the group of I. Bloch observed them for the first time an one-dimensional quantum gas in an optical lattice with NN-interactions [173]. By quenching the system, they reveal the time evolution of correlations in their system and show that the propagations of correlations is bound to a light cone for NN-interactions. Despite these ground-breaking results, due to their spin encoding⁴³ it is only possible to measure two-point correlation functions in a single basis. This enabled them to measure correlations between the two sides of the wavefront, however, lacking the ability to perform measurements in different bases it is impossible to make statements regarding the quantumness of those correlations.

The section here presents work published in ‘*Quasiparticle engineering and entanglement propagation in a quantum many-body system*’ [26]. A major result is the experimental observation of entanglement propagating along the wavefront. In addition, it is shown that the light-cone-like picture becomes less and less valid as the spatial interaction range is increased. A simultaneously published, but independent, investigation of Lieb-Robinson bounds in a trapped ion quantum simulator is presented in [210].

5.5.1. Propagation of entanglement

As described in the previous sections an H_{XY} -Hamiltonian, that is $B \gg J_0$, is set up for a chosen α . Then, the spins are optically pumped into the ground state $|\downarrow\downarrow \dots \downarrow\downarrow\rangle$ and, by making use of the single-ion addressing, a single spin is quenched (excited) giving the initial state

$$|\psi_i\rangle = |\downarrow\downarrow \dots \uparrow \dots \downarrow\downarrow\rangle. \quad (5.19)$$

For most of the experiments the center spin of the spin chain is flipped, if not stated otherwise. Such a single-spin quenched system can be pictured as an equal superposition of spin wave modes with positive and negative momentum $\pm k$. If such an initial state is time-evolved, the initially localized excitation will disperse and distribute entanglement through the system, where group velocities are determined by the dispersion relation. This spread of information from the quenched side can be spatially and temporarily observed by measuring the resolved single-spin magnetization

⁴²The term information here is used in a very wide context, ranging from desired (quantum) correlations down to unwanted noise introducing decoherence in the system.

⁴³They encode a two level system into doublons (excess particle) and holons (holes), that are two atoms on the same site of the optical lattice and lack of atoms in a site, respectively.

$\langle \sigma_j^z(t) \rangle$, as shown in figure 5.13 a) for a $N = 7$ spin system⁴⁴. It is clearly visible that spin wave

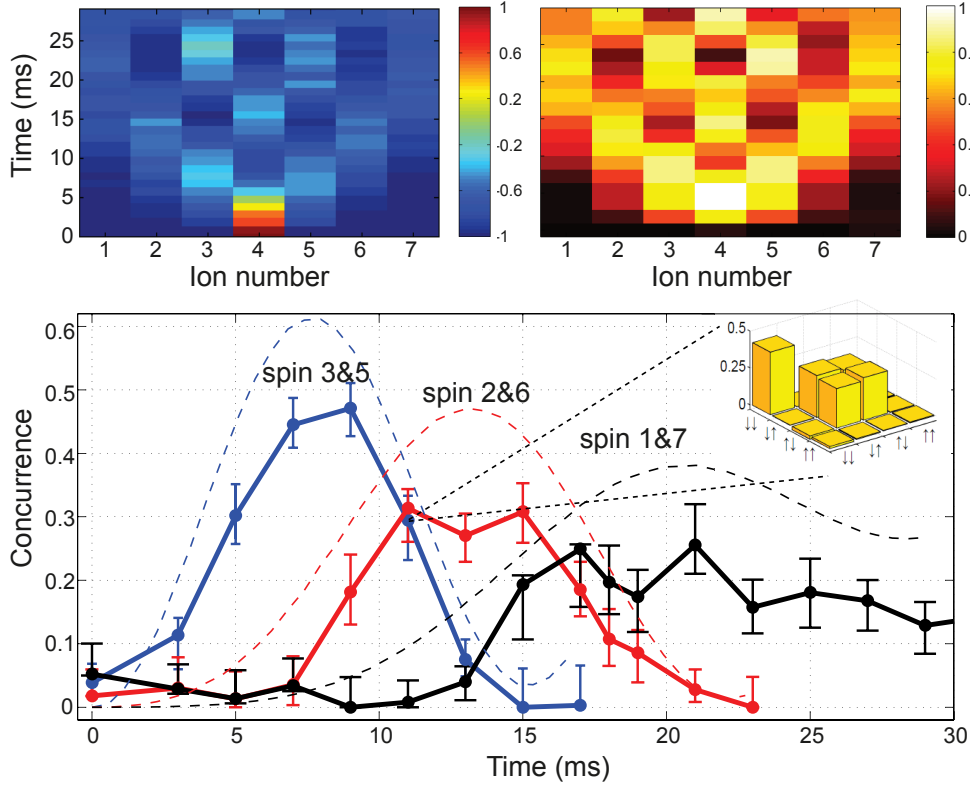


Figure 5.13: a) Measured time-evolution of the single-spin magnetization for a locally quenched system. b) Single-spin von Neumann entropy $\text{Tr}(\rho \log(\rho)) / \log(2)$ reconstructed from single-qubit state tomographies. High entropy states indicate high correlation with the rest of the system. c) Time-evolution of the pairwise concurrence (measure of two-qubit entanglement) between pairs 3 & 5 (blue), 2 & 6 (red) and 1 & 7 (black). Dashed lines show theoretical predictions and dots are experimental data reconstructed from two-qubit state tomographies. Error bars are calculated from Monte Carlo simulation of quantum projection noise [211]. **Inset** An exemplary reconstructed density matrix $\rho_{3,5}^{9 \text{ ms}}$ between spins 3 & 5 at time $\tau = 9$ ms. The measured fidelity with the theoretical state $|\psi_{\text{ideal}}\rangle$ is $\mathcal{F} = 0.975 \pm 0.005$.

packets radiate away from the quench site and eventually reach the boundaries of the system where they get reflected from. In order to investigate correlations distributed in the system single-qubit and two-qubit state tomographies were measured. From the reconstructed single-qubit states it is possible to calculate the single-spin von Neumann entropy, see figure 5.13 b). High entropy values indicate that the spin under investigation is highly quantum correlated with the rest of the system, however, no statement can be made with which part of the system. The two-qubit state tomographies are taken between spin pairs symmetrically located with respect to the quench site, where each basis configuration is measured 400 times to gain enough statistics. In order to speed up the experimental procedure, the tomography measurements are performed ‘bundle-wise’, that is spins 1, 2, 3, 4 and spins 5, 6, 7 are grouped together. By doing so, not only the measurement time is decreased but additional information is available, i.e. one can extract all two-qubit combinations between ‘left’ and ‘right’ spins. As we are mainly interested in the correlations carried by the wavefront, spin pairs 3 & 5, 2 & 6 and 1 & 7 are analysed. The density matrices are reconstructed

⁴⁴ $\omega_{\text{ax}} = 219 \text{ kHz}$, $\omega_{\text{rad}_x} = 2.6545 \text{ MHz}$, $\omega_{\text{rad}_y} = 2.6195 \text{ MHz}$, $\Delta_t = 120 \text{ kHz} \rightarrow \alpha \approx 1.75$, $\delta_c = 3 \text{ kHz}$, $\Omega_{\text{bic}} = 2\pi \times 102.46 \text{ kHz} \rightarrow J_0 \approx 2\pi \times 8 \text{ Hz}$.

via maximum-likelihood estimation [211] and the entanglement is quantified by the concurrence [212]

$$C(\rho) \equiv \max(0, \lambda_1 - \lambda_2 - \lambda_3 - \lambda_4) \quad (5.20)$$

where λ_i are the eigenvalues of the Hermitian matrix

$$R \equiv \sqrt{\sqrt{\rho} (\sigma_1^y \otimes \sigma_2^y) \rho^* (\sigma_1^y \otimes \sigma_2^y) \sqrt{\rho}}. \quad (5.21)$$

Figure 5.13 c) shows the time evolution of the reconstructed concurrence $C(\rho)(t)$ compared to the theoretical prediction. It is immediately visible that the quasiparticles spreading from the quench site first entangle the spins closest to the perturbation, then the next spin pair becomes entangled, whereas the former disentangles and so on. This is the first time clear evidence of the wavefront carrying entanglement around the system is observed.

The error bars given in Fig. 5.13 c) are computed from Monte Carlo simulations of quantum projection noise and represent a quantile of 15, 85%. Regarding the discrepancy between theoretical prediction and our data, it has to be mentioned that the concurrence is a very tight measure of entanglement and any noise process or miscalibration in the tomography pulse sequence will strongly affect the reconstructed value. Further, the observation that the concurrence $C(\rho)(\tau) > 0$ at time $\tau = 0$ ms is non-zero, despite the fact the initial state is a product state, is also attributed to noise in the reconstruction. Here, a separability measure instead of an entanglement measure might be better suited [213, 214].

5.5.2. Tuning the interaction range and Lieb-Robinson bounds

Having the ability to tune the interaction range α , it is possible to investigate the propagation of entanglement and the Lieb-Robinson bounds for different regimes of α . As entanglement distributed in the system coincides with the wavefront observable in the magnetization, we settle for measuring only the time-dependent magnetizations $\langle \sigma_i^z(t) \rangle$, however, for a larger system size $N = 15$ in order to decrease finite-size effects. Figure 5.14 a) shows the time-evolution of the resolved magnetization for three different values of $\alpha \approx 1.41$ ⁴⁵, $\alpha \approx 1.07$ ⁴⁶ and $\alpha \approx 0.75$ ⁴⁷ and compares it with numerical simulations for the exact J_{ij} coupling matrix using experimental parameters (Fig. 5.14 b)) and with numerical simulations (Fig. 5.14 c)) where J_{ij} has a proper power law decay $\sim 1/|i-j|^\alpha$ and α is estimated by exploiting the method described in section 5.3.3. It is remarkable how good the experimental time evolution fits the numerical simulations even with regards to the interference fringes resulting from the reflections of the system boundaries. Interestingly, the comparison to a pure power law decay shows only marginal deviations.

As the interaction range becomes larger, that is α decreases, the fitted arrival times (red dashed line, for more details regarding the fit see figure 5.15) of the wave packet become shorter and

⁴⁵ $\omega_{\text{ax}} = 150$ kHz, $\omega_{\text{rad}_x} = -2.658$ MHz, $\omega_{\text{rad}_y} = 2.617$ MHz, $\Delta_t = 120$ kHz $\rightarrow \alpha \approx 1.41$, $\delta_c = 3$ kHz, $\Omega_{\text{bic}} = 2\pi \times 230.94$ kHz $\rightarrow J_0 \approx 2\pi \times 12$ Hz.

⁴⁶ $\omega_{\text{ax}} = 219$ kHz, $\omega_{\text{rad}_x} = 2.655$ MHz, $\omega_{\text{rad}_y} = 2.621$ MHz, $\Delta_t = 40$ kHz $\rightarrow \alpha \approx 1.07$, $\delta_c = 3$ kHz, $\Omega_{\text{bic}} = 2\pi \times 212.77$ kHz $\rightarrow J_0 \approx 2\pi \times 31$ Hz.

⁴⁷ $\omega_{\text{ax}} = 150$ kHz, $\omega_{\text{rad}_x} = 2.71$ MHz, $\omega_{\text{rad}_y} = 2.68$ MHz, $\Delta_t = 15$ kHz $\rightarrow \alpha \approx 0.75$, $\delta_c = -1$ kHz, $\Omega_{\text{bic}} = 2\pi \times 123.92$ kHz $\rightarrow J_0 \approx 2\pi \times 22$ Hz.

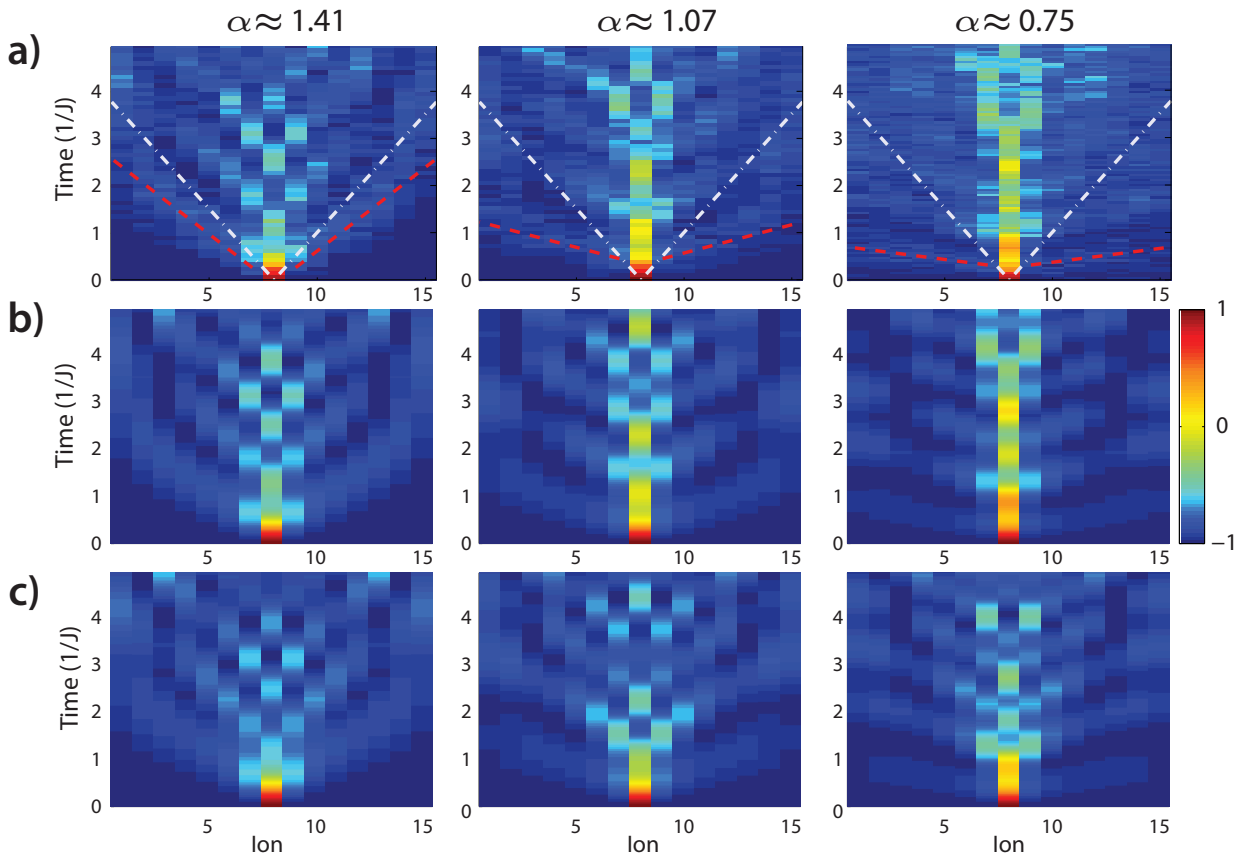


Figure 5.14. Time evolution of a locally quenched system with $N = 15$ spins for different interaction ranges $\alpha \approx 1.41$, $\alpha \approx 1.07$ and $\alpha \approx 0.75$. **a)** Experimentally measured time-evolution of resolved single-spin magnetization $\langle \sigma_j^z(t) \rangle$. Red dashed lines are fits to the arrival times of the wave packet (see text and Fig. 5.15) and grey dashed lines are the theoretical light cones for NN-interactions. **b)** Numerical simulation with experimental parameters and the exact J_{ij} coupling matrix. **c)** Numerical simulation for a system with pure power law decay. α is estimated as described in section 5.3.3.

thus the propagation velocity increases as expected. Moreover, with decreasing α the wavefront becomes fainter and the light-cone-like bounds become less and less distinct. In fact, for the long range case, $\alpha \approx 0.75$, the magnetization dynamics is not entirely within the nearest-neighbour Lieb-Robinson bounds, that is at early times the magnetization is almost instantly increased even for large distances, whereas for the short range case, $\alpha \approx 1.41$, basically all measured points are within the calculated bounds as shown in figure 5.16 a) and b), respectively. Our observations confirm that for long range interactions, correlations can spread immediately to distant neighbours and the findings are consistent with generalized Lieb-Robinson bounds for power law decays. In fact, for $\alpha < 1$ the bounds are trivial, that is there is no restriction on the velocity of information spreading [194, 195]. A derivation of the exact form of nearest-neighbour Lieb-Robinson bounds in our system can be found in [26, Supplementary material].

The observed behaviour can be further understood by qualitatively analysing the data, i.e. estimating the maximal group velocity v_g^{\max} from the wave packet arrival times at different spin sites as shown in figure 5.15 a)- c). Here, the magnetization $\langle \sigma_i^z(t) \rangle$ of spin i is fitted with a Gaussian and the different Gaussian maxima are plotted as a function of the distance from the quench site.

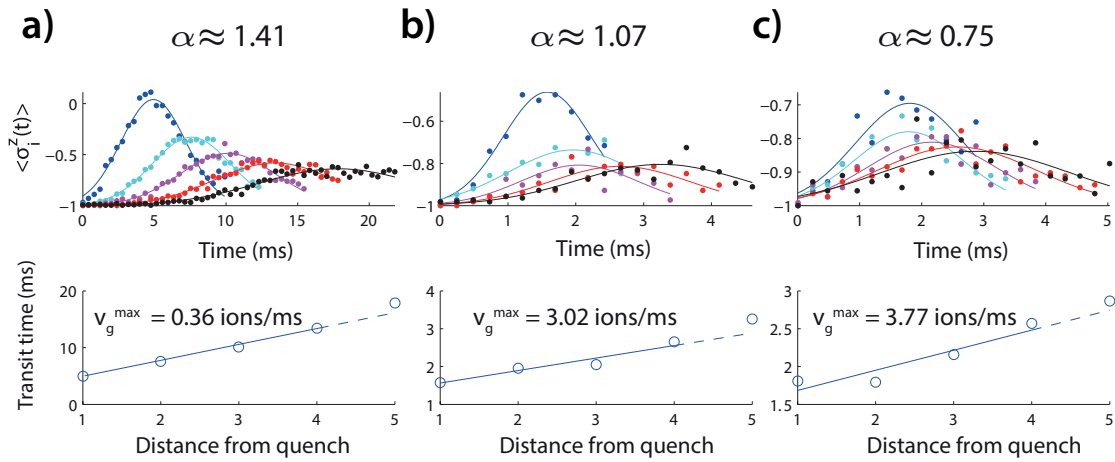


Figure 5.15.: a) - c), **Top** The Magnetization is averaged over symmetric pairs of spins around the centre spin and plotted as a function of time: spins 7 & 9 (blue); spins 6 & 10 (cyan); spins 5 & 11 (purple); spins 4 & 12 (red); spins 3 & 13 (black). Dots are the measured data sets and lines are Gaussian fits. **Bottom** The maxima of the different Gaussian fits are plotted against the distance from the quench site and a linear fit reveals an estimate of the maximal group velocity v_g^{\max} .

A linear fit reveals an estimate for the maximal group velocities and shows that the long range case is more than an order of magnitude faster than the short range one.

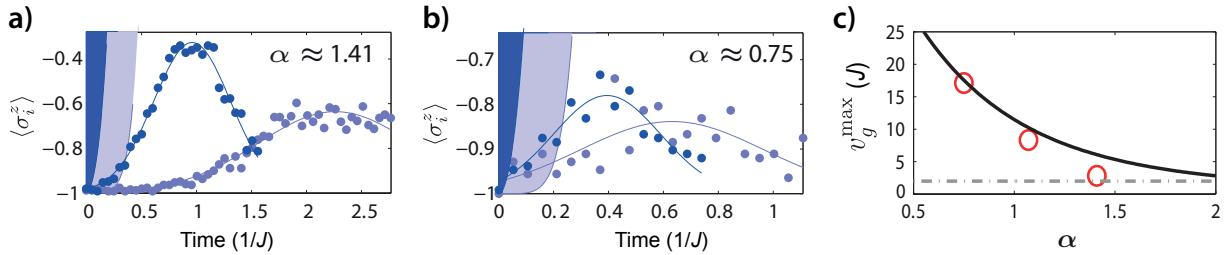


Figure 5.16.: a) & b) Magnetization of spin 6 (dark blue) and spin 13 (light blue) fitted with a Gaussian for two α 's. The shaded areas represent the part outside the causal region given by NN-interaction Lieb-Robinson bounds. For the short range case ($\alpha \approx 1.41$) all of the dynamics are within the bounds, whereas for long range interactions ($\alpha \approx 0.75$) the magnetization spreads immediately at early times. c) The estimated maximal group velocities v_g^{\max} plotted against α . The short range case is close to the NN-interaction group velocity (grey dashed line), while v_g^{\max} diverges for long range interaction as predicted.

By plotting the estimated group velocities against α , figure 5.16 c) (red circles), one can see that v_g^{\max} for $\alpha \approx 1.41$ is close to the theoretical value given for nearest-neighbour interactions (grey dashed line). As the interaction range is increased, the maximal group velocity starts to diverge as predicted by [193]. However, there is an ultimate bound on the speed of propagation given by the underlying physical system and that is the speed of sound in the ion chain [215]. Even the infinite range interactions are mediated by the motional modes and thus are limited by the phonon speed.

Interestingly, despite the fast ejection of quasiparticles for long range interactions, the initial local perturbation stays more localized during the time evolution in that case. This observation is consistent with the dispersion relation as discussed in section 5.2. For long range interactions only a small fraction of the spin wave modes have a divergent group velocity, resulting in a fast ejection from the quench site, whereas the majority of the k -modes are in the flat region of the dispersion

relation with small group velocities.

5.6. Discussion and Outlook

This chapter presented a trapped ion based analogue quantum simulator⁴⁸, specifically built to implement models of interacting spins, such as the transverse field Ising model or the XY-model. Its versatility arises from the high degree of ability to independently and fully control many experimental parameters, allowing us to explore and answer interesting, non-trivial physics' questions. Moreover, the high controllability is further reflected in the extremely good overlap between experimental data and numerical simulations, where in fact no free parameters are used⁴⁹.

A major part of this thesis was to implement such a quantum simulator in an existing trapped ion experiment, ranging from stabilization of radial modes to beam shaping of the laser light field inducing the effective spin-spin interactions and ac-Stark compensations. As with every experiment, techniques have to be developed in order to calibrate the system and to have means of assuring a proper functioning of the experiment. In the light of quantum simulation, there is an additional philosophical, more specifically an epistemological, question: "If a quantum simulator is designed to solve problems intractable by classical means, how can we trust the outcomes of a simulator which is always subject to experimental noise and errors?" [216]. This problem is directly related to the Hilbert space size yielding a follow-up question: "If the Hilbert space is too big to compute, how can we efficiently measure and extract information of a simulated quantum state, since methods such as full state tomography are non-scalable and destined to fail for large system sizes?" The obvious strategy is to take one step after the other, starting from a small system, trivially solvable, and advancing to larger and more complex system. On this path, it is important to develop new tools, procedures and protocols to unlock the black box of a quantum simulator.

In this thesis a method, based on a spectroscopic protocol, is presented in order to qualitatively measure the energy spectrum of an emulated Hamiltonian. The spectroscopic procedure not only provides means to calibrate the simulator and to increase the trust in its outcomes, but also demonstrates the high degree of control to deliberately manipulate its constituents. By individually controlling and preparing superpositions of the system's eigenstates, it allows us to probe important quantities such as the dispersion relation of the quasiparticles and, even more, it provides means to observe and quantitatively describe interactions between those quasiparticles.

Apart from answering questions related solely to the quantum simulator, one can start to tackle wider physics questions. In the view of quantum information, a fundamental question is related to the maximal speed with which information or correlations can be transported in an interacting many-body system. In this thesis we investigate this question from two sides. First, experimental evidence is provided that correlations spreading in a locally excited system are indeed quantum correlations, specifically entanglement. Secondly, by tuning the spin-spin interaction from short range to long range, we could observe that correlations in the short range case are bound by so called Lieb-Robinson bounds, whereas in the longer range case those bounds become less stringent

⁴⁸Some authors refer to it as an emulator, since a physical system is used to emulate a system of interest that is otherwise experimentally or theoretically inaccessible.

⁴⁹Except for an overall scaling of the Rabi frequency which is always less than 5%.

and correlations can exist outside.

Despite the astonishingly good agreement between experiment and numerical simulations, there are a few limits as to the size of the spin string and the maximal coupling strength. An elaborate list of experimental issues setting ‘soft’ limitations on the number of spins is given in chapter 4.3. Fortunately, none of these limitations seem to be fundamentally insurmountable and can be overcome with clever engineering, as well as redesigning certain parts of the experimental setup as described in the aforementioned chapter. In light of the simulations presented here, major sources of decoherence are laser intensity fluctuations and heating of motional modes. Laser intensity fluctuations cause the spin-spin coupling strength to fluctuate which results in fluctuations of the Hamiltonian energy levels broadening the spectroscopic signal and, to a lesser degree, smearing out the time dynamics in the quench experiments. At the time of writing this thesis, this problem has been tackled by implementing a ‘sample and hold’ stabilization loop⁵⁰ that significantly improves the stability. A less obvious limitation is caused by heating of the motional modes which increases proportionally with the number of ions (at least for the COM-mode). The main effect is that during the time evolution some populations leave the protected subspace, such as in the case of the single-spin quench experiments. After some time, due to heating, one will find the neighbouring subspaces, i.e. zero and two-excitation, to be populated. As a consequence, these populations cause the system to be subject to ambient magnetic field noise and therefore an additional decoherence channel is opened. There seems no obvious fix to this problem, as to my best knowledge, there isn’t even a widely accepted consensus among the professional world with regards to the detailed mechanisms of heating⁵¹.

Another limitation is the rather small spin-spin coupling strength on the order of a few tens of Hertz, or even less depending on the detuning Δ_t . For the experiments presented here, the low coupling strength is less critical, since all time evolutions are performed in the decoherence-free subspace. However, measuring for instance very tiny coupling elements of the J_{ij} -matrix requires to evolve the system for more than 100 ms and, at these times, the limited life time of the $D_{5/2}$ -state kicks in as almost 10% of the populations decay to the ground state $S_{1/2}$. This limitation will be of greater importance as soon as quantum simulations of H_{Ising} are performed, where the subspaces are not uncoupled any more.

The spin-spin coupling strength will also further decrease with increasing ion number, as it scales with the ion string mass $m \sim 1/m \propto \eta_i \eta_j$, see equation 3.78. An obvious way to solve this problem is to increase the laser intensity if more intensity is available⁵². Another approach is to encode the qubit in the two Zeeman sub-levels of the $S_{1/2}$ -state and to couple these states via a Raman transition⁵³ (between the two P-states). This has some very desirable advantages: first, due to the

⁵⁰At the beginning of every experimental sequence (cycle), a 729 nm ‘calibration pulse’ with a predefined length (few ms) is turned on during the Doppler-cooling sequence and, during this time, the intensity is sampled and stabilized by a PID-loop controlling the RF-power of the AOM. After the sampling time, the calibration pulse is turned off, and the stabilized RF-power value is held for the rest of the sequence. This is then repeated for every single experimental cycle.

⁵¹A larger trap, that is larger blade-to-ion distance, and cryogenic temperatures seem to help. Also replacing Macor with sapphire improves the heating rates. It is also reported in the literature that surface cleaning of the blades by an Argon ion beam can change the heating rate.

⁵²We have a new TiSa-laser system from MSquared which is able to produce > 4.5 W of 729 nm light, but it has yet to be stabilized to an ultra-high finesse cavity.

⁵³The MSquared TiSa has an additional external doubling cavity which can produce up to 2 W of 395 nm-light.

shorter wavelength (395 nm) the Lamb-Dicke parameter is almost doubled resulting in almost four times higher spin-spin coupling strength. Moreover, it is a two-photon process, thus gaining two momentum kicks for driving the motional sidebands yielding a doubling of the spin-spin coupling. Secondly, there exist so called ‘magic wavelengths’ where all induced ac-Stark shifts due to dipole-coupling are cancelled, making the third compensation light field obsolete. A third advantage is that the laser doesn’t have to be locked to an ultra-high finesse cavity simplifying the everyday operation significantly. However, there is no free lunch, and therefore one must pay also attention to possible obstacles. Despite lacking the necessity for an absolute frequency stabilization, the two light fields of the Raman beams have to be phase stable relative to each other. This is a non-trivial task, since the two light fields have to come in with different \vec{k} -vectors and hence the optical setup on the table has to be interferometrically stable. In addition, stray light of the high power UV-beams (395 nm) will eventually create charges on the trap blades and tips, resulting in additional electric field noise⁵⁴. As we will install Raman gates in the near future, these issues will be investigated and eventually solved.

In terms of experimental projects there is a wide-open range of interesting questions and here we hold an amazing physicist’s play ground for exploring and addressing many of these. There are too many possibilities to list them all, but to name just a few quantum phenomena of high current interest and fundamental relevance, we could investigate: transport [217, 218], thermalisation [219], many-body localization [220], entanglement growth [221] and dynamical phase transitions [222].

⁵⁴This could influence the heating rate, the micromotion and even the single-ion addressing as the additional field might push the ions away to a new position.

6. Measurement-based quantum computation

The fact that there is not a unique model of quantum computation, but many conceptually very different models, as mentioned in chapter 2, highlights the importance of investigating these models and their physical implementations and feasibilities. This chapter will introduce and focus on one specific model; the measurement-based computation approach (MBQC) implemented in ionic qubits. In contrast to the most well-known model — the quantum circuit model — in the MBQC approach a paradigm shift occurred in the sense that sequences of adaptive measurements drive the quantum computation, rather than sequences of quantum gates. There are two prominent examples of MBQC, the ‘teleportation-based approach’ [59, 61] and the ‘one-way quantum computer’ [29, 58]. While the former requires joint measurements, that is Bell-measurements to create entanglement, the latter consists only of single-qubit measurements on large entangled resource states, known as graph or cluster states¹. Nowadays, the ‘one-way quantum computer’ is the most studied MBQC-model, theoretically and experimentally, and it is often synonymously set with MBQC, as it will be throughout this text unless stated otherwise.

In the last decade, key elements of MBQC have been demonstrated in photonic systems [225–228], neutral atoms in optical lattices [229]² and trapped ions [30, 230].

This chapter will provide an introduction to the MBQC framework by first defining the resource states and then giving tutorial examples on the basic operation blocks, i.e. how single-qubit measurements can provide arbitrary single-qubit rotations and two-qubit entangling-gates (a universal set of logic gates with which any algorithm can be implemented). The experimental part will focus on the publication ‘*Measurement-Based Quantum Computation with Trapped Ions*’ [30], discussing its results and providing additional, experimentally relevant information.

6.1. Graph and cluster states

Graph and cluster states³ provide the main quantum resources in the MBQC-scheme [29, 56, 58]. These states find applications in quantum error correction (QEC) schemes as code words [231] and serve as a theoretical framework for studying multipartite entanglement [57, 232] and multipartite Bell inequalities [233, 234]. This section will introduce these states mathematically and their main properties will be discussed. However, the focus will be set upon an introduction and summary: for detailed derivations and extended discussions, the reader should refer to [235], whereas an extensive

¹There are other, less well-known, resource states such as the 2D Affleck-Kennedy-Lieb-Tasaki (AKLT) states [223, 224].

²With this system, only the generation of cluster states was shown, and not the basic operations of MBQC, due to a lack of single-atom control.

³Cluster states are a subclass of graph states, see paragraph 6.1.1. However, some authors make equivalent use of both terms.

tutorial introduction can be found in [236].

6.1.1. Definitions

First, the mathematical notion of graphs will be introduced. Second, this notion will be expanded onto physical qubits, and thus graph states will be defined. Two different, but equivalent descriptions of such states will be presented, in particular the *interaction pattern formalism* and *stabilizer formalism*. The former formalism is concerned with the generation of graph states and the latter is especially useful in the context of QEC, where graph states are proposed as code words. A final part introduces cluster states as a special instance of graph states.

Graphs Mathematically, graphs are a collection of vertices (V) and their connections, called edges (E) [237]. Each graph can be represented in a graphical diagram, where vertices are drawn as points in space and edges are arcs connecting these vertices (Fig. 6.1 a). In general, vertices can be ‘self-connected’ by an edge (loops) or vertices can be connected by multiple edges, however, these possibilities are discarded here. This pictorial visualization allows for the representation of many concepts concerning graphs in a clear way.

Formally, a *graph* is a pair

$$G = (V, E) \quad (6.1)$$

of a finite set $V = \{1 \dots N\}$ and a set $E \subset [V]^2$, the elements of which are subsets of V with two elements each [237]. Two vertices $a, b \in V$ connected by an edge, i.e. being the endpoints of an edge, are called *adjacent*. The relationship of which vertex is adjacent with another one is represented by an *adjacency matrix* Γ , where the elements of this symmetric $N \times N$ -matrix are given by

$$\Gamma_{ab} = \begin{cases} 1, & \text{if } \{a, b\} \in E \\ 0, & \text{otherwise} \end{cases} \quad (6.2)$$

An important concept is the *neighbourhood* of a given vertex $a \in V$. The neighbourhood $N_a \subset V$ is defined as the set of vertices b for which $\{a, b\} \in E$. This means the neighbourhood are all vertices adjacent to a given vertex. A vertex without a neighbourhood is called *isolated*.

If there exists a path $\{a, b\}$, i.e. an ordered list of vertices $a = a_1, a_2, \dots, a_{n-1}, a_n = b$, such that a_i and a_{i+1} are adjacent for all i , a graph is called *connected* and otherwise *disconnected*. The deletion of vertices $a' \in V'$ and all edges incident with a , where $V' \subset V$ is a subset of all vertices in the graph $G = (V, E)$, yields a new graph often denoted by $G - V'$. The same is true when edges are deleted.

Since there are $2^{\binom{N}{2}}$ different possible graphs for N vertices, the major goal in graph theory is to find relationships between these graphs and under which permutations they are *isomorphic*.

Graph states The physical, quantum mechanical implementation of graphs are graph states, which are pure states in a Hilbert space $\mathcal{H}_V = (\mathbb{C}^2)^{\otimes V}$. Here, each vertex is associated with a physical

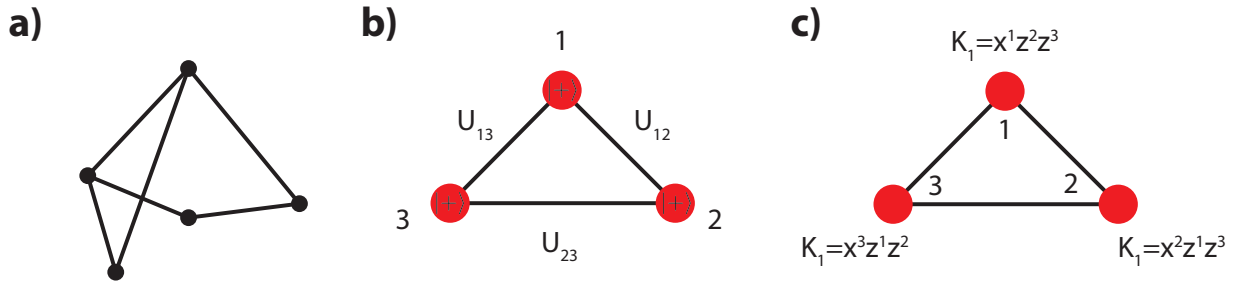


Figure 6.1.: **a)** An example of a simple graph $G = (V, E)$. The vertices $a \in V$ are represented by points in the plane and the arcs are called edges. **b)** A visual presentation of a graph state $|G\rangle$ shown in the interaction pattern formalism. The qubits are represented by vertices and the edges are controlled phase gates U_{ab}^{CZ} , see text. **c)** The same state as before, however shown in the stabilizer formalism. The correlation operators K_a uniquely define the graph state.

qubit in state

$$|\Psi\rangle = \frac{|0\rangle_z + |1\rangle_z}{\sqrt{2}} = |+\rangle_x =: |+\rangle \quad (6.3)$$

and each edge $\{a, b\} \in E$ represents an interaction between two adjacent vertices of the type

$$H_{ab} = \left(\frac{\mathbb{I}^a - \sigma_z^a}{2} \right) \otimes \left(\frac{\mathbb{I}^b - \sigma_z^b}{2} \right) = \frac{1}{4} (\mathbb{I}_{ab} - \sigma_z^a - \sigma_z^b + H_{ab}^I), \quad (6.4)$$

where σ_z^a is the z -Pauli operator acting on the Hilbert space of qubit a and H_{ab}^I is an Ising-type qubit-qubit interaction. The time evolution of 6.4⁴

$$U_{ab}(\varphi) = e^{-i\frac{\varphi}{4}} e^{i\frac{\varphi}{4}\sigma_z^a} e^{i\frac{\varphi}{4}\sigma_z^b} U_{ab}^I(\varphi) \quad (6.5)$$

periodically creates maximally entangled states at times $\varphi = \pi, 3\pi, \dots (2k+1)\pi$ with $k \in \mathbb{Z}$ when applied to the initial state of all qubits being in $|+\rangle$. In other words, the unitary transformation $U_{ab}(\pi) := U_{ab}^{CZ}$ is a controlled phase- or c-phase-gate (up to a global phase and single qubit rotations)

$$U_{ab}^{CZ} = \begin{pmatrix} 1 & 0 & 0 & 0 \\ 0 & 1 & 0 & 0 \\ 0 & 0 & 1 & 0 \\ 0 & 0 & 0 & -1 \end{pmatrix}. \quad (6.6)$$

Applying U_{ab}^{CZ} to the state $|\psi\rangle_{ab} = |+\rangle^a |+\rangle^b$ leads to $U_{ab}^{CZ} |\psi\rangle_{ab} = (|0\rangle^a |+\rangle^b + |1\rangle^a |-\rangle^b) / \sqrt{2}$, a maximally entangled *Bell state* (up to local unitary transformations).

A graph state is generated by preparing all qubits in a product state $|+\rangle^{\otimes V}$, an *empty graph*, and by applying the c-phase gate U_{ab}^{CZ} to all adjacent vertices in G . This formalism is also known as *interaction pattern* formalism.

In a mathematically more formal way, each graph $G = (V, E)$ corresponds to a graph state $|G\rangle$

⁴Note: All terms in Eq. 6.4 commute resulting in a straight forward time-evolution, where the order of terms does not matter.

with a pure state vector

$$|G\rangle = \prod_{\{a,b\} \in E} U_{ab}^{CZ} |+\rangle^{\otimes V}. \quad (6.7)$$

For many tasks in quantum information theory, such as in QEC, the *stabilizer* formalism is more convenient [238]. It is also a powerful tool box to develop the description of local unitary (LU) equivalence [235], that is the equivalence of two graph states $|G\rangle$ and $|G'\rangle$ up to local unitary transformation.

Given the Pauli group \mathcal{P}_N on N qubits, an N -fold tensor product of all Pauli operators including the phase factors⁵ ± 1 and $\pm i$, the stabilizer $S \subset \mathcal{P}_N$ is a commutative subset of \mathcal{P}_N which does not contain $\{-\mathbf{I}, \pm i\}$. An N -qubit stabilizer state $|\Psi_N\rangle$ is then defined as the $+1$ eigenstate of N independent operators S_n

$$S_n |\Psi_N\rangle = |\Psi_N\rangle. \quad (6.8)$$

As a consequence, any graph state can be uniquely defined by its stabilizers [235]. A graph state $|G\rangle$ is then the common eigenvector to the set of commuting observables:

$$K_a = \sigma_x^a \prod_{b \in N_a} \sigma_z^b = \sigma_x^a \prod_{b \in V} (\sigma_z^b)^{\Gamma_{ab}} \quad (6.9)$$

such that

$$K_a |G\rangle = +1 |G\rangle \quad (6.10)$$

for all $a \in V$, where N_a is the neighbourhood of a and Γ_{ab} is the adjacency matrix as defined above. The difference of the two definitions is depicted in figure 6.1 (b & c). In a less formal way, the interaction pattern formalism defines a graph state via the ‘recipe’ used to create such graph state, whereas the stabilizer formalism defines the same graph state via the created correlations between the qubits.

Cluster states Cluster states $|C\rangle$ are a special subset of graph states $|G\rangle$, with the limitation that the neighbourhood N_a and thus the adjacency matrix Γ_{ab} are not arbitrary [239]. Specifically, the vertices are laid out on a d -dimensional square lattice and only nearest-neighbours are adjacent, as shown in figure 6.2.

A rigorous mathematical definition goes as follows: let each lattice site be specified by a d -tuple of integers $\vec{r} \in \mathbb{Z}^d$, where each lattice site $l(\vec{r})$ has $2d$ neighbouring sites. A cluster $\mathcal{C} \subset \mathcal{A}$ is then defined as a subset of \mathcal{A} , where \mathcal{A} is the set specifying all occupied sites, such that any two sites $c, c' \in \mathcal{C}$ are connected (see 6.1.1) and any sites $c \in \mathcal{C}$ and $a \in \mathcal{A} \setminus \mathcal{C}$ are not connected.

Defining the cluster adjacency matrix $\Gamma_{\langle a,b \rangle}^d$, for $d = 2, 3$

$$\Gamma_{\langle a,b \rangle}^{(2)} = \begin{pmatrix} 1 & 0 \\ 0 & 1 \end{pmatrix} \quad \text{and} \quad \Gamma_{\langle a,b \rangle}^{(3)} = \begin{pmatrix} 1 & 0 & 0 \\ 0 & 1 & 0 \\ 0 & 0 & 1 \end{pmatrix} \quad (6.11)$$

⁵For example, the group \mathcal{P}_1 is given by $\mathcal{P}_1 = \pm \mathbf{I}, \pm i\mathbf{I}, \pm X, \pm iX, \pm Y, \pm iY, \pm Z, \pm iZ$.

it is possible to express the pure cluster state vector in the known form as

$$|C\rangle = \prod_{a,b \in \mathcal{C} | b-a \in \Gamma_{(a,b)}^d} U_{a,b} |+\rangle. \quad (6.12)$$

This is the formal (and complicated) way to express that all occupied lattice sites interact via a nearest-neighbour c-phase gate $U_{(a,b)}^{CZ}$. Figure 6.2 shows two examples of a $d = 2$ and $d = 3$ dimensional cluster state.

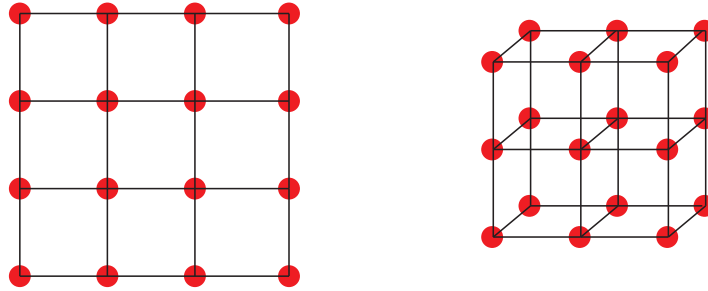


Figure 6.2.: An example of a two dimensional (left) and a three dimensional (right) cluster state. The vertices are laid-out on a d -dimensional square lattice and only nearest-neighbour vertices are adjacent.

An important finding in the MBQC-framework is that $2D$ -cluster states provide a class of universal resource states [240, 241], that is: any possible quantum state can be generated from a sufficiently large cluster state by local operations and classical communication (LOCC). With regards to quantum computation, any algorithm can be performed on a $2D$ -cluster state by performing single qubit measurements, as will be demonstrated in the following section. Furthermore, three dimensional cluster states have been theoretically proposed for fault-tolerant quantum computation [242, 243].

6.2. Computing via measurement and feedforward

The theory of measurement in quantum physics is a whole topic on its own. There are different kinds of quantum measurements including *projective measurements* (von-Neumann measurement), *positive operator-valued measurements* (POVM) [12], *weak measurements* [244] and even philosophical discussions on what measurements really are and how they disturb the measured state. However, for the purpose of this thesis, this section will solely focus on projective measurements and on the question of how such measurements can be applied to cluster states to carry out quantum computations. In MBQC, projective measurements and feedforward play the roles of logic gates in the circuit model, and in the following it will be shown how the MBQC and the gate model are equivalent.

Let's consider two qubits, one qubit being in an unknown state $|\Psi\rangle = \alpha|0\rangle + \beta|1\rangle$ and the other one in $|+\rangle = (|0\rangle + |1\rangle) / \sqrt{2}$. A controlled-phase gate (CZ) acting on these two qubits will generate an entangled pair of the form

$$\frac{1}{\sqrt{2}} (\alpha|0\rangle|+\rangle + \beta|1\rangle|-\rangle). \quad (6.13)$$

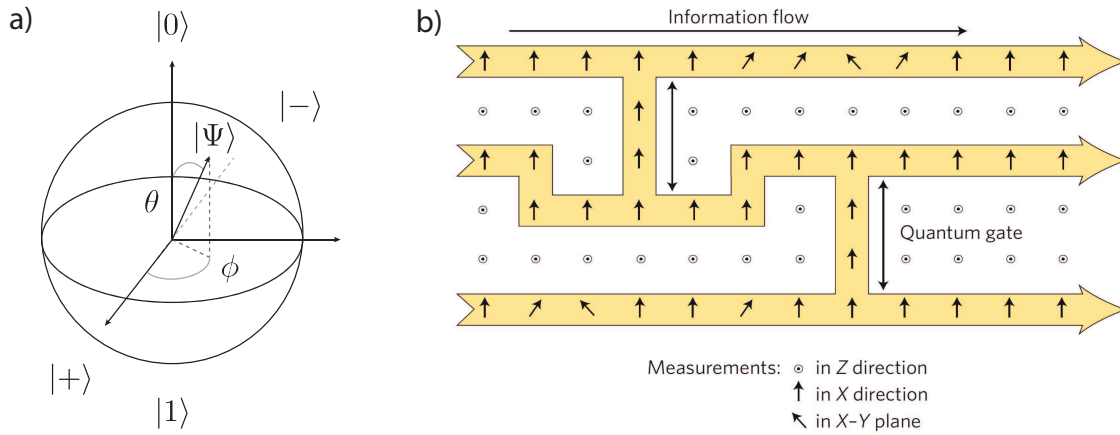


Figure 6.3: **a)** A qubit in the Bloch-sphere representation, where an arbitrary pure state $|\Psi\rangle$ can be described by the angles θ and ϕ . **b)** An illustration of a measurement pattern performing a quantum algorithm on a cluster state by single qubit measurements (reprinted from [29] ©APS, 2001). Since each measurement has a random outcome modifying the upcoming measurement bases, the information flows in a time-ordered fashion from left to right.

If we define $B(\phi)$ as the measurement basis with eigenvectors $\{|+\phi\rangle, |-\phi\rangle\}$ in the $x-y$ plane where

$$|\pm\phi\rangle = \frac{1}{\sqrt{2}} (|0\rangle \pm e^{i\phi} |1\rangle), \quad (6.14)$$

and ϕ is an angle as depicted in figure 6.3 a), then a projective measurement on the first qubit will give two outcomes for the second qubit depending on the measurement result of qubit one. The two outcomes for qubit two are

$$\begin{aligned} \alpha |+\rangle + e^{i\phi} \beta |-\rangle, & \quad \text{if } +1 \text{ eigenvalue} \\ \alpha |+\rangle - e^{i\phi} \beta |-\rangle, & \quad \text{if } -1 \text{ eigenvalue} \end{aligned} \quad (6.15)$$

depending on the measured eigenvalue. In either case, the initial state of qubit two has now been rotated by an unitary $U(\phi, \theta)$, where θ is a function of α and β . A more compact representation of the final state of qubit two is achieved by introducing a binary digit $m \in \{0, 1\}$, where $(-1)^m$ is the measurement outcome eigenvalue of qubit one. The final state of qubit two is then given by:

$$\sigma_x^m H U_z(\phi) |\Psi\rangle, \quad (6.16)$$

where σ_x^m is the Pauli matrix in x and H is a Hadamard operation.

The result above can be interpreted in a different way. The act of the measurement has transferred the unknown state $|\Psi\rangle$ of the first qubit to the second qubit - up to a unitary $U_z(\phi)$ rotation around the z -axis and a Hadamard transformation H (i.e. a Bell measurement), where the angle θ is set by the chosen measurement basis. In addition, a Pauli x -transformation is applied depending on the measurement outcome. This is a key feature of the MBQC approach. Since the measurement outcomes of qubit one are random, the unitary transformation of qubit two is non-deterministic. However, the two possible final states of qubit two only differ by a Pauli-operator. A feedforward of the measurement outcomes, as well as applying the Pauli-correction based upon the outcomes, al-

allows one to implement a deterministic, unitary operation⁶. These Pauli-operators are a by-product of the randomness of the quantum measurement and are therefore called *by-product operators* [29].

6.2.1. Arbitrary single qubit rotations

According to Euler's theorem of rotations, any arbitrary rotation $U(\vartheta)$ can be decomposed into a product of three successive rotations $U_z(\gamma)U_x(\beta)U_z(\alpha)$, involving rotations around only two different axes. Hence, extending the 2-qubit example above to a 4-qubit linear cluster, see figure 6.4 a), allows one to implement any desired single qubit rotation, up to additional Hadamards and random, but known (from the measurement outcomes), Pauli-operators.

In order to have a better understanding of these by-product operators from each measurement, let's have a closer look. We assign m_j to every binary outcome of the measurement of qubit j and, by using the identity $\sigma_x H = H \sigma_z$, an arbitrary unitary can be written as

$$U = H \sigma_z^{m_3} U_z(\phi_3) H \sigma_z^{m_2} U_z(\phi_2) H \sigma_z^{m_1} U_z(\phi_1), \quad (6.17)$$

where the unitary U is achieved by sequentially measuring qubits 1 to 3 in the measurement basis $\{|+\phi_j\rangle, |-\phi_j\rangle\}$, see equations 6.14 and 6.16. The unitary given in equation 6.17 is applied to the state encoded in the read-out qubit, in this case qubit 4 (of Fig. 6.4 a)), and can be rewritten into

$$U = \sigma_x^{m_3} \sigma_z^{m_2} \sigma_x^{m_1} H U_z \{(-1)^{m_2}(\phi_3)\} U_x \{(-1)^{m_1}(\phi_2)\} U_z(\phi_1) \quad (6.18)$$

by applying the following identities: $H \sigma_z H = \sigma_x$, $H U_z(\phi) H = U_x(\phi)$, $\sigma_x U_z(\phi) = U_z(-\phi) \sigma_x$ and $\sigma_z U_x(\phi) = U_x(-\phi) \sigma_z$.

In the same way as in section 6.2, the operation U is split into two parts: by-product operators and unitary transformations. These unitaries are non-deterministic and depend on the measurement outcome of the previous qubit. However, by measuring the qubits sequentially and adjusting the upcoming measurements bases by *feedforward*, such that $\phi_1 = \alpha$, $\phi_2 = (-1)^{m_1} \beta$ and $\phi_3 = (-1)^{m_2} \gamma$ the unitary U becomes deterministic. This requirement of sequential measurements defines a time-order and determines the direction of information-flow across the cluster state, as shown in figure 6.3 b). The remaining Pauli by-product operators don't need to be implemented physically, as they can always be taken into account in classical post-processing by reinterpreting the final result.

6.2.2. Two qubit gates and Clifford gates

In order to build a universal quantum computer, not only arbitrary single qubit rotations are needed, but also two-qubit entangling gates e.g. the controlled phase (CZ) gate. Within the MBQC framework, implementing the equivalence of a CZ-gate (in the circuit model) is straight forward as the edges between two vertices represent CZ-interactions. By measuring qubits 1 & 4 (Fig. 6.4 b), top) an equivalent circuit (Fig. 6.4 b), bottom) can be implemented where the quantum information is stored in qubits 2 & 3.

⁶Note in this simple example the Pauli-correction doesn't have to be implemented physically as the final state can be simply reinterpreted.

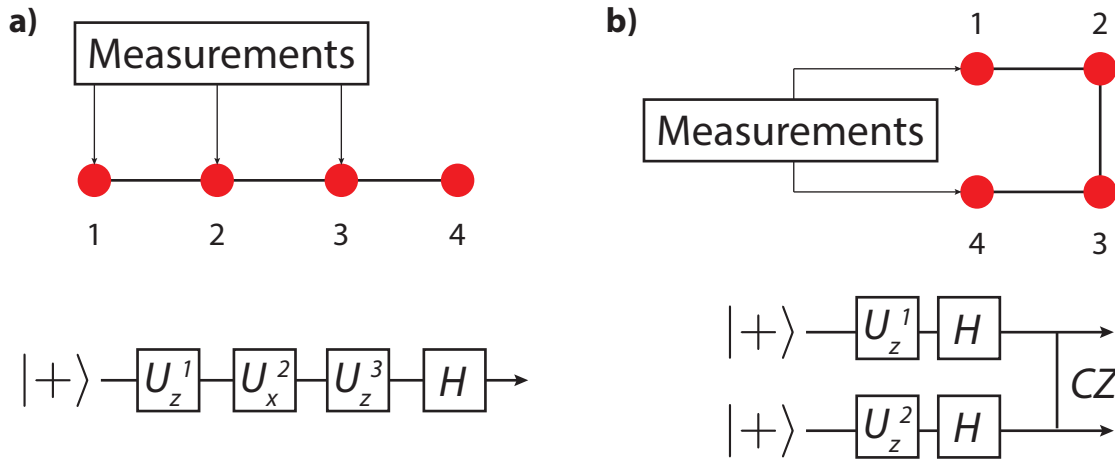


Figure 6.4.: a) Measuring the qubits of a linear cluster state from 1 to 3 sequentially and forwarding the measurement outcomes, allows for implementation of an arbitrary single qubit rotation with an additional Hadamard gate. The equivalent circuit is shown at the bottom. b) Measuring qubits 1 & 4 allows for implementing the equivalent circuit shown at the bottom, where the outcome is stored in qubits 2 & 3 (top).

The *Clifford group* is an important class of gates playing a crucial role in many quantum algorithms, error correction codes and entanglement purification protocols. The group itself is generated by the CZ-gate, the 1-qubit Hadamard-gate and the $U_z(\pi/4)$ -rotation. In the MBQC framework the Clifford group operations have a special meaning, since they can be solely achieved by implementing Pauli-measurements alone⁷. This means there is no need for feedforward, as only by-product operators are left, which can be taken into account in the reinterpretation of the final result⁸.

6.3. Experimental implementation of cluster and graph states

The first time cluster states have been experimentally generated in trapped ion systems is published in 'Measurement-Based Quantum Computation with Trapped Ions' [30] and is the core of this section. In contrast to photonic systems and neutral atoms in optical lattices, the creation of clusters with ions is conceptually quite different. Compared to clusters created with photons [225, 226], the cluster states in our work are generated deterministically instead of probabilistically, which is advantageous with regards to scalability. In the case of optical lattices, where cluster states can emerge quite naturally due to the nearest-neighbour interaction on a square optical lattice, ions in our experiment are trapped in a linear fashion and the entangling interaction between the ions is of infinite range (MS gate). Due to this fact, in our system a few important tricks, such as *refocussing* and *hiding*, are needed to implement a desired cluster state. These techniques will be explained with the help of two examples, specifically the *box cluster* and the *linear cluster*. The linear cluster is used to show arbitrary single qubit rotations and a two-qubit entangling gate, which both together form a universal set of gates for quantum computation. Fidelities of states produced by these gates are measured in the case of perfect feedforward, which is done by post-processing as explained later. In the last step, graph states of different sizes (3, 5 & 7) are used as code words

⁷Measurements in the eigenbases of the operators σ_x , σ_y and σ_z .

⁸Note that the Clifford group of gates is not universal for quantum computation.

for error correction, and their persistency is tested against different phase-flip error probabilities.

6.3.1. Box cluster

The box cluster is a unit-building-block for larger cluster states consisting of four qubits on a square lattice with only nearest neighbours being adjacent, see figure 6.5 a). Instead of generating the edges via CZ-gates, we generated the edges in our graph states via the MS-gate, see section 3.3.2. This gate corresponds to a $\sigma_x\sigma_x$ interaction, which is equivalent to the CZ-gate up to local transformations⁹. However, the way we implement the MS-gate, all pairs of ionic qubits interact with equal strength resulting in a fully connected graph state where all vertices are adjacent. This long range character of the MS-gate requires us to apply additional pulses to undo undesired interactions (i.e. remove certain edges). In order to understand this, let's start off with a chain of 4 qubits in the state $|0\rangle^{\otimes 4}$ and apply a full entangling MS-gate $U_{MS} = \exp\left(-i\frac{1}{4}\sum_{j,i}\sigma_x^i\sigma_x^j\right)$. The resulting state is a 4-qubit Green-Horn-Zeilinger state (GHZ):

$$|\text{GHZ-4}\rangle = \frac{1}{\sqrt{2}}\left(|0\rangle^{\otimes 4} + |1\rangle^{\otimes 4}\right) = \frac{1}{\sqrt{2}}(|0000\rangle + |1111\rangle). \quad (6.19)$$

In the graph framework, a GHZ state¹⁰ can be drawn as a fully connected graph¹¹, where each vertex is adjacent with each other, as shown in figure 6.5 b). The question is now, how to remove undesired edges or to prevent them from being generated in the first place. There are two strategies, one of them being the technique of refocussing and the other one is hiding.

The basic idea behind *refocussing* [245] is to split the entangling operations into pieces, and insert single qubit operations carefully between the pieces. This allows interactions between certain qubit pairs to be refocussed to the identity operation. The key feature is to use *half entangling* gates, that is

$$U_{MS/2} = \exp\left(-i\frac{1}{8}\sum_{j,i}\sigma_x^i\sigma_x^j\right). \quad (6.20)$$

Such a gate is set up in the very same way as a full entangling gate, with the only difference that the Rabi-frequency is set to

$$\Omega_{MS/2} = \frac{1}{\sqrt{2}}\frac{|\Delta_t|}{4\eta}, \quad (6.21)$$

which is a factor $1/\sqrt{2}$ smaller than for a full entangling gate, as described in section 3.3.2. Here, Δ_t is the laser detuning from the motional mode and η is the Lamb-Dicke parameter. A more figurative way of understanding a half entangling gate is to use the phase-space picture. While in the MS-interaction the wave-function closes a single loop with an area such that the picked up phase is enough to generate fully entangled states, in the MS/2-interaction the enclosed area is half the size, hence half the picked up phase.

⁹These local transformations do not play a role in the generation of cluster states, but they have to be dealt with when it comes to interpreting the single-qubit measurements as described in section 6.3.3.

¹⁰Up to local unitary transformations.

¹¹Note there is a locally equivalent graph state where a center vertex is adjacent to the 3 other vertices, however these 3 vertices are not adjacent with each other

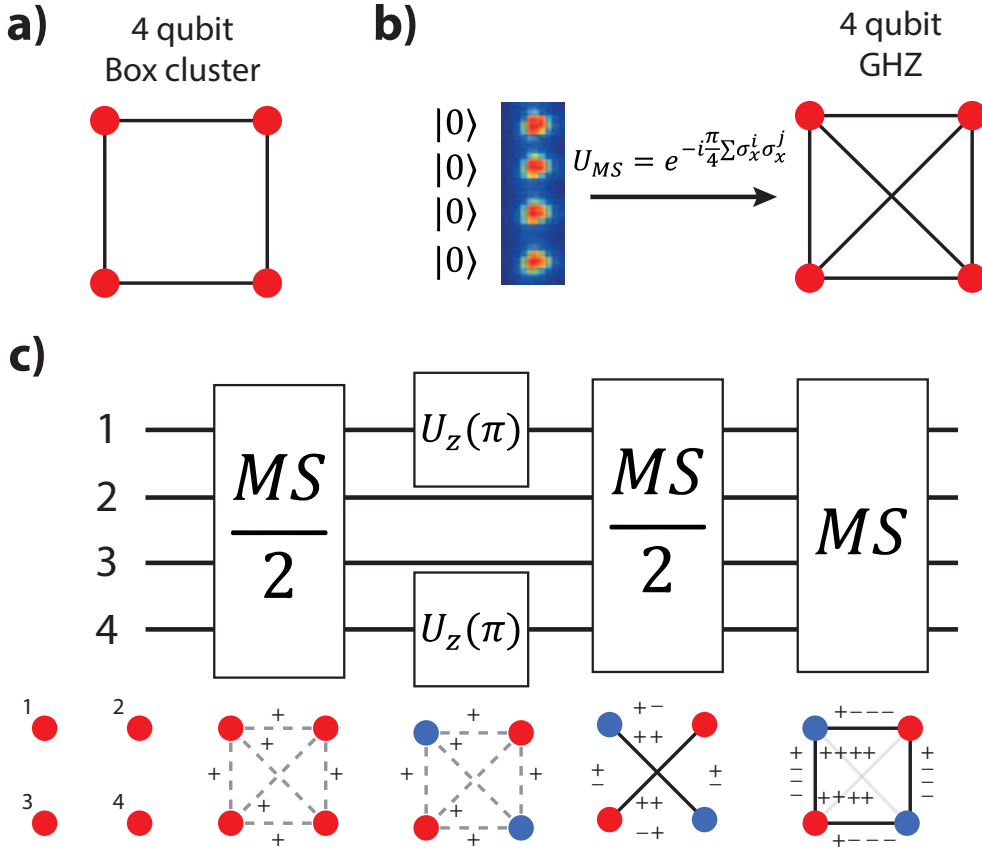


Figure 6.5: **a)** A four qubit box cluster state. The qubits (vertices) are depicted by red dots and the CZ-interactions (edges) are drawn as black lines. **b)** Starting from 4 qubits in the state $|0\rangle^{\otimes 4}$ and applying a full entangling MS-gate $U_{MS} = \exp\left(-i\frac{\pi}{4}\sum_{j,i}\sigma_x^i\sigma_x^j\right)$ leads to a four qubit GHZ-state, which is a fully connected graph. **c)** The pulse sequence to generate a box cluster (panel a)) is shown. At the bottom, each pulse is examined in the graph formalism: An $MS/2$ -gate applied on four qubits in $|0\rangle^{\otimes 4}$ will generate *half edges* between all vertices (red) depicted as grey dashed lines with a positive sign ‘+’ (the sign corresponds to the sign of the interaction used to generate the edge, i.e. $\pm\sigma_x^i\sigma_x^j$). Two single-qubit rotations $U_z(\pi)$ on qubit 1 & 4 add an additional π -phase to vertices 1 & 4 changing their color (blue). Every additional $MS/2$ will add a *half edge* according to the color rule of qubit pairs: Same colors ‘+’; different colors ‘-’. Two opposite ‘+-’ or ‘-+’ annihilate each other, i.e. first creating a *half edge* then removing it, $U(MS/2)U(-MS/2) = \mathbb{I}$. Two operations with the same signs, $U(MS/2)U(MS/2) = U(-MS/2)U(-MS/2) = U(MS)$, correspond to a full entangling gate which creates a *full edge*. The generation of two *full edges*, that is ‘+ + + +’ = ‘- - - -’ = $U(MS)^2 = \mathbb{I}$, is the identity operations (up to LU). Note the resulting experimental box cluster will be denoted as $|eBC\rangle$ and is equivalent to a box cluster generated by CZ gates up to local unitary transformations.

The pulse sequence that we used to generate a box cluster is given in figure 6.5 c) with a detailed explanation of every pulse and its action upon the quantum state given in the caption. Starting from an initial state with all qubits in $|0\rangle$ and applying an $MS/2$ -gate, $U(MS/2)$, will create *half edges* between all pairs of qubits. By using single qubit rotations (refocussing) on ions 1 & 4, these qubits are rotated around the z-axis by π , which corresponds to a unitary rotation $U_z(\pi)$. These refocussing pulses add an extra π -phase shift between qubits 1 & 2, 2 & 3, 3 & 4 and 1 & 4, which effectively reverses the entangling interaction of the second $U(MS/2)$ -pulse between those qubit pairs.

A useful interpretation is that the additional π -phase shift inverts the sign of the second $MS/2$ -

interaction, $U(-MS/2) = \exp\left(i\frac{1}{8}\sum_{j,i}\sigma_x^i\sigma_x^j\right) = U(-)$, which can be regarded as a time-inverted MS/2-interaction. From $U(\pm) = U(\mp)^\dagger$, it follows that $U(\pm)U(\mp) = U(\pm)U(\pm)^\dagger = \mathbb{I}$. In other words, $U(+)$ and $U(-)$ annihilate each other. When two MS/2-gates are applied with the same sign between two vertices, a full edge (black line) is generated, as in the case of a single MS-gate. By applying four times the MS/2-interaction on a pair of qubits, the qubits become disentangled again, which effectively removes an edge ($U(+)^4 = U(-)^4 = \mathbb{I}$, up to local unitary transformations). The final state is a box cluster, which is a building block of the 2D cluster state.

Experimental details In order to perform the experiment, 4 ions are trapped at $\omega_{\text{ax}} \approx 2\pi \times 1.22$ MHz and $\omega_{\text{rad}} \approx 2\pi \times 3.4$ MHz forming a linear Coulomb crystal. The ions are optically pumped into the $|S_{1/2}, m_j = 1/2\rangle = |1\rangle$ state and the 729 nm-laser frequency is set to drive the excited level $|D_{5/2}, m_j = 3/2\rangle = |0\rangle$. Following 3 ms of standard Doppler cooling, 4.5 ms of ground state cooling is applied to the axial COM and stretch mode. The MS-gate is set up on the axial COM with a detuning $\Delta_t \approx |10 \text{ kHz}|$, yielding a full $U(MS)$ gate time of $\tau_{MS} \approx 100$ ms. A detailed description on setting up MS-gates can be found in [98, Chapter 6]. However, there are two main differences: first, the Rabi-frequency is set to realise an MS/2 gate in 100 μs , this corresponds to $\Omega \approx 2 * \pi \times 35$ kHz in our experiment (see equation 6.21). Secondly, the ac-Stark shifts induced on the qubit transition by the laser beam are compensated by centerline detuning δ_c in contrast to bichromatic power imbalancing as given in [98, Section 6.1.2]. An advantage of centerline detuning is the ease of setting it up in the lab: as the detuning is scanned, one can directly monitor the excitation of the unwanted populations (odd number of excited qubits), thus allowing immediate feedback when minimising them via the centre-frequency detuning. For a description of ac-Stark shift compensation regarding MS-gates, see [98, Section 3.5.1]. The value used in the experiment for the given parameters is $\delta_c \approx +700$ Hz. However, the challenge with centerline detuning is to keep track of all relevant phases between the laser-pulses involved in creating and measuring the cluster state.

In order to verify the experimentally-generated state is indeed a box cluster, a full-state tomography¹² [12, 246] is performed and the state is reconstructed via the maximum-likelihood reconstruction method [247]. The real and imaginary parts of the reconstructed density matrices are shown in appendix figure D.1 and compared to the ideal matrices, yielding a fidelity of $\mathcal{F} = 0.847 \pm 0.008$. The errors given in this section are estimated by Monte Carlo simulations of projection noise around the experimentally estimated expectation values [211], for a detailed discussion on quantum projection noise due to a finite number of measurements see Section 7.2. These simulations produce a distribution of density matrices according to the projection noise, from which the error bars of the derived properties are estimated. The measured state has a purity $P(\rho) = 0.75 \pm 0.013$.

There is an important distinction to make between the experimentally generated box cluster state $|eBC\rangle$ and the theoretical box cluster $|BC\rangle$ according to the definition given in section 6.1. While $|BC\rangle$ is generated by CZ-gates acting on the input state $|+\rangle^{\otimes 4}$, here $|eBC\rangle$ is created with MS-gates acting on $|0\rangle^{\otimes 4}$. These two clusters, $|eBC\rangle$ and $|BC\rangle$, are locally equivalent as they can be transformed into each other by the local unitaries given in table 6.1.

¹²For 4 qubits, this corresponds to measuring in $3^4 = 81$ combinations of Pauli-basis, that is $\sigma_1^\alpha \sigma_2^\beta \sigma_3^\gamma \sigma_4^\delta$, where $\alpha, \beta, \gamma, \delta = x, y, z$. Here, we measured each basis 200 times to gain enough statistics.

Qubit 1	$H\sigma_x\sigma_z$
Qubit 2	$H\sigma_x$
Qubit 3	$H\sigma_x$
Qubit 4	$H\sigma_x\sigma_z$

Table 6.1.: These are the unitary transformations which have to be applied to each qubit in order to transform $|eBC\rangle$ into $|BC\rangle$.

6.3.2. Linear cluster

Even though the linear cluster might seem less complex than the box cluster, since there are less edges to be created, experimentally it is quite the opposite. As mentioned above, due to the long range interactions that we exploit to generate cluster states in ions, additional tricks need to be applied to prevent edges from being generated. In addition to refocussing, for linear cluster states (figure 6.4) *hiding* and *unhiding* [206, 248] pulses are employed. The key concept behind hiding/unhiding is to prevent certain qubits to interact with the laser field by ‘parking’ them into other Zeeman levels. Since the Zeeman states are several MHz (~ 7 MHz at ~ 4.11 Gauss) apart, hidden qubits do not interact resonantly with the MS-interaction¹³.

However, the hidden qubits are subject to light-shifts imprinting additional phases, which have to be taken care of. Luckily, in the pulse sequence which generates the cluster state (Fig. 6.6) these additional phases turn out to be global phases, since the qubits to be hidden and unhiddden are not in a superposed state but the ground state $|0\rangle$. The light-shift induced phase shifts can therefore be disregarded. The experimental generation of the 4-qubit linear cluster $|eLC\rangle$ is divided into two

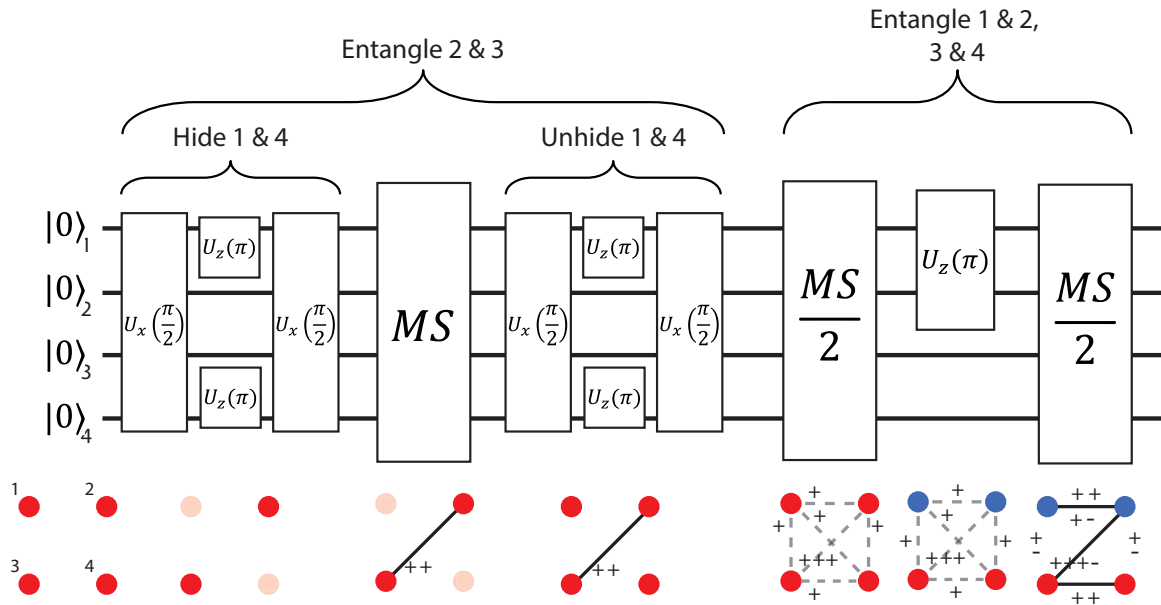


Figure 6.6.: The pulse sequence to generate a linear cluster consists of two parts. The first part entangles qubits 2 & 3 by hiding ions 1 & 4 and the second part uses refocussing to entangle ions 1 & 2 and 3 & 4.

parts. First, the qubits 1 & 4 are hidden in a different Zeeman level, $|D_{5/2}, m_j = 5/2\rangle$, such that the MS-gate acts only on qubits 2 & 3, creating a full edge between them. A short sequence of

¹³A detailed description of hiding/unhiding can be found in [98, Section 7.2 and A.2]. Details of our current single ion addressing are given in [119, Section 3.5].

pulses unhides ions 1 & 4 and brings them back into the computational subspace $|D_{5/2}, m_j = 3/2\rangle$. In the second part, refocussing is used to create entanglement between qubits 1 & 2 and 3 & 4. The resulting state is a linear cluster with a fidelity of $\mathcal{F} = 0.841 \pm 0.007$ and a purity of $P(\rho) = 0.816 \pm 0.012$. The fidelities of both states, the experimental box cluster $|eBC\rangle$ and the linear cluster $|eLC\rangle$, are well above the threshold of $\mathcal{F}_{\text{thres}} = 0.5$ to detect *genuine* multipartite entanglement [249].

The experimental linear cluster $|eLC\rangle$ can be transformed into the commonly defined linear cluster $|LC\rangle$ by applying the local transformations given in table 6.2.

Qubit 1	$H\sigma_z e^{-i\frac{\pi}{4}\sigma_x}$
Qubit 2	$H\sigma_x\sigma_x$
Qubit 3	$H\sigma_x$
Qubit 4	$H e^{-i\frac{\pi}{4}\sigma_x}$

Table 6.2.: In order to transform $|eLC\rangle$ into $|LC\rangle$, the unitary transformations given above have to be applied to each qubit.

6.3.3. Realization of MBQC with a 4-qubit linear cluster state

The linear cluster state can be used to implement both arbitrary single-qubit rotations and two-qubit gates (Fig. 6.4), i.e. a universal set of gates, by measuring specific qubits in the right order and feedforwarding their outcomes. However, experimental realizations of single-qubit measurements¹⁴ (in contrast to single-qubit readout) and fast feedforward are quite demanding techniques, and their experimental demonstrations have already been shown in trapped ion systems [250, 251]. Here, for the proof of principle experiment, a different approach is chosen. Instead of implementing active feedforward, the states are fully characterized by an over-complete set of measurements and the action of feedforward is simulated via post-processing, i.e. by reinterpreting certain expectation values. This method of post-processing can be interpreted as a perfect feedforward and gives an upper bound to achievable fidelities.

The first part of this section will give a detailed explanation of the data processing and, in the second part, the results based on the linear cluster will be presented and discussed.

Data processing In order to compare our experimental results with the general description of cluster states, i.e. by using the same language, the unitary transformations U_{LC} in table 6.2 are applied in order to reinterpret the measurement bases. For example: if the qubits 1 – 4 of $|LC\rangle$ were to be measured in $\sigma_z, \sigma_z, \sigma_x, \sigma_x$, respectively, this would correspond to measuring the qubits of $|eLC\rangle$ in the same order, but different bases $\sigma_y, \sigma_x, \sigma_z, \sigma_z$. (Note: from $|LC\rangle = U_{LC}|eLC\rangle$ follows $\hat{A}_{eLC} = U_{LC}^\dagger \hat{A}_{LC} U_{LC}$.) The unitary transformation, and thus reinterpretation of measurements, is the very first step in data processing. The next step is to simulate feedforward: there are two kinds of feedforward actions to be simulated.

The first kind of feedforward can be commuted all the way through a measurement-based protocol and acts only on the output state. These by-product operators depend on previous measurements, but they do not change the basis of succeeding measurements in the measurement-based protocol.

¹⁴Measuring a single qubit out of many without affecting the others

The two-qubit gate (and error correction, see section 6.3.4) demonstrated here requires only this kind of feedforward and the analysis procedure is the following: in a $(p+q)$ -qubit graph state, with q output qubits and p qubits which are involved in the measurement procedure of the MBQC, there are 2^p possible outcomes for a given measurement configuration of the p qubits. As a consequence there are 2^p output states of the q -qubits, which are all related by the by-product operators in the ideal case. We perform full state-tomography on all $p+q=4$ qubits and this allows us to fully characterise each of the 2^p different q -qubit output states. Specifically, we estimate the probabilities of observing all 2^q eigenstates of all 3^q observables built from combinations of products of Pauli operators and each probability is associated with an eigenstate. The by-product operators are then implemented by reassigning this association, that is changing the eigenstates. Finally, a single set of $2^q \times 3^q$ probabilities is established by summing up all 2^p instances (one for each output state), and the output density matrix is reconstructed via maximum-likelihood tomography.

The second kind of feedforward is that the measurement basis of subsequent measurements is changed. This type of feedforward is relevant for the single-qubit rotations demonstrated with the 4-qubit linear state. As described in section 6.2.1, an arbitrary single qubit rotation can be implemented by sequentially measuring the p -qubits 1-3 (Fig. 6.4 a)) and feedforwarding the measurement outcomes in order to adjust the succeeding measurement bases. The angles of rotations are defined as ϕ_1 , ϕ_2 and ϕ_3 , see equation 6.17. Measurements in the basis $B(\phi_1)$ project qubit 1 onto the state $|\pm\phi_1\rangle = \frac{1}{\sqrt{2}}(|0\rangle \pm e^{i\phi_1}|1\rangle)$. The measurement outcome determines the sign of the following measurement basis of qubits 2 and 3, i.e. $B(\pm\phi_2)$ and $B(\pm\phi_3)$. The final state is then stored in qubit 4 (q -qubit) to which the by-product operators are applied in the same way as for the first kind of feedforward. There are four possible measurement basis combinations, each with 2^3 possible outcomes (eigenvalues). We again perform a full state-tomography on all 4 qubits, which gives us an over-complete set of expectation values, required to characterise a one-qubit state, for all 4×2^3 outcomes. The by-product operators of each set are included as described in the first part of this section. This results in a single set of expectation values that is used to reconstruct the one-qubit output state (qubit 4). Examples of the reconstructed output states represented on the Bloch sphere are shown in figure 6.8. As an important note, this whole process is simplified by choosing ϕ_1 and ϕ_2 from the set $\{0, \pm\pi/2\}$, such that $B(\pm\phi_1)$ and $B(\pm\phi_2)$ are the same observables up to a global phase. In order to perform rotations with angles different than $\{0, \pm\pi/2\}$, additional measurements (other than the ones for full state-tomography) are taken in the appropriate basis.

Results Depending on the measurement order on a 4-qubit linear cluster, see figure 6.4, either a two-qubit gate (plus local unitaries) or arbitrary single qubit rotations can be implemented. When measuring the input qubits 1 & 4 (Fig. 6.7 a), output qubits 2 & 3 become either entangled or not, depending in which bases the former qubits are measured. If they are measured in the bases $B(\alpha)$ and $B(\beta)$ with $\alpha = \pi/2$ and $\beta = -\pi/2$, respectively, the output qubits become entangled. A reconstruction of the output state (Fig. 6.7 b)) allows quantifying the entanglement by the tangle τ [252], yielding a strong entanglement of $\tau = 0.59 \pm 0.05$. The fidelity with the theoretical state is measured to be $\mathcal{F} = 0.88 \pm 0.02$, where the errors are estimated by Monte Carlo simulations. On the other hand, if the input qubits are measured in $\alpha = 0$ and $\beta = 0$, the resulting state should be

a separable pure state. We observe $\tau = 0.02 \pm 0.01$ and a fidelity $\mathcal{F} = 0.83 \pm 0.01$ with the ideal state, see figure 6.7 c).

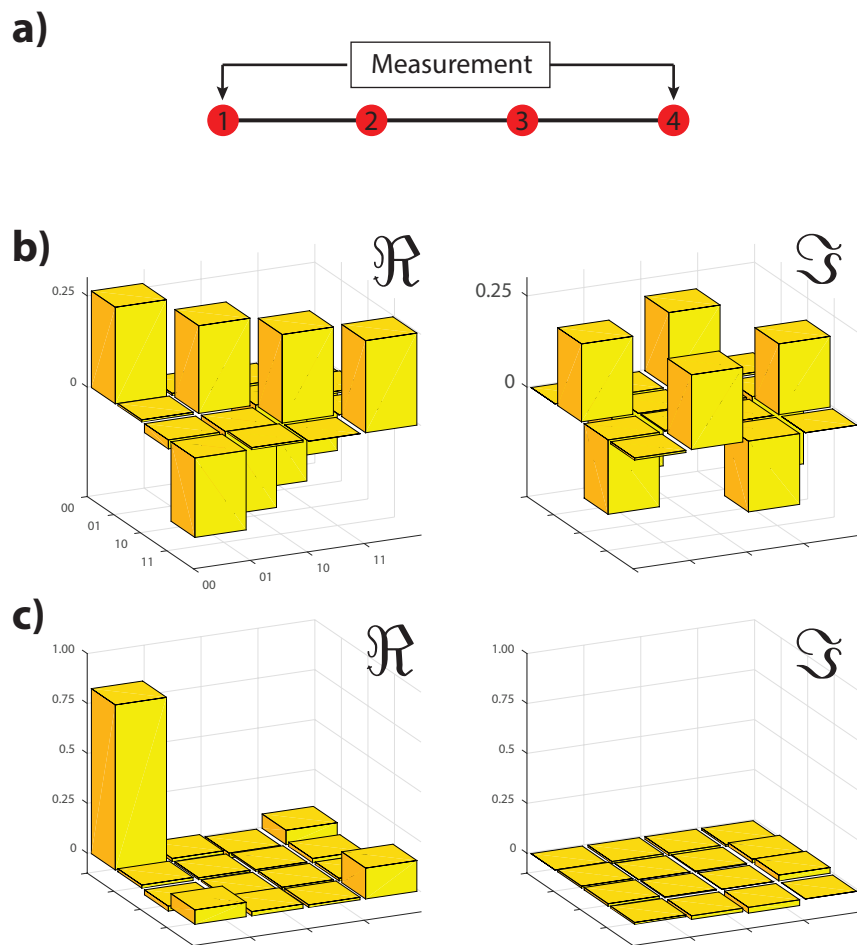


Figure 6.7.: a) Measurements of qubits 1 & 4 projects the qubits 2 & 3 into either an entangled state or a product state, depending on the measurement basis $B(\alpha)$ and $B(\beta)$ of 1 & 4. For $\alpha = \pi/2$ and $\beta = -\pi/2$ (b), the output state is entangled and for $\alpha = 0$ and $\beta = 0$ (c) it is separable. **b)** Reconstructed density matrix of the output state yielding a tangle of $\tau = 0.59 \pm 0.05$ and a fidelity with the ideal state $\mathcal{F} = 0.88 \pm 0.02$. **c)** Reconstructed density matrix of the output state yielding a tangle of $\tau = 0.02 \pm 0.01$ and a fidelity with the ideal state $\mathcal{F} = 0.83 \pm 0.01$.

Projecting the qubits 1, 2 & 3 into the bases, $B(\alpha)$, $B(\beta)$ and $B(\gamma)$, respectively, implements a rotation (plus Hadamard) on the fourth qubit. The measurements and feedforward actions are implemented as previously described for a variety of basis combinations (for details see figure caption 6.8), demonstrating a range of different single-qubit rotations of the encoded qubit. The final output state of qubit 4 is characterized by full-state tomography and maximum likelihood reconstruction, yielding an average fidelity over all implemented instances of $\mathcal{F} = 0.92 \pm 0.01$.

6.3.4. Error correction

Since qubits can't be completely decoupled from their environments in an experimental setup, they will always be subject to noise and decoherence. Similar to classical bits, where error correction is used to yield the accurate results, there is the quantum mechanical counterpart known as quantum

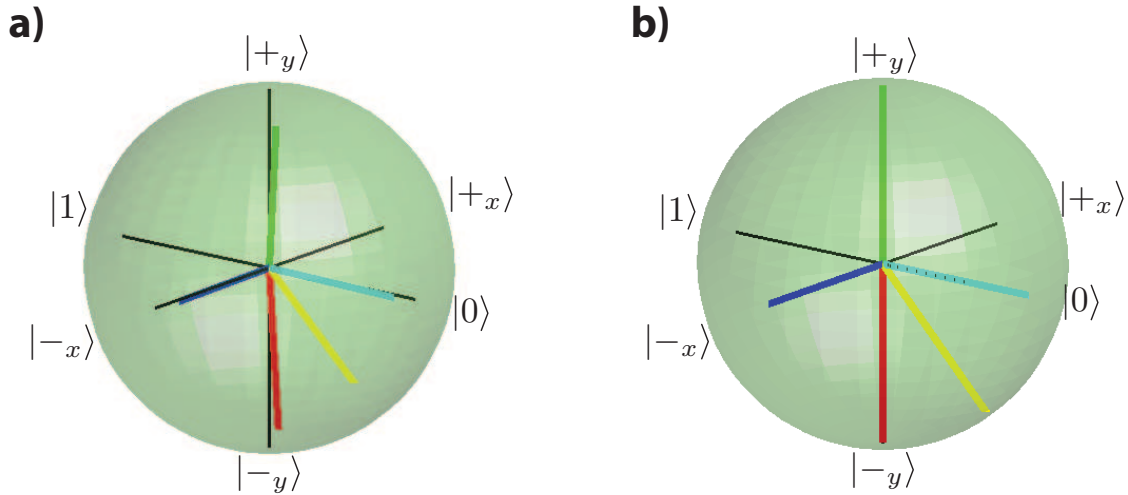


Figure 6.8.: Single qubit rotations $U_z(\alpha)U_x(\beta)U_z(\gamma)H$ implemented by measuring qubits 1, 2 & 3 in the bases $B(\alpha)$, $B(\beta)$ and $B(\gamma)$, respectively, showing the experimental output state **a)** and the ideal output state **b)**. The measurements are performed for different combinations of bases denoted by the color: **red** $\{\alpha, \beta, \gamma\} = \{\pi/2, 0, 0\}$, **green** $\{0, 0, -\pi/2\}$, **blue** $\{\pi/2, -\pi/2, 0\}$, **cyan** $\{\pi/2, 0, -\pi/2\}$ and **yellow** $\{\pi/4, 0, 0\}$.

error correction (QEC) [12, 238, 253–255]. The principals of QEC in the framework of the circuit model have been experimentally demonstrated in e.g. NMR [256, 257], trapped ions [18, 19, 258], linear optics [259] and solid-state qubits [260].

QEC has also been developed for the MBQC-model [231] by using graph states as code words¹⁵. Moreover, the MBQC framework allows a very compact way of implementation, since the operations for encoding/decoding and syndrome measurements only involve Clifford gates and Pauli measurements, see [261]. The general form of a graph state $|EC_n\rangle$ suited for *phase-flip error* correction consists of $(n+2)$ -qubits, where qubits A and B are read-in (encode) and read-out (decode) qubits, respectively, and the code word is made of n qubits denoted by C_n as shown in figure 6.9 a).

We generate such graph states by the first part of the laser pulse sequence given in Fig. 6.9 b). This creates the experimental state $|eEC_n\rangle$, which in turn is transformed into $|EC_n\rangle$ by applying the local unitaries given in table 6.3. Graph states $|eEC_n\rangle$ of increasing code word length $n = 1, 3, 5$ (corresponding to 3, 5 and 7 physical qubits) are implemented. For $n = 1, 3$, the fidelities are measured to be $\mathcal{F}_1 = 0.92 \pm 0.005$ and $\mathcal{F}_3 = 0.843 \pm 0.005$, respectively, see appendix D.3 and D.4¹⁶.

The experimentally generated states $|eEC_n\rangle$ are given by

$$2|eEC_n\rangle = \left(-i|-\rangle_A|0\rangle^{\otimes n} + |+\rangle_A|1\rangle^{\otimes n}\right)|-\rangle_B + \left(|-\rangle_A|1\rangle^{\otimes n} + i|+\rangle_A|0\rangle^{\otimes n}\right)|+\rangle_B \quad (6.22)$$

and can be transformed into $|EC_n\rangle$

$$2|EC_n\rangle = \left(|0\rangle_A|+\rangle^{\otimes n} + |1\rangle_A|-\rangle^{\otimes n}\right)|0\rangle_B + \left(|0\rangle_A|-\rangle^{\otimes n} + |1\rangle_A|+\rangle^{\otimes n}\right)|1\rangle_B \quad (6.23)$$

¹⁵In fact, graph states can also be used as code words in the circuit model.

¹⁶For $|eEC_5\rangle$ we did not measure full-state tomography as this would require to measure $3^7 = 2187$ different combination of Pauli-operators. This is not completely impossible, but experimentally inconvenient.

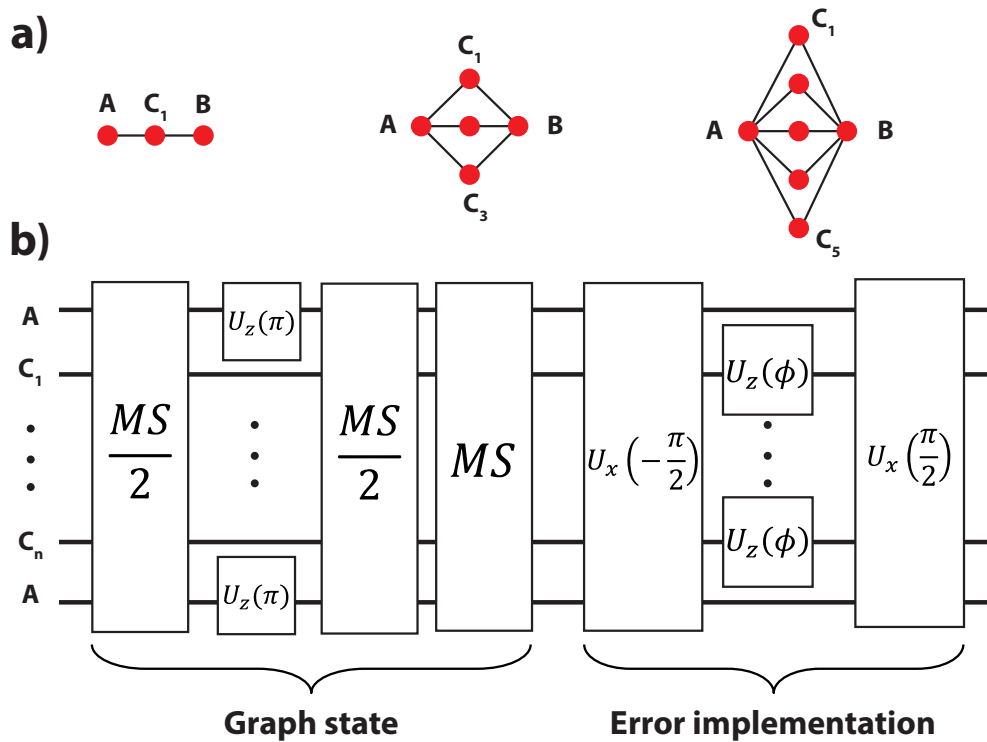


Figure 6.9.: a) Three different graph states suited for error correction (phase error) with increasing code word length C_n . An input state is encoded by measuring the read-in qubit A and decoded by qubit B . b) The experimental pulse sequence is divided into two parts. The first part is the generation of the error correction cluster states (see box cluster states 6.3.1). The second part implements a phase-flip error on qubits C_n (either on a subset or on all, see text) by single-qubit rotations $U_z(\phi/2) = \exp(-i\phi/2\sigma_z)$ with an error probability given by $p = \sin^2(\phi/2)$. The angle ϕ is determined by the Rabi-frequency and the pulse-length.

by the local unitary transformations given in table 6.3.

The state $|EC_n\rangle$ ¹⁷ is capable of correcting full phase-flips (σ_z) on up to $(n-1)/2$ code word qubits. Measurements of the code word qubits C_n in the σ_x -basis, where the temporal order is not relevant, yield 2^n outcomes each revealing an error syndrome. By applying the recovery operators to the output qubit B , an example for $n=3$ is given in table 6.4, restores the initial state encoded in qubit A . A very useful interpretation of the MBQC error correction is to think of teleporting a state from A to B through a noisy channel affecting the qubits C_n .

Qubit A	$H\sigma_z e^{-i\frac{\pi}{4}\sigma_x}$
Qubits C_n	H
Qubit B	$H\sigma_z e^{-i\frac{\pi}{4}\sigma_x}$

Table 6.3.: In order to transform $|eEC\rangle$ into $|EC\rangle$, the unitary transformations given above have to be applied to each qubit.

In our work, the persistency of these error correction codes is investigated against increasing (phase-flip) error probability and their performance is tested for increasing code word lengths. The experimental protocol is the following:

- 1) Preparation of a graph state $|eEC_n\rangle$.

¹⁷This state, $|EC_n\rangle$, is related to the stabilizer repetition code (with code words $|0_L\rangle = |000\rangle$ and $|1_L\rangle = |111\rangle$) [238].

Qubit C_1	+	+	+	+	-	-	-	-
Qubit C_2	+	+	-	-	+	+	-	-
Qubit C_3	+	-	+	-	+	-	+	-
Recovery operator	\mathbb{I}	\mathbb{I}	\mathbb{I}	σ_z	\mathbb{I}	σ_z	σ_z	σ_z

Table 6.4.: Recovery operators have to be applied on qubit B depending on the measurement outcomes on the code word qubits C_n . This here is an example for the $n = 3$ error correction graph state $|EC_3\rangle$.

2) A measurement of qubit A in the appropriate basis encodes a 1-qubit state $|\Psi\rangle$ into the graph state, or the orthogonal state, depending on the measurement outcome. The measurement basis for A is chosen such that the states to be encoded are the measurement eigenstates. We choose to encode the four eigenstates of the σ_x and σ_y Pauli-operators, since they are affected the most by phase-flip errors.

3) To implement phase-flip errors, a controlled unitary phase rotation $U_z(\frac{\phi}{2}) = \exp(-i\frac{\phi}{2}\sigma_z)$ is applied by means of single qubit addressing to all, or a subset of, C_n (see second part of the pulse sequence shown in figure 6.9 b)). The individual, incoherent error probability of each qubit C_n is given by $p = \sin^2(\frac{\phi}{2})$ and the angle ϕ is set by the laser pulse length and the Rabi-frequency.

4) Measuring the code word qubits C_n in the σ_x Pauli-basis simultaneously discretizes the error probability into a definite number of phase-flip errors.

5) Applying the recovery operators to B , which depend on the 2^n possible outcomes from step 4), restores the initially encoded state. These recovery operators, see table 6.4 for example, are implemented in post-processing.

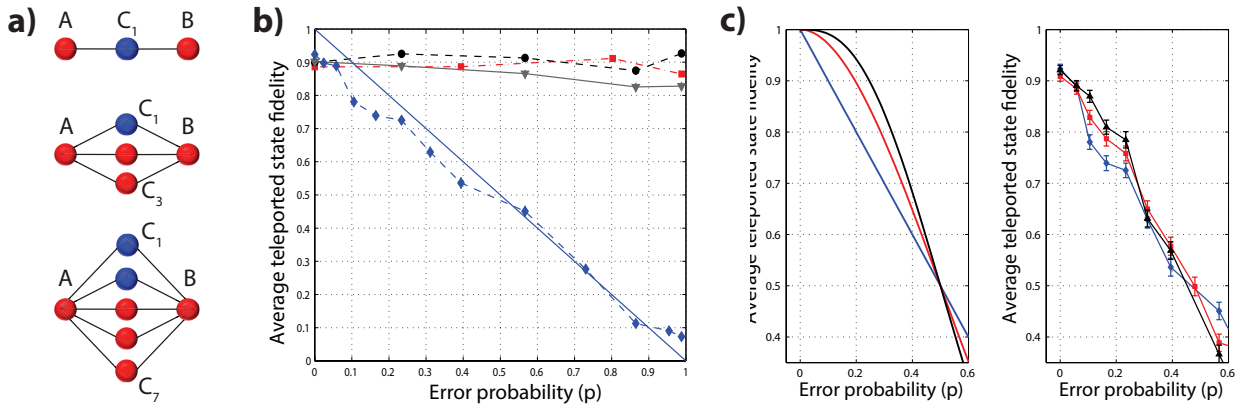


Figure 6.10.: a) Error correction graph states $|EC_n\rangle$ of increasing code word size $n = 1, 3, 5$ are tested against different phase-flip error probabilities on a subset of (b) or on all (c) qubits C_n (blue). b) Performance of error correction against increasing phase-flip error probability p on C_1 for $n = 1$ experimental data (blue diamonds) and ideal case (solid blue line); $n = 3$ (red); $n = 5$ (black). In the case of $|EC_5\rangle$ the phase flip error is also applied onto two qubits (grey). The error with probability p is induced by single qubit rotations $U_z(\phi/2)$, where the probability is proportional to the rotation angle $p = \sin^2(\phi/2)$. The persistency of the codes is quantified by the average teleportation fidelity (see text) and the initial drop in fidelity is due to imperfect state preparation. c) The phase flip rotation is applied to all qubits simultaneously with the same error probability p and the ideal case (left) is compared with experimental data (right) for $n = 1$ (blue), $n = 3$ (red) and $n = 5$ (black). Despite the higher experimental complexity in generating larger graph states, there is a region where quantum information is better protected by larger code word sizes.

In a first experiment, errors are applied to a subset of the code word qubits, see figure 6.10 a). We quantify the persistency, or quality, of the code by the average teleportation fidelity (ATF), i.e. how

well an input state at site A is recovered at site B after measuring the error syndrome and applying the recovery operators accordingly. The fidelities with the ideal encoded states in A , $|+\rangle$, $|-\rangle$, $|i+\rangle$ and $|i-\rangle$, are gained by state-tomography/maximum-likelihood reconstruction of the density matrix of B . The ATF is then the average fidelity over those four input states. As expected, the shortest code word $n = 1$ is not capable of protecting against errors, as the fidelity drops linearly with the error probability p (Fig. 6.10 b), blue). However, the longer code words $n = 3$ and $n = 5$ show no loss of fidelity as the error probability is increased even up to $p = 1$. Moreover, $|eEC_5\rangle$ is also tested against an error on 2 qubits simultaneously (grey), showing no significant reduction in fidelity and thus proving the persistency of this code against single and two-qubit phase-flips. The initial drop in fidelity at $p = 0$ is due to imperfect state generation which has several reasons, as discussed in section 6.4.

A more realistic scenario is that all code word qubits are subject to noise. This is modelled by introducing the same error probability on all qubits (equal phase-flip rotation applied to all) and measuring the ATF. Figure 6.10 c) shows the side-by-side comparison between the ideal case (left) and the experimental data (right) for different code word lengths $n = 1$ (blue), 3 (red) and 5 (black). In the ideal case, as n becomes larger, the error code tends towards perfect correction for the whole range up to $p < 0.5$. Quite outstandingly, there is a region of experimental states with larger n , where the input state is better protected against errors, despite the increasing complexity in generating these larger graph states in the lab. To our knowledge, this is the first experimental demonstration that quantum information can be better protected by larger code words even with increasing experimental overhead.

6.4. Conclusion

The measurement-based framework has led to new and conceptually different insights into quantum information theory and processing. From the theoretical side, new tools have been developed to understand quantum many-body correlations and entanglement, not to mention the theoretical horizon on how quantum information might be processed has been drastically extended. On the other hand, many experimental investigations were triggered showing proof-of-principal demonstrations, with one being presented in this thesis.

We present the deterministic generation of different cluster states with trapped ions, such as the box and the linear cluster. The linear cluster is also used to demonstrate the principal implementation of 1 and 2-qubit gates, that is a universal set of gates. The required feedforward operations are ‘simulated’ by post-processing the measured data. In addition, graph states are generated which are especially suited for error correction in the MBQC-framework. These error codes are tested against increasing error probability with impressive results: for the first time it could be shown that larger error codes are able to better protect quantum information against a certain type of error (phase-flip errors) despite the larger complexity in their experimental creation.

In order to exceed the proof-of-principal stage, further steps need to be taken. One of them is to implement active feedforward, as has already been shown in our group [250]. This would require additional hiding/unhiding — in order to measure single ionic qubits without affecting the

others in the crystal — fast data processing and decision logic, additional single qubit rotations and ‘recooling’ to the ground-state within the pulse sequence.

The main limitations in creating ideal states in our experiment are laser intensity fluctuations and fluctuating electric fields that lead to motional heating. Since the MS-gates are based on motional modes, such heating will introduce decoherence in the state generation. Nevertheless, the measured fidelities of all states implemented, including the error correction graph states, are quite outstanding. This has been achieved by constant improvement of the experimental setup by many people over the years. Despite the ongoing technological progress and the high gate fidelities, scaling up to large cluster states¹⁸ to perform arbitrary algorithms is out of reach in our current experimental setup for the moment (for a detailed discussion on limitations see Chapter 8). The complexity of pulse-sequences to generate large clusters is steadily increasing and, in addition to that, there are experimental challenges with long ion chains ($N > 20$) in our setup, see Chapter 8.

Here, other systems might be more suitable, such as neutral atoms in optical lattices, where the naturally present interactions might allow implementation of huge 2D and even 3D cluster states. However, the lack of proper single qubit controllability confronts the optical lattice approach with technological challenges. In contrast, systems based on photons suffer far less decoherence and single qubit measurements are easier to achieve (although feedforward has to be ultrafast on the time-scale of ns) but the key disadvantage is the heralded entanglement generation. This leads to an exponential overhead as the cluster state size is increased, which is less dramatic for trapped ion systems.

As is often the case in the science of quantum information, there is not ‘the’ perfect system (yet) for quantum computations, moreover, there isn’t even ‘the-one-and-only’ way of quantum computing, leaving the scientific endeavour with an open end full of excitement.

¹⁸Large is a very vague statement, however depending on the algorithm, and if error correction is included or not, estimates range from $N = 10^3$ to $N = 10^7$ qubits for a ‘useful’ computation [262–264, and many others]. For MBQC I could not find such an estimate on the ‘useful’ size of the cluster-state, but there is a procedure to translate gate-based algorithms into the language of MBQC [265].

7. Generation of quantum discord via noise

In quantum information theory, *quantum discord* is known as a measure of *non-classical* correlations between two systems and it is often also referred as the *quantumness* of correlations.

Triggered from the theoretical observation that certain highly mixed states, even without ‘much entanglement’ can be used for quantum information processing [33], H. Olliver and W.H. Zurek [31], and independently L. Henderson and V. Vedral [32], introduced the notion of quantum discord as a measure for quantum correlations beyond entanglement in early 2000. Over the past decade, significant progress has been made in understanding quantum discord, with focus on its characterization and application. In fact, it was soon realized that discord carries properties identifiable as a resource for quantum computation [34, 266]. Moreover, quantum correlations also play a crucial role at the quantum phase transition in models of spin chains [267, 268] and many other quantum-many body effects, as discussed in chapter 5. In the last few years a vast amount of theoretical studies on the topic of discord has been published, in the year 2015 alone, over 200 articles related to the topic are found based on a ‘web of science’-search, showing the importance in understanding quantum discord as a principal concept in quantum mechanics similar to entanglement.

On the experimental side, improved control of quantum systems in the laboratory has allowed the creation and observation of discordant quantum states in photonic systems [269–271, to name a few] and trapped ion systems [230, 272]. At the core of this chapter is our publication ‘*Experimental Generation of Quantum Discord via Noisy Processes*’ [230]. Here, we generate different discordant states via two methods, amplitude damping and correlated dephasing. These states are analysed and quantified by the measure discord D and the correlation rank R . In this chapter, experimental methods, data analysis and results will be presented and discussed in detail.

7.1. Theoretical framework

In order to understand the findings published [230], quantum discord shall be introduced to the reader via its most common definition: the difference between two definitions of mutual information. Furthermore, important properties of discord will be presented and the concept of correlation ranks will be introduced. A detailed review on quantum discord can be found in [48]. Since the main focus is to generate discord by noisy a process, the second part will focus on the theoretical description of non-unitary quantum operations and noise, such as amplitude damping, dephasing and depolarization.

7.1.1. Quantum discord

In *classical* information theory [273, 274], the *mutual information* $\mathcal{I}(A : B)$, which quantifies the correlation between two random variables of systems \mathcal{A} and \mathcal{B} , is given by

$$\mathcal{I}(A : B) = H(A) + H(B) - H(A, B), \quad (7.1)$$

where $H(A)$ is the Shannon entropy $H(A) = -\sum_a p_a \log p_a$ with probability p_a to find that a is the realisation of the random variable A (same holds for B). The joint entropy of A and B is defined as $H(A, B) = -\sum_{a,b} p_{a,b} \log p_{a,b}$, where $p_{a,b}$ is the joint probability to find a and b being realized by A and B , respectively. By applying Bayes' rule of conditional probabilities, equation 7.1 can be re-expressed as

$$\mathcal{J}(A : B) = H(A) - H(A|B), \quad (7.2)$$

where $H(A|B) = -\sum_{a|b} p_{a|b} \log p_{a|b}$ is the conditional Shannon entropy and $p_{a|b}$ is the conditional probability to find a given that b is the realisation of B . Classical correlations between systems \mathcal{A} and \mathcal{B} can be interpreted as an information gain about system \mathcal{A} by measuring system \mathcal{B} (and vice versa). Classically, the two expressions of mutual information, Eq. 7.1 & Eq. 7.2, are strictly equivalent. However, in quantum mechanical systems, where the Shannon entropy is exchanged with the von Neumann entropy, the expressions 7.1 and 7.2 are generally not equivalent, since measuring a quantum system disturbs the quantum states. This discrepancy leads to the definition of the *quantum discord* [31, 32].

Definition The following paragraph follows the discussion of [48, 275]. Consider a composite quantum system $\mathcal{H}_{AB} = \mathcal{H}_A \otimes \mathcal{H}_B$, with dimension d_A and d_B of each subsystem and $d_{AB} = d_A d_B$ of the composite system. The mutual information (7.1) is then expressed as

$$\mathcal{I}(\rho) = H(\rho_A) + H(\rho_B) - H(\rho_{AB}), \quad (7.3)$$

where $H(\rho_i) = -\text{Tr}(\rho_i \log \rho_i)$ is the von Neumann entropy, ρ_{AB} is the density matrix of the composite system and $\rho_A = \text{Tr}_B(\rho)$ ($\rho_B = \text{Tr}_A(\rho)$) is the reduced density matrix obtained by the partial trace Tr_B (Tr_A) over the basis of system B (A). The quantum analogon of the conditional entropy is $H(\rho_{A|B})$, where

$$\rho_{A|k} = \text{Tr}_B(E_k \otimes \mathbb{I}_B \rho) / \text{Tr}(E_k \otimes \mathbb{I}_B \rho) \quad (7.4)$$

is the state of A conditioned on outcome k in B , and $\{E_k\}$ represents the set of positive operator valued measure elements [275]. An optimization over all possible measurements in B leads to a re-expression of Eq. 7.5 into

$$\mathcal{J}_B(\rho) = H(\rho_A) - \min_{\{E_k\}} \sum_k p_k H(\rho_{A|k}) \quad (7.5)$$

In general, $\mathcal{I}(\rho)$ and $\mathcal{J}_B(\rho)$ are not equal and the discrepancy between these two mutual informations defines the quantum discord as

$$D_B(\rho) := \mathcal{I}(\rho) - \mathcal{J}_B(\rho) \quad (7.6)$$

and equivalently for $D_A(\rho)$. Here, the label $D_A(\rho) = D_A$ ($D_B(\rho) = D_B$) denotes the discord when considering measurements on system A (B).

The optimization process in equation 7.2 might be heavy in terms of numerical calculations and other measures for discord have been found which are better suited for certain instances (for an extended review see [48] and references therein).

Properties The most important properties of quantum discord can be summarized to:

- $\mathbf{D}_A(\rho) \neq \mathbf{D}_B(\rho)$ Discord is in general non-symmetric due to the asymmetry of the conditional entropy $H(\rho_{A|B})$. However, one can find cases with $\mathbf{D}_A(\rho) = \mathbf{D}_B(\rho)$.
- $\mathbf{D}_A(\rho) \geq 0$ Discord is a strictly positive measure, which is a consequence of the concavity of conditional entropy ¹ [48, 276].
- $\mathbf{D}_A(\rho) = \mathbf{D}_B(\rho) = 0$ Discord vanishes only for *completely* classically correlated states. Consequently, any entangled state has non-zero discord [277].
- $\mathbf{D}_A(\rho) = \mathbf{D}_A(\mathbf{U}\rho\mathbf{U}^\dagger)$ Discord is invariant under local unitary transformations $U = U_A \otimes U_B$.
- $\mathbf{D}_A(\rho) \leq \mathbf{H}(\rho_A)$ Discord has an upper bound.

A quantum state ρ_{AB} consisting of two subsystems A and B has zero discord $D_A(\rho_{AB}) = 0$ if and only if there is a von Neumann measurement $\{\Pi_k^A = |\Psi_k^A\rangle\langle\Psi_k^A|\}$ such that [40]

$$\sum_k \left(\Pi_k^A \otimes \mathbb{I}_B \right) \rho_{AB} \left(\Pi_k^A \otimes \mathbb{I}_A \right) = \rho_{AB}, \quad (7.7)$$

where $\{|\Psi_k^A\rangle\}$ is an arbitrary set of orthonormal basis, such that $\langle\Psi_k^A|\Psi_l^A\rangle = \delta_{kl}$. The statement above can be re-expressed as

$$\rho_{AB} = \sum_k p_k |\Psi_k^A\rangle\langle\Psi_k^A| \otimes \rho_k^B, \quad (7.8)$$

where ρ_k^B are the states of B occurring with probability p_k , $\sum_k p_k = 1$. Any quantum state which can be written in the form given in Eq. 7.8 has zero discord. As an example of such a state is the state prepared in the amplitude damping process (see section 7.2) and it is given by

$$\rho_{AB} = \frac{1}{2} \left({}_A\langle+| \otimes {}_B\langle+| \otimes {}_B\langle+| + {}_A\langle-| \otimes {}_B\langle-| \otimes {}_B\langle-| \right) \quad (7.9)$$

¹For a density matrix $\rho = \lambda_1\rho_1 + \lambda_2\rho_2$, where $\lambda_1, \lambda_2 \geq 0$ and $\lambda_1 + \lambda_2 = 1$, concavity states that the inequality $S(\rho) \geq \lambda_1 S(\rho_1) + \lambda_2 S(\rho_2)$ holds [276].

Contrariwise, one can find discordant² states which are *mixed* and *separable*³, as long as there is no such set of orthonormal bases $\{|\Psi_k^A\rangle\}$. An example of a mixed, separable state with no entanglement but with non-vanishing discord⁴ is given by

$$\begin{aligned} \rho_{AB} = \frac{1}{4} & \left({}_A\langle 0| \langle 0|_A \otimes {}_B\langle +| \langle +|_B + {}_A\langle 1| \langle 1|_A \otimes {}_B\langle -| \langle -|_B \right. \\ & \left. + {}_A\langle +| \langle +|_A \otimes {}_B\langle 1| \langle 1|_B + {}_A\langle -| \langle -|_A \otimes {}_B\langle 0| \langle 0|_B \right). \end{aligned} \quad (7.10)$$

Correlation matrix rank The measure of quantum discord given in equation 7.6 does not necessarily determine the amount of quantum correlation but rather the *quantumness* of these correlations [278]. There are different kinds of discordant states with various amounts of ‘usefulness’ in terms of a resource for quantum information processing. By studying the necessary and sufficient conditions under which quantum states have zero discord, the authors of [275] introduced a new measure based on the rank R of the correlation matrix M (of a quantum state). It turns out, quantum discord is a necessary but not sufficient condition to show that correlations are non-classical, which becomes clear in the analysis of R [278]. The correlation rank can be used to study and quantify discordant states with respect to quantum information protocols, such as quantum state transmission [279].

Consider a set of local Hermitian operators $\{A_n\}$ and $\{B_m\}$ with $n = 1, \dots, d_A^2$ and $m = 1, \dots, d_B^2$. (For a two-qubit system $d_A = d_B = 2$ and $\{A_n\} = \{B_m\} = \{\mathbb{I}, \sigma_x, \sigma_y, \sigma_z\}$). A quantum state ρ_{AB} can be decomposed into

$$\rho_{AB} = \sum_{nm} r_{nm} A_n \otimes B_m, \quad (7.11)$$

where the coefficients r_{nm} define a $d_A^2 \times d_B^2$ matrix M , also known as the correlation matrix. One can find the singular value decomposition (SVD) of M , that is $UMW^T = \text{diag}[c_1, c_2, \dots]$, where U and W are orthogonal, unitary matrices with dimensions $d_A^2 \times d_B^2$. The SVD defines a new set of local bases $S_n = \sum_{n'} U_{nn'} A_{n'}$ and $F_m = \sum_{m'} W_{mm'} B_{m'}$, such that the state ρ_{AB} can be rewritten in the new bases

$$\rho_{AB} = \sum_n^R c_n S_n \otimes F_n. \quad (7.12)$$

Here, R is the rank of the correlation matrix M defined as the number of non-zero eigenvalues c_n . In other words R determines the minimum number of bipartite product operators needed to represent ρ_{AB} , which allows us to gain information regarding the total amount of correlations [278].

Some of the most important properties of R are:

- $\mathbf{R}_{\max} \leq \mathbf{d}_{\min}^2$ The maximal achievable rank is bound by $d_{\min}^2 = \min\{d_A^2, d_B^2\}$. In the case of two-qubit states $R_{\max} = 4$, since $d_A = d_B = 2$.
- $\mathbf{R} = 1$ A completely uncorrelated state.
- $\mathbf{R} = 2$ A state containing classical correlations, may or may not contain discord.

²States containing discord.

³Consequently, such states have zero entanglement, as they are separable.

⁴This state has discord $D_A(\rho) = D_B(\rho) = 0.311$ but no entanglement, i.e. concurrence $C(\rho) = 0$. Its purity is $P(\rho) = 0.375$.

- $\mathbf{R} > 2$ A non-zero discordant state.
- $\mathbf{R} \geq 3$ A state which can be used for QI transmission protocols of pure and mixed states, similar to teleportation [280].

7.1.2. Quantum operations and noise

Any physical system has some coupling to its environment and thus is prone to random fluctuations, i.e. noise introduced by the environment. Such noise typically leads to loss of information encoded into the physical system (or a quantum system), where the information is irretrievably dissipated into the environment. A common description of these non-unitary quantum operations is given by the *operator-sum* representation [12]

$$\rho_{\text{out}} = \varepsilon(\rho_{\text{in}}) = \sum_i E_i \rho_{\text{in}} E_i^\dagger, \quad (7.13)$$

where a *quantum operation* ε acts on an input state ρ_{in} yielding the final state ρ_{out} . The operators $\{E_i\}$ are known as the *operation elements* of ε or *Kraus operators*. Even though the operator-sum representation is not unique in the sense that the same process can be decomposed into different sets of operators $\{E_i\}$, a unique description can be derived from the χ_{ij} -matrix [281] of a quantum process for a fixed set of orthogonal operators, e.g. the Pauli-operators. However, equation 7.13 is sufficient for the purpose of this chapter.

A prominent example of a non-unitary quantum operation is *amplitude damping* describing the information loss due to energy dissipation. Consider a qubit in a superposition state $|\psi\rangle = \alpha|0\rangle + \beta|1\rangle$, where $|0\rangle$ is the ground state of a two-level system and $|1\rangle$ is a meta-stable state, such as in optical atomic qubits. The excited state will eventually decay due to spontaneous emission and the final state will be mapped to $|0\rangle$, such that all information about α and β is eventually lost. The action of amplitude damping can be described by a map $\varepsilon_{ad}(\rho_{\text{in}})$ with two *Kraus*-operators

$$E_0 = \begin{bmatrix} 1 & 0 \\ 0 & \sqrt{1-p} \end{bmatrix} \quad E_1 = \begin{bmatrix} 0 & \sqrt{p} \\ 0 & 0 \end{bmatrix} \quad (7.14)$$

where the damping parameter p is related to the decay rate of the excited state. A visual representation of this process on a single qubit is given in figure 7.1 a).

Another important process is *phase damping* describing random phase-fluctuations, for instance caused by an external noisy B -field coupling to a qubit with a magnetic-field sensitive energy gap between its ground and excited state. Consider such a qubit, e.g. an ion qubit, being in a superposition state $|\psi\rangle = \alpha|0\rangle + \beta|1\rangle$. Any fluctuating B -field induces rotations $R_z(\theta) = \exp(-\frac{\theta}{2}\sigma_z)$ with random angle θ . For markovian noise processes it is reasonable to model these random *phase kicks* with a Gaussian distribution around a mean value 0 and a variance λ . The output state is then given by

$$\varepsilon_{pd}(\rho_{\text{in}}) = \frac{1}{\sqrt{2\pi\lambda}} \int_{-\infty}^{\infty} R_z(\theta) \rho_{\text{in}} R_z^\dagger(\theta) e^{-\theta^2/2\lambda} d\theta = \begin{bmatrix} |\alpha|^2 & \alpha\beta^* e^{-\lambda/2} \\ \alpha^*\beta e^{-\lambda/2} & |\beta|^2 \end{bmatrix}. \quad (7.15)$$

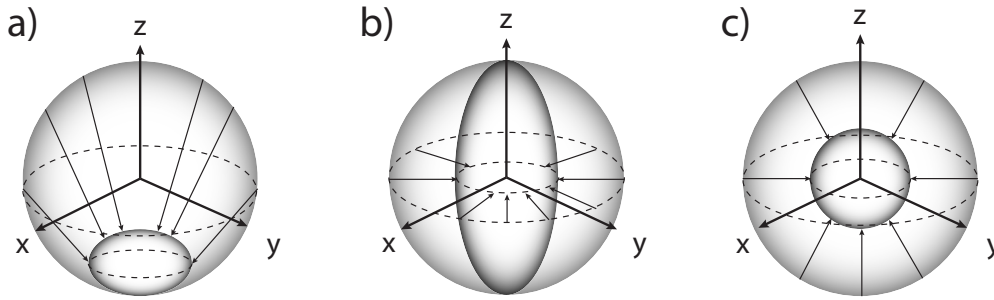


Figure 7.1.: The different quantum operations illustrated on the Bloch-sphere for a single qubit. **a)** Amplitude damping describes the spontaneous decay of an excited state used to encode quantum information. The Bloch sphere contracts towards the ground-state. **b)** Dephasing describes, for instance, magnetic field fluctuations (in our ionic qubit), where the phase information is lost. The Bloch sphere narrows towards the z -axis. **c)** Depolarization is interpreted as exchanging a pure state with some probability by a complete mixture. The Bloch sphere contracts towards the center.

The random phase kicks will cause the off-diagonal elements in the density matrix to decay exponentially with λ . Due to the non-uniqueness of the operator-sum representations, an equivalent description of phase damping [12] is given by the Kraus operators

$$E_0 = \sqrt{p} \begin{bmatrix} 1 & 0 \\ 0 & 1 \end{bmatrix} \quad E_1 = \sqrt{1-p} \begin{bmatrix} 1 & 0 \\ 0 & -1 \end{bmatrix} \quad (7.16)$$

which is also known as the *phase flip channel* with probability p . The action of phase damping on a single qubit is shown in figure 7.1 b). With respect to generating discord via correlated dephasing, it is useful to extend equation 7.15 to N qubits and an arbitrary *dephasing axis* \vec{n}

$$\varepsilon_{cpd}^{\vec{n}}(\rho_{in}) = \frac{1}{\sqrt{2\pi}} \int_0^{2\pi} K_{\vec{n}}(\theta) \rho_{in} K_{\vec{n}}^\dagger(\theta) d\theta. \quad (7.17)$$

For correlated noise, the rotations $K_{\vec{n}}(\theta)$ are simple tensor products of $R_{\vec{n}}(\theta)^{\otimes N} = [\exp(-i\theta\vec{n} \cdot \vec{\sigma}/2)]^{\otimes N}$ acting on all qubits equally, where \vec{n} is the normalized dephasing axis vector and $\vec{\sigma} = (\sigma_x, \sigma_y, \sigma_z)$. Note that the integral in Eq. 7.17 goes from 0 to 2π , describing the effect of *complete dephasing*; for an extended derivation see E.2.1 and [282]. An analytical analysis regarding more general conditions, e.g. considering time-dependent dynamic and arbitrary noise distributions, can be found in [283].

For the sake of completeness, *depolarizing* shall be mentioned, as shown in figure 7.1 c). It is a homogenous ‘shrinking’ of the Bloch sphere towards a completely mixed state $\mathbb{I}/2$. Depolarizing can be expressed as

$$\varepsilon_{dpol}(\rho_{in}) = p \frac{\mathbb{I}}{2} + (1-p)\rho_{in}. \quad (7.18)$$

By substituting $\mathbb{I}/2 = \frac{\rho + \sigma_x \rho \sigma_x + \sigma_y \rho \sigma_y + \sigma_z \rho \sigma_z}{4}$, equation 7.18 can be rewritten in the operator-sum form

$$\varepsilon_{dpol}(\rho) = \left(1 - \frac{3p}{4}\right) \rho + \frac{p}{4} (\sigma_x \rho \sigma_x + \sigma_y \rho \sigma_y + \sigma_z \rho \sigma_z), \quad (7.19)$$

where p denotes the error probability.

7.2. Discord via local damping

As the first part of the studies presented in our paper [230], we investigated how local quantum operations [284, 285], in this case amplitude damping of one qubit out of two, can generate discord between them. Starting from a classically correlated, separable two-qubit mixed state ρ_1 , one of the qubits is exposed to controlled amplitude damping induced by a sequence of coherent pulses and optical pumping. The discord is then quantified by state-tomography and maximum-likelihood reconstruction for a variety of amplitude damping probabilities. This section here is divided into 3 parts: state preparation, discussion of measurement results and effects of quantum projection noise due to a finite number of measurements.

State preparation Intuitively, one might guess that preparing classically correlated states should be much easier than preparing states which carry entanglement or any other kinds quantum correlation. However, rather surprisingly the opposite is the case in our experimental setup, where classical correlations are generated by first establishing quantum correlations and then removing the *quantumness* by irreversibly deleting the phase information between both qubits.

In order to prepare the desired initial state ρ_1

$$\rho_1 = \frac{1}{2} \left(|+_A \rangle \langle +_A| \otimes |+_B \rangle \langle +_B| + |-_A \rangle \langle -_A| \otimes |-_B \rangle \langle -_B| \right) \quad (7.20)$$

two ions are trapped at $\omega_{\text{ax}} = 1.22$ MHz and $\omega_{\text{rad}} \approx 3.5$ MHz and the qubit states $|0\rangle$ and $|1\rangle$ are encoded into $|S_{1/2}, m_j = 1/2\rangle$ and $|D_{5/2}, m_j = 3/2\rangle$, respectively (Fig. 7.2 a)). After optically pumping into the ground state $|0\rangle$, Doppler cooling and side-band cooling to the motional ground-state of the axial COM mode and the axial stretch mode, a full-entangling MS-gate on the COM-mode with $\Delta_t = 20$ kHz and $\tau_{MS} = 50$ μs creates a Bell pair $(|00\rangle - i|11\rangle) / \sqrt{2}$. A series of additional coherent, global 729 nm-pulses create a superposition of the two *ancilla*-levels $(|dd\rangle - i|aa\rangle) / \sqrt{2}$, see figure 7.2 a). By coupling the $|d\rangle$ -state to the short-lived $P_{3/2}$ -state with the help of an 854 nm laser pulse, the $|d\rangle$ -state can only spontaneously decay into $|0\rangle$, due to selection rules. This creates a mixed state $(|aa\rangle \langle aa| + |00\rangle \langle 00|) / \sqrt{2}$. Finally, a π -pulse on the $|a\rangle \leftrightarrow |1\rangle$ -transition followed by a $\pi/2$ -pulse on the $|0\rangle \leftrightarrow |1\rangle$ -transition prepares the desired state ρ_1 .

The procedure for implementing a controlled amplitude damping with probability p is the following. Using single-ion addressing, a fraction of the population $|1\rangle$ of qubit B is transferred to $|a\rangle$, this allows us to precisely control p by adjusting the pulse-length. Next, a 397 nm laser pulse with circular polarization incoherently transfers all the population from $|a\rangle$ to $|0\rangle$. This implements amplitude damping of qubit B , by the fraction of the component of its excited state that was transferred to the ancillary state. The total experimental time is roughly 500 μs , of which 460 μs correspond to preparing the state ρ_1 and the remaining time is used for the amplitude damping process. In order to check the influence of the 397 nm optical pumping on the remaining superposition of the qubit states $|1\rangle$ and $|0\rangle$, Ramsey experiments were performed showing no significant effect.

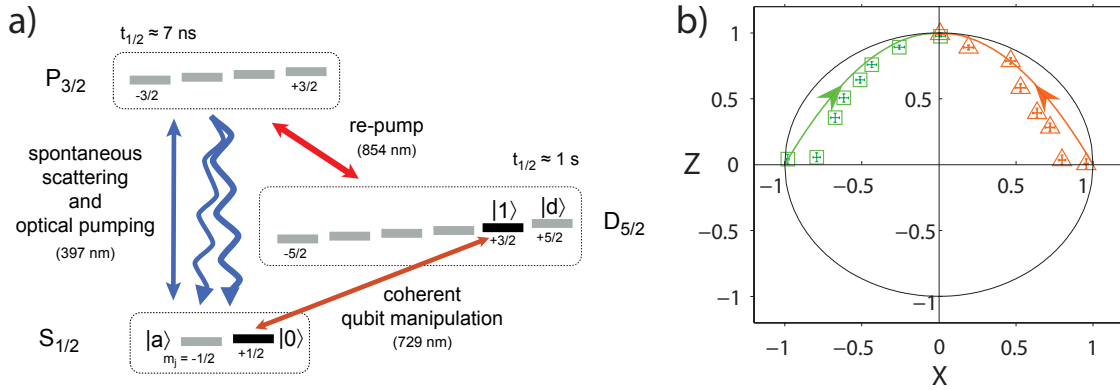


Figure 7.2: a) The relevant Zeeman levels used in order to prepare the classically correlated state ρ_1 by a sequence of coherent 729 nm-pulses and spontaneous decay with the help of 854 nm-light. The amplitude damping is implemented by means of 397 nm optical pumping from $|a\rangle$ to $|0\rangle$, for a detailed description see text. b) The ideal trajectories of τ_B^+ (orange line) and τ_B^- (green line) in the $X - Z$ plane of the Bloch sphere for different amplitude damping probabilities. Experimental results (symbols) are derived from reconstructed density matrices after tracing out qubit A .

During the amplitude damping process, the state ρ_1 undergoes a mapping

$$\varepsilon_{ad}(\rho_1) = \frac{1}{2} \left({}_A \langle + | \otimes \tau_B^+ + {}_A \langle - | \otimes \tau_B^- \right), \quad (7.21)$$

where $\tau_B^\pm = \varepsilon_{ab} ({}_B \langle \pm | \otimes | \pm \rangle)$ are the amplitude damped (with probability p) density matrices of qubit B . Due to the damping, τ_B^\pm become non-orthogonal and, as such, less distinguishable as they move towards $|0\rangle$, see figure 7.2 b). Consequently, there is no von Neumann measurement on qubit B , such that $\varepsilon_{ad}(\rho_1)$ is unaffected (see Eq. 7.7) and the discord D_B is non-zero.

Results After measuring two-qubit state-tomographies (at least $n = 1000$ measurements per basis⁵, the effect of projection noise is going to be discussed in the following paragraph) for a wide range of p , the experimental density matrix is reconstructed via the maximum-likelihood (MLH) method [211]. The quantum discord is then derived from the reconstructed density matrix via numerical optimization over all possible single qubit measurements, see Eq. 7.5 and [31, 269].

In figure 7.3 a) the amplitude damping results are presented for increasing damping probability p . The quantum discord D_B shows a statistically significant increase before it drops almost to zero for a completely amplitude damped quantum system. On the other hand, D_A is expected to be exactly zero throughout the process and the data show that it remains constant and zero within error bars. Due to the strict positivity $D \geq 0$, any noise, such as quantum projection noise can lead to a non-vanishing discord, as discussed in the upcoming paragraph. All the measured states are separable, containing less than 0.001 tangle [252].

In order to estimate the error bars, Monte Carlo simulations (MCS) of projection noise (around the measured expectation values) are performed. The MCSs produce a distribution of noisy density matrices, from which we can calculate quantities of interest. If the values of a certain quantity derived from the noisy matrices follow a Gaussian distribution, it is a sensible approach to present

⁵There are $3^2 = 9$ bases to be measured for a 2-qubit state.

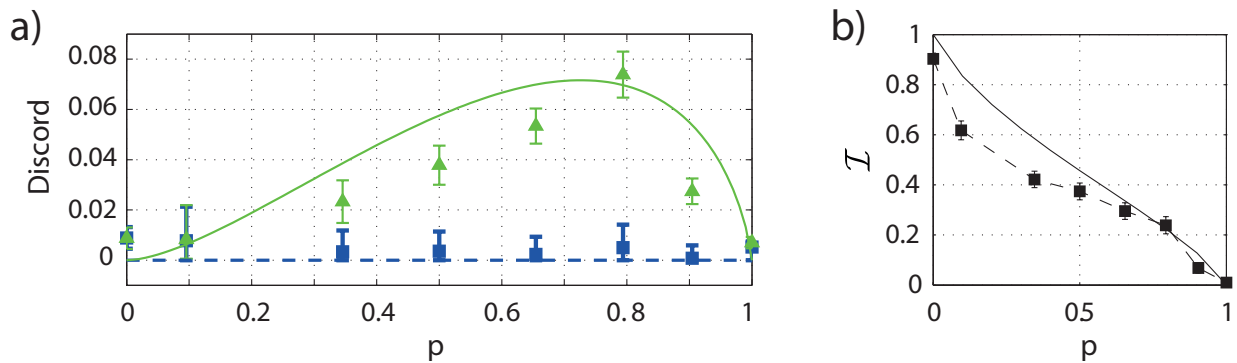


Figure 7.3.: **a)** The results of the amplitude damped $\varepsilon_{ad}(\rho_1)$ for different damping probabilities p (see text for details). The discord D_B (green) is compared between theory (solid line) and data (triangles), as well as discord D_A (blue) between theory (dashed line) and data (squares). The experimental discord is quantified from the experimentally reconstructed density matrices by using the definition of discord given in Eq. 7.5 & 7.6. **b)** The total correlation \mathcal{I} (Eq. 7.3) calculated for the ideal case (line) and extracted from the experimental data (squares).

the mean value with one standard deviation as the error bar of the given quantity. However, it is not guaranteed that the distribution is [35, and references therein], especially if the quantity of interest is close to a lower or upper boundary, leading to a skewed distribution. Since quantum discord has a lower boundary $D \geq 0$ and the derived values for D are close to it, we perform the MCS analysis in a slightly different way. Instead of presenting the mean value, we present the median of the MCS distribution as the estimate for the desired property. The upper (lower) error bar is then defined as a point in the distribution, where the cumulative probability between the median and this point is equal to 0.341. In this way, if the distribution becomes Gaussian, the median will be equal to the mean and the error bars become symmetric and equivalent to one standard deviation.

Even though the qubits A and B become more and more quantum correlated throughout the one-qubit amplitude damping process, the mutual information \mathcal{I} , see Eq. 7.3, shows that the total amount of correlations is not increased by local quantum operations. In fact, the mutual information \mathcal{I} decreases with higher amplitude damping probability, see figure 7.3 b). The correct interpretation is that the generation of quantum correlations, i.e. discord, is coming directly at the expense (reduction) of classical correlations. During the process, the classical correlations in the initial state are converted to quantum correlations. However, the loss of classical correlations is higher than the gain in quantum correlations, resulting in a reduction of \mathcal{I} . As a consequence, if the initial state is completely uncorrelated, then $D_A = D_B = 0$ for all p .

These findings are supported by analysing the correlation rank derived from the experimentally reconstructed density matrix, as shown in figure 7.4. The ideal initial state ρ_1 (Eq. 7.20) has a correlation rank $R = 2$ and the correlation rank can not be increased throughout the process of amplitude damping. Moreover, for total damping $p = 1$, the correlation rank is decreased to $R = 1$ yielding a completely uncorrelated state $\varepsilon_{ac}(\rho_1)$. Our results show that local quantum operations can generate discord at the expense of the total amount of correlations. Indeed, there is only a very restricted class of discordant states, which are achievable via local operations, and the measure of

this set is zero in the total set⁶ [278].

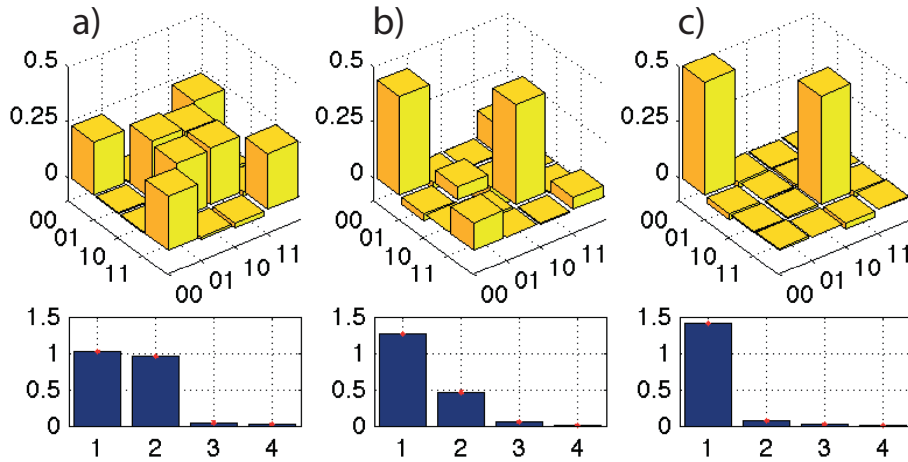


Figure 7.4.: Reprinted from our paper [230]. The reconstructed density matrices of $\varepsilon_{ad}(\rho_1)$ (upper part) and the singular values of the corresponding correlation matrix (lower part) are shown for various amplitude damping probabilities **a)** $p = 0.00$, **b)** $p = 0.79$, and **c)** $p = 1.00$. The rank R corresponds to the number of non-zero values and the error bars (red ‘dot’) are derived from MCS, see text. The fidelities of all experimental states are greater than 0.98.

Effects of quantum projection noise The set of non-discordant two-qubit states is of zero measure in the total set of all possible states [286, 287]. In other words, there is an ‘infinitely larger’ amount of states containing discord than without it. Consequently, any white noise, for instance quantum projection noise (QPN), is likely to generate discordant states in the reconstruction process. The question here to be asked is “can the deviation from $D_A = 0$ truly be due to QPN, or are state preparation/measurement infidelities and maybe other unknown noise sources to blame?”

In quantum mechanics, an observable has to be measured an infinite number of times to find its expectation value exactly. This is obviously impractical and experimentally we estimate the expectation value after a finite number n of measurements on (repeatedly made) copies of the state. Finding n_i instances of a measurement outcome i , a probability $p_i = n_i/n$ is assigned. A von Neumann quantum measurement is like a coin-flip between the two eigenvalues and follows a binomial distribution - to each probability p_i an uncertainty is assigned by one standard deviation $\sqrt{p_i(1-p_i)/n}$.

The effects of QPN are quantified by Monte Carlo simulations of the ideal state ρ_1 (Eq. 7.20), which has zero discord ($D_A = D_B = 0$), zero tangle and a correlation rank $R = 2$ (correlation matrix singular values are $[CM1, CM2, CM3, CM4] = [1, 1, 0, 0]$). The distribution width of each observable⁷ is set by n . In this way 70 ‘noisy’ copies of the density matrix are produced (using Matlab) and the values of interest are calculated for each copy leading to a distribution of these values. Figure 7.5 shows the mean value and one standard deviation for discord, tangle and the singular values as a function of n . Even for a perfectly separable, non-discordant state ρ_1 ,

⁶Less formally, this means that there is an ‘infinitely larger’ number of discordant states, which can not be generated by local operations.

⁷ 3^2 combinations of Pauli-measurements, i.e. $\sigma_1^\alpha \sigma_2^\alpha$ with $\alpha = x, y, z$, are used in the maximum-likelihood reconstruction.

QPN (via the MLH-reconstruction) will ‘generate’ significant amounts of discord and tangle in the reconstructed state (Fig. 7.5 a)). The simulation shows that at least $n = 1000$ measurements are required to yield zero discord and tangle within one standard deviation. A similar observation is made regarding the singular values of the correlation matrix (Fig. 7.5 b) - c)). However, these seem to be even more sensitive resulting in a full rank $R = 4$ state beyond one standard deviation even after $n = 1000$.

These simulations imply that our observed results presented in figure 7.3 are consistent with the effects of a finite number of measurements.

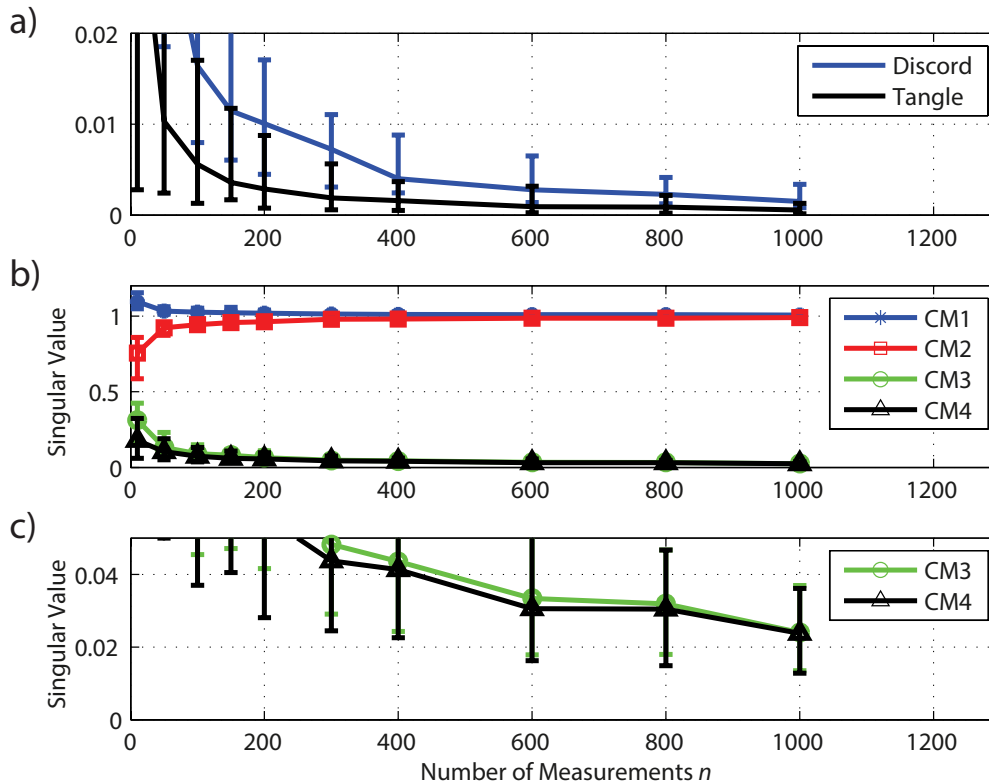


Figure 7.5.: Reprinted from our paper [230] **a)** Monte Carlo simulations of tangle and discord as function of measurements n showing the effects of quantum projection noise, by sampling over 70 ‘noisy’ copies of the density matrix. Ideally, tangle and discord are zero for ρ_1 . **b)** Monte Carlo simulations of the singular values of ρ_1 . Without projection noise, the ideal singular values are $[CM1, CM2, CM3, CM4] = [1, 1, 0, 0]$. **c)** A close-up of b).

7.3. Discord via correlated noise

As a second part of the studies presented in [230] we investigated the effects of *correlated noise* with regards to discord and especially the correlation matrix rank R . The type of noise channel used here is correlated dephasing, which can be modelled by equation 7.17. Since the qubit is encoded into Zeeman-levels (Fig. 7.2 a) any B-field fluctuations will cause dephasing in the z -basis, i.e. $\vec{n} \cdot \vec{\sigma} = \vec{e}_z \cdot \vec{\sigma} = \sigma_z$, with an angle θ proportional to the B-field strength. Due to the close proximity of two ions ($\approx 5 \mu\text{m}$ at $\omega_{\text{ax}} = 1.2 \text{ MHz}$), the B-field is identical for both qubits and so are B-field fluctuations, hence correlated dephasing. The coherence time of the $S_{1/2} \leftrightarrow D_{3/2}$ -transition is

on the order of a few ms in the μ -metal shielding, see Section 4.2, figure 4.3 d). In order to achieve *complete* dephasing, the qubits are exposed to a noisy B-field environment for 10 ms. This could have been sped up by applying white noise to the quantization B-field coils and thus increasing the noise amplitude, however, exposure to the naturally occurring fluctuations was experimentally less demanding and faster to implement.

The general procedure is the following: 1) state preparation, 2) wait time of 10 ms⁸ to allow for correlated dephasing to naturally occur and 3) full-state tomography. We investigate a variety of different initial states being subject to this kind of noise. The first state under investigation is ρ_1 (Eq. 7.20) as described in the former section, and the results for $\varepsilon_{cpd}^{\vec{n}}(\rho_1)$ with $\vec{n} = \vec{e}_z$ are presented in figure 7.6 a). In the ideal case (theory), correlated dephasing can raise the rank of ρ_1 from $R = 2$ to $R = 3$ for $\varepsilon_{cpd}^{\vec{n}}(\rho_1)$. The results ρ_1 (Fig. 7.4 a)) and $\varepsilon_{cpd}^{\vec{n}}(\rho_1)$ (Fig. 7.6 a)) are consistent with the theoretical values. Further, the symmetric discord, that is $D_A = D_B = D$ is increased from $D = 0.010^{+0.014}_{-0.005}$ to $D = 0.19^{+0.03}_{-0.03}$. A comparison between the density matrices of ρ_1 (Fig. 7.4 a), top) and $\varepsilon_{cpd}^{\vec{e}_z}(\rho_1)$ (Fig. 7.6 a), top) shows that the coherences elements $|00\rangle\langle 11|$ in the latter state completely vanish due to the dephasing, whereas the matrix elements $|01\rangle\langle 01|$ stay unaffected, since they are part of a decoherence-free subspace, with respect to the noise applied [145].

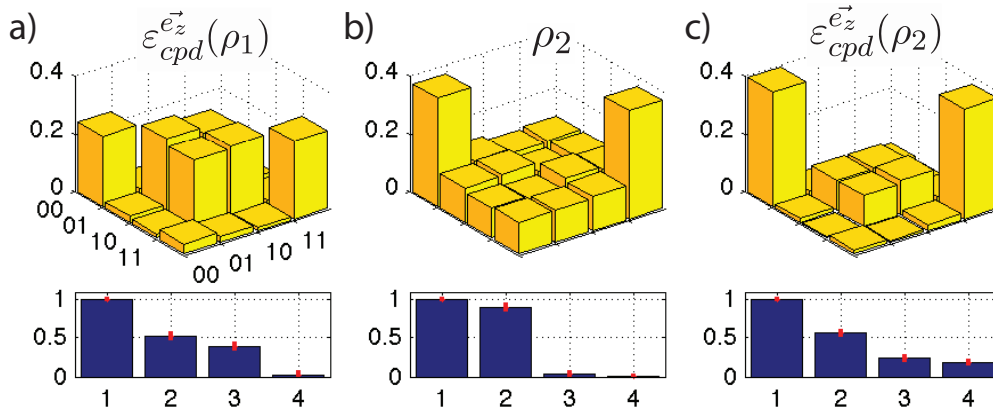


Figure 7.6.: The reconstructed real part of the density matrix and the singular values of the corresponding correlation matrix shown for **a)** $\varepsilon_{cpd}^{\vec{e}_z}(\rho_1)$ with $D = 0.19^{+0.03}_{-0.03}$ and $R = 3$, **b)** ρ_2 (definition see text) with $D = 0.01^{+0.01}_{-0.01}$ and $R = 2$ **c)** $\varepsilon_{cpd}^{\vec{e}_z}(\rho_2)$ with $D = 0.19^{+0.02}_{-0.03}$ and $R = 4$. The measured tangle is less than 0.003 for all states and the imaginary components are ≤ 0.003 .

The question ‘‘How much can the correlation rank be increased by correlation noise?’’ can be answered by considering a simple geometric picture, developed by our collaborator M. Gessner [288]. The picture relates the dephasing axis \vec{n} and two real valued vectors \vec{v} and \vec{w} , which effectively describe the ‘correlations direction’ between qubit A and B (a detailed derivation can be found in appendix E.2). A completely mixed, classically correlated state ρ (e.g. ρ_1) can always be brought into a form

$$\rho = \frac{1}{4} (\mathbb{I} \otimes \mathbb{I} + d \vec{v} \cdot \vec{\sigma} \otimes \vec{w} \cdot \vec{\sigma}), \quad (7.22)$$

⁸This is much longer than the experimental time in the amplitude damping procedure, where correlated B-field fluctuations can be neglected.

where d is the only non-zero singular value of the SVD⁹. The final rank R is then related by the overlap between \vec{n} and the vectors \vec{v} and \vec{w} . In the case of ρ_1 the vectors \vec{v} and \vec{w} are $\vec{v} = \vec{w} = \vec{e}_x$, since qubit A and B are correlated in x -direction. With a dephasing around z , i.e. $\vec{n} = \vec{e}_z$, it follows $\vec{n} \cdot \vec{v} = \vec{n} \cdot \vec{w} = 0$ and a final rank $R = 3$ is generated, see table E.1.

However, if the dephasing axis is neither equal nor orthogonal to the ‘correlation axes’, that is $0 < \vec{n} \cdot \vec{v} < 1$ and $0 < \vec{n} \cdot \vec{w} < 1$, the maximal rank $R = 4$ for two qubits is achievable. Since we can not easily change the direction of dephasing, we use coherent pulses to rotate the qubit states with respect to the dephasing axis. By transforming the state ρ_1 into

$$\rho_2 := U_y(\pi/8)\rho_1 U_y^\dagger(\pi/8), \quad (7.23)$$

where $U_y(\pi/8) = \exp(-i\pi\sigma_y/16)^{\otimes 2}$ is a local unitary rotation on both qubits, and exposing the state again to our correlated noisy B-field environment, its rank is consistent with the increase from $R = 2$ (ρ_2) to $R = 4$ ($\varepsilon_{cpd}^{\vec{e}_z}(\rho_2)$), as shown in figures 7.6 b) and 7.6 c), respectively. The measured discords $D(\varepsilon_{cpd}^{\vec{e}_z}(\rho_1)) = 0.19_{-0.03}^{+0.03}$ and $D(\varepsilon_{cpd}^{\vec{e}_z}(\rho_2)) = 0.19_{-0.03}^{+0.02}$ are the same, however, the ranks are different. This shows that it is not enough to describe non-classical correlations only by the measure $D(\rho)$, since states with the same $D(\rho)$, can have completely different kinds of correlations.

Up to now we have only considered states with pre-existing classical correlations in order to generate discord. What about completely uncorrelated states such as product states $\rho = \rho_a \otimes \rho_B$ with rank $R = 1$? Any such product state can be written in terms of the reduced Bloch-vectors \vec{r}_A and \vec{r}_B as

$$\rho = \frac{1}{2}(\mathbb{I} + \vec{r}_A \cdot \vec{\sigma}) \otimes \frac{1}{2}(\mathbb{I} + \vec{r}_B \cdot \vec{\sigma}), \quad (7.24)$$

for more information see Appendix E.2.2. The final rank, after correlated dephasing, is again related by a geometrical picture. If the dephasing axis \vec{n} is equal to either \vec{r}_A or \vec{r}_B , then the rank is unchanged and remains $R = 1$. However if \vec{n} differs from both reduced Bloch-vectors, then the final rank can be converted to $R = 3$. In order to experimentally demonstrate this we prepare the state

$$\rho_3 := {}_A \langle + | \otimes {}_B \langle + | \quad (7.25)$$

with $|+\rangle = (|0\rangle + |1\rangle)/\sqrt{2}$ and $\vec{r}_A = \vec{r}_B = \vec{e}_x$. Figure 7.7 a) shows the reconstructed density matrix of ρ_3 and the corresponding singular values which are consistent with a rank $R = 1$, up to projection noise. After dephasing in $\vec{n} = \vec{e}_z$, i.e. $\vec{n} \cdot \vec{r}_A = \vec{n} \cdot \vec{r}_B = 0$, the rank is converted to $R = 3$ and the discord $D(\rho_3) = 0.012_{-0.005}^{+0.004}$ is increased to $D(\varepsilon_{cpd}^{\vec{e}_z}(\rho_3)) = 0.23_{-0.02}^{+0.02}$, as shown in figure 7.7 b)¹⁰.

The rank can be even further increased to a full ranked state $R = 4$ by first preparing $\varepsilon_{cpd}^{\vec{e}_z}(\rho_2)$, as described above. This state is then transformed by unitary rotations into

$$\rho_4 := U_y(\pi/2)\varepsilon_{cpd}^{\vec{e}_z}(\rho_3)U_y^\dagger(\pi/2), \quad (7.26)$$

⁹This is not the same SVD as discussed in Eq. 7.12, since here the identity is treated separately. Hence, there are two non-zero singular values and in this representation the rank is $R' = 1 + R$, see Eq. E.8.

¹⁰Note that $D_A = D_B$ is symmetric in both cases, since we start from a product state and apply correlated dephasing to both qubits.

and is subject to a second dephasing around z resulting in the full ranked state $\varepsilon_{cpd}^{\vec{e}_z}(\rho_4)$ with $R = 4$ and $D(\varepsilon_{cpd}^{\vec{e}_z}(\rho_3)) = 0.12_{-0.04}^{+0.03}$, see figure 7.7 c). This shows that even completely uncorrelated product states can be converted to highly quantum correlated, full ranked states by exposing them to correlated experimental noise in two orthogonal directions.

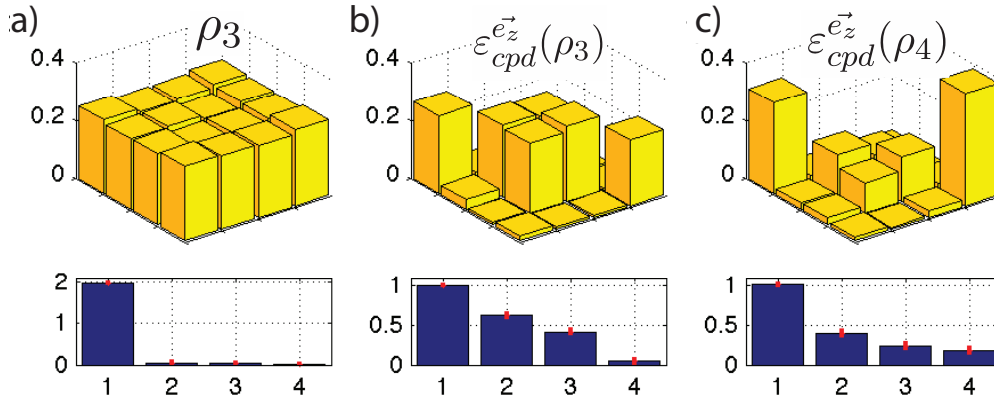


Figure 7.7.: The reconstructed real part of the density matrix and the singular values of the corresponding correlation matrix shown for **a)** $\varepsilon_{cpd}^{\vec{e}_z}(\rho_1)$ with $D = 0.19_{-0.03}^{+0.03}$ and $R = 3$, **b)** ρ_2 (definition see text) with $D = 0.01_{-0.01}^{+0.01}$ and $R = 2$, **c)** $\varepsilon_{cpd}^{\vec{e}_z}(\rho_2)$ with $D = 0.19_{-0.03}^{+0.02}$ and $R = 4$. The measured tangle is less than 0.003 for all states and the imaginary components are ≤ 0.003 .

7.4. Conclusion

The notion of quantum discord [31, 32] extended our knowledge about the boundary between our classical everyday world and the one described by quantum mechanics. It gave us a new tool to investigate the question of what quantum correlations beyond entanglement are, and to classify quantum correlations in general. Here in this thesis, the first study of discordant states in atomic qubits is reported, based on the publication [230]. We experimentally demonstrate how local quantum operations, such as amplitude damping on a subsystem, can convert classical correlations into quantum correlations between two qubits. A measure to quantify these correlations is the aforementioned quantum discord.

However, as it was shown [275, 278], the measure of discord is not enough to capture the whole picture, since discord describes rather the *quantumness* of correlation than its total amount. Hence, another measure, based on the rank of the correlation matrix, is used to quantify discordant states. By using the rank as a measure, we show that local quantum operations cannot increase the rank, rather they convert pre-existing classical correlations to generate discord. Nevertheless, there are processes, such as correlated classical noise on both qubits, which can increase the rank even to the maximum of $R = 4$ for qubit systems. We investigate different input states, ranging from classically correlated mixed states to completely uncorrelated product states, under which conditions correlated B-field noise affects the rank of these states. A simple geometric picture is used to infer the relation between the dephasing axis and the ‘correlation axes’ of the subsystems under investigation (see appendix E). We create states of rank $R = 3$ and $R = 4$ even for a completely uncorrelated input state. This is especially interesting, as product states are simple to prepare

in the lab and letting them evolve under naturally occurring noise sources yields states which are useful in terms of resource states for quantum information processing, specifically deterministic QI transmission protocols [279].

In contrast to entanglement, quantum discord seems to be more robust against certain noisy processes as these processes can generate the latter one. However, recent studies show that dissipative processes can lead to steady-states containing entanglement [289–292].

Our results find relevance in a wide range of different experimental setup, since the generation of discord via noise is not limited to atomic systems, but can be applied to any other qubit system interacting with a noisy environment. Moreover, the notion of discord is not only restricted to two-qubit systems but can be expanded beyond qubits (qutrit and higher dimensions) with multiple particles.

8. Limitations of the current setup and open questions

Knowing and understanding the limitations is the first step towards improvement.

The ultimate goal in quantum information processing is to build a device capable of solving arbitrary large scale problems, which a classical machine cannot do. Over the last 30 years, a remarkable progress has been made towards a quantum computer or/and a quantum simulator, and the principal building blocks have been demonstrated in different physical platforms.

Trapped ions have proven to be a leading platform in terms of quantum control, such as initialization, single/two-qubit gates and read-out. However, a remaining challenge towards a full-scale quantum computer is the size of the systems or, more precisely, the number of qubits. At the time of writing this thesis, the largest system size in our setup is $N = 20$. In order to increase the number of qubits, first the limitations and unsolved questions have to be identified and addressed. The last chapter of this thesis is devoted to this discussion by addressing issues encountered with long ion strings and, if possible, providing answers and solutions to the problems.

Limits on trapping As mentioned in Chapter 4.3, for experiments regarding quantum information processing with ions trapped in a linear Paul trap, any zig-zag configurations must be avoided. By relaxing the axial and/or increasing the radial confinement, it is possible to avoid the zig-zag crossing and keep the crystal linear. However, there are practical limits to the confinement achievable. Radially, we are limited by the amount of RF power that can be generated and efficiently sent to the trap. As we send in more RF power, more power is dissipated (for instance in the Macor[®]¹ holder, for more information see [119, Chapter 3.1]), heating the trap. In [119], our trap temperature is estimated to have $\approx 100^\circ\text{C}$ at a standard RF power of about $\approx 4 - 5\text{W}$. It is advisable to keep the trap temperature low, as the different materials (blades and holder) have different thermal expansion coefficients which could lead to stress. We also have to lower the radial confinement, in order to recrystallize the ion string after a collision with residual back ground gas, which changes the trap temperature. By doing so, we see the ions moving on the CCD camera after changing the RF power from $P_{\text{RF}} = 5\text{W}$ to $P_{\text{RF}} = 2\text{W}$ (after micromotion compensation), due to the thermal expansion. Such temperature changes are expected to be larger for a ‘hotter’ trap. Further, it has been reported in [119, Chapter 4.7] that the axial heating rate strongly depends on the RF confinement. Lastly, the higher the radial confinement the harder it is to couple the bichromatic light into the fiber due to the larger frequency separation of the two light fields, as mentioned in section 4.2.

¹Macor has a rather high loss tangent: $\approx 10^{-3}$ at RT.

On the other hand, lowering the axial confinement introduces other issues. The most obvious one is that the size of the ion string increases which makes the homogeneous illumination, imaging and single-ion addressing towards the edges more challenging, as discussed in the following paragraphs. Less obvious is that at a low axial potential, < 30 V, the ion string's position is changing in time, likely due to local charging and discharging of the trap². We frequently observe that the change in position is enough to affect the camera read out which is based on the ion-positions (see [119, Chapter 3.4]). In this case we repeatedly calibrate the camera images and fit the ion positions every ≈ 10 min. Further, we observe that the axial mode temperature exceeds the Doppler-temperature by a factor of 5 – 6 which introduces many new issues, as discussed in the following paragraphs.

In our current setup we perform experiments with 15 – 20 ions on a regular basis and we could increase the number by a few more ions without substantial changes to the setup, depending on the experimental procedure. However, going beyond $N = 50$ ions, new conceptual approaches are needed. The discussion regarding the scalability of ion traps has a long tradition starting from the early 2000s. Without going into details, I will just mention a few of the conceptual milestones: anharmonic potentials within segmented traps [293], quantum charge-coupled device architectures with a large numbers of interconnected ion traps [294], quantum ion-photon networks where ion traps are interconnected with fibers [295], and 2D-arrays of traps [296, 297].

Axial temperature Most of the experiments during this thesis, where more than 10 ions are trapped, are performed at an axial confinement of $\omega_{ax} \approx 2\pi \times 220$ kHz. For the given harmonic potential we can calculate the mean phonon number at the Doppler limit. Using the relation $\bar{n} = \Gamma/2\omega_{ax}$, where $\Gamma = 2\pi \times 22.4$ MHz is the linewidth of the cooling transition, we would expect $\bar{n} \approx 50$. In order to check the single ion temperature after Doppler cooling, we take a spectrum of

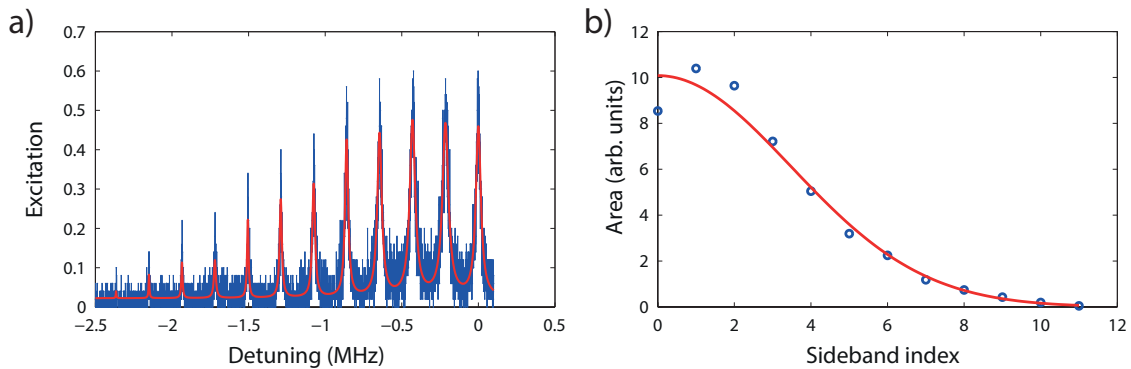


Figure 8.1: **a)** (blue) The motional red sideband spectrum of a single Doppler cooled ion at low axial confinement $\omega_{ax} \approx 2\pi \times 220$ kHz and (red) multi-Lorentzian fits of the spectrum. Due to this low confinement and high temperature, the 11th motional sideband is visible. **b)** (blue) The fitted area beneath each order of the axial sideband and (red) a Gaussian fit of all areas. From the standard deviation σ we can estimate the mean phonon number $\bar{n} \approx 280$.

the vibrational modes. Figure 8.1 a) shows such a spectrum of the red sidebands, where a single ion is excited along the trap axis. Here, we see sidebands up to the 11th order, indicating a very high thermal population. The peaks are fitted with a Lorentzian and the area beneath each spectral

²We haven't done any elaborate investigation on charging, but this is our best guess as the cause. Charges could be generated by stray-light of the photoionizations laser (375 nm and 422 nm), or the Doppler-cooling beam (397 nm).

peak is plotted against the sideband-order index, Fig. 8.1 b). We model the distribution of the plotted areas with a Maxwell-Boltzmann distribution, where the standard deviation σ is directly related to the mean phonon number $\bar{n} = \frac{\sigma^2}{\eta^2}$ (for more details see appendix B.2). According to the measured spectrum and the fits in Fig. 8.1, we get $\bar{n} \approx 280$ which is significantly higher than the Doppler limit. The reason for this discrepancy remains unclear and further investigations are needed.

Despite the high axial temperatures, experiments can still be performed with the ‘horizontal’ beam. This beam has negligible overlap with the axial modes, i.e. the axial temperature has no influence on the Rabi frequency to the first order. Furthermore, second order Doppler effects can be neglected, since the most probable speed in the distribution is given by $v_p = \sqrt{2k_B T/m} = \sqrt{2\bar{n}\hbar\omega_{\text{ax}}/m} \approx 1 \text{ m s}^{-1}$.

Limitation on coherent Rabi oscillations Currently, there are two main limitations for single qubit operations on long ion strings:

- 1) Laser power and beam shaping of the 729 nm and 397 nm beams.
- 2) Imaging optics.

For global single qubit operations and entangling gates it is necessary to have a homogeneous coupling strength distribution, which is not given for a Gaussian light-field. In figure 8.2 a) Rabi oscillations on a string of 52 ions are shown. The ions are trapped at $\omega_{\text{ax}} = 2\pi \times 135 \text{ kHz}$ with a string size of $240 \mu\text{m}$ (Fig. 8.2 b) and are driven from the ‘horizontal’ port with an elliptically shaped beam $33 \mu\text{m} \times 380 \mu\text{m}$. Nevertheless, a distribution of the different Rabi frequencies is clearly visible. Section 4.4 discussed the issues of a specially inhomogeneous coupling strength and limitations of beam shaping in detail.

The edge of the chain exposes another issue: the ions become fainter the further away they are from the center. This is partly due to the elliptical spot size ($\approx 460 \mu\text{m} \times 110 \mu\text{m}$) of the 397 nm not illuminating all ions equally. However, it does not explain why ions 1 – 3 and 49 – 52 are hardly visible, as even these ions should be within $\sim 60\%$ of the peak intensity.

Another limitation is set by the imaging optics³. Zemax simulations show spherical aberrations of the divergent point source (ion) on the imaging plane (camera) as show in figure 8.2 c). In addition to the spherical aberrations, ions further away from the optical axis experience an astigmatism, which becomes apparent in the elliptical image of the outer ions. Due to these aberrations the edge of the chain appears dimmer.

The optical imaging system in our setup was never designed for a large field of view such as for > 50 ions. Since designing and manufacturing new objectives is very time-consuming and expensive, a more pragmatic approach to solve this problem could be via software. One idea is to divide the chain into separate regions of interest (ROI) on the camera with individual signal integration times. This allows for balancing the different intensities.

³Silloptics, Germany: a five-lens custom-made objective with anti-reflection coating for 397 nm and 729 nm. The focal length is $f \approx 50 \text{ mm}$, the clear aperture $D_{\text{obj}} = 38 \text{ mm}$ and $NA > 0.25$. Spherical aberrations induced by the fused silica view-port should be corrected by the lens-design.

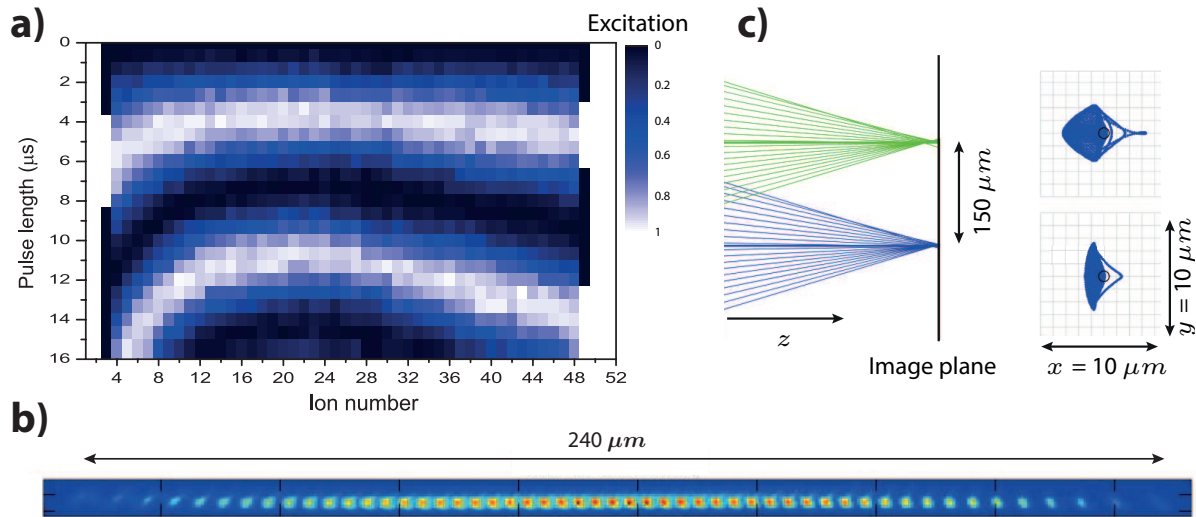


Figure 8.2: **a)** Coherent Rabi flops on 52 ions driven from the ‘horizontal’ port with trapping frequency $\omega_{\text{ax}} = 2\pi \times 135 \text{ kHz}$. The intensity distribution of the elliptically shaped beam (see 4.4.1) is clearly visible. **b)** Due to limitations in the imaging (and partly due to limited 397 nm spot size) the ions 1 – 3 and 49 – 52 are very faint and can not be discriminated properly. A closer look on these edge ions shows an astigmatism, whereas the middle ions project a coma, indicating spherical aberrations. **c)** Zemax simulation of the image of two ions 150 μm apart. (**left**) The blue ray traces belong to the ion on the optical axis and green for the other one. Both ray traces show spherical aberrations due to the divergent point sources (ions) and the limited aperture of the objective. Additionally, the image of the ion 150 μm away from the optical axis shows astigmatism. (**right**) A cut through the x-y plane.

Single ion addressing The imaging system is not only used to collect fluorescence and image the ions onto the camera, but also to focus 729 nm light onto a single ion. For this purpose the beam is enlarged with a Galilean beam expander to $D \approx 25 \text{ mm}$ which gives a theoretical $1/e^2$ -spot diameter of $2w_0 = (4\lambda/\pi)(f/D) \approx 1.8 \mu\text{m}$ at the diffraction limit. In order to address different ions, the 729 nm beam is steered with an AOD which displaces the expanded beam with respect to the objective. In addition to the aberrations mentioned above, the clear aperture of the objective, $D_{\text{obj}} = 38 \text{ mm}$, and the size of the expanded beam, D , set a limit on the number of addressable ions.

Figure 8.3 a) shows an AOD frequency scan where the focused beam is swept over 20 ions (108 μm) with a constant pulse length⁴. The excitation of each ion is proportional to the intensity of the beam as we perform a composite pulse sequence, $\frac{\pi}{2}_{\text{carrier}} - t_{\text{AC-stark}} - \frac{\pi}{2}_{\text{carrier}}$, in order to reduce addressing errors. As the expanded beam gets displaced by changing the AOD frequency, the objective will eventually clip the 729 nm beam. (Note: the frequency bandwidth of the AOD⁵ is larger than the scanning range and cannot explain the reduction in intensity.)

In addition to the limits set by the optics, there is another interesting effect related to the expansion of the wavefunction along the axial direction. Due to the low axial potential we use for trapping multiple ions, the ground state wave-expansion for a single ion is $x_0 = \sqrt{\hbar/m\omega} \approx 30 \text{ nm}$. This is considerably smaller than the focussed spot size. However, the large axial temperature, $\bar{n} \approx 250$,

⁴The pulse length is such that the ion with the strongest coupling performs a π -rotation.

⁵AOD: $f_{\text{center}} = 70 \text{ MHz}$, $\text{BW} = 15 \text{ MHz}$ at 90%-efficiency

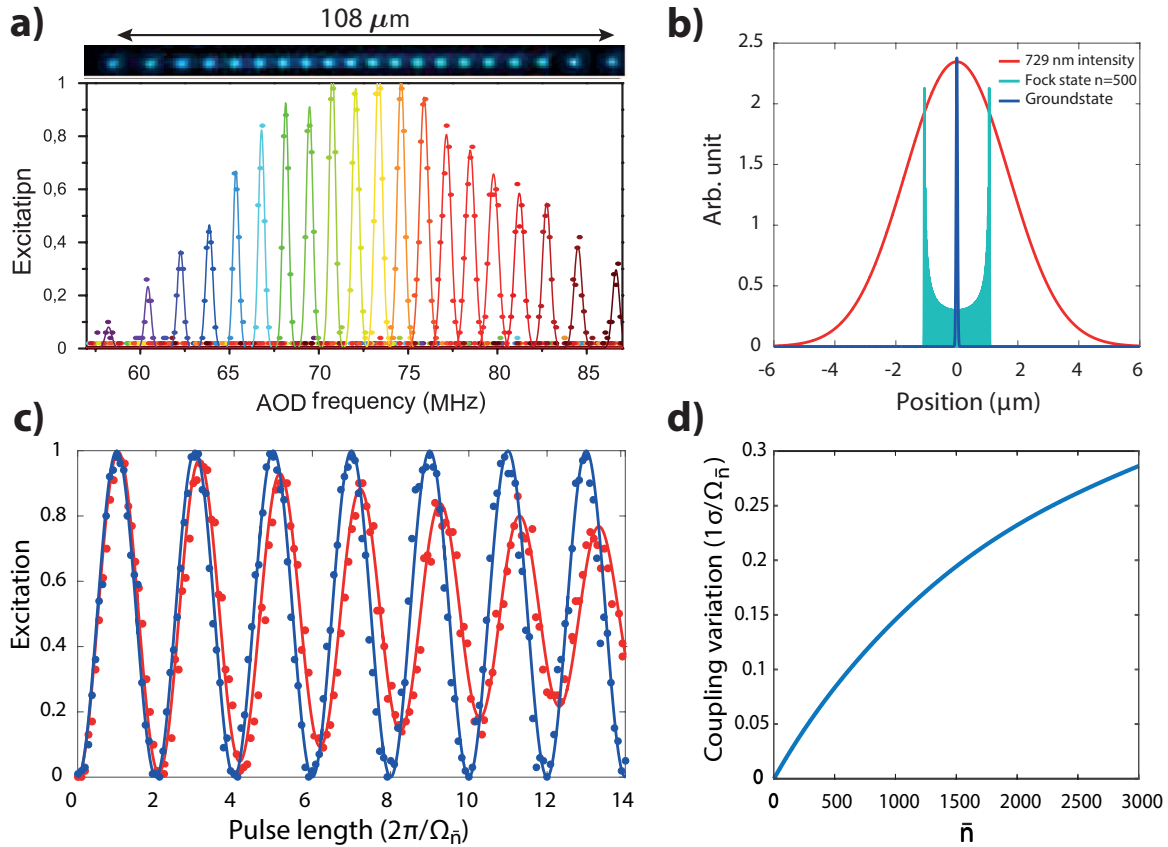


Figure 8.3.: **a)** A frequency scan of the AOD sweeps the focused laser beam across the ion string. Due to the displacement of the expanded beam with respect to the objective, the objective clips the beam when the outer ions are addressed. **b)** The ground state wave-function expansion and the expansion of a higher Fock state ($n = 500$) are compared to the intensity distribution of the focused beam size (FWHM = $4 \mu\text{m}$). Due to the smaller overlap of the higher Fock states with the Gaussian beam, the coupling frequency Ω is reduced. The thermal distribution of the Fock states leads to coupling strength fluctuations. **c)** Addressed Rabi oscillations are compared for a single ion trapped at 220 kHz (red) and 1.2 MHz (blue). The pulse length is normalized by the mean coupling frequency $\Omega_{\bar{n}}$. Experimental data (dots) and theoretical calculations (line) are in very good agreement. **d)** A theoretical calculation of the coupling strength variation as a function of the thermal distribution \bar{n} .

populates very high Fock states $\Psi_n(x)$ with $n_{\text{max}} \approx 10 * \bar{n} \approx 2500^6$. As the wavefunction's size scales with $\sqrt{\bar{n}}$, its size becomes macroscopic for very high Fock states. Figure 8.3 b) compares the size of the ground state and the Fock state $n = 500$ with the intensity profile $I(x)$ of a focused beam with FWHM = $4 \mu\text{m}$. The expansion of the higher Fock state is half the beam size with a significantly reduced overlap function

$$S_n = \int_{-\infty}^{\infty} |\Psi_n(x)|^2 I(x) dx. \quad (8.1)$$

This overlap function is directly proportional to the coupling strength Ω_n and the thermal distribution causes the coupling strength to fluctuate.

When the trapping potential is stiff (1.2 MHz, $\bar{n} \approx 4$ after Doppler cooling) no damping of the addressed Rabi flops can be observed, see Fig. 8.3 c)(blue). However, in the shallow trap (220 kHz),

⁶A rule of thumb for the highest population in a thermal distribution.

the oscillation damps rapidly (red). The measured values (dots) are in superb agreement with numerical simulation (lines). The model used to calculate the damping oscillations has no free parameters and can be found in appendix B.3. Figure 8.3 d) shows the coupling strength variation (one standard deviation σ divided by the mean coupling $\Omega_{\bar{n}}$) as a function of the thermal distribution \bar{n} .

These coupling strength fluctuations become less extensive when more ions are loaded, as shown in figure 8.4. Here, 9 ions are trapped at 220 kHz and the middle ion is addressed. Compared to the oscillations of a single ion trapped in the same trapping potential, there is no damping observable. The reasons for this are the additional axial modes, which contribute in two different ways.

The first one is purely statistical. For the sake of argument, we assume all L axial modes have the same frequency $\omega_{ax}^l = \omega_{ax}$, with $l \in L$ and $\bar{n}^l = \bar{n}$. Then, the fluctuations will be reduced by $\sim \sqrt{1/L}$ as they average out over all modes. A similar argument has been given in [78, Section: 4.4.5]. This, however overestimates the fluctuations. In addition to this statistical averaging, the higher frequency modes have smaller amplitudes x_0^l and lower thermal distributions \bar{n}_l , which both scale with $\sim \sqrt{1/\omega_l}$.

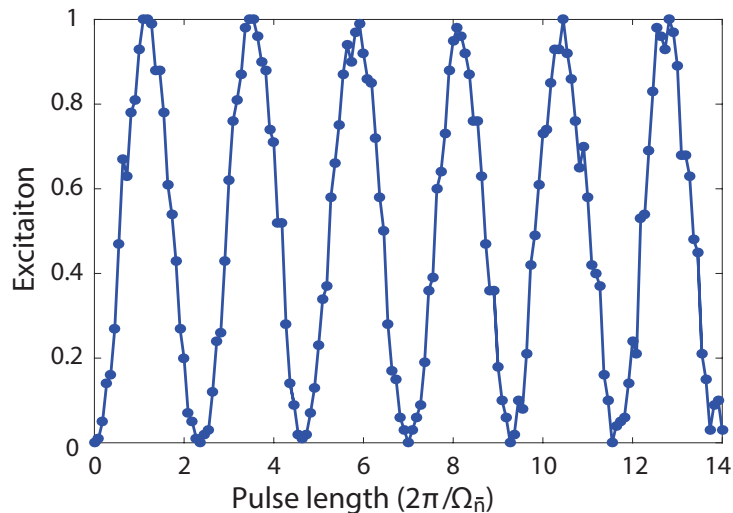


Figure 8.4.: Addressed Rabi flops of the middle ion in a 9 ion string trapped at 220 kHz. Compared to the Rabi oscillation on a single trapped ion, there is no damping observable. The reason for this are the additional axial modes, as described in the main text.

Micromotion An interesting observation is shown in figure 8.5. Here, Rabi oscillations of the ‘vertical’ and the ‘horizontal’ micromotional sidebands are presented (5 out of 9 ions). The axial confinement is increased to $\omega_{ax} = 2\pi \times 700$ kHz, in order to be able to drive the ‘vertical’ micromotion (the ‘vertical’ beam has substantial overlap with the axial modes). This is ~ 50 kHz away from the zig-zag transition. When the oscillation of each ion is examined individually, one observes that ions close to the middle damp faster compared to the edge ions. The argument that the string is too close to the zig-zag transition is insufficient, since $\beta \ll 1$ for all ions (remember, in the zig-zag configuration not all ions can be on the RF nodal line). If the *excess* micromotion is completely compensated, electric field noise can kick the ion randomly through the RF null introducing a

dephasing of the motion. This might explain the observations made in the ‘horizontal’ case, where the middle ion seems to have the lowest *excess* micromotion and decoheres faster than the other ones. However, it does not explain the ‘vertical’ oscillation. Here, all ions show the same coupling strength on the micromotional sideband, but again the middle ions damp faster. It is not yet clear why the Rabi oscillations of the micromotional sideband damp at all. Moreover, in the 20 ion case, the damping is significantly less pronounced.

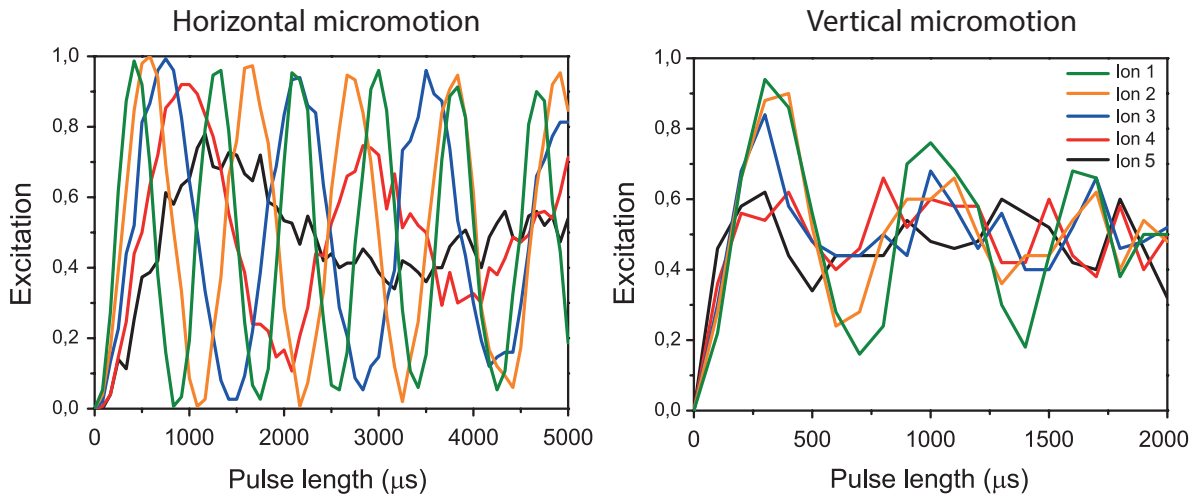


Figure 8.5.: The ‘horizontal’ and the ‘vertical’ micromotional sideband of a 9 ion string trapped at $\omega_{\text{ax}} = 2\pi \times 700$ kHz are driven. Only one half of the chain, ions 1 - 5, are shown for better visibility. It is not clear yet why ions close to the middle (ion 5) decohere faster than ions at the edge.

Heating rates Heating of the motional modes is yet another source of decoherence in our MS-gates and spin-spin interactions. The random kicks in phase-space lead to a dephasing during the time-evolutions. There is quite some extended literature, to name just a few [298–301], regarding the origins and the microscopic mechanism of motional heating. A general consensus is that external electric field noise couples to the ion’s charge and exerts randomly fluctuating forces, which heat the ion’s motion.

However, most of the literature treats the heating of a single ion. For long ion strings the mechanism becomes more complex due to the spatial extension of the string and the additional modes. In addition to the spectral density of the external field noise, the coupling of the modes depends also on the spatial correlation length of the noise compared to the mode-wavelength. In the limit of perfectly correlated noise, such that the noise has the same amplitude and phase at each ion’s position, the heating rate of the COM mode is $\Gamma_H^{\text{COM}} = N\Gamma_H$, where Γ_H is the single ion heating rate [301, Section II.C.3]. All other modes do not couple to the noise, i.e. $\Gamma_H^m = 0$. If the noise correlation length gets close to the wavelength of mode m , this mode will experience the strongest coupling. In the case of completely uncorrelated noise, the heating rate does not depend on the ion number N , but only on the mode frequency, $\Gamma_H^m \simeq (\omega_{\text{COM}}/\omega_m)\Gamma_H$.

Considering the trap and the ion string size, it is valid to assume that most of the noise is correlated across whole string. By relaxing the axial confinement, the string expands and one might expect to see changes in the heating rates of the other modes as well. Table 8.1 compares the heating

	200 kHz		700 kHz	
	$\omega_m/2\pi$ (MHz)	Γ_H^m ($\bar{\text{ns}}^{-1}$)	$\omega_m/2\pi$ (MHz)	Γ_H^m ($\bar{\text{ns}}^{-1}$)
COM, $m = 1$	3.324	27.17 ± 1.84	3.324	30.35 ± 2.98
'Tilt', $m = 2$	3.317	0.24 ± 0.04	3.249	2.04 ± 0.34
'Rock', $m = 3$	3.306	0.14 ± 0.07	3.141	2.38 ± 0.32
$m = 9$	3.193		1.561	27.4 ± 3.58

Table 8.1.: Comparison of heating rates of a 9 ion crystal at two trapping confinements.

rates of the different modes in a string of 9 ions trapped at two confinements, 220 kHz \sim 65 μm and 700 kHz \sim 30 μm .

The observations are very surprising and completely opposite to what we expected. As the confinement is increased, the heating rates of the lower radial modes increase, even though the string size shrinks. Quite outstanding is the lowest mode ($m = 9$); its heating rate is as big as the heating rate of the COM mode. One might be inclined to think that in the high trapping potential, the string undergoes a phase-transition to a zig-zag configuration, despite being 50 kHz off from the phase-transition. However, measurements presented in 4.3 suggest no zig-zag configuration at all. A possible explanation might be resonant three mode coupling [86] between the axial and radial modes. If the anisotropic parameter $\alpha = (\omega_{\text{ax}}/\omega_{\text{rad}})^2 \approx 0.0479$ is higher than $\alpha_{\text{res}} = 4\alpha_{\text{crit}}/(\alpha_{\text{crit}} + 6) \approx 0.0374$, where α_{crit} is the critical point of the zig-zag transition, three mode mixing cannot be excluded. More elaborate experiments need to be performed to investigate this hypothesis.

9. Summary and outlook

The work presented in this thesis can be divided into three main topics regarding quantum information science: quantum simulations of many-body interacting systems, proof of principle demonstration of a measurement-based quantum computer and investigation of quantum correlations, specifically discord, under the influence of noise. All of the discussed experiments are performed with $^{40}\text{Ca}^+$ ions trapped in a linear, macroscopic Paul trap. The ions are first Doppler cooled and then sideband cooled to the ground state of the trapping potential [14]. Further, the qubit is encoded in two Zeeman levels of the $S_{1/2}$ ground state and the $D_{5/2}$ meta-stable state of the valence electron. For the coherent qubit manipulation, such as arbitrary single qubit rotations, entangling gates and engineered spin-spin interactions, a narrow-linewidth 729 nm laser is used.

There are two experiments presented in this work with regards to quantum simulation. Both implement a transverse Ising Hamiltonian with tunable spin-spin couplings J_{ij} . The interactions are engineered with a Mølmer-Sørensen type interaction [93, 99], where a bichromatic 729 nm light field couples off-resonantly to the radial motional modes. By changing the detuning of the bichromatic light field with respect to the modes, the interaction range, which falls off by a power law decay over distance, can be tuned from infinite range to dipole-dipole coupling. In addition, an effective transverse B-field, B , can be applied by off-resonantly driving the Mølmer-Sørensen type interaction, where magnitude is proportional to the detuning. In both experiments we operated in the high field regime, i.e. $\max(J_{ij}) \ll B$, which allows for taking advantage of decoherence-free subspaces (DFS). Further, in this regime the transverse Ising Hamiltonian can be mapped onto an XY-Hamiltonian with hopping terms preserving the number of excitations in the system.

The first experiment demonstrates a newly developed spectroscopic method for investigating the low-lying energy states based on superpositions of approximate eigenstates of the H_{xy} , which allows for probing the energy splittings between those eigenstates. We applied this method to a string of seven ions, first by preparing a superposition of the ground state and one low-lying energy level, then evolving the system under the given Hamiltonian. A Fourier transformation of the oscillating signal reveals the energy splitting between both states. However, as the ground state and the excited state do not belong to the same DFS, the time dynamics is limited by decoherence allowing measurement of only one or two oscillation periods, which limits the resolution. Despite this, valuable information can still be retrieved such as the sign of the coupling matrix J_{ij} , that is, determining if it is ferromagnetic or anti-ferromagnetic coupling.

In a similar fashion, superpositions between two excited states of the same subspace were created and the time dynamics is Fourier analysed. This provides means to fully and accurately measure the dispersion relation of the quasiparticles of the underlying many-body interaction system. Moreover, by cleverly post-selecting the data with two excitations, it is possible to measure quasiparticle

interactions and energy shifts due to these interactions. A perturbation theory treatment qualitatively explains the experimental observations, however overestimates the effects as for a seven spin system two excitations are no longer a small perturbation.

The second experiment reports for the first time on the direct observation of entanglement propagation. A system of seven spins, initially prepared in the ground state, is locally quenched: that is, locally excited by flipping a single spin, and the time evolution is measured. By exploiting the single-ion addressability, it is possible to measure state tomographies at different times and hence reconstruct the time-evolved quantum state. This allows for quantifying two-spin entanglement as a function of time, and indeed the entanglement propagates away from the quench side towards the boundaries of the system. The tunability of the interaction range α allows for further investigation of Lieb-Robinson bounds for short-range and long-range interactions. As predicted by theory, we observe the vanishing of a clear light cone as the interaction range is increased, up to the point where the light cone picture becomes an invalid description of the system.

There are many ideas for possible quantum simulation experiments with the current setup. A project being wrapped up at the time of writing this thesis uses the entanglement spreading to generate large entangled states of up to 20 spins. The main objective of this project is to demonstrate new techniques for reconstructing the quantum state based on matrix product state reconstruction, rather than full-state tomography, as this becomes impractical for system sizes beyond 7-8 ions. Another project which has been started is to observe so called dynamical quantum phase transitions, which correspond to non-analyticities in the time dynamics of certain observables. Other ideas are concerned with many-body localization, where a random potential landscape is imprinted onto the spins. This could be achieved by applying more than a single frequency to the AOD resulting in many tightly focussed, individually controllable laser beams. In this way, each spin gets a local B-field B_i that can be controlled. Further, if the $B_i(t)$ are time-dependent on the scale of the spin-spin coupling, one could study fluctuation- or decoherence-enhanced tunnelling, a phenomenon found in biological systems. There are too many possibilities to list them all, much less to describe them in detail.

A limitation with regards to the quantum simulation experiments is the rather tiny spin-spin coupling of about $\max J_{ij} \approx 2\pi \times 20 \text{ Hz} - 100 \text{ Hz}$, depending on the experimental parameters such as detuning and Rabi frequency. This should significantly improve with the new laser system that will be mentioned later. Laser frequency fluctuations and B-field noise hardly play a role in the regime of $\max(J_{ij}) \ll B$, by taking advantage of the decoherence-free subspace. However, motional heating is an issue which could lead to leaking out of the protected subspace, and it is not yet exactly clear how big these effects are. Moreover, there is no immediate solution as it most likely requires new trap designs, potentially with other materials such as sapphire instead of Macor, for the blade holders. For future experiments which are not performed in the decoherence-free subspace, laser frequency and B-field noise will be relevant, and their exact influence on the quantum simulations has to be first investigated.

The second main topic presented in this thesis showcases the results of our proof of principle experiment regarding measurement-based quantum computation. A first main result is the deterministic

generation of linear and box cluster states, the basic building blocks of larger clusters used as a resource in the MBQC-model. Both states are generated with high fidelities of $\mathcal{F} = 0.846 \pm 0.005$ for the box cluster and $\mathcal{F} = 0.841 \pm 0.005$ for the linear cluster. As the MBQC-approach requires feedforward, i.e. subsequent measurement bases have to be adjusted according to the previous measurement outcomes, we simulate a perfect feedforward by post-selection. In this way, the basic single and two-qubit operations are demonstrated and their performance is quantified, given a perfect feedforward.

In addition, certain cluster states of different sizes, used as code words in QEC, are prepared and their persistence against phase flip errors is investigated. Despite requiring more experimental resources in generating larger states, usually resulting in lower fidelities, we present evidence that larger states indeed protect quantum information better against errors. To the best of our knowledge, this is the first experimental demonstration that larger code words provide better protection.

A next step towards MBQC would be to implement fast feedforward, as it has already been demonstrated by our group a few years previously. However, even though the fidelities achieved in our setup for creating small cluster states are still unrivalled, there seem to be better suited physical systems to implement an MBQC-computer. Appropriate platforms are, for instance, optical lattices where the intrinsic interaction and the lattice structure naturally lead to large cluster states - however, with the disadvantage of less controllability for the time being.

The last experiment presented here is dedicated to quantum correlations, specifically quantum discord in a two-qubit system with the results being published in [230]. The experimental results can be divided into two main parts, both reporting on the generation of quantum discord via noisy processes, however, with two different types of noise. In the first part, quantum discord is analysed as a function of amplitude damping in one of the qubits of a classically correlated, mixed two-qubit state and is quantified by the measure *discord* D . As the amplitude damping probability is increased, the measured D increases at the expense of classical correlations, demonstrating that local noise can only convert correlations, not create them. Quantum discord decreases towards a fully damped qubit, where all quantum information of this particular qubit is lost.

The second part examines quantum discord under correlated B-field fluctuations acting on both qubits. Here, it is demonstrated that correlated noise can create highly correlated two-qubit states, quantified by the rank R , even if the initial state has no (classical) correlations at all. Depending on the basis the noise acts in, different states are created. These states range from low rank states $R = 2$, which might contain discord, up to fully ranked states $R = 4$, which can be useful in certain quantum information protocols, such as probabilistic quantum teleportation protocols.

A near-future improvement to the system will be the installation of a new TiSa-laser system providing almost an order of magnitude more intensity of 729 nm-light. Alternatively, the 729 nm-light can be frequency-doubled to 395 nm endowing the possibility of Raman gates - increasing the

effective spin-spin coupling as well by at least an order of magnitude¹. Further, beam shaping could be improved by diffractive optics or spatial light modulators, however, some careful thought must be put into redesigning the existing optical setup, such that everything fits inside the μ -metal shielding. At the time of writing this thesis, a new generation of RF-power stabilization circuit has been built in, further improving the frequency stability of the radial modes down to ~ 10 Hz. Additionally, a sample-and-hold PID circuit has been setup for intensity stabilization of the 729 nm single-ion addressing pulses. The same circuit will be implemented to other 729 nm-light paths, allowing increased intensity stability. With respect to B-field stability, permanent magnets such as $\text{Sm}_2\text{Co}_{17}$ ² promise an increase of coherence time by a factor of ten as reported in [302].

¹Due to the shorter wavelength the Lamb-Dicke factor increases by a factor of two, which is a factor of four for the effective spin-spin coupling. Moreover, the Raman process is a two-photon process yielding another factor of two. The remaining question is what Rabi frequencies can effectively be achieved.

² $\text{Sm}_2\text{Co}_{17}$ magnets are known to have a very low dependency of remanence on temperature of about $-0.03\%/K$.

A. List of Publications

Publications discussed in this thesis

1. P. Jurcevic, P. Hauke, C. Maier, C. Hempel, B. P. Lanyon, R. Blatt, C. F. Roos
Spectroscopy of interacting quasiparticles in trapped ions
Phys. Rev. Lett. **115**, 100501 (2015)
2. P. Jurcevic, B.P. Lanyon, P. Hauke, C. Hempel, P. Zoller, R. Blatt, C.F. Roos
Observation of entanglement propagation in a quantum many-body system
Nature **511** (2014), 202-205
3. B. P. Lanyon, P. Jurcevic, M. Zwerger, C. Hempel, E.A. Martinez, W. Dür, H.J. Briegel, R. Blatt, C.F. Roos,
Measurement-based quantum computation with trapped ions
Phys. Rev. Lett. **111**, 210501 (2013)
4. B. P. Lanyon, P. Jurcevic, C. Hempel, M. Gessner, V. Vedral, R. Blatt, C.F. Roos
Experimental generation of quantum discord via noisy processes Phys. Rev. Lett. **111**, 100504 (2013)

Further publications

5. P. Jurcevic, P. Jurcevic, H. Shen, P. Hauke, C. Maier, T. Brydges, C. Hempel, B. P. Lanyon, M. Heyl, R. Blatt, C. F. Roos
Direct observation of dynamical quantum phase transitions in an interacting many-body system
arXiv:1612.06902 (2016), submitted to Nature
6. B. P. Lanyon, C. Maier, M. Holzäpfel, T. Baumgratz, C. Hempel, P. Jurcevic, I. Dhand, A. S. Buyskikh, A. J. Daley, M. Cramer, M. B. Plenio, R. Blatt, C. F. Roos
Efficient tomography of a quantum many-body system
arXiv:1612.08000 (2016), submission in preparation
7. R. Lechner, C. Maier, C. Hempel, P. Jurcevic, B. P. Lanyon, T. Monz, M. Brownnutt, R. Blatt, C. F. Roos
Electromagnetically-induced-transparency ground-state cooling of long ion strings
Phys. Rev. A **93**, 053401 (2016)

8. B. P. Lanyon, M. Zwerger, P. Jurcevic, C. Hempel, W. Dür, H. J. Briegel, R. Blatt, C. F. Roos
Experimental violation of multipartite bell inequalities with trapped ions
Phys. Rev. Lett. **112**, 100403 (2014)
9. C. Hempel, B. P. Lanyon, P. Jurcevic, R. Gerritsma, R. Blatt, C. F. Roos
Entanglement-enhanced detection of single-photon scattering events
Nature Photonics **7**, 630 (2013)
10. A. Beck, A.D. Tsamaloukas, P. Jurcevic, H. Heerklotz
Additive action of two or more solutes on lipid membranes
Langmuir **24**(16), 8833-8840 (2008)

B. Extended derivations

B.1. Derivation of the effective spin-spin Hamiltonian

We start with the Hamiltonian H_{Int} describing the interaction of trapped ions with an external coherent light field with frequency ω_L and phase Φ_L (as given in equation 3.59):

$$H_{\text{Int}} = \hbar \frac{\Omega}{2} \left[e^{-i(\Delta t - \Phi_L)} \sigma^+ \left(1 + i\eta (ae^{-i\omega_t t} + a^\dagger) e^{i\omega_t t} \right) + h.c. \right]. \quad (\text{B.1})$$

Here, we take a few assumptions:

- We are in the Lamb-Dicke regime: $\eta \ll 1$
- We consider a single mode, i.e. COM: $\rightarrow \eta_{i,m} = \eta$
- All ions have an equal coupling strength: $\Omega_i = \Omega$
- $\sigma^+ = \sum_i \sigma_i^+$, $\sigma_i^\pm = \sigma_i^x \pm i\sigma_i^y$
- $\Delta = \omega_L - \omega_0$ is the detuning of the laser frequency from the atomic transition
- ω_t is the trapping frequency, i.e. the COM-mode frequency
- Δ_t is the detuning from ω_t , see Eq. B.2 and B.3
- δ_c is the center line detuning, see Eq. B.2 and B.3

B.1.1. Blue/Red Side Band

We set $\Phi_L = \Phi_b$ and $\Delta = \omega_t + \Delta_t + \delta_c$

$$\begin{aligned}
H_b &= \hbar \frac{\Omega}{2} \left[e^{-i((\omega_t + \Delta_t + \delta_c)t - \Phi_b)} \sigma^+ (1 + i\eta(ae^{-i\omega_t t} + a^\dagger)e^{i\omega_t t}) + h.c. \right] \\
&= \hbar \frac{\Omega}{2} \left[\begin{array}{c} \xrightarrow{\text{RWA}} \\ \sigma^+ e^{-i((\omega_t + \Delta_t + \delta_c)t - i\Phi_b)} \\ \xrightarrow{\text{RWA}} \end{array} + i\eta \left(\begin{array}{c} \xrightarrow{\text{RWA}} \\ \sigma^+ a e^{-i(2\omega_t + \Delta_t + \delta_c)t + i\Phi_b} \\ \xrightarrow{\text{RWA}} \end{array} \right) \right. \\
&\quad \left. + \sigma^+ a^\dagger e^{-i(\Delta_t + \delta_c)t} e^{i\Phi_b} \right] + h.c. \\
&= \hbar \frac{\Omega}{2} i\eta \left[\sigma^+ a^\dagger e^{-i(\Delta_t + \delta_c)t} e^{i\Phi_b} - \sigma^- a e^{i(\Delta_t + \delta_c)t} e^{-i\Phi_b} \right] \tag{B.2}
\end{aligned}$$

and similarly for the red sideband: $\Phi_L = \Phi_r$ and $\Delta = -\omega_t - \Delta_t + \delta_c$

$$\begin{aligned}
H_r &= \hbar \frac{\Omega}{2} \left[e^{+i((\omega_t + \Delta_t - \delta_c)t + \Phi_r)} \sigma^+ (1 + i\eta(ae^{-i\omega_t t} + a^\dagger)e^{i\omega_t t}) + h.c. \right] \\
&= \hbar \frac{\Omega}{2} \left[\begin{array}{c} \xrightarrow{\text{RWA}} \\ \sigma^+ e^{+i((\omega_t + \Delta_t - \delta_c)t + i\Phi_r)} \\ \xrightarrow{\text{RWA}} \end{array} + i\eta \left(\begin{array}{c} \xrightarrow{\text{RWA}} \\ \sigma^+ a e^{+i(\Delta_t - \delta_c)t + i\Phi_r} \\ \xrightarrow{\text{RWA}} \end{array} \right) \right. \\
&\quad \left. + \sigma^+ a^\dagger e^{+i(2\omega_t - \Delta_t - \delta_c)t} e^{i\Phi_r} \right] + h.c. \\
&= \hbar \frac{\Omega}{2} i\eta \left[\sigma^+ a e^{+i(\Delta_t - \delta_c)t} e^{i\Phi_r} - \sigma^- a^\dagger e^{-i(\Delta_t - \delta_c)t} e^{-i\Phi_r} \right]. \tag{B.3}
\end{aligned}$$

The Hamiltonian describing a bichromatic light field is a sum of

$$\begin{aligned}
H_{\text{bic}} &= H_r + H_b \\
&= i\eta \frac{\hbar\Omega}{2} \left[\left(\sigma^+ a e^{+i(\Delta_t - \delta_c)t} e^{i\Phi_r} - \sigma^- a^\dagger e^{-i(\Delta_t - \delta_c)t} e^{-i\Phi_r} \right) \right. \\
&\quad \left. + \left(\sigma^+ a^\dagger e^{-i(\Delta_t + \delta_c)t} e^{i\Phi_b} - \sigma^- a e^{+i(\Delta_t + \delta_c)t} e^{-i\Phi_b} \right) \right] \\
&= i\eta \frac{\hbar\Omega}{2} \left[a \left(\sigma^+ e^{+i(\Delta_t - \delta_c)t} e^{i\Phi_r} - \sigma^- e^{-i(\Delta_t + \delta_c)t} e^{-i\Phi_b} \right) \right. \\
&\quad \left. + a^\dagger \left(\sigma^+ e^{-i(\Delta_t + \delta_c)t} e^{i\Phi_b} - \sigma^- e^{-i(\Delta_t - \delta_c)t} e^{-i\Phi_r} \right) \right] \\
&= i\eta \frac{\hbar\Omega}{2} \left[a e^{i\Delta_t t} e^{-i\frac{\Phi_r - \Phi_b}{2}} e^{-i\frac{\pi}{2}} \left(\sigma^+ e^{-i\delta_c t} e^{i\frac{\Phi_r + \Phi_b}{2}} e^{i\frac{\pi}{2}} + \sigma^- e^{i\delta_c t} e^{-i\frac{\Phi_r + \Phi_b}{2}} e^{-i\frac{\pi}{2}} \right) + \dots \right] \\
&= i\eta \frac{\hbar\Omega}{2} \left[a e^{i\Delta_t t} e^{-i\Phi_M} (-i) \left(\sigma^+ e^{-i\delta_c t} e^{i\Phi_S} + \sigma^- e^{i\delta_c t} e^{-i\Phi_S} \right) + \dots \right], \tag{B.4}
\end{aligned}$$

where the phases $\Phi_M = \frac{\Phi_r - \Phi_b}{2}$ and $\Phi_S = \frac{\Phi_r + \Phi_b}{2} + \pi$. Since Φ_b and Φ_r can be chosen independently, we set them to $\Phi_b = \Phi_r = -\frac{\pi}{2}$, such that $\Phi_M = \Phi_S = 0$. This simplifies equation B.4 to:

$$H_{\text{bic}} = \eta \frac{\hbar\Omega}{2} \left[a e^{i\Delta_t t} + a^\dagger e^{-i\Delta_t t} \right] \left[\sigma^+ e^{-i\delta_c t} + \sigma^- e^{i\delta_c t} \right] \tag{B.5}$$

B.1.2. Time Evolution - Magnus Expansion

In order to calculate the time-evolution of H_{bic} the Magnus-expansion is applied up to the second order:

$$U(t) = T \left[e^{-i \int_a^t dt_1 H(t_1)/\hbar} \right] = e^{-(\Omega_1 + \Omega_2 + \Omega_3 \dots)},$$

where T is the time-ordering parameter. The first order is given by:

$$\begin{aligned} \Omega_1(t) &= \frac{i}{\hbar} \int_0^t dt_1 H(t_1) = i\eta \frac{\Omega}{2} \int_0^t dt_1 \left[a e^{i\Delta_t t_1} + a^\dagger e^{-i\Delta_t t_1} \right] \left[\sigma^+ e^{-i\delta_c t_1} + \sigma^- e^{i\delta_c t_1} \right] \\ &= a \left(\sigma^+ \frac{\left(e^{i(\Delta_t - \delta_c)t} - 1 \right)}{\delta_c - \Delta_t} - \sigma^- \frac{\left(e^{i(\delta_c + \Delta_t)t} - 1 \right)}{\delta_c + \Delta_t} \right) \\ &\quad + a^\dagger \left(\sigma^+ \frac{\left(e^{-i(\delta_c + \Delta_t)t} - 1 \right)}{\delta_c + \Delta_t} - \sigma^- \frac{\left(e^{i(\delta_c - \Delta_t)t} - 1 \right)}{\delta_c - \Delta_t} \right). \end{aligned} \tag{B.6}$$

Equation B.6 consists of two types of terms, constant, time-independent terms and a rotating one. The time-independent parts only introduce a global phase (constant energy off-set) and can therefore be neglected. Further, the experiments regarding quantum simulations are carried out in the regime where $\Delta_t \gg \eta\Omega$. This means that terms oscillating at $e^{\pm i(\Delta_t \pm \delta_c)t}$ will average out over the time scale set by $1/\eta\Omega$. Hence, we can adiabatically eliminate these terms and completely ignore the first order. A more intuitive reason why we can ignore these terms is that the wave-packet trajectory in phase-space is small enough³, such that its overlap with the origin is ≈ 1 at any time of the evolution.

³For small excitations of Fock states.

B.1.3. Second Order

Now let's take a look at the second order:

$$\Omega_2(t) = \frac{1}{2\hbar^2} \int_0^t dt_1 \int_0^{t_1} dt_2 [H(t_1), H(t_2)]. \quad (\text{B.7})$$

Before continuing the commutator of $[H_{BIC}(t_1), H_{BIC}(t_2)]$ has to be calculated first:

$$\begin{aligned} &= - \left(\frac{\hbar\Omega\eta}{2} \right)^2 \left[\sum_i (ae^{i\Delta_t t_1} + a^\dagger e^{-i\Delta_t t_1}) (\sigma_i^+ e^{-i\delta_c t_1} + \sigma_i^- e^{i\delta_c t_1}), \right. \\ &\quad \left. \sum_j (ae^{i\Delta_t t_2} + a^\dagger e^{-i\Delta_t t_2}) (\sigma_j^+ e^{-i\delta_c t_2} + \sigma_j^- e^{i\delta_c t_2}) \right] \\ &= - \left(\frac{\hbar\Omega\eta}{2} \right)^2 \left\{ (a + a^\dagger) \left[\sum_i \sigma_i^+ e^{-i\delta_c t_1} + \sum_i \sigma_i^- e^{i\delta_c t_1}, \sum_j \sigma_j^+ e^{-i\delta_c t_2} + \sum_j \sigma_j^- e^{i\delta_c t_2} \right] (a + a^\dagger) \right. \\ &\quad \left. + \sum_i \sum_j (\sigma_i^+ + \sigma_i^-) \left[ae^{i\Delta_t t_1} + a^\dagger e^{-i\Delta_t t_1}, ae^{i\Delta_t t_2} + a^\dagger e^{-i\Delta_t t_2} \right] (\sigma_j^+ + \sigma_j^-) \right\} \\ &= - \left(\frac{\hbar\Omega\eta}{2} \right)^2 \left\{ \sum_i (ae^{i\Delta_t t_1} + a^\dagger e^{-i\Delta_t t_1}) (ae^{i\Delta_t t_2} + a^\dagger e^{-i\Delta_t t_2}) (\sigma_i^z e^{-i\delta_c(t_1-t_2)} - \sigma_i^z e^{i\delta_c(t_1-t_2)}) \right. \\ &\quad \left. + \sum_{i,j} (\sigma_i^+ e^{-i\delta_c t_1} + \sigma_i^- e^{i\delta_c t_1}) (\sigma_j^+ e^{-i\delta_c t_2} + \sigma_j^- e^{i\delta_c t_2}) (e^{i\Delta_t(t_1-t_2)} - e^{-i\Delta_t(t_1-t_2)}) \right\} \\ &= -2i \left(\frac{\hbar\Omega\eta}{2} \right)^2 \left\{ \left(aa e^{i\Delta_t(t_1+t_2)} + (N_{ph} + 1) e^{i\Delta_t(t_1-t_2)} \right) \right. \\ &\quad \left. + \sum_i N_{ph} e^{-i\Delta_t(t_1-t_2)} + a^\dagger a^\dagger e^{-i\Delta_t(t_1+t_2)} \right) \sigma_i^z \sin(\delta_c(t_2 - t_1)) \\ &\quad + \sum_{i,j} \left(\sigma_i^+ \sigma_j^+ e^{-i\delta_c(t_1+t_2)} + \sigma_i^+ \sigma_j^- e^{-i\delta_c(t_1-t_2)} \right. \\ &\quad \left. + \sigma_i^- \sigma_j^+ e^{i\delta_c(t_1-t_2)} + \sigma_i^- \sigma_j^- e^{i\Delta_t(t_1+t_2)} \right) \sin(\Delta_t(t_1 - t_2)) \left. \right\}. \quad (\text{B.8}) \end{aligned}$$

Here, are a few useful relationships used in the derivation above:

- $[AB, CD] = A[B, CD] + [A, CD]B = A[B, C]D + AC[B, D] + [A, C]DB + C[A, D]B$
- $e^{i\alpha} - e^{-i\alpha} = 2i \sin(\alpha)$
- $[\sigma_i^+, \sigma_j^-] = \sigma_i^z \delta_{ij}$
- $[a, a^\dagger] = 1$
- $a^\dagger a = N_{ph}$, where N_{ph} is the number operator

There are 8 different terms in Eq. B.8, where four of them carry the spin-spin coupling operators. By inserting Eq. B.8 into Eq. B.7 the second order can be calculated. An adiabatic elimination

(AE) of the fast rotating terms containing Δ_t and $\Delta_t \pm \delta_c$ yields.

$$\begin{aligned}
\Omega_2(t) = & -i \left(\frac{\Omega\eta}{2} \right)^2 \left\{ \right. \\
& (aa) \cancel{e^{i\Delta_t t} (\dots)} \xrightarrow{AE} \\
& + \sum_i (N_{ph} + 1) \sigma_i^z \left(-\frac{\delta_c^3 t}{(\delta_c^2 - \Delta_t^2)^2} + \frac{\delta_c \Delta_t^2 t}{(\delta_c^2 - \Delta_t^2)^2} + \cancel{e^{i\Delta_t t} (\dots)} \xrightarrow{AE} \right) \\
& + \sum_i N_{ph} \sigma_i^z \left(-\frac{\delta_c^3 t}{(\delta_c^2 - \Delta_t^2)^2} + \frac{\delta_c \Delta_t^2 t}{(\delta_c^2 - \Delta_t^2)^2} + \cancel{e^{i\Delta_t t} (\dots)} \xrightarrow{AE} \right) \\
& + (a^\dagger a^\dagger) \cancel{e^{i\Delta_t t} (\dots)} \xrightarrow{AE} \\
& + \sum_{i,j} \sigma_i^+ \sigma_j^+ \left(\frac{\Delta_t e^{-i\delta_c t} \sin(\delta_c t)}{\delta_c^3 - \delta_c \Delta_t^2} + \cancel{\sin(\Delta_t t) (\dots)} \xrightarrow{AE} \right) \\
& + \sum_{i,j} \sigma_i^+ \sigma_j^- \left(-\frac{\delta_c^2 \Delta_t t}{(\delta_c^2 - \Delta_t^2)^2} + \frac{\Delta_t^3 t}{(\delta_c^2 - \Delta_t^2)^2} + \cancel{\sin(\Delta_t t) (\dots)} \xrightarrow{AE} \right) \\
& + \sum_{i,j} \sigma_i^- \sigma_j^+ \left(-\frac{\delta_c^2 \Delta_t t}{(\delta_c^2 - \Delta_t^2)^2} + \frac{\Delta_t^3 t}{(\delta_c^2 - \Delta_t^2)^2} + \cancel{\sin(\Delta_t t) (\dots)} \xrightarrow{AE} \right) \\
& \left. + \sum_{i,j} \sigma_i^- \sigma_j^- \left(\frac{\Delta_t e^{i\delta_c t} \sin(\delta_c t)}{\delta_c^3 - \delta_c \Delta_t^2} + \cancel{\sin(\Delta_t t) (\dots)} \xrightarrow{AE} \right) \right\}.
\end{aligned}$$

A simple rearrangement results in

$$\begin{aligned}
\Omega_2(t) = & -i \left(\frac{\Omega\eta}{2} \right)^2 \left\{ \sum_i (2N_{ph} + 1) \sigma_i^z \left(-\frac{\delta_c^3 t}{(\delta_c^2 - \Delta_t^2)^2} + \frac{\delta_c \Delta_t^2 t}{(\delta_c^2 - \Delta_t^2)^2} \right) \right. \\
& + \sum_{i,j} \left(\sigma_i^+ \sigma_j^+ e^{-i\delta_c t} + \sigma_i^- \sigma_j^- e^{i\delta_c t} \right) \left(\frac{\Delta_t \sin(\delta_c t)}{\delta_c^3 - \delta_c \Delta_t^2} \right) \\
& \left. + \sum_{i,j} \left(\sigma_i^+ \sigma_j^- + \sigma_i^- \sigma_j^+ \right) \left(-\frac{\delta_c^2 \Delta_t t}{(\delta_c^2 - \Delta_t^2)^2} + \frac{\Delta_t^3 t}{(\delta_c^2 - \Delta_t^2)^2} \right) \right\}. \tag{B.9}
\end{aligned}$$

The equation B.9 can be further simplified by using a Taylor expansion with respect to $\frac{\delta_c}{\Delta_t}$ to second order. This leads to the following $\Omega_2(t)$:

$$\begin{aligned}
\Omega_2(t) = & -i \left(\frac{\Omega\eta}{2} \right)^2 \left\{ \sum_i (2N_{ph} + 1) \frac{\delta_c}{\Delta_t^2} \sigma_i^z t \right. \\
& + \sum_{i,j} \sin(\delta_c t) \left(\sigma_i^+ \sigma_j^+ e^{-i\delta_c t} + \sigma_i^- \sigma_j^- e^{i\delta_c t} \right) \left(\frac{1}{\delta_c \Delta_t} + \frac{\delta_c}{\Delta_t^3} \right) \\
& \left. + \sum_{i,j} \left(\sigma_i^+ \sigma_j^- + \sigma_i^- \sigma_j^+ \right) \left(\frac{1}{\Delta_t} + \frac{\delta_c^2}{\Delta_t^3} \right) t \right\}. \tag{B.10}
\end{aligned}$$

B.1.4. Effective Hamiltonian

The effective time evolution of the system is $U_{\text{eff}}(t) = e^{-\Omega_2(t)} = e^{-\frac{i}{\hbar} \int_0^t dt H_{\text{eff}}}$. In order to get H_{eff} the derivative of $\Omega_2(t)$ with respect to t has to be taken.

$$\begin{aligned}
H_{\text{eff}} &= \left(\frac{\Omega\eta}{2}\right)^2 \left\{ \sum_i (2N_{ph} + 1) \frac{\delta_c}{\Delta_t^2} \sigma_i^z \right. \\
&\quad + \sum_{i,j} \delta_c \left(\frac{1}{\delta_c \Delta_t} + \frac{\delta_c}{\Delta_t^3} \right) \left(\sigma_i^+ \sigma_j^+ e^{-i\delta_c t} + \sigma_i^- \sigma_j^- e^{i\delta_c t} \right) \cos(\delta_c t) \\
&\quad + \sum_{i,j} \delta_c \left(\frac{1}{\delta_c \Delta_t} + \frac{\delta_c}{\Delta_t^3} \right) \left(-\sigma_i^+ \sigma_j^+ e^{-i\delta_c t} + \sigma_i^- \sigma_j^- e^{i\delta_c t} \right) i \sin(\delta_c t) \\
&\quad \left. + \sum_{i,j} \left(\sigma_i^+ \sigma_j^- + \sigma_i^- \sigma_j^+ \right) \left(\frac{1}{\Delta_t} + \frac{\delta_c}{\Delta_t^3} \right) \right\} \\
&= \left(\frac{\Omega\eta}{2}\right)^2 \left\{ \sum_i (2N_{ph} + 1) \frac{\delta_c}{\Delta_t^2} \sigma_i^z \right. \\
&\quad \left. + \sum_{i,j} \left(\frac{1}{\Delta_t} + \frac{\delta_c^2}{\Delta_t^3} \right) \left(\sigma_i^+ \sigma_j^+ e^{-2i\delta_c t} + \sigma_i^+ \sigma_j^- + \sigma_i^- \sigma_j^+ + \sigma_i^- \sigma_j^- e^{2i\delta_c t} \right) \right\}. \tag{B.11}
\end{aligned}$$

Equation B.11 reveals that there are terms depending on the number of phonons in the motional mode for $\delta_c \neq 0$. This asymmetrical detuning leads to slightly different coupling strengths in the red and blue sidebands, from where the phonon number dependency arises.

By comparing Δ_t and δ_c there are three different regimes of H_{eff} to be identified:

1. $\Delta_t \gg \delta_c \gg J$ This is the regime where $H_{\text{eff}} = H_{XY}$
2. $\Delta_t \gg J \gg \delta_c \approx 0$
3. $\Delta_t \gg \delta_c \approx J$, but $\delta_c t \ll 1$

Here, we define $J = \left(\frac{\Omega\eta}{2\sqrt{\Delta_t}}\right)^2$ as the spin-spin coupling strength.

Regime 1 In this case it is admissible to apply the adiabatic elimination to terms rotating at $e^{2i\delta_c t}$ and ignoring terms $\propto \frac{1}{\Delta_t^3}$. This gives

$$\mathbf{H}_{\text{eff}} = J \sum_{i,j} \left(\sigma_i^+ \sigma_j^- + \sigma_i^- \sigma_j^+ \right) + J \frac{\delta_c (2N_{ph} + 1)}{\Delta_t} \sum_i \sigma_i^z = \mathbf{H}_{\mathbf{XY}}. \tag{B.12}$$

Interestingly, a small transverse field, which scales with $J \frac{\delta_c (2N_{ph} + 1)}{\Delta_t}$ is still left. If we plug in typical numbers: $\Delta_t = 80$ kHz, $\delta_c = 5$ kHz and $J = 0.5$ kHz we get a transverse field strength of ≈ 30 Hz for a ground-state cooled mode. This may not be much, at the first glance, since it is an order of magnitude smaller than J . However, if sideband cooling fails to work, there are easily tens of phonons populating the mode after Doppler cooling. And all modes, except for the COM mode, have a non-uniform distribution of the mode-vector amplitudes across the string. This will imprint

a differential AC-shift onto the ions, which will fluctuate randomly with a thermal distribution and could be of the same order of magnitude as J . To prevent this problem, one needs to cool the modes to the ground state, to keep this term as small as possible and the thermal distribution as narrow as possible. However, there are heating processes during the time-evolution. Even though the modes might be perfectly ground state cooled, they will eventually heat up. Luckily, the mode with the highest heating rate, the COM, has uniform mode-vector amplitudes causing all ions to get the same AC-stark shift at any time.

Regime 2. This is the easiest case where $\delta_c \rightarrow 0$ (note: $\sigma^\pm = \sigma^x \pm i\sigma^y$):

$$\begin{aligned} \mathbf{H}_{\text{eff}} &= J \sum_{i,j} \left(\sigma_i^+ \sigma_j^+ + \sigma_i^+ \sigma_j^- + \sigma_i^- \sigma_j^+ + \sigma_i^- \sigma_j^- \right) \\ &= J \sum_{i,j} \left((\sigma_i^+ + \sigma_i^-) (\sigma_j^+ + \sigma_j^-) \right) \\ &= J \sum_{i,j} \sigma_i^x \sigma_j^x = \mathbf{H}_{\mathbf{XX}}. \end{aligned} \quad (\text{B.13})$$

Regime 3 This is the trickiest case, since the rotating term must not be eliminated and we have to change into a rotating frame to derive the transverse field H_{Ising} . For the sake of simplicity we go the other way around and show that transforming H_{Ising} gives H_{eff} . We use the transformation $H' = U^\dagger H U - i\hbar U^\dagger \dot{U}$ with $U = e^{-iH_0 t/\hbar}$, such that

$$\begin{aligned} H' &= e^{iH_0 t/\hbar} H_0 e^{-iH_0 t/\hbar} + e^{iH_0 t/\hbar} H_1 e^{-iH_0 t/\hbar} - i\hbar e^{iH_0 t/\hbar} (-i) H_0 e^{-iH_0 t/\hbar} \\ &= e^{iH_0 t/\hbar} H_1 e^{-iH_0 t/\hbar}. \end{aligned}$$

We will apply the transformation to the Ising Hamiltonian

$$H_{\text{Ising}} = \underbrace{-\frac{\hbar\delta_c}{2} \sum_i \sigma_i^z}_{H_0} + \underbrace{J \sum_{i,j} \left(\sigma_i^+ \sigma_j^+ + \sigma_i^+ \sigma_j^- + h.c. \right) + J \frac{\delta_c (2N_{ph} + 1)}{\Delta_t} \sum_{i,j} \sigma_i^z}_{H_1}. \quad (\text{B.14})$$

Let's start with the easy term (note: $[e^{-i\sigma_i^z}, \sigma_i^z] = 0$)

$$\begin{aligned} H'_{1,3} &= e^{iH_0 t/\hbar} J \frac{\delta_c (2N_{ph} + 1)}{\Delta_t} \sigma_i^z e^{-iH_0 t/\hbar} \\ &= J \frac{\delta_c (2N_{ph} + 1)}{\Delta_t} \sum_i \sigma_i^z. \end{aligned}$$

For the next two terms we use the following relation: $e^{i\frac{\alpha}{2}\sigma^z} \sigma^\pm e^{i\frac{\alpha}{2}\sigma^z} = e^{i\alpha} \sigma^\pm$:

$$\begin{aligned} H'_{1,1} &= e^{iH_0 t/\hbar} J \sum_{i,j} \left(\sigma_i^+ \sigma_j^+ + \sigma_i^- \sigma_j^- \right) e^{-iH_0 t/\hbar} \\ &= J \sum_{i,j} \left(\sigma_i^+ \sigma_j^+ e^{-2i\delta_c t} + \sigma_i^- \sigma_j^- e^{2i\delta_c t} \right) \end{aligned}$$

and

$$\begin{aligned} H'_{1,2} &= e^{iH_0t/\hbar} J \sum_{i,j} \left(\sigma_i^+ \sigma_j^- + \sigma_i^- \sigma_j^+ \right) e^{-iH_0t/\hbar} \\ &= J \sum_{i,j} \left(\sigma_i^+ \sigma_j^- + \sigma_i^- \sigma_j^+ \right). \end{aligned}$$

So finally we get:

$$\begin{aligned} \mathbf{H}_{\text{eff}} &= J \sum_{i,j} \left(\sigma_i^+ \sigma_j^+ e^{-2i\delta ct} + \sigma_i^+ \sigma_j^- + \sigma_i^- \sigma_j^+ + \sigma_i^- \sigma_j^- e^{2i\delta ct} \right) + \frac{\delta_c (2N_{ph} + 1)}{\Delta_t} \sum_i \sigma_i^z \\ &= U^\dagger \mathbf{H}_{\text{Ising}} U - i\hbar U^\dagger \dot{U}. \end{aligned} \quad (\text{B.15})$$

B.2. Temperature estimate from sideband-order index distribution

Here I will give a detailed derivation of the relations $\bar{n} = \frac{\sigma^2}{2\eta^2}$ used in section 8 to estimate the axial temperature of single, Doppler cooled ion. The sideband can be construed as a Doppler-shift

$$\Delta\omega = \frac{v}{c}\omega, \quad (\text{B.16})$$

where v is the velocity of the particle along the \vec{k} -vector of the light-field, c is the speed of light and ω is the frequency of the atomic transition. For high temperatures we can model the velocity distribution with the Maxwell-Boltzmann distribution

$$p(v) = C e^{-\frac{mv^2}{2k_B T}} = C e^{-\frac{v^2}{2\sigma^2}}. \quad (\text{B.17})$$

Here, $p(v)$ is the probability density function, m is the mass of a single particle, $\sigma = \sqrt{k_B T/m}$ is the standard deviation of the distribution and C is a normalization factor, such that $\int_{-\infty}^{\infty} p(v) dv = 1$. Using the relation $k_B T = \hbar\omega\bar{n}$ and equation B.16 we get

$$p(v) \propto \exp \left[-\frac{mc^2}{\hbar\omega\bar{n}} \left(\frac{\Delta\omega}{\omega} \right)^2 \right] = \exp \left[-\frac{1}{2\sigma^2} \left(\frac{\Delta\omega}{\omega} \right)^2 \right] \quad (\text{B.18})$$

with $\frac{\Delta\omega}{\omega}$ as the sideband-order index. From Eq. B.18 we get

$$\begin{aligned} \sigma^2 &= \frac{\hbar\omega\bar{n}}{2mc^2} = \frac{\hbar k}{2mc} \bar{n} \\ &= \frac{\hbar}{2m\omega} k^2 \bar{n} = k^2 x_0 \bar{n} \\ &= \eta^2 \bar{n} \end{aligned} \quad (\text{B.19})$$

B.3. Coupling strength fluctuations on an addressed ion due to hot axial modes

Due to the high phonon population ($\bar{n} \approx 200$) in the axial mode at shallow trapping potentials (220 kHz), the wave-function of a single ion expands into macroscopic regimes. The spread of the zero-point wavefunction is given by:

$$x_0 = \sqrt{\frac{\hbar}{2m\omega}}. \quad (\text{B.20})$$

This results in $x \approx 30$ nm for the ground state. Since the ion is confined in a harmonic potential, the wave-function increases with \sqrt{n} . We define the size of the wave-function as the distance between the two points of highest probability amplitude (classically these are the reversal points of an oscillator). A Fock-state of $n = 500$ has an expansion on the order of 750 nm

$$\Psi_n(x) = \frac{1}{\sqrt{2^n n!}} \left(\frac{m\omega}{\pi\hbar}\right)^{1/4} H_n\left(\sqrt{\frac{m\omega}{\hbar}}x\right) e^{-\frac{m\omega}{2\hbar}x^2}. \quad (\text{B.21})$$

Here, H_n is the n^{th} Hermite polynomial which can be calculated with the following recurrence relation

$$H_0(x) = 1 \quad (\text{B.22})$$

$$H_1(x) = 2x \quad (\text{B.23})$$

$$H_{n+1}(x) = 2xH_n(x) - H'_n(x) \quad (\text{B.24})$$

$$= 2xH_n(x) - 2nH_{n-1}(x). \quad (\text{B.25})$$

The last step is valid because the Hermite polynomials constitute an Appell sequence, i.e. they satisfy the relation: $\frac{d}{dx}p_n(x) = 2np_{n-1}(x)$. In order to calculate the coupling strength for a Fock state $\Psi_n(x)$ with a given intensity distribution of a laser-beam $I(x) \sim \exp(-x^2/2\sigma^2)$, we compute the overlap integral:

$$S_n = \int_{-\infty}^{\infty} |\Psi_n(x)|^2 I(x) dx. \quad (\text{B.26})$$

Then, the normalized coupling strength is given by:

$$\tilde{\Omega}_n = S_n/S_0. \quad (\text{B.27})$$

Note: The way we define $\tilde{\Omega}_n$ it is proportional to the intensity I . The decay of the addressed Rabi-oscillation is then computed by drawing the $\tilde{\Omega}_n$ from a thermal distribution \bar{n} .

C. Derivation of spectroscopic signals

These derivations are taken from [28, Supplemental Material] and provide additional and detailed information regarding the analysis of the spectroscopic signals presented in section 5.4.

C.1. Spectroscopic signals for single quasiparticle states

We perform spectroscopy of a trapped-ion system modelled by the XY Hamiltonian, Eq. (5.4), of N coupled spins. As discussed in Fig. 5.8 in section 5.4, the spectrum of H_{XY} splits into uncoupled subspaces with integer total excitation number (number of up-pointing spins), allowing us to study each subspace individually or to compare the energy of states within one subspace against the energy of a reference state in another subspace. In the single-excitation subspace, one can calculate the eigenenergies (E_k) and eigenmodes ($|k\rangle = \sigma_k^+ |0\rangle$), with $\sigma_k^+ = \sum_j \tilde{A}_j^k \sigma_j^z$ from the model Hamiltonian simply by diagonalizing the $N \times N$ matrix J_{ij} .

To spectroscopically measure the energies E_k , we aim to create a superposition of the ground state $|0\rangle$ with the eigenstate $|k\rangle$. This superposition can be approximated by an initial product state

$$\begin{aligned} |\psi_\theta\rangle &= \bigotimes_{j=1}^N \left[\cos(\theta_j) |\downarrow\rangle_j + \sin(\theta_j) |\uparrow\rangle_j \right] \\ &= C \left[1 + \sum_j \tan(\theta_j) \sigma_j^+ + \sum_{i,j} \tan(\theta_i) \tan(\theta_j) \sigma_i^+ \sigma_j^+ \right. \\ &\quad \left. + \mathcal{O}(\tan(\theta)^3) \right] |0\rangle. \end{aligned} \quad (\text{C.1a})$$

Here, $C \equiv \prod_{j=1}^N \cos(\theta_j)$ provides the overall normalization of the wave function. The angles θ_j are chosen such that $\tan \theta_j = \gamma A_j^k$ where $A_j^k = \sqrt{\frac{2}{N+1}} \sin\left(\frac{kj\pi}{N+1}\right)$ are the coefficients of a generic standing wave. For this choice, the initial state is given by

$$|\psi_k\rangle = C \left[|0\rangle + \gamma \sum_j A_j^k \sigma_j^+ |0\rangle + \mathcal{O}(\gamma^2) \right] \quad (\text{C.2})$$

$$\approx C \left[|0\rangle + \gamma |k\rangle + \mathcal{O}(\gamma^2) \right]. \quad (\text{C.3})$$

The variable γ determines the probabilities p_n of generating n spin excitations. In particular, we

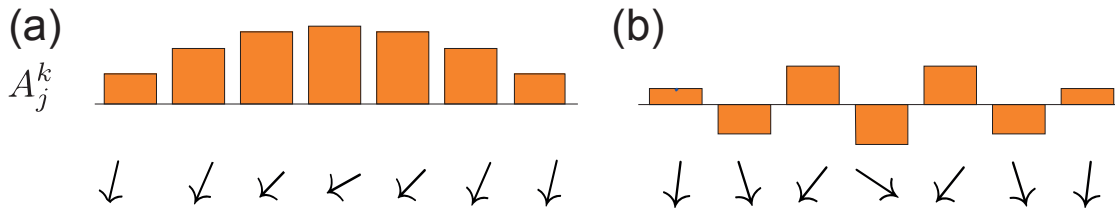


Figure C.1.: Two schematic examples of spinwaves where each spin j is rotated by the angle θ_j . (a) is an example for the highest spinwave mode $|k = 1\rangle$ and (b) for the lowest spinwave mode $|k = 7\rangle$.

have

$$p_0 = |\langle \psi_k | 0 \rangle|^2 = C^2 = \prod_j \frac{1}{1 + (\gamma A_j^k)^2}, \quad (\text{C.4})$$

$$p_1 = C^2 \sum_j \tan^2 \theta_j = \gamma^2 p_0 \sum_j (A_j^k)^2, \quad (\text{C.5})$$

$$p_2 = C^2 \sum_{i < j} \tan^2 \theta_i \tan^2 \theta_j = \gamma^4 p_0 \sum_{i < j} (A_i^k A_j^k)^2. \quad (\text{C.6})$$

Similarly, for the measurement of energy differences $E_k - E'_k$, we would like to create superposition states $|k\rangle + |k'\rangle$. In this case we choose $\tan \theta_j = \gamma(A_j^k + A_j^{k'})$ in order to create

$$|\psi_{kk'}\rangle \approx C \left[|0\rangle + \gamma(|k\rangle + |k'\rangle) + \mathcal{O}(\gamma^2) \right]. \quad (\text{C.7})$$

For the calculation of the probabilities in this case, one has to replace A_j^k by $A_j^k + A_j^{k'}$ in Eqs. (C.4–C.6).

In our experiment, the product states $|\psi_\theta\rangle$ are generated by a series of laser pulses rotating each spin by the desired angle θ_j . A particularity of the states of type $|\psi_\theta\rangle$ is that all spins lie in a single plane of the Bloch sphere spanned by the y and z axes. Figure C.1 shows schematic examples of two spin waves and their corresponding A_j^k . To create the states, the system is first prepared into the ground state $|\downarrow\rangle^{\otimes N} = |0\rangle$ by optical pumping. Then, a global resonant laser pulse rotates all spin simultaneously around the y -axis into the equatorial plane of the Bloch sphere such that they are aligned with the x -axis. Next, a steerable, tightly focussed off-resonant laser beam induces a rotation on individual ions around the z -axis via an ac-Stark shift induced mostly by dipole transitions connecting the spin states to other electronic states. By controlling the pulse length we control the rotation angle of each ion j . However, the sense of the rotation cannot be changed which slightly complicates the creation of states with both positive and negative rotation angles θ_j . Replacing rotations with negative angles θ_j by $2\pi + \theta_j$ could result in unnecessarily large rotation angles if $\theta_j \ll 1$. Instead, we rotate each spin by $\theta_j + |\min\{\theta_i\}|$. This over-rotation allows us to reach negative values θ_j by applying a second global, resonant pulse reversing the very first rotation around the y -axis followed by a final rotation around the x -axis which corrects for the over-rotation of $|\min\{\theta_i\}|$ yielding $|\psi_\theta\rangle$ with the right amplitudes and phases. With a slightly more complicated pulse sequence it would also be possible to generate any product state of spins.

C.1.1. Absolute quasiparticle energies

For the spectroscopy of absolute energy values E_k , we choose $\tan(\theta_j) = \gamma A_j^k$ to generate the initial state $|\psi_k\rangle$. The time-evolved state is then $|\psi(t)\rangle = e^{-iH_{XY}t} |\psi_k\rangle$. If this state is measured directly in the x -basis, with respect to the frame of Eqn. (5.4), the signal would read:

$$\begin{aligned} \langle \psi(t) | \sigma_i^x | \psi(t) \rangle &= \langle \psi_k | e^{iH_{XY}t} \sigma_i^x e^{-iH_{XY}t} | \psi_k \rangle & (C.8a) \\ &= C^2 \gamma \left(e^{-iE_k t/\hbar} \langle 0 | \sigma_i^x \sigma_k^+ | 0 \rangle + \text{c.c.} \right) + \mathcal{O}(\gamma^3) \\ &= C^2 \gamma \left(e^{-iE_k t/\hbar} A_i^k + \text{c.c.} \right) + \mathcal{O}(\gamma^3) \end{aligned}$$

This observable contains a strong oscillation at the quasiparticle energy E_k . The contributions from individual spins (ions) can be constructively summed to $\sum_i A_i^k \langle \psi(t) | \sigma_i^x | \psi(t) \rangle = \langle 0 | \sigma_k^-(t) \sigma_k^+ | 0 \rangle + \text{c.c.} + \mathcal{O}(\gamma^3)$, with $\sigma_k^-(t) = e^{iH_{XY}t} \sigma_k^- e^{-iH_{XY}t}$. Note, to leading order this is equivalent to the single-particle Greens function [303].

However, we do not measure directly in the x -basis (or y -basis) of Eq. (5.4), as assumed in Eq. (C.8). Measurements of the magnetization in the x - y plane of the Bloch sphere are carried out by first performing $\pi/2$ pulses with a laser resonant with the pseudo-spin transition followed by a fluorescence measurement projecting the spin onto either $|\uparrow\rangle$ or $|\downarrow\rangle$. This corresponds to measurement of $\langle \sigma_x \rangle$ or $\langle \sigma_y \rangle$ in the reference frame of the Hamiltonian (B.1). When changing into the reference frame of the Hamiltonians (5.1) or (5.4), these single-spin measurements correspond to measurements of

$$\sigma^{\tilde{x}} = e^{i\frac{\delta}{2}t\sigma^z} \sigma^x e^{-i\frac{\delta}{2}t\sigma^z} = \cos(\delta t) \sigma^x - \sin(\delta t) \sigma^y \quad (C.9)$$

$$\sigma^{\tilde{y}} = e^{i\frac{\delta}{2}t\sigma^z} \sigma^y e^{-i\frac{\delta}{2}t\sigma^z} = \sin(\delta t) \sigma^x + \cos(\delta t) \sigma^y \quad (C.10)$$

$$\sigma^{\tilde{z}} = e^{i\frac{\delta}{2}t\sigma^z} \sigma^z e^{-i\frac{\delta}{2}t\sigma^z} = \sigma^z. \quad (C.11)$$

Note that measurements in the logical (z -basis) are unaffected by this frame change. The consequence of measuring in a rotated frame in the x or y basis is simply that we observe oscillations due to energy gaps $\epsilon_k = E_k - 2B$, as presented in Fig. 5.10.

C.1.2. Relative quasiparticle energies

To observe beatnotes between different eigenenergies within the single-excitation subspace, we prepare approximate superpositions of two eigenfunctions, $\tan \theta_j = \gamma (A_j^{k_1} + A_j^{k_2})$, yielding the initial state $|\psi_{kk'}\rangle$. When measuring the observable σ_i^z for spin i in the time evolved state $|\psi(t)\rangle =$

$e^{-iH_{XY}t}|\psi_{kk'}\rangle$, the observed signal is

$$\begin{aligned}
\langle\psi(t)|\sigma_i^z|\psi(t)\rangle &= \langle\psi_{kk'}|e^{iH_{XY}t}\sigma_i^ze^{-iH_{XY}t}|\psi_{kk'}\rangle = \\
&C^2\left[\langle 0|\sigma_i^z|0\rangle\right. \\
&+ \gamma^2\langle 0|\left(\sigma_{k_1}^-e^{iE_{k_1}t/\hbar}+\sigma_{k_2}^-e^{iE_{k_2}t/\hbar}\right)\sigma_i^z\left(\sigma_{k_1}^+e^{-iE_{k_1}t/\hbar}+\sigma_{k_2}^+e^{-iE_{k_2}t/\hbar}\right)|0\rangle \\
&+ \gamma^4\langle 0|\left(\sigma_{k_1}^-+\sigma_{k_2}^-\right)^2e^{iH_{XY}t}\sigma_i^ze^{-iH_{XY}t}\left(\sigma_{k_1}^++\sigma_{k_2}^+\right)^2|0\rangle \\
&\left.+ \mathcal{O}(\gamma^6)\right]. \tag{C.12a}
\end{aligned}$$

When measuring σ_i^z , post-selecting measurement outcomes with a fixed number of total spin-up excitations (n) allows the dynamics (and therefore energy gaps) in different subspaces to be studied independently. We define projection operators, Π_n , which denotes the projector onto the subspace with excitation number n . To study the single excitation subspace we extract the observable

$$\begin{aligned}
\langle\psi(t)|\Pi_1\sigma_i^z\Pi_1|\psi(t)\rangle &= C^2\gamma^2\left[\langle k_1|\sigma_i^z|k_1\rangle\right. \\
&+ \langle k_2|\sigma_i^z|k_2\rangle \\
&\left.+ 2\Re\left(e^{i(E_{k_1}-E_{k_2})t/\hbar}\langle k_1|\sigma_i^z|k_2\rangle\right)\right], \tag{C.13}
\end{aligned}$$

Here, the signal oscillates with a frequency given by the energy difference of the eigenmodes. For the initial state where $\tan(\theta_j) = \gamma(A_j^{k_1} + A_j^{k_2})$, the oscillations have amplitude proportional to $2A_j^{k_1}A_j^{k_2}$ (for $k_1 \neq k_2$). The average signal from various spins is therefore maximized by Fourier-transforming the weighted sum

$$M_1(t) = \sum_j \text{sign}\left(A_j^{k_1}A_j^{k_2}\right)\langle\Pi_1\sigma_j^z\Pi_1\rangle. \tag{C.14a}$$

C.2. Spectroscopic signals for two quasiparticle states

The dynamics in higher excitation subspaces becomes more complicated because the quasiparticle modes that diagonalize H_{XY} in the single-excitation subspace are subject to the hard-core constraint $\sigma_j^+\sigma_j^+ = 0$. In a dilute system, i.e., when there are few excitations, $\sum_j \sigma_j^+\sigma_j^-/N \ll 1$, the excitations become approximately independent. We can then construct a perturbation theory around the non-interacting eigenmodes without any hard-core constraint.

C.2.1. Mapping spin operators to bosonic operators

A formal way to construct a perturbation theory around the non-interacting eigenmodes is by applying the Holstein–Primakoff transformation [208] to obtain bosonic creation and annihilation

operators \tilde{b}_i^\dagger and \tilde{b}_i ,

$$\sigma_j^- \rightarrow \sqrt{2S} \sqrt{1 - \frac{\tilde{b}_j^\dagger \tilde{b}_j}{2S}} \tilde{b}_j, \quad (\text{C.15a})$$

$$\sigma_j^+ \rightarrow \sqrt{2S} \tilde{b}_j^\dagger \sqrt{1 - \frac{\tilde{b}_j^\dagger \tilde{b}_j}{2S}}, \quad (\text{C.15b})$$

$$\sigma_j^z \rightarrow -S + \tilde{b}_j^\dagger \tilde{b}_j, \quad (\text{C.15c})$$

where $S = \frac{1}{2}$ is the length of the spin (we keep the factor $2S$ as it provides a convenient way to distinguish different perturbative contributions). The Holstein–Primakoff transformation conserves the bosonic commutation relations between spins on different sites $[\sigma_i^-, \sigma_j^+] = 0$, $i \neq j$, and the onsite hard-core constraint $\sigma_j^+ \sigma_j^+ = 0$. In linear spin-wave theory (LSWT) [304], one expands the spin Hamiltonian to leading order in the bosonic occupations, which amounts to neglecting the constraint by setting $\sqrt{1 - \frac{\tilde{b}_j^\dagger \tilde{b}_j}{2S}} \rightarrow 1$. The result is the approximation

$$H_{XY} \approx H_{\text{LSWT}} = 2S \sum_{i < j} J_{ij} (\tilde{b}_i^\dagger \tilde{b}_j + h.c.), \quad (\text{C.16})$$

It is straightforward to diagonalize the linear spin-wave Hamiltonian H_{LSWT} to find its eigenenergies E_k and eigenmodes $b_k^\dagger = \sum_j A_j^k \tilde{b}_j^\dagger$ (the spin waves), which reproduce the exact physics in the single-excitation subspace. If there was no hard-core constraint, combinations of spin waves would also define the eigenstates in higher occupation subspaces. For low spin-wave densities, one can expect this constraint to only play a perturbative role, motivating the use of Hamiltonian H_{LSWT} as starting point for a perturbative expansion in the spin-wave interactions.

C.2.2. Perturbative treatment of spin-wave interactions

One can obtain leading corrections due to hard-core interactions by expanding the square roots to next order in the spin-wave density $\langle \tilde{b}_j^\dagger \tilde{b}_j | / |2S\rangle$, yielding

$$H_{XY} \approx H_{\text{LSWT}} + \hat{V}, \quad (\text{C.17})$$

with $\hat{V} = -\frac{1}{2} \sum_{i,j} J_{ij} (\tilde{b}_j^\dagger \tilde{b}_j^\dagger \tilde{b}_j \tilde{b}_i + \tilde{b}_j^\dagger \tilde{b}_i^\dagger \tilde{b}_i \tilde{b}_j)$. The eigenstates of the unperturbed system are given by $|k_1, k_2\rangle_{\text{SW}} = b_{k_1}^\dagger b_{k_2}^\dagger |0\rangle / \sqrt{1 + \delta_{k_1, k_2}}$, where $|0\rangle = |\downarrow\rangle^{\otimes N}$ is the spin-wave vacuum and the δ_{k_1, k_2} takes care of correct normalisation. The perturbative shifts of the corresponding energies are in first order

$$V_{k_1, k_2} \equiv \langle k_1, k_2 | \hat{V} | k_1, k_2 \rangle_{\text{SW}} = -\frac{2(E_{k_1} + E_{k_2}) \mathcal{M}_{k_1 k_2}^{k_1 k_2}}{1 + \delta_{k_1 k_2}}. \quad (\text{C.18})$$

The strength of the interactions is determined by the geometrical overlap between different spin-wave modes,

$$\mathcal{M}_{k_1, k_2}^{k_3, k_4} = \sum_j A_j^{k_1} A_j^{k_2} A_j^{k_3} A_j^{k_4}, \quad (\text{C.19})$$

and can be visualised as a contact interaction vertex between two incoming and two outgoing waves. In this picture, the factor $1/2$ in the case $k_1 = k_2$ can be understood from the fact that for indistinguishable waves there is only one outgoing channel, whereas there are two for distinguishable waves.

C.2.3. Expected signal

We can use these approximate energies to evaluate the expected signal in the two-excitation manifold. To this end, we approximate the time evolution as

$$e^{-iH_{XY}t/\hbar} |k_1, k_2\rangle \approx e^{-i(H_{LSWT} + \hat{V})t/\hbar} (|k_1, k_2\rangle_{SW} + |\delta\psi(k_1, k_2)\rangle). \quad (\text{C.20})$$

If we are interested only in the strongest frequencies, we can neglect corrections $|\delta\psi(k_1, k_2)\rangle$ to the states $|k_1, k_2\rangle = \sigma_{k_1}^+ \sigma_{k_2}^+ |0\rangle$, which correspond to scattering into other spin-wave modes, and approximate

$$e^{-iH_{XY}t/\hbar} |k_1, k_2\rangle \approx e^{-i(E_{k_1} + E_{k_2} + V_{k_1, k_2})t/\hbar} |k_1, k_2\rangle. \quad (\text{C.21})$$

We now define $\Delta E_{k_1, k_2} = E_{k_1} - E_{k_2}$. For any observable \mathcal{O}^z that is diagonal in the σ^z Pauli matrices, the observed signal in the two-excitation subspace is

$$\begin{aligned} & \langle \psi(t) | \Pi_2 \mathcal{O}^z \Pi_2 | \psi(t) \rangle \approx \\ & \mathcal{C}^2 \gamma^4 [\langle k_1 k_1 | \mathcal{O}^z | k_1 k_1 \rangle + \langle k_2 k_2 | \mathcal{O}^z | k_2 k_2 \rangle + 4 \langle k_1 k_2 | \mathcal{O}^z | k_1 k_2 \rangle \\ & + 2 \cos\left(\frac{2\Delta E_{k_1, k_2} + V_{k_1, k_1} - V_{k_2, k_2}}{\hbar} t\right) \langle k_1 k_1 | \mathcal{O}^z | k_2 k_2 \rangle \\ & + 4 \cos\left(\frac{\Delta E_{k_1, k_2} + V_{k_1, k_1} - V_{k_1, k_2}}{\hbar} t\right) \langle k_1 k_1 | \mathcal{O}^z | k_1 k_2 \rangle \\ & + 4 \cos\left(\frac{\Delta E_{k_1, k_2} + V_{k_1, k_2} - V_{k_2, k_2}}{\hbar} t\right) \langle k_1 k_2 | \mathcal{O}^z | k_2 k_2 \rangle \\ & + \text{corrections from other states}]. \end{aligned} \quad (\text{C.22})$$

This formula neglects all higher-order contributions in \hat{V} , including scatterings into other than the initially prepared modes k_1, k_2 . As long as perturbation theory is a good description of the two-excitation subspace, we thus expect predominantly three frequencies in the time-evolution of the magnetization signal, which lie at $h\nu_a = |\Delta E_{k_1, k_2} + V_{k_1, k_1} - V_{k_1, k_2}|$, $h\nu_b = |\Delta E_{k_1, k_2} + V_{k_1, k_2} - V_{k_2, k_2}|$, and $h\nu_c = |2\Delta E_{k_1, k_2} + V_{k_1, k_1} - V_{k_2, k_2}|$. Indeed, this three-peak structure with $\nu_a + \nu_b = \nu_c$ is what we observe in the data for $\{k_1 = 1, k_2 = 7\}$, as presented in Fig. 5.12.

To derive simple quantitative estimates, we use sine-wave amplitudes for the eigenfunctions, $A_j^k = \sqrt{\frac{2}{N+1}} \sin(k \cdot j \frac{\pi}{N+1})$, yielding the interaction-shifted frequencies $\nu_a = (1 - 0.113)\Delta E_{k_1, k_2}/h$, $\nu_b = (1 - 0.262)\Delta E_{k_1, k_2}/h$, and $\nu_c = (2 - 0.375)\Delta E_{k_1, k_2}/h$ for $\{k_1 = 1, k_2 = 7\}$.

C.2.4. Summation of spin-spin correlation measurements

In the two-particle subspace, we study weighted sums of two-spin projectors $\mathcal{P}_{ij}^z = \frac{1}{4} (\sigma_i^z + 1) (\sigma_j^z + 1)$, i.e., the probability that both ions i and j are in the state $|\uparrow\rangle$. The corresponding expectation values

are

$$\frac{1}{4} \langle k_1 k_2 | (\sigma_i^z \sigma_j^z + \sigma_i^z + \sigma_j^z + 1) | k_3 k_4 \rangle = \left(A_i^{k_1} A_j^{k_2} + A_i^{k_2} A_j^{k_1} \right) \left(A_i^{k_3} A_j^{k_4} + A_i^{k_4} A_j^{k_3} \right). \quad (\text{C.23})$$

For the component with oscillation frequency ν_c , we have $\frac{1}{4} \langle k_1 k_1 | (\sigma_i^z \sigma_j^z + \sigma_i^z + \sigma_j^z + 1) | k_2 k_2 \rangle = 4A_j^{k_1} A_i^{k_1} A_j^{k_2} A_i^{k_2}$, so that the signal is maximised by

$$M_{2a}(t) = \sum_{l < m} \text{sign} \left(A_j^{k_1} A_i^{k_1} A_j^{k_2} A_i^{k_2} \right) \langle \mathcal{P}_{ij}^z \rangle. \quad (\text{C.24})$$

For $\{k_1, k_2\} = \{1, 7\}$, this choice simultaneously suppresses the expectation values associated to the other two oscillation frequencies, so that it allows one to cleanly extract a single one of the three expected Fourier components.

Similarly, the component oscillating with ν_a has an amplitude $2|A_i^{k_1}|^2 A_j^{k_1} A_i^{k_2} + 2|A_j^{k_1}|^2 A_i^{k_1} A_j^{k_2}$. If we use

$$M_{2b}(t) = \sum_{i < j} \left(\text{sign} \left(A_i^k A_j^{k'} \right) + \text{sign} \left(A_i^{k'} A_j^k \right) \right) \langle \mathcal{P}_{ij}^z \rangle, \quad (\text{C.25})$$

the signals due to this component and the one at ν_b are maximized while the one at ν_c gets suppressed.

C.2.5. Validity of first-order perturbation theory: additional experimental data

The quality of the first-order perturbation theory for given eigenstates can be estimated by considering how well a state $|k_1 k_2\rangle$ remains localized in the two-excitation state space when taking the hard-core constraint into account. This amounts to acting on the vacuum $|0\rangle$ with $b_{k_1}^\dagger b_{k_2}^\dagger$ and computing the overlap of the resulting state to the exact eigenstates. The state $|k_1 = 1, k_2 = 7\rangle$, constructed from single-particle states at the edge of the spectrum, for example, remains well localized in few exact eigenstates, and therefore qualitative predictions of simple first-order perturbation theory in the spin-wave interaction work quite well. Other combinations, on the other hand, such as $|k_1 = 1, k_2 = 4\rangle$ (Fig. C.2) show many other spectral features deviating from the three-peak structure predicted by the perturbation theory. This comes from a considerable overlap with many of the true eigenstates in the two-excitation subspace, resulting in a diminished reliability of perturbation theory.

Since the spin-wave scattering is proportional to the overlaps $\mathcal{M}_{k_1, k_2}^{k_3, k_4}$, which decrease with reduced excitation density, estimates from perturbation theory will improve with increasing system size (if the excitation number is kept fixed). For the small system considered, the overlaps are quite large, lying in the range $\mathcal{M}_{k_1, k_2}^{k_3, k_4} \approx 0.1 - 0.25$, which explains the lack of quantitative reliability of non-linear spin-wave theory. For $N \rightarrow \infty$, however, corrections such as $\mathcal{M}_{k_1, k_2}^{k_3, k_4}$ go to 0 as $1/N$, and the states $|k_1 k_2\rangle_{\text{SW}}$ provide accurate approximations to the true eigenstates of the two-excitation subspace of H_{XY} .

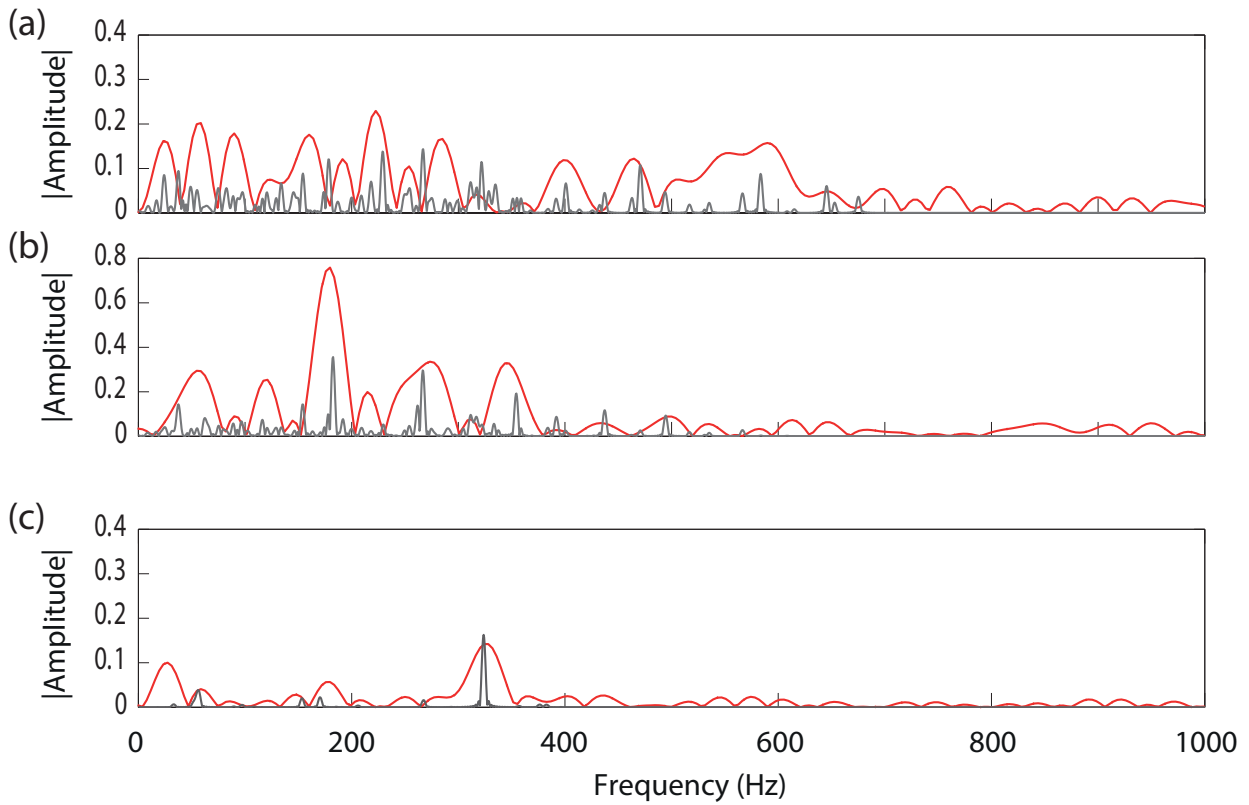


Figure C.2.: Spectroscopy of quasiparticle interactions. (a,b) Fourier spectra of the two-quasiparticle state $|\psi_{k,k'=1,4}^{(2)}\rangle$, obtained from summed signals (red curves), with $M_{2a}(t)$ to enhance $\nu_c = \nu_a + \nu_b$ (panel a) and $M_{2a}(t)$ to increase signals at $\nu_{a,b}$ (panel b). The measured peak positions compare well with those of a simulated evolution with longer times, yielding a narrower bandwidth (grey curves). However due to strong quasiparticle scattering a large number of frequencies components becomes apparent. The weakly interacting single-particle eigenmodes no longer provide a good basis for describing the system.

D. Reconstructed density matrices for MBQC

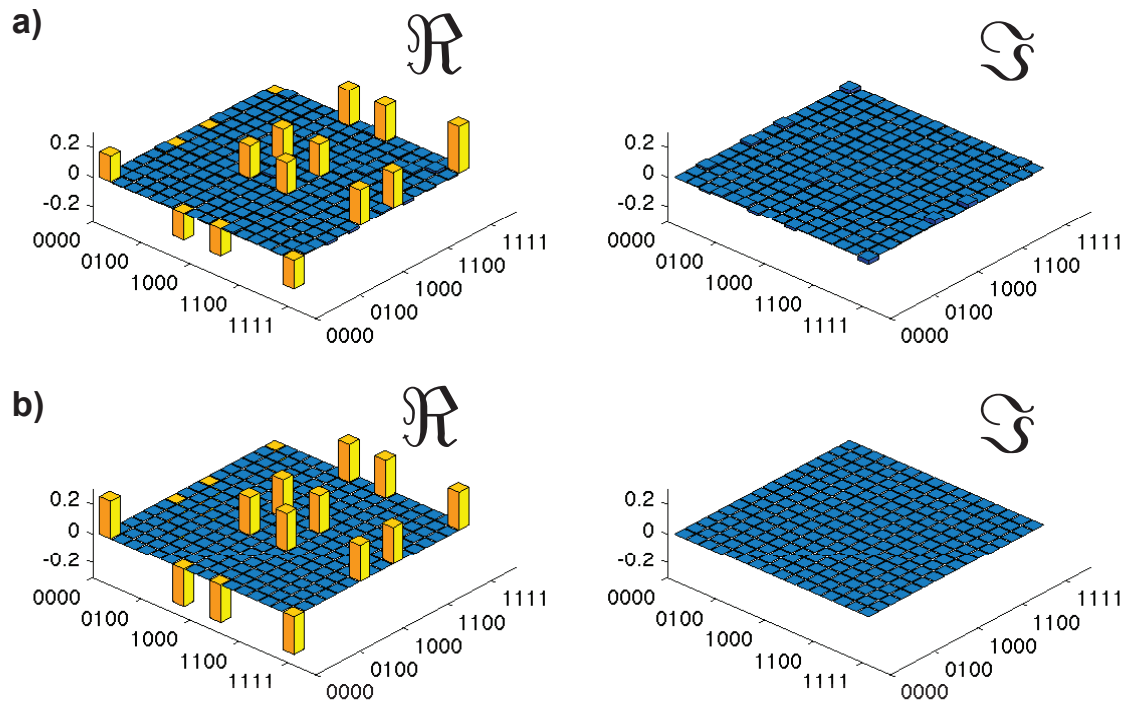


Figure D.1.: Box cluster a) The reconstructed density matrix of a box cluster state $|eBC\rangle$ using maximum likelihood reconstruction. The real \Re and the imaginary \Im are shown separately. b) The theoretical density matrix $|BC\rangle$ is plotted for comparison. The fidelity is calculated to be $\mathcal{F} = 0.846 \pm 0.005$ and the errors are estimated with Monte Carlo simulations.

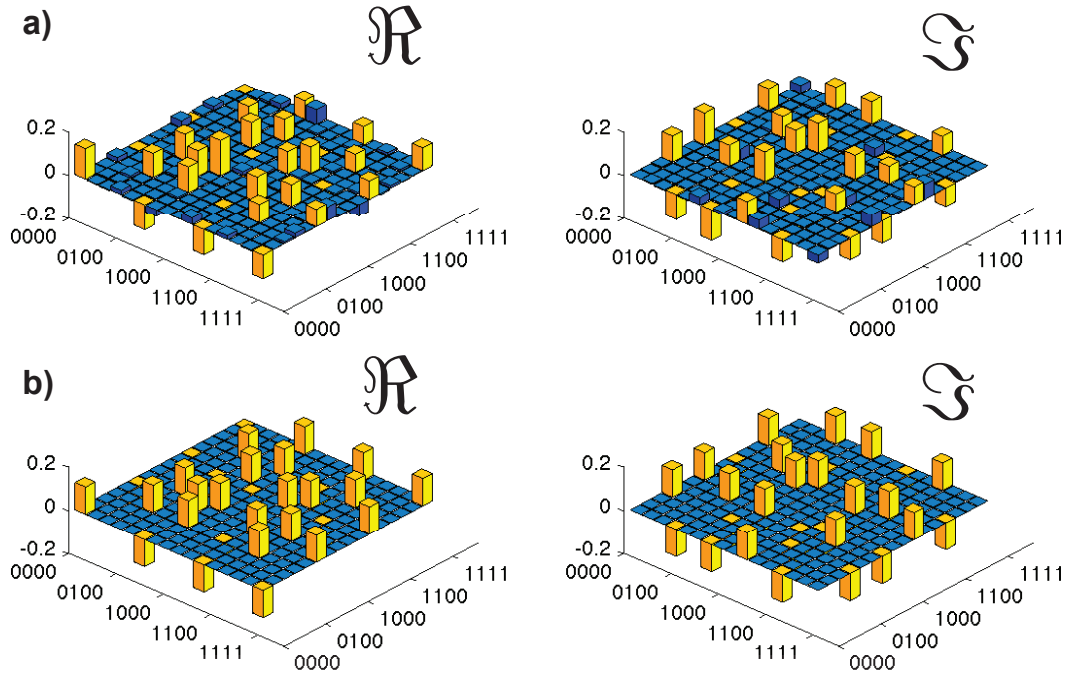


Figure D.2.: Linear cluster a) The real \Re and the imaginary \Im of the reconstructed experimental linear cluster $|eLC\rangle$. b) The theoretical density matrix $|LC\rangle$ is plotted for comparison. The fidelity is calculated to be $\mathcal{F} = 0.841 \pm 0.005$.

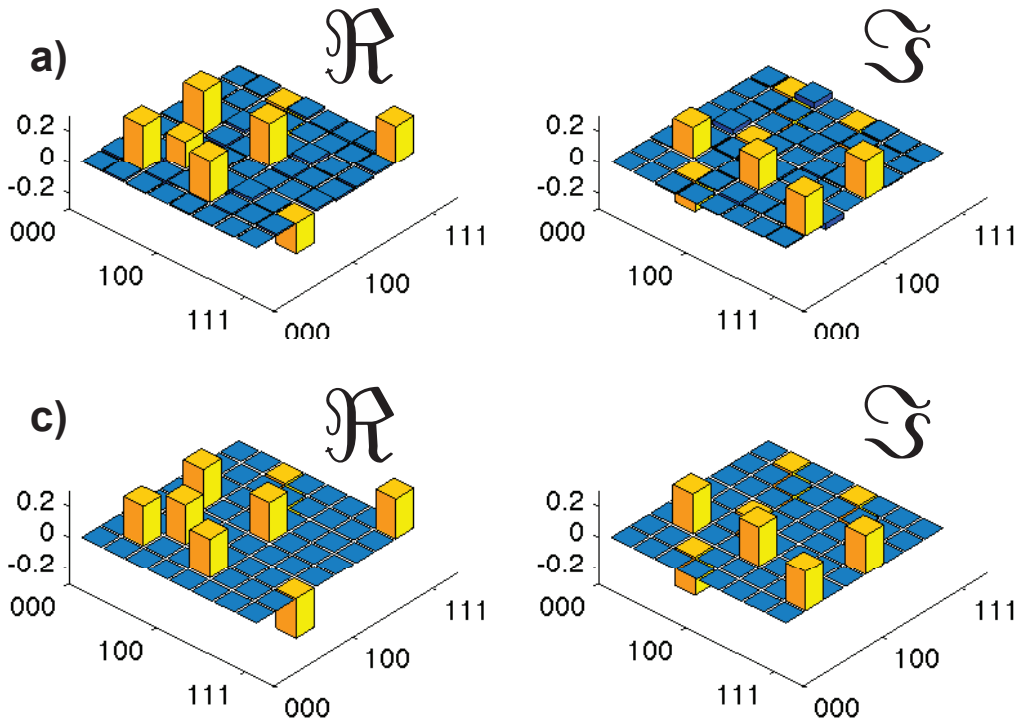


Figure D.3.: Error correction cluster EC_1 a) The real \Re and the imaginary \Im of the reconstructed experimental linear cluster $|eEC_1\rangle$. b) The theoretical density matrix $|EC_1\rangle$ is plotted for comparison. The fidelity is calculated to be $\mathcal{F} = 0.920 \pm 0.005$.

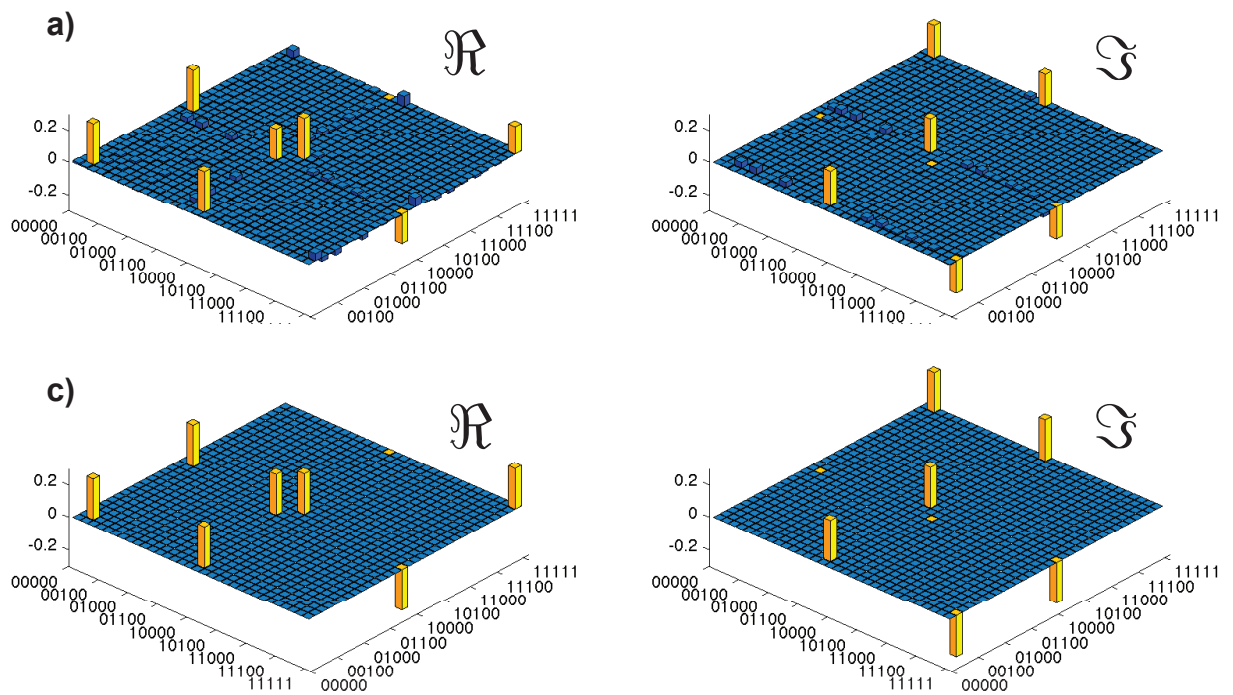


Figure D.4.: Error correction cluster EC_3 a) The real \Re and the imaginary \Im of the reconstructed experimental linear cluster $|eEC_3\rangle$. b) The theoretical density matrix $|EC_3\rangle$ is plotted for comparison. The fidelity is calculated to be $\mathcal{F} = 0.843 \pm 0.005$.

E. Correlated dephasing on two qubits

This appendix is taken from and is identical to the supplementary material of [230]. A more general analysis with regards to time-dependent dynamics and arbitrary noise distributions can be found in [283].

E.1. Separable operations can increase the correlation rank

In this section we show that applying a separable operation to a bipartite density matrix can increase the rank of the correlation matrix [252], henceforth called the correlation rank. We consider a bipartite Hilbert space $\mathcal{H} = \mathcal{H}_A \otimes \mathcal{H}_B$ and sets of arbitrary quantum operations $\{\epsilon_i^A\}$, $\{\epsilon_i^B\}$ working on the subspaces \mathcal{H}_A and \mathcal{H}_B , respectively. We call an operation ϵ_{sep} on \mathcal{H} *separable* if it can be put into the form $\epsilon_{\text{sep}} = \sum_{i=1}^P p_i \epsilon_i^A \otimes \epsilon_i^B$, with probabilities p_i and P denotes the number of terms in the sum. In order to introduce the notation which we will use in the following, we first review the definition of the correlation matrix. First, we represent the initial state ρ in terms of arbitrary, fixed bases of Hermitian operators $\{A_i\}$ and $\{B_i\}$ on \mathcal{H}_A and \mathcal{H}_B , respectively:

$$\rho = \sum_{i=1}^{d_A} \sum_{j=1}^{d_B} r_{ij} A_i \otimes B_j, \quad (\text{E.1})$$

where d_A and d_B denote the dimensions of \mathcal{H}_A and \mathcal{H}_B . The correlation matrix $M = (r_{ij})$ can be decomposed into its singular value decomposition, using orthogonal matrices U and V : $M = U \text{diag}(c_1, \dots, c_L, 0, \dots) V^T$. Here, c_i represent the nonzero singular values and R defines the correlation rank. Introducing $S_i = \sum_j u_{ji} A_j$ and $F_i = \sum_j v_{ji} B_j$, where $U = (u_{ij})$ and $V = (v_{ij})$, we can rewrite ρ as [252]

$$\rho = \sum_{i=1}^R c_i S_i \otimes F_i. \quad (\text{E.2})$$

In Ref. [275] it was shown that *unilocal* operations, defined as operations of the form $\epsilon^A \otimes \mathbb{I}$, cannot increase the correlation rank. First of all, we assure that this also holds for a *bilocal* operation $\epsilon^A \otimes \epsilon^B$, which requires access to both subsystems. We find

$$\rho' = (\epsilon^A \otimes \epsilon^B) \rho = \sum_{i=1}^R \sum_{k=1}^{d_A} \sum_{j=1}^{d_B} c_i d_{ik} e_{ij} A_k \otimes B_j, \quad (\text{E.3})$$

with $\epsilon_A(S_i) = \sum_k d_{ik} B_k$ and $\epsilon_B(F_i) = \sum_j e_{ij} B_j$. The rank of ρ' is now given by the rank of the matrix $F = (f_{kj})$, with $f_{kj} = \sum_{i=1}^R c_i d_{ik} e_{ij}$ which is still limited by the minimum of the rank of

the three matrices $C = \text{diag}(c_1, \dots, c_L, 0, \dots)$, $D = (d_{ik})$, and $E = (e_{ij})$, hence, by R . Hence, even bilocal operations cannot increase the correlation rank. However, if we allow for arbitrary separable maps the correlation rank can be increased:

$$\rho' = \sum_{i=1}^P p_i (\epsilon_i^A \otimes \epsilon_i^B) \rho = \sum_{i=1}^P \sum_{j=1}^R \sum_{k=1}^{d_A^2} \sum_{l=1}^{d_B^2} p_i c_j d_{jk}^i e_{jl}^i A_k \otimes B_l. \quad (\text{E.4})$$

We have introduced $\epsilon_i^A(S_j) = \sum_{k=1}^{d_A^2} d_{jk}^i A_k$ and $\epsilon_i^B(F_j) = \sum_{l=1}^{d_B^2} e_{jl}^i B_l$. Now, the rank of the correlation matrix $f_{kl} = \sum_{i=1}^P \sum_{j=1}^R p_i c_j d_{jk}^i e_{jl}^i$ can in principle go up to $\min\{P \cdot R, d_A^2, d_B^2\}$.

E.2. Correlated dephasing on two qubits

We assume a state of two qubits with reduced Bloch vectors \vec{r}^A and \vec{r}^B , expressing the reduced density matrices of subsystems \mathcal{H}_A and \mathcal{H}_B as

$$\rho_{A,B} = \frac{1}{2} (\mathbb{I} + \vec{r}^{A,B} \cdot \vec{\sigma}). \quad (\text{E.5})$$

Here $\vec{\sigma}$ denotes the vector of Pauli-matrices $\vec{\sigma} = (\sigma_x, \sigma_y, \sigma_z)^T$. The correlations between the qubits is contained in a real-valued matrix $\beta = (\beta_{ij})$, such that the total state can be represented in terms of Pauli matrices and the identity in its Fano-Form (see, e.g., [305]):

$$\rho = \frac{1}{4} \left(\mathbb{I} \otimes \mathbb{I} + \sum_{i=1}^3 r_i^A \sigma_i \otimes \mathbb{I} + \sum_{i=1}^3 r_i^B \mathbb{I} \otimes \sigma_i + \sum_{i=1}^3 \sum_{j=1}^3 \beta_{ij} \sigma_i \otimes \sigma_j \right). \quad (\text{E.6})$$

The correlation matrix is given by

$$M = \frac{1}{4} \begin{pmatrix} 1 & (\vec{r}^B)^T \\ \vec{r}^A & \beta \end{pmatrix}, \quad (\text{E.7})$$

where \vec{r}^T denotes the 1×3 matrix $\vec{r}^T = (r_x, r_y, r_z)$. The rank R of the correlation matrix M is given by [306]

$$R = 1 + \text{rk}(\beta - \vec{r}^A \otimes \vec{r}^B). \quad (\text{E.8})$$

Here $\vec{r}^A \otimes \vec{r}^B$ denotes the outer product: $(\vec{r}^A \otimes \vec{r}^B)_{ij} = r_i^A r_j^B$. In general, the matrix β can be decomposed into singular values, $\beta_{ij} = \sum_{k=1}^3 v_{ik} d_k w_{jk}$, with orthogonal matrices $V = (v_{ij})$ and $W = (w_{ij})$. Introducing two sets of orthonormal vectors $(\vec{v}_k)_i = v_{ik}$ and $(\vec{w}_k)_j = w_{jk}$ as the columns of V and W , we rewrite the state ρ as

$$\rho = \frac{1}{4} \left(\mathbb{I} \otimes \mathbb{I} + \vec{r}^A \cdot \vec{\sigma} \otimes \mathbb{I} + \mathbb{I} \otimes \vec{r}^B \cdot \vec{\sigma} + \sum_{k=1}^3 d_k \vec{v}_k \cdot \vec{\sigma} \otimes \vec{w}_k \cdot \vec{\sigma} \right). \quad (\text{E.9})$$

E.2.1. Dephasing by fluctuating rotations

Single-qubit rotations of a Bloch vector \vec{r} around an axis determined by the normalized vector \vec{n} are described by the operator $R_{\vec{n}}(\theta) = e^{-i\theta\vec{n}\cdot\vec{\sigma}/2}$. Using the relation

$$(\vec{n} \cdot \vec{\sigma})(\vec{r} \cdot \vec{\sigma}) = (\vec{n} \cdot \vec{r})\mathbb{I} + i(\vec{n} \times \vec{r}) \cdot \vec{\sigma}, \quad (\text{E.10})$$

we obtain

$$\begin{aligned} (\vec{n} \cdot \vec{\sigma})(\vec{r} \cdot \vec{\sigma})(\vec{n} \cdot \vec{\sigma}) &= (\vec{n} \cdot \vec{r})(\vec{n} \cdot \vec{\sigma}) - (\vec{n} \times \vec{r} \times \vec{n}) \cdot \vec{\sigma} \\ &= 2(\vec{n} \cdot \vec{r})(\vec{n} \cdot \vec{\sigma}) - (\vec{r} \cdot \vec{\sigma}). \end{aligned} \quad (\text{E.11})$$

In combination with $e^{-i\theta\vec{n}\cdot\vec{\sigma}/2} = \cos(\theta/2)\mathbb{I} + i\sin(\theta/2)\vec{n} \cdot \vec{\sigma}$, this allows us to describe an arbitrary rotation of a Bloch vector \vec{r} around \vec{n} by

$$\begin{aligned} e^{-i\theta\vec{n}\cdot\vec{\sigma}/2}\vec{r} \cdot \vec{\sigma}e^{i\theta\vec{n}\cdot\vec{\sigma}/2} &= \left[\cos^2\left(\frac{\theta}{2}\right) - \sin^2\left(\frac{\theta}{2}\right) \right] \vec{r} \cdot \vec{\sigma} - 2i\sin\left(\frac{\theta}{2}\right)\cos\left(\frac{\theta}{2}\right) (\vec{r} \times \vec{n}) \cdot \vec{\sigma} \\ &\quad + 2\sin^2\left(\frac{\theta}{2}\right) (\vec{n} \cdot \vec{r})\vec{n} \cdot \vec{\sigma}. \end{aligned} \quad (\text{E.12})$$

Averaging uniformly over the angle θ generates a dephasing effect. The new Bloch vector points into the direction \vec{n} of the rotation:

$$\frac{1}{2\pi} \int_0^{2\pi} d\theta e^{-i\theta\vec{n}\cdot\vec{\sigma}/2}\vec{r} \cdot \vec{\sigma}e^{i\theta\vec{n}\cdot\vec{\sigma}/2} = (\vec{n} \cdot \vec{r})\vec{n} \cdot \vec{\sigma}. \quad (\text{E.13})$$

Correlated dephasing

A separable map describing correlated dephasing in both subsystems is generated by

$$\begin{aligned} \epsilon_{cd}^{\vec{n}}(\vec{v} \cdot \vec{\sigma} \otimes \vec{w} \cdot \vec{\sigma}) &= \frac{1}{2\pi} \int_0^{2\pi} d\theta R_{\vec{n}}(\theta)\vec{v} \cdot \vec{\sigma}R_{\vec{n}}^\dagger(\theta) \otimes R_{\vec{n}}(\theta)\vec{w} \cdot \vec{\sigma}R_{\vec{n}}^\dagger(\theta) \\ &= \frac{1}{2\pi} \int_0^{2\pi} d\theta e^{-i\theta\vec{n}\cdot\vec{\sigma}/2}\vec{v} \cdot \vec{\sigma}e^{i\theta\vec{n}\cdot\vec{\sigma}/2} \otimes e^{-i\theta\vec{n}\cdot\vec{\sigma}/2}\vec{w} \cdot \vec{\sigma}e^{i\theta\vec{n}\cdot\vec{\sigma}/2} \\ &= \frac{1}{2}\vec{v} \cdot \vec{\sigma} \otimes \vec{w} \cdot \vec{\sigma} - \frac{1}{2}\vec{v} \cdot \vec{\sigma} \otimes (\vec{n} \cdot \vec{w})\vec{n} \cdot \vec{\sigma} - \frac{1}{2}(\vec{n} \cdot \vec{v})\vec{n} \cdot \vec{\sigma} \otimes \vec{w} \cdot \vec{\sigma} \\ &\quad - \frac{1}{2}(\vec{v} \times \vec{n}) \cdot \vec{\sigma} \otimes (\vec{w} \times \vec{n}) \cdot \vec{\sigma} + \frac{3}{2}(\vec{n} \cdot \vec{v})\vec{n} \cdot \vec{\sigma} \otimes (\vec{n} \cdot \vec{w})\vec{n} \cdot \vec{\sigma}. \end{aligned} \quad (\text{E.14})$$

Kraus representation

Correlated dephasing can be given in form of a Kraus representation:

$$\epsilon_{cd}^{\vec{n}}(\rho) = \frac{1}{2}K_1\rho K_1 + \frac{1}{4}K_2\rho K_2 + \frac{1}{4}K_3\rho K_3, \quad (\text{E.15})$$

with the self-adjoint Kraus operators

$$\begin{aligned} K_1 &= \frac{1}{\sqrt{2}} (-\mathbb{I} \otimes \mathbb{I} + \vec{n} \cdot \vec{\sigma} \otimes \vec{n} \cdot \vec{\sigma}) \\ K_2 &= \frac{1}{\sqrt{2}} (\mathbb{I} \otimes \mathbb{I} + \vec{n} \cdot \vec{\sigma} \otimes \vec{n} \cdot \vec{\sigma}) \\ K_3 &= \frac{1}{\sqrt{2}} (-\mathbb{I} \otimes \vec{n} \cdot \vec{\sigma} + \vec{n} \cdot \vec{\sigma} \otimes \mathbb{I}). \end{aligned} \quad (\text{E.16})$$

E.2.2. Initial rank-1 states

We show that $R = 1$ if and only if $\rho = \rho_A \otimes \rho_B$: First, if ρ is a product state then obviously $R = 1$, as ρ_A and ρ_B can be seen as elements of operator bases of \mathcal{H}_A and \mathcal{H}_B , respectively. Conversely, assume that $R = 1$, then, according to Eq. (E.7), we find that $(1, \vec{r}^B) = c_1(r_1^A, \vec{\beta}_1) = c_2(r_2^A, \vec{\beta}_2) = c_3(r_3^A, \vec{\beta}_3) \in \mathbb{R}^4$ with $\beta = (\vec{\beta}_1, \vec{\beta}_2, \vec{\beta}_3)$. From this we conclude that $c_i = 1/r_i^A$ and $\vec{\beta}_i = r_i^A \vec{r}^B$. Inserting this into Eq. (E.6) yields

$$\begin{aligned} \rho &= \frac{1}{4} \left(\mathbb{I} \otimes \mathbb{I} + \vec{r}^A \cdot \vec{\sigma} \otimes \mathbb{I} + \mathbb{I} \otimes \vec{r}^B \cdot \vec{\sigma} + \vec{r}^A \cdot \vec{\sigma} \otimes \vec{r}^B \cdot \vec{\sigma} \right) \\ &= \frac{1}{2} (\mathbb{I} + \vec{r}^A \cdot \vec{\sigma}) \otimes \frac{1}{2} (\mathbb{I} + \vec{r}^B \cdot \vec{\sigma}). \end{aligned} \quad (\text{E.17})$$

This concludes the proof and implies that $\text{rk}(\beta) \leq 1$ for product states. Moreover, if $\text{rk}(\beta) = 1$ then the left- and right-singular vectors of β are given by the reduced Bloch vectors \vec{r}^A and \vec{r}^B , respectively and $\beta = \vec{r}^A \otimes \vec{r}^B$, in agreement with Eq. (E.8). We now determine the rank of the product state after being subject to correlated dephasing along \vec{n} . The correlation matrix of the state after application of the map is given by

$$\epsilon_{cd}^{\vec{n}}(M) = \frac{1}{4} \left(\begin{array}{c|c} 1 & (\vec{r}^B \cdot \vec{n}) \vec{n}^T \\ \hline (\vec{r}^A \cdot \vec{n}) \vec{n} & \epsilon_{cd}^{\vec{n}}(\vec{r}^A \otimes \vec{r}^B) \end{array} \right), \quad (\text{E.18})$$

with the rank

$$\begin{aligned} \text{rk}(\epsilon_{cd}^{\vec{n}}(M)) &= 1 + \text{rk} \left(\epsilon_{cd}^{\vec{n}}(\vec{r}^A \otimes \vec{r}^B) - (\vec{r}^B \cdot \vec{n})(\vec{r}^B \cdot \vec{n}) \vec{n} \otimes \vec{n} \right) \\ &= 1 + \text{rk} \left(\frac{1}{2} \left(\vec{r}^A \otimes \vec{r}^B - \vec{r}^A \otimes (\vec{r}^B \cdot \vec{n}) \vec{n} - (\vec{r}^A \cdot \vec{n}) \vec{n} \otimes \vec{r}^B - (\vec{r}^A \times \vec{n}) \otimes (\vec{r}^B \times \vec{n}) \right. \right. \\ &\quad \left. \left. + (\vec{r}^B \cdot \vec{n})(\vec{r}^B \cdot \vec{n}) \vec{n} \otimes \vec{n} \right) \right) \\ &= 1 + \text{rk} \left(\frac{1}{2} \left((\vec{r}^A - (\vec{r}^A \cdot \vec{n}) \vec{n}) \otimes (\vec{r}^B - (\vec{r}^B \cdot \vec{n}) \vec{n}) - (\vec{r}^A \times \vec{n}) \otimes (\vec{r}^B \times \vec{n}) \right) \right). \end{aligned} \quad (\text{E.19})$$

We obtain $\text{rk}(\epsilon_{cd}^{\vec{n}}(M)) = 1$ if and only if $\vec{n} = \vec{r}^A/r^A$ or $\vec{n} = \vec{r}^B/r^B$, with $r^A = \sqrt{\vec{r}^A \cdot \vec{r}^A}$ and $r^B = \sqrt{\vec{r}^B \cdot \vec{r}^B}$. Otherwise, the final rank is 3.

E.2.3. Initial rank-2 states

We consider states with maximally mixed reduced density matrices, i.e., $\vec{r}^A = \vec{r}^B = \vec{0}$. The rank of the correlation matrix is then given by $R = \text{rk}(\beta) + 1$. Hence, classical states with maximally mixed

marginals have $\text{rk}(\beta) \leq 1$ and $\beta = \mathbf{0}$ corresponds to the overall maximally mixed state, which has $R = 1$. Let's assume we have $R = 2$, hence, only one singular value of β is non-zero. Such a state has always zero discord as it can be written as

$$\rho_0 = \frac{1}{4} (\mathbb{I} \otimes \mathbb{I} + d\vec{v} \cdot \vec{\sigma} \otimes \vec{w} \cdot \vec{\sigma}). \quad (\text{E.20})$$

The matrix β is given by the outer product $\beta = d\vec{v} \otimes \vec{w}$.

We will use the following relation:

$$\text{rk} \left(\sum_{k=1}^3 \vec{v}_k \otimes \vec{w}_k \right) = \text{rk}(VW^T) \leq \min\{\text{rk}V, \text{rk}W\}, \quad (\text{E.21})$$

where the rank of the matrices V and W is determined by the number of linear independent vectors \vec{v}_k and \vec{w}_k , respectively. If one of the two sets is linearly independent, the rank is given by the number of linear independent vectors of the other set. Using this it is possible to specify a combination of conditions which guarantee the conversion of a classical rank-2 state with maximally mixed marginals into a fully correlated rank-4 state by correlated dephasing. Correlated dephasing on (E.20) yields the state

$$\begin{aligned} \epsilon_{cd}^{\vec{n}}(\rho_0) = \frac{1}{4} \left(\mathbb{I} \otimes \mathbb{I} + \frac{d}{2} [\vec{v} \cdot \vec{\sigma} \otimes (\vec{w} - (\vec{n} \cdot \vec{w})\vec{n}) \cdot \vec{\sigma} + (\vec{n} \cdot \vec{v})\vec{n} \cdot \vec{\sigma} \otimes (3(\vec{n} \cdot \vec{w})\vec{n} - \vec{w}) \cdot \vec{\sigma} \right. \\ \left. - (\vec{v} \times \vec{n}) \cdot \vec{\sigma} \otimes (\vec{w} \times \vec{n}) \cdot \vec{\sigma}] \right). \end{aligned} \quad (\text{E.22})$$

The set $\{\vec{v}, (\vec{n} \cdot \vec{v})\vec{n}, -\vec{v} \times \vec{n}\}$ is linearly independent if and only if \vec{n} is neither equal nor orthogonal to \vec{v} (or put equivalently $0 < \vec{n} \cdot \vec{v} < 1$, since both \vec{v} and \vec{n} are normalized to one). The latter implies that \vec{n} should be different from all the left-singular vectors of β , even those with singular value zero. According to Eq. (E.21), the rank of β after the correlated dephasing is now given by the number of linearly independent vectors in the set $\{\vec{w} - (\vec{n} \cdot \vec{w})\vec{n}, 3(\vec{n} \cdot \vec{w})\vec{n} - \vec{w}, \vec{w} \times \vec{n}\}$. Again, all three vectors are linearly independent if and only if $0 < \vec{n} \cdot \vec{w} < 1$. A rank-2 state with maximally mixed marginals is therefore converted into a rank-4 state if and only if $0 < \vec{n} \cdot \vec{v} < 1$ and $0 < \vec{n} \cdot \vec{w} < 1$. For states which are symmetric under permutation of the two qubits ($\vec{v} = \vec{w}$), this can be expressed directly in terms of β as the condition

$$0 < \vec{n}^T \beta \vec{n} / d < 1, \quad (\text{E.23})$$

where the Hilbert Schmidt norm of β is given by $d = \|\beta\| = \sqrt{\text{Tr}\beta^T\beta}$.

The above analysis tells us how to create rank-4 states. When do we obtain a state of rank 1, 2 or 3? If $\vec{n} = \vec{v}$ we get

$$\epsilon_{cd}^{\vec{n}}(\rho_0) = \frac{1}{4} (\mathbb{I} \otimes \mathbb{I} - d(\vec{v} \cdot \vec{w})\vec{v} \cdot \vec{\sigma} \otimes \vec{v} \cdot \vec{\sigma}), \quad (\text{E.24})$$

which has rank 2 if $\vec{v} \cdot \vec{w} > 0$, otherwise rank 1. The same holds for $\vec{n} = \vec{w}$. For $\vec{n} \cdot \vec{v} = 0$ the final

	$\vec{n} = \vec{w}$	$\vec{n} \cdot \vec{w} = 0$	$0 < \vec{n} \cdot \vec{w} < 1$
$\vec{n} = \vec{v}$	2	1	2
$\vec{n} \cdot \vec{v} = 0$	1	3	3
$0 < \vec{n} \cdot \vec{v} < 1$	2	3	4

Table E.1.: Rank of the correlation matrix after application of correlated dephasing to a rank-2 state with maximally mixed marginals.

state

$$\epsilon_{cd}^{\vec{n}}(\rho_0) = \frac{1}{4} \left(\mathbb{I} \otimes \mathbb{I} + \frac{d}{2} [\vec{v} \cdot \vec{\sigma} \otimes (\vec{w} - (\vec{n} \cdot \vec{w})\vec{n}) \cdot \vec{\sigma} - (\vec{v} \times \vec{n}) \cdot \vec{\sigma} \otimes (\vec{w} \times \vec{n}) \cdot \vec{\sigma}] \right) \quad (\text{E.25})$$

has rank 3 as long as $\vec{n} \cdot \vec{w} < 1$ (equivalent to $\vec{n} \neq \vec{w}$), which is also the case for $\vec{n} \cdot \vec{w} = 0$ if $\vec{n} \cdot \vec{v} < 1$.

E.2.4. Summary

For initial rank-1 states $\rho = \rho_A \otimes \rho_B$, with nonzero reduced Bloch vectors \vec{r}^A and \vec{r}^B , correlated dephasing around \vec{n} yields a state of

R=1 if \vec{n} is equal to either \vec{r}^A or \vec{r}^B ,

R=3 if \vec{n} differs from both \vec{r}^A and \vec{r}^B .

For initial rank-2 states with maximally mixed reduced density matrices ($\vec{r}^A = \vec{r}^B = 0$), correlated dephasing around \vec{n} yields a state of

R=1 if $\vec{n} = \vec{v}$ ($\vec{n} = \vec{w}$) and $\vec{n} \perp \vec{w}$ ($\vec{n} \perp \vec{v}$),

R=2 if $\vec{n} = \vec{v}$ ($\vec{n} = \vec{w}$) and $\vec{n} \not\perp \vec{w}$ ($\vec{n} \not\perp \vec{v}$),

R=3 if $\vec{n} \neq \vec{w}$ ($\vec{n} \neq \vec{v}$) and $\vec{n} \perp \vec{v}$ ($\vec{n} \perp \vec{w}$),

R=4 if \vec{n} is neither equal nor orthogonal to \vec{v} and \vec{w} ,

where \vec{v} and \vec{w} denote the left- and right-singular vectors of the matrix $\beta = d\vec{v} \otimes \vec{w}$ in Eq. (E.6). These results are summarized in Tab. E.1. For the special case of $\vec{v} = \vec{w}$, we obtain $R = 4$ if and only if

$$0 < \frac{\vec{n}^T \beta \vec{n}}{\sqrt{\text{Tr} \beta^T \beta}} < 1. \quad (\text{E.26})$$

The present analysis can be extended beyond qubit-systems based on the definitions of the Fano form, rotations and generalized Bloch vectors for higher dimensions [305].

Bibliography

- [1] E. Schrödinger, *The British Journal for the Philosophy of Science* **3**, 109 (1952), URL <http://www.jstor.org/stable/685552>.
- [2] W. Paul and H. Steinwedel, *Zeitschrift für Naturforschung A* **8**, 448 (1953).
- [3] W. Neuhauser, M. Hohenstatt, P. Toschek, and H. Dehmelt, *Phys. Rev. Lett.* **41**, 233 (1978), URL <http://link.aps.org/doi/10.1103/PhysRevLett.41.233>.
- [4] D. J. Wineland, R. E. Drullinger, and F. L. Walls, *Phys. Rev. Lett.* **40**, 1639 (1978), URL <http://link.aps.org/doi/10.1103/PhysRevLett.40.1639>.
- [5] W. Neuhauser, M. Hohenstatt, P. E. Toschek, and H. Dehmelt, *Phys. Rev. A* **22**, 1137 (1980), URL <http://link.aps.org/doi/10.1103/PhysRevA.22.1137>.
- [6] W. Nagourney, J. Sandberg, and H. Dehmelt, *Physical Review Letters* **56**, 2797 (1986), URL <http://dx.doi.org/10.1103/PhysRevLett.56.2797>.
- [7] T. Sauter, W. Neuhauser, R. Blatt, and P. Toschek, *Physical Review Letters* **57**, 1696 (1986), URL <http://dx.doi.org/10.1103/PhysRevLett.57.1696>.
- [8] J. Bergquist, R. Hulet, W. Itano, and D. Wineland, *Physical Review Letters* **57**, 1699 (1986), URL <http://dx.doi.org/10.1103/PhysRevLett.57.1699>.
- [9] P. Benioff, *Journal of Statistical Physics* **22**, 563 (1980), ISSN 1572-9613, URL <http://dx.doi.org/10.1007/BF01011339>.
- [10] Y. I. Manin, *Sov. Radio* pp. 13–15. (1980).
- [11] R. Feynman, *International Journal Of Theoretical Physics* **21**, 467 (1982), URL <http://dx.doi.org/10.1007/BF02650179>.
- [12] M. A. Nielsen and I. L. Chuang, *Quantum Computation and Quantum Information* (Cambridge University Press, Cambridge, U.K., 2000).
- [13] J. Cirac and P. Zoller, *Physical Review Letters* **74**, 4091 (1995), URL <http://link.aps.org/doi/10.1103/PhysRevLett.74.4091>.
- [14] F. Diedrich, J. Bergquist, W. M. Itano, and D. J. Wineland, *Physical Review Letters* **62**, 403 (1989), URL <http://link.aps.org/doi/10.1103/PhysRevLett.62.403>.
- [15] T. D. Ladd, F. Jelezko, R. Laflamme, Y. Nakamura, C. Monroe, and J. L. O'Brien, *Nature* **464**, 45 (2010), ISSN 0028-0836, URL <http://dx.doi.org/10.1038/nature08812>.

- [16] J. Benhelm, G. Kirchmair, C. F. Roos, and R. Blatt, *Nat. Phys.* **4**, 463 (2008), ISSN 1745-2473, URL <http://dx.doi.org/10.1038/nphys961>.
- [17] C. J. Ballance, T. P. Harty, N. M. Linke, M. A. Sepiol, and D. M. Lucas, arXiv:1512.04600 (2015).
- [18] P. Schindler, J. T. Barreiro, T. Monz, V. Nebendahl, D. Nigg, M. Chwalla, M. Hennrich, and R. Blatt, *Science* **332**, 1059 (2011), URL <http://dx.doi.org/10.1126/science.1203329>.
- [19] D. Nigg, M. Müller, E. A. Martinez, P. Schindler, M. Hennrich, T. Monz, M. A. Martin-Delgado, and R. Blatt, *Science* **345**, 302 (2014), ISSN 0036-8075, <http://science.sciencemag.org/content/345/6194/302.full.pdf>, URL <http://science.sciencemag.org/content/345/6194/302>.
- [20] R. Reichle, D. Leibfried, E. Knill, J. Britton, R. B. Blakestad, J. D. Jost, C. Langer, R. Ozeri, S. Seidelin, and D. J. Wineland, *Nature* **443**, 838 (2006), ISSN 0028-0836, URL <http://dx.doi.org/10.1038/nature05146>.
- [21] T. Monz, P. Schindler, J. Barreiro, M. Chwalla, D. Nigg, W. Coish, M. Harlander, W. Hänsel, M. Hennrich, and R. Blatt, *Physical Review Letters* **106** (2011), URL <http://dx.doi.org/10.1103/PhysRevLett.106.130506>.
- [22] B. P. Lanyon, C. Maier, M. Holzäpfel, T. Baumgratz, C. Hempel, P. Jurcevic, I. Dhand, A. J. Buyskikh, A. S. and Daley, M. Cramer, M. B. Plenio, et al., arXiv:1612.08000 (2016).
- [23] S. Gulde, Ph.D. thesis, Universität Innsbruck (2003), available at <http://quantumoptics.at>.
- [24] K.-A. Brickman, P. C. Haljan, P. J. Lee, M. Acton, L. Deslauriers, and C. Monroe, *Phys. Rev. A* **72**, 050306 (2005), URL <http://link.aps.org/doi/10.1103/PhysRevA.72.050306>.
- [25] T. Monz, D. Nigg, E. A. Martinez, M. F. Brandl, P. Schindler, R. Rines, S. X. Wang, I. L. Chuang, and R. Blatt, *Science* **351**, 1068 (2016), ISSN 0036-8075, <http://science.sciencemag.org/content/351/6277/1068.full.pdf>, URL <http://science.sciencemag.org/content/351/6277/1068>.
- [26] P. Jurcevic, B. P. Lanyon, P. Hauke, C. Hempel, P. Zoller, R. Blatt, and C. F. Roos, *Nature* **511**, 202 (2014), ISSN 0028-0836, URL <http://dx.doi.org/10.1038/nature13461>.
- [27] E. H. Lieb and D. W. Robinson, *Comm. Math. Phys.* **28**, 251 (1972), URL <http://projecteuclid.org/euclid.cmp/1103858407>.
- [28] P. Jurcevic, P. Hauke, C. Maier, C. Hempel, B. P. Lanyon, R. Blatt, and C. F. Roos, *Phys. Rev. Lett.* **115**, 100501 (2015), URL <http://link.aps.org/doi/10.1103/PhysRevLett.115.100501>.

- [29] R. Raussendorf and H. J. Briegel, Phys. Rev. Lett. **86**, 5188 (2001), URL <http://link.aps.org/doi/10.1103/PhysRevLett.86.5188>.
- [30] B. P. Lanyon, P. Jurcevic, M. Zwerger, C. Hempel, E. A. Martinez, W. Dür, H. J. Briegel, R. Blatt, and C. F. Roos, Physical Review Letters **111**, 210501 (2013).
- [31] H. Ollivier and W. H. Zurek, Phys. Rev. Lett. **88**, 017901 (2001), URL <http://link.aps.org/doi/10.1103/PhysRevLett.88.017901>.
- [32] L. Henderson and V. Vedral, Journal of Physics A: Mathematical and General **34**, 6899 (2001), URL <http://stacks.iop.org/0305-4470/34/i=35/a=315>.
- [33] E. Knill and R. Laflamme, Phys. Rev. Lett. **81**, 5672 (1998), URL <http://link.aps.org/doi/10.1103/PhysRevLett.81.5672>.
- [34] A. Datta, A. Shaji, and C. M. Caves, Phys. Rev. Lett. **100**, 050502 (2008), URL <http://link.aps.org/doi/10.1103/PhysRevLett.100.050502>.
- [35] T. Monz, Ph.D. thesis, Universität Innsbruck (2011), available at <http://quantumoptics.at>.
- [36] A. Holevo, Problems of Information Transmission pp. 177–183 (1973).
- [37] D. Gottesman, in *Proceedings of the 23rd International Colloquium on Group Theoretical Methods in Physics* (International Press, Cambridge, 1999), pp. 32–43.
- [38] G. Vidal, Phys. Rev. Lett. **91**, 147902 (2003), URL <http://link.aps.org/doi/10.1103/PhysRevLett.91.147902>.
- [39] G. Vidal, Phys. Rev. Lett. **93**, 040502 (2004), URL <http://link.aps.org/doi/10.1103/PhysRevLett.93.040502>.
- [40] A. Datta, Ph.D. thesis, The University of New Mexico (2008).
- [41] C. E. Shannon, The Bell System Technical Journal **27**, 623 (1948).
- [42] R. DORNER and V. VEDRAL, International Journal of Modern Physics B **27**, 1345017 (2013), <http://www.worldscientific.com/doi/pdf/10.1142/S0217979213450173>, URL <http://www.worldscientific.com/doi/abs/10.1142/S0217979213450173>.
- [43] H. Araki and E. H. Lieb, Comm. Math. Phys. **18**, 160 (1970), URL <http://projecteuclid.org/euclid.cmp/1103842506>.
- [44] R. Horodecki, P. Horodecki, M. Horodecki, and K. Horodecki, Rev. Mod. Phys. **81**, 865 (2009), URL <http://link.aps.org/doi/10.1103/RevModPhys.81.865>.
- [45] E. Schrödinger, Die Naturwissenschaften **23**, 807 (1935), URL <http://dx.doi.org/10.1007/BF01491891>.

- [46] W. Dür, G. Vidal, and J. I. Cirac, Phys. Rev. A **62**, 062314 (2000), URL <http://link.aps.org/doi/10.1103/PhysRevA.62.062314>.
- [47] M. Horodecki, P. Horodecki, and R. Horodecki, Physics Letters A **223**, 1 (1996), ISSN 0375-9601, URL <http://www.sciencedirect.com/science/article/pii/S0375960196007062>.
- [48] K. Modi, A. Brodutch, H. Cable, T. Paterek, and V. Vedral, Rev. Mod. Phys. **84**, 1655 (2012), URL <http://link.aps.org/doi/10.1103/RevModPhys.84.1655>.
- [49] *Quantum algorithm zoo*, NIST Webpage, URL <http://math.nist.gov/quantum/zoo/>.
- [50] D. Deutsch, Proceedings of the Royal Society of London A: Mathematical, Physical and Engineering Sciences **400**, 97 (1985), ISSN 0080-4630, <http://rspa.royalsocietypublishing.org/content/400/1818/97.full.pdf>, URL <http://rspa.royalsocietypublishing.org/content/400/1818/97>.
- [51] P. W. Shor, Symposium on Foundations of Computer Science **35**, 124 (1994), URL <http://dx.doi.org/10.1109/SFCS.1994.365700>.
- [52] A. M. Turing, Proc. London Math. Soc. **s2-42**, 230 (1937).
- [53] P. Kaye, R. Laflamme, and M. Mosca, *An Introduction to Quantum Computing* (Oxford University Press, 2007).
- [54] S. M. Barnett, *Quantum Information*, Oxford Master Series in Atomic, Optical and Laser Physics (Oxford University Press, 2009).
- [55] D. P. DiVincenzo, Fortschritte der Physik **48**, 771 (2000), ISSN 1521-3978, URL [http://dx.doi.org/10.1002/1521-3978\(200009\)48:9/11<771::AID-PROP771>3.0.CO;2-E](http://dx.doi.org/10.1002/1521-3978(200009)48:9/11<771::AID-PROP771>3.0.CO;2-E).
- [56] H. J. Briegel, D. E. Browne, W. Dur, R. Raussendorf, and M. Van den Nest, Nat. Phys. pp. 19–26 (2009), ISSN 1745-2473, URL <http://dx.doi.org/10.1038/nphys1157>.
- [57] M. Hein, J. Eisert, and H. J. Briegel, Phys. Rev. A **69**, 062311 (2004), URL <http://link.aps.org/doi/10.1103/PhysRevA.69.062311>.
- [58] R. Raussendorf, D. E. Browne, and H. J. Briegel, Phys. Rev. A **68**, 022312 (2003), URL <http://link.aps.org/doi/10.1103/PhysRevA.68.022312>.
- [59] D. Gottesman and I. L. Chuang, Nature **402**, 390 (1999), ISSN 0028-0836, URL <http://dx.doi.org/10.1038/46503>.
- [60] E. Knill, R. Laflamme, and G. J. Milburn, Nature **409**, 46 (2001), ISSN 0028-0836, URL <http://dx.doi.org/10.1038/35051009>.
- [61] M. A. Nielsen, Physics Letters A **308**, 96 (2003), ISSN 0375-9601, URL <http://www.sciencedirect.com/science/article/pii/S0375960102018030>.

- [62] E. Farhi, J. Goldstone, S. Gutmann, J. Lapan, A. Lundgren, and D. Preda, *Science* **292**, 472 (2001), ISSN 0036-8075, <http://science.sciencemag.org/content/292/5516/472.full.pdf>, URL <http://science.sciencemag.org/content/292/5516/472>.
- [63] S. Sachdev, *Quantum Phase Transitions* (Cambridge University Press, 2011), 2nd ed., ISBN 9780521514682.
- [64] R. Islam, C. Senko, W. C. Campbell, S. Korenblit, J. Smith, A. Lee, E. E. Edwards, C. C. J. Wang, J. K. Freericks, and C. R. Monroe, *Science* **340**, 583 (2013), URL <http://dx.doi.org/10.1126/science.1232296>.
- [65] D. Aharonov, W. van Dam, J. Kempe, Z. Landau, S. Lloyd, and O. Regev, *SIAM Journal on Computing* **37**, 166 (2007), <http://dx.doi.org/10.1137/S0097539705447323>, URL <http://dx.doi.org/10.1137/S0097539705447323>.
- [66] S. W. Shin, G. Smith, J. A. Smolin, and U. Vazirani, arXiv:1401.7087 [quant-ph] (2014).
- [67] S. Boixo, T. F. Ronnow, S. V. Isakov, Z. Wang, D. Wecker, D. A. Lidar, J. M. Martinis, and M. Troyer, *Nat. Phys.* **10**, 218 (2014), ISSN 1745-2473, URL <http://dx.doi.org/10.1038/nphys2900>.
- [68] A. Kitaev, *Annals of Physics* **303**, 2 (2003), ISSN 0003-4916, URL <http://www.sciencedirect.com/science/article/pii/S0003491602000180>.
- [69] C. Nayak, S. H. Simon, A. Stern, M. Freedman, and S. Das Sarma, *Rev. Mod. Phys.* **80**, 1083 (2008), URL <http://link.aps.org/doi/10.1103/RevModPhys.80.1083>.
- [70] J. K. Pachos, *Introduction to Topological Quantum Computation* (Cambridge University Press, 2012).
- [71] M. H. Freedman, A. Kitaev, M. J. Larsen, and Z. Wang, *Journal: Bull. Amer. Math. Soc.* **40**, 31 (2003).
- [72] A. Stern, *Nature* **464**, 187 (2010), ISSN 0028-0836, URL <http://dx.doi.org/10.1038/nature08915>.
- [73] R. L. Willett, C. Nayak, K. Shtengel, L. N. Pfeiffer, and K. W. West, *Phys. Rev. Lett.* **111**, 186401 (2013), URL <http://link.aps.org/doi/10.1103/PhysRevLett.111.186401>.
- [74] S. Lloyd, *Science* **273**, 1073 (1996), URL <http://dx.doi.org/10.1126/science.273.5278.1073>.
- [75] I. M. Georgescu, S. Ashhab, and F. Nori, *Reviews Of Modern Physics* **86**, 153 (2014), URL <http://dx.doi.org/10.1103/RevModPhys.86.153>.
- [76] I. Buluta and F. Nori, *Science* **326**, 108 (2009), URL <http://dx.doi.org/10.1126/science.1177838>.

- [77] P. K. Ghosh, *Ion Traps* (Clarendon Press Oxford, 1995).
- [78] D. J. Wineland, C. R. Monroe, W. M. Itano, D. Leibfried, B. King, and D. Meekhof, *Journal of Research of NIST* **103**, 259 (1998), URL <http://dx.doi.org/10.6028/jres.103.019>.
- [79] D. Leibfried, R. Blatt, C. Monroe, and D. Wineland, *Reviews of Modern Physics* **75**, 281 (2003), URL <http://dx.doi.org/10.1103/RevModPhys.75.281>.
- [80] F. L. Claude Cohen-Tannoudji, Bernard Diu, *Quantum Mechanics Vol 1 & 2* (Wiley-VCH, 1992).
- [81] J. J. Sakurai, *Modern Quantum Mechanics* (Addison-Wesley, 1993).
- [82] R. Shankar, *Principles of Quantum Mechanics* (Springer, 1994).
- [83] D. James, *Applied Physics B-Lasers And Optics* **66**, 181 (1998), URL <http://dx.doi.org/10.1007/s003400050373>.
- [84] A. Steane, *Applied Physics B* **64**, 623 (1997), ISSN 1432-0649, URL <http://dx.doi.org/10.1007/s003400050225>.
- [85] T. P. Meyrath and D. F. James, *Physics Letters A* **240**, 37 (1998), ISSN 0375-9601, URL <http://www.sciencedirect.com/science/article/pii/S0375960198000450>.
- [86] C. Marquet, F. Schmidt-Kaler, and D. James, *Applied Physics B* **76**, 199 (2003), ISSN 1432-0649, URL <http://dx.doi.org/10.1007/s00340-003-1097-7>.
- [87] S. Kotler, N. Akerman, N. Navon, Y. Glickman, and R. Ozeri, *Nature* **510**, 376 (2014), ISSN 0028-0836, URL <http://dx.doi.org/10.1038/nature13403>.
- [88] J. P. Gaebler, T. R. Tan, Y. Lin, Y. Wan, R. Bowler, A. C. Keith, S. Glancy, K. Coakley, E. Knill, D. Leibfried, et al., arXiv:1604.00032 (2016).
- [89] R. Loudon, *The Quantum Theory of Light* (Oxford University Press, 2000), 3rd ed.
- [90] C. J. Foot, *Atomic Physics*, Oxford Master Series in Atomic, Optical and Laser Physics (Oxford University Press, 2005).
- [91] C. R. Monroe, D. M. Meekhof, B. E. King, and D. J. Wineland, *Science* **272**, 1131 (1996), URL <http://dx.doi.org/10.1126/science.272.5265.1131>.
- [92] C. Hempel, B. P. Lanyon, P. Jurcevic, R. Gerritsma, R. Blatt, and C. F. Roos, *Nature Photonics* **7**, 630 (2013).
- [93] A. Sørensen and K. Mølmer, *Physical Review Letters* **82**, 1971 (1999), URL <http://dx.doi.org/10.1103/PhysRevLett.82.1971>.
- [94] A. Sørensen and K. Mølmer, *Physical Review A* **62**, 22311 (2000), URL <http://dx.doi.org/10.1103/PhysRevA.62.022311>.

- [95] E. Solano, R. de Matos Filho, and N. Zagury, *Physical Review A* **59**, R2539 (1999), URL <http://dx.doi.org/10.1103/PhysRevA.59.R2539>.
- [96] G. Kirchmair, J. Benhelm, F. Zähringer, R. Gerritsma, C. F. Roos, and R. Blatt, *New Journal of Physics* **11**, 023002 (2009), URL <http://dx.doi.org/10.1088/1367-2630/11/2/023002>.
- [97] C. F. Roos, *New Journal of Physics* **10**, 013002 (2008), URL <http://dx.doi.org/10.1088/1367-2630/10/1/013002>.
- [98] G. Kirchmair, Ph.D. thesis, Universität Innsbruck (2010), available at <http://quantumoptics.at>.
- [99] D. Porras and J. I. Cirac, *Phys. Rev. Lett.* **92**, 207901 (2004), URL <http://link.aps.org/doi/10.1103/PhysRevLett.92.207901>.
- [100] X.-L. Deng, D. Porras, and J. I. Cirac, *Phys. Rev. A* **72**, 063407 (2005), URL <http://link.aps.org/doi/10.1103/PhysRevA.72.063407>.
- [101] K. Kim, S. Korenblit, R. Islam, E. E. Edwards, M.-S. Chang, C. Noh, H. Carmichael, G.-D. Lin, L.-M. Duan, C. C. J. Wang, et al., *New Journal of Physics* **13**, 105003 (2011), URL <http://stacks.iop.org/1367-2630/13/i=10/a=105003>.
- [102] C. Schneider, D. Porras, and T. Schaetz, *Reports on Progress in Physics* **75**, 024401 (2012), URL <http://stacks.iop.org/0034-4885/75/i=2/a=024401>.
- [103] P. Nevado and D. Porras, *Phys. Rev. A* **93**, 013625 (2016), URL <http://link.aps.org/doi/10.1103/PhysRevA.93.013625>.
- [104] P. Schindler, D. Nigg, T. Monz, J. T. Barreiro, E. Martinez, S. X. Wang, S. Quint, M. F. Brandl, V. Nebendahl, C. F. Roos, et al., *New Journal of Physics* **15**, 123012 (2013), URL <http://dx.doi.org/10.1088/1367-2630/15/12/123012>.
- [105] F. Schmidt-Kaler, S. Gulde, M. Riebe, T. Deuschle, A. Kreuter, G. Lancaster, C. Becher, J. Eschner, H. Häffner, and R. Blatt, *Journal of Physics B: Atomic, Molecular and Optical Physics* **36**, 623 (2003), URL <http://stacks.iop.org/0953-4075/36/i=3/a=319>.
- [106] H. Häffner, C. F. Roos, and R. Blatt, *Physics Reports* **469**, 155 (2008), URL <http://dx.doi.org/10.1016/j.physrep.2008.09.003>.
- [107] M. Chwalla, Ph.D. thesis, Universität Innsbruck (2009), available at <http://quantumoptics.at>.
- [108] D. Rotter, Master's thesis, Universität Innsbruck (2003), [in German], available at <http://quantumoptics.at>.
- [109] R. Lechner, Master's thesis, Universität Innsbruck (2010), available at <http://quantumoptics.at>.

- [110] R. Hendricks, D. Grant, P. Herskind, A. Dantan, and M. Drewsen, *Appl. Phys. B* **88**, 507 (2007).
- [111] D. R. Leibbrandt, R. J. Clark, J. Labaziewicz, P. Antohi, W. Bakr, K. R. Brown, and I. L. Chuang, *Phys. Rev. A* **76**, 055403 (2007), URL <http://link.aps.org/doi/10.1103/PhysRevA.76.055403>.
- [112] M. Guggemos, D. Heinrich, O. A. Herrera-Sancho, R. Blatt, and C. F. Roos, *New Journal of Physics* **17**, 103001 (2015), URL <http://stacks.iop.org/1367-2630/17/i=10/a=103001>.
- [113] M. Guggemos, Ph.D. thesis, Universität Innsbruck (2016).
- [114] M. Hettrich, T. Ruster, H. Kaufmann, C. F. Roos, C. T. Schmiegelow, F. Schmidt-Kaler, and U. G. Poschinger, *Phys. Rev. Lett.* **115**, 143003 (2015), URL <http://link.aps.org/doi/10.1103/PhysRevLett.115.143003>.
- [115] R. Gerritsma, G. Kirchmair, F. Zähringer, J. Benhelm, R. Blatt, and C. F. Roos, *The European Physical Journal D* **50**, 13 (2008), URL <http://dx.doi.org/10.1140/epjd/e2008-00196-9>.
- [116] P. Barton, C. Donald, D. Lucas, D. Stevens, A. Steane, and D. Stacey, *Physical Review A* **62**, 032503 (2000), URL <http://dx.doi.org/10.1103/PhysRevA.62.032503>.
- [117] J. Jin and D. A. Church, *Physical Review Letters* **70**, 3213 (1993), URL <http://dx.doi.org/10.1103/PhysRevLett.70.3213>.
- [118] H. G. Dehmelt, *Bulletin of the American Physical Society* **20** (1975), URL http://www.nobelprize.org/nobel_prizes/physics/laureates/1989/dehmelt-bio.html.
- [119] C. Hempel, Ph.D. thesis, Universität Innsbruck (2014).
- [120] C. Roos, T. Zeiger, H. Rohde, H. Nägerl, J. Eschner, D. Leibfried, F. Schmidt-Kaler, and R. Blatt, *Physical Review Letters* **83**, 4713 (1999), URL <http://dx.doi.org/10.1103/PhysRevLett.83.4713>.
- [121] G. Kirchmair, Master's thesis, Universität Innsbruck (2006), available at <http://quantumoptics.at>.
- [122] J. Benhelm, Ph.D. thesis, Universität Innsbruck (2008), available at <http://quantumoptics.at>.
- [123] C. F. Roos, Ph.D. thesis, Universität Innsbruck (2000), available at <http://quantumoptics.at>.
- [124] P. Schindler, Ph.D. thesis, Universität Innsbruck (2013), available at <http://quantumoptics.at>.
- [125] N. F. Ramsey, *Reviews of Modern Physics* **62**, 541 (1990), URL <http://link.aps.org/doi/10.1103/RevModPhys.62.541>.

- [126] S. Kotler, N. Akerman, Y. Glickman, A. Keselman, and R. Ozeri, *Nature* **473**, 61 (2011), URL <http://dx.doi.org/10.1038/nature10010>.
- [127] S. Kotler, N. Akerman, Y. Glickman, and R. Ozeri, *Physical Review Letters* **110**, 110503 (2013), URL <http://dx.doi.org/10.1103/PhysRevLett.110.110503>.
- [128] D. H. E. Dubin and T. M. O'Neil, *Rev. Mod. Phys.* **71**, 87 (1999), URL <http://link.aps.org/doi/10.1103/RevModPhys.71.87>.
- [129] J. P. Schiffer, *Phys. Rev. Lett.* **70**, 818 (1993), URL <http://link.aps.org/doi/10.1103/PhysRevLett.70.818>.
- [130] S. Fishman, G. De Chiara, T. Calarco, and G. Morigi, *Phys. Rev. B* **77**, 064111 (2008), URL <http://link.aps.org/doi/10.1103/PhysRevB.77.064111>.
- [131] D. G. Enzer, M. M. Schauer, J. J. Gomez, M. S. Gulley, M. H. Holzscheiter, P. G. Kwiat, S. K. Lamoreaux, C. G. Peterson, V. D. Sandberg, D. Tupa, et al., *Phys. Rev. Lett.* **85**, 2466 (2000), URL <http://link.aps.org/doi/10.1103/PhysRevLett.85.2466>.
- [132] D. H. E. Dubin, *Phys. Rev. Lett.* **71**, 2753 (1993), URL <http://link.aps.org/doi/10.1103/PhysRevLett.71.2753>.
- [133] E. Shimshoni, G. Morigi, and S. Fishman, *Phys. Rev. Lett.* **106**, 010401 (2011), URL <http://link.aps.org/doi/10.1103/PhysRevLett.106.010401>.
- [134] E. Shimshoni, G. Morigi, and S. Fishman, *Phys. Rev. A* **83**, 032308 (2011), URL <http://link.aps.org/doi/10.1103/PhysRevA.83.032308>.
- [135] T. W. B. Kibble, *Journal of Physics A: Mathematical and General* **9**, 1387 (1976), URL <http://stacks.iop.org/0305-4470/9/i=8/a=029>.
- [136] A. del Campo and W. H. Zurek, *International Journal of Modern Physics A* **29**, 1430018 (2014), <http://www.worldscientific.com/doi/pdf/10.1142/S0217751X1430018X>, URL <http://www.worldscientific.com/doi/abs/10.1142/S0217751X1430018X>.
- [137] G. D. Chiara, A. del Campo, G. Morigi, M. B. Plenio, and A. Retzker, *New Journal of Physics* **12**, 115003 (2010), URL <http://stacks.iop.org/1367-2630/12/i=11/a=115003>.
- [138] A. del Campo, G. De Chiara, G. Morigi, M. B. Plenio, and A. Retzker, *Phys. Rev. Lett.* **105**, 075701 (2010), URL <http://link.aps.org/doi/10.1103/PhysRevLett.105.075701>.
- [139] R. Nigmatullin, A. del Campo, G. De Chiara, G. Morigi, M. B. Plenio, and A. Retzker, *arXiv:1112.1305* (2015).
- [140] K. Pyka, J. Keller, H. L. Partner, R. Nigmatullin, T. Burgermeister, D. M. Meier, K. Kuhlmann, A. Retzker, M. B. Plenio, W. H. Zurek, et al., *Nat. Commun.* **4**, (2013), URL <http://dx.doi.org/10.1038/ncomms3291>.

- [141] S. Ulm, J. Roßnagel, G. Jacob, C. Degünther, S. T. Dawkins, U. G. Poschinger, R. Nigmatullin, A. Retzker, M. B. Plenio, F. Schmidt-Kaler, et al., *Nat. Commun.* **4**, (2013), URL <http://dx.doi.org/10.1038/ncomms3290>.
- [142] S. Ejtemaee and P. C. Haljan, *Phys. Rev. A* **87**, 051401 (2013), URL <http://link.aps.org/doi/10.1103/PhysRevA.87.051401>.
- [143] H. Landa, B. Reznik, J. Brox, M. Mielenz, and T. Schaetz, *New Journal of Physics* **15**, 093003 (2013), URL <http://stacks.iop.org/1367-2630/15/i=9/a=093003>.
- [144] D. Berkeland, J. Miller, J. Bergquist, W. M. Itano, and D. J. Wineland, *Journal of Applied Physics* **83**, 5025 (1998), URL <http://dx.doi.org/10.1063/1.367318>.
- [145] M. Chwalla, K. Kim, T. Monz, P. Schindler, M. Riebe, C. Roos, and R. Blatt, *Applied Physics B* **89**, 483 (2007), ISSN 1432-0649, URL <http://dx.doi.org/10.1007/s00340-007-2867-4>.
- [146] W. M. Itano, *J. Res. Natl. Inst. Stand. Technol.* **105**, 829 (2000).
- [147] C. F. Roos, M. Chwalla, K. Kim, M. Riebe, and R. Blatt, *Nature* **443**, 316 (2006), ISSN 0028-0836, URL <http://dx.doi.org/10.1038/nature05101>.
- [148] C. F. Roos, arXiv:quant-ph/0508148 (2005).
- [149] H. S. Margolis, G. P. Barwood, G. Huang, H. A. Klein, S. N. Lea, K. Szymaniec, and P. Gill, *Science* **306**, 1355 (2004), ISSN 0036-8075, <http://science.sciencemag.org/content/306/5700/1355.full.pdf>, URL <http://science.sciencemag.org/content/306/5700/1355>.
- [150] Holo-OR, *TopHat - Stable Top Beamshaper* (Laser Components, 2015).
- [151] S. Schunke, Master's thesis, Universität Innsbruck (2015).
- [152] H. Häffner, S. Gulde, M. Riebe, G. Lancaster, C. Becher, J. Eschner, F. Schmidt-Kaler, and R. Blatt, *Physical Review Letters* **90** (2003), URL <http://dx.doi.org/10.1103/PhysRevLett.90.143602>.
- [153] A. Kaplan, M. Fredslund Andersen, and N. Davidson, *Phys. Rev. A* **66**, 045401 (2002), URL <http://link.aps.org/doi/10.1103/PhysRevA.66.045401>.
- [154] R. G. Unanyan and M. Fleischhauer, *Phys. Rev. Lett.* **90**, 133601 (2003), URL <http://link.aps.org/doi/10.1103/PhysRevLett.90.133601>.
- [155] W. Sichak, *Proceedings of the IRE* **42**, 1315 (1954), ISSN 0096-8390.
- [156] W. W. MacAlpine and R. O. Schildknecht, *Proceedings of the IRE* **47**, 2099 (1959), URL <http://dx.doi.org/10.1109/JRPROC.1959.287128>.
- [157] A. Zverev and H. Blinichikoff, *IRE Transactions on Component Parts* **8**, 99 (1961), URL <http://dx.doi.org/10.1109/TCP.1961.1136604>.

- [158] J. D. Siverns, L. R. Simkins, S. Weidt, and W. K. Hensinger, *Applied Physics B* **107**, 921 (2012), URL <http://dx.doi.org/10.1007/s00340-011-4837-0>.
- [159] C. F. Roos, T. Monz, K. Kim, M. Riebe, H. Häffner, D. F. V. James, and R. Blatt, *Phys. Rev. A* **77**, 040302 (2008), URL <http://link.aps.org/doi/10.1103/PhysRevA.77.040302>.
- [160] B. Odom, D. Hanneke, B. D’Urso, and G. Gabrielse, *Phys. Rev. Lett.* **97**, 030801 (2006), URL <http://link.aps.org/doi/10.1103/PhysRevLett.97.030801>.
- [161] I. Marzoli, J. I. Cirac, R. Blatt, and P. Zoller, *Physical Review A* **49**, 2771 (1994), URL <http://link.aps.org/doi/10.1103/PhysRevA.49.2771>.
- [162] G. Morigi, J. Eschner, and C. H. Keitel, *Phys. Rev. Lett.* **85**, 4458 (2000), URL <http://link.aps.org/doi/10.1103/PhysRevLett.85.4458>.
- [163] C. F. Roos, D. Leibfried, A. Mundt, F. Schmidt-Kaler, J. Eschner, and R. Blatt, *Phys. Rev. Lett.* **85**, 5547 (2000), URL <http://link.aps.org/doi/10.1103/PhysRevLett.85.5547>.
- [164] F. Schmidt-Kaler, J. Eschner, G. Morigi, C. Roos, D. Leibfried, A. Mundt, and R. Blatt, *Applied Physics B* **73**, 807 (2001), ISSN 1432-0649, URL <http://dx.doi.org/10.1007/s003400100721>.
- [165] Y. Lin, J. P. Gaebler, T. R. Tan, R. Bowler, J. D. Jost, D. Leibfried, and D. J. Wineland, *Phys. Rev. Lett.* **110**, 153002 (2013), URL <http://link.aps.org/doi/10.1103/PhysRevLett.110.153002>.
- [166] R. Lechner, C. Maier, C. Hempel, P. Jurcevic, B. P. Lanyon, T. Monz, M. Brownnutt, R. Blatt, and C. F. Roos, *Phys. Rev. A* **93**, 053401 (2016), URL <http://link.aps.org/doi/10.1103/PhysRevA.93.053401>.
- [167] C. H. Tseng, S. Somaroo, Y. Sharf, E. Knill, R. Laflamme, T. F. Havel, and D. G. Cory, *Phys. Rev. A* **62**, 032309 (2000), URL <http://link.aps.org/doi/10.1103/PhysRevA.62.032309>.
- [168] Y. S. Weinstein, S. Lloyd, J. Emerson, and D. G. Cory, *Phys. Rev. Lett.* **89**, 157902 (2002), URL <http://link.aps.org/doi/10.1103/PhysRevLett.89.157902>.
- [169] J. Du, N. Xu, X. Peng, P. Wang, S. Wu, and D. Lu, *Phys. Rev. Lett.* **104**, 030502 (2010), URL <http://link.aps.org/doi/10.1103/PhysRevLett.104.030502>.
- [170] D. Banerjee, M. Bögli, M. Dalmonte, E. Rico, P. Stebler, U.-J. Wiese, and P. Zoller, *Phys. Rev. Lett.* **110**, 125303 (2013), URL <http://link.aps.org/doi/10.1103/PhysRevLett.110.125303>.
- [171] M. Greiner, O. Mandel, T. Esslinger, T. W. Hänsch, and I. Bloch, *Nature* **415**, 39 (2002), ISSN 0028-0836, URL <http://dx.doi.org/10.1038/415039a>.

- [172] J. Simon, W. S. Bakr, R. Ma, M. E. Tai, P. M. Preiss, and M. Greiner, *Nature* **472**, 307 (2011), ISSN 0028-0836, URL <http://dx.doi.org/10.1038/nature09994>.
- [173] M. Cheneau, P. Barmettler, D. Poletti, M. Endres, P. Schausz, T. Fukuhara, C. Gross, I. Bloch, C. Kollath, and S. Kuhr, *Nature* **481**, 484 (2012), ISSN 0028-0836, URL <http://dx.doi.org/10.1038/nature10748>.
- [174] T. Fukuhara, A. Kantian, M. Endres, M. Cheneau, P. Schausz, S. Hild, D. Bellem, U. Schollwöck, T. Giamarchi, C. Gross, et al., *Nat. Phys.* **9**, 235 (2013), ISSN 1745-2473, URL <http://dx.doi.org/10.1038/nphys2561>.
- [175] I. Bloch, J. Dalibard, and S. Nascimbene, *Nat. Phys.* **8**, 267 (2012), ISSN 1745-2473, URL <http://dx.doi.org/10.1038/nphys2259>.
- [176] X.-s. Ma, B. Dakic, W. Naylor, A. Zeilinger, and P. Walther, *Nat. Phys.* **7**, 399 (2011), ISSN 1745-2473, URL <http://dx.doi.org/10.1038/nphys1919>.
- [177] A. Aspuru-Guzik and P. Walther, *Nat. Phys.* **8**, 285 (2012), ISSN 1745-2473, URL <http://dx.doi.org/10.1038/nphys2253>.
- [178] A. Friedenauer, H. Schmitz, J. T. Glueckert, D. Porras, and T. Schaetz, *Nature Physics* **4**, 757 (2008), URL <http://dx.doi.org/10.1038/nphys1032>.
- [179] R. Gerritsma, G. Kirchmair, F. Zaehring, E. Solano, R. Blatt, and C. F. Roos, *Nature* **463**, 68 (2010), URL <http://dx.doi.org/10.1038/nature08688>.
- [180] K. Kim, M. S. Chang, S. Korenblit, R. Islam, E. E. Edwards, J. K. Freericks, G. D. Lin, L. M. Duan, and C. R. Monroe, *Nature* **465**, 590 (2010), URL <http://dx.doi.org/10.1038/nature09071>.
- [181] J. T. Barreiro, M. Mueller, P. Schindler, D. Nigg, T. Monz, M. Chwalla, M. Hennrich, C. F. Roos, P. Zoller, and R. Blatt, *Nature* **470**, 486 (2011), URL <http://www.nature.com/doifinder/10.1038/nature09801>.
- [182] B. P. Lanyon, C. Hempel, D. Nigg, M. Müller, R. Gerritsma, F. Zähringer, P. Schindler, J. T. Barreiro, M. Rambach, G. Kirchmair, et al., *Science* **334**, 57 (2011).
- [183] J. W. Britton, B. C. Sawyer, A. C. Keith, C. C. J. Wang, J. K. Freericks, H. Uys, M. J. Biercuk, and J. J. Bollinger, *Nature* **484**, 489 (2012), URL <http://dx.doi.org/10.1038/nature10981>.
- [184] R. Blatt and C. F. Roos, *Nature Physics* **8**, 277 (2012), URL <http://www.nature.com/doifinder/10.1038/nphys2252>.
- [185] A. A. Houck, H. E. Tureci, and J. Koch, *Nat. Phys.* **8**, 292 (2012), ISSN 1745-2473, URL <http://dx.doi.org/10.1038/nphys2251>.
- [186] M. Haeberlein, F. Deppe, A. Kurcz, J. Goetz, A. Baust, P. Eder, K. Fedorov, M. Fischer, E. P. Menzel, M. J. Schwarz, et al., arXiv:1506.09114 (2015).

- [187] C. Eichler, J. Mlynek, J. Butscher, P. Kurpiers, K. Hammerer, T. J. Osborne, and A. Wallraff, *Phys. Rev. X* **5**, 041044 (2015), URL <http://link.aps.org/doi/10.1103/PhysRevX.5.041044>.
- [188] Y. Salathé, M. Mondal, M. Oppliger, J. Heinsoo, P. Kurpiers, A. Potočnik, A. Mezzacapo, U. Las Heras, L. Lamata, E. Solano, et al., *Phys. Rev. X* **5**, 021027 (2015), URL <http://link.aps.org/doi/10.1103/PhysRevX.5.021027>.
- [189] R. Barends, L. Lamata, J. Kelly, L. Garcia-Alvarez, A. G. Fowler, A. Megrant, E. Jeffrey, T. C. White, D. Sank, J. Y. Mutus, et al., *Nat. Commun.* **6**, (2015), URL <http://dx.doi.org/10.1038/ncomms8654>.
- [190] R. J. Elliott, *Phys. Rev.* **124**, 346 (1961), URL <http://link.aps.org/doi/10.1103/PhysRev.124.346>.
- [191] M. E. Fisher and W. Selke, *Phys. Rev. Lett.* **44**, 1502 (1980), URL <http://link.aps.org/doi/10.1103/PhysRevLett.44.1502>.
- [192] W. Selke, *Physics Reports* **170**, 213 (1988), ISSN 0370-1573, URL <http://www.sciencedirect.com/science/article/pii/0370157388901408>.
- [193] P. Hauke and L. Tagliacozzo, *Phys. Rev. Lett.* **111**, 207202 (2013), URL <http://link.aps.org/doi/10.1103/PhysRevLett.111.207202>.
- [194] M. B. Hastings, in *Les Houches summer school* (2010), URL <http://arxiv.org/abs/1008.5137>.
- [195] B. Nachtergaele and R. Sims, *IAMP News Bulletin* pp. 22–29 (2010).
- [196] M. Kliesch, C. Gogolin, and J. Eisert, *Many-Electron Approaches in Physics, Chemistry and Mathematics: A Multidisciplinary View* (Springer International Publishing, Cham, 2014), chap. Lieb-Robinson Bounds and the Simulation of Time-Evolution of Local Observables in Lattice Systems, pp. 301–318, ISBN 978-3-319-06379-9, URL http://dx.doi.org/10.1007/978-3-319-06379-9_17.
- [197] D. W. Robinson, *The Journal of the Australian Mathematical Society. Series B. Applied Mathematics* **19**, 387 (1976).
- [198] M. B. Hastings and T. Koma, *Communications in Mathematical Physics* **265**, 781 (2006), ISSN 1432-0916, URL <http://dx.doi.org/10.1007/s00220-006-0030-4>.
- [199] B. Nachtergaele and R. Sims, *Communications in Mathematical Physics* **265**, 119 (2006), ISSN 1432-0916, URL <http://dx.doi.org/10.1007/s00220-006-1556-1>.
- [200] Z.-X. Gong, M. Foss-Feig, S. Michalakis, and A. V. Gorshkov, *Phys. Rev. Lett.* **113**, 030602 (2014), URL <http://link.aps.org/doi/10.1103/PhysRevLett.113.030602>.
- [201] M. Foss-Feig, Z.-X. Gong, C. W. Clark, and A. V. Gorshkov, *Phys. Rev. Lett.* **114**, 157201 (2015), URL <http://link.aps.org/doi/10.1103/PhysRevLett.114.157201>.

- [202] M. F. Maghrebi, Z.-X. Gong, M. Foss-Feig, and A. V. Gorshkov, *Phys. Rev. B* **93**, 125128 (2016), URL <http://link.aps.org/doi/10.1103/PhysRevB.93.125128>.
- [203] P. Zanardi and M. Rasetti, *Phys. Rev. Lett.* **79**, 3306 (1997), URL <http://link.aps.org/doi/10.1103/PhysRevLett.79.3306>.
- [204] D. A. Lidar, I. L. Chuang, and K. B. Whaley, *Phys. Rev. Lett.* **81**, 2594 (1998), URL <http://link.aps.org/doi/10.1103/PhysRevLett.81.2594>.
- [205] C. Senko, J. Smith, P. Richerme, A. Lee, W. C. Campbell, and C. Monroe, *Science* **345**, 430 (2014), ISSN 0036-8075, <http://science.sciencemag.org/content/345/6195/430.full.pdf>, URL <http://science.sciencemag.org/content/345/6195/430>.
- [206] H. Häffner, W. Hänsel, C. F. Roos, J. Benhelm, D. Chek-al kar, M. Chwalla, T. Körber, U. D. Rapol, M. Riebe, P. O. Schmidt, et al., *Nature* **438**, 643 (2005), ISSN 0028-0836, URL <http://dx.doi.org/10.1038/nature04279>.
- [207] P. Pfeuty, *Annals of Physics* **57**, 79 (1970), ISSN 0003-4916, URL <http://www.sciencedirect.com/science/article/pii/0003491670902708>.
- [208] T. Holstein and H. Primakoff, *Phys. Rev.* **58**, 1098 (1940), URL <http://link.aps.org/doi/10.1103/PhysRev.58.1098>.
- [209] P. Calabrese and J. Cardy, *Journal of Statistical Mechanics: Theory and Experiment* **2005**, P04010 (2005), URL <http://stacks.iop.org/1742-5468/2005/i=04/a=P04010>.
- [210] P. Richerme, Z.-X. Gong, A. Lee, C. Senko, J. Smith, M. Foss-Feig, S. Michalakis, A. V. Gorshkov, and C. Monroe, *Nature* **511**, 198 (2014), ISSN 0028-0836, URL <http://dx.doi.org/10.1038/nature13450>.
- [211] D. F. V. James, P. G. Kwiat, W. J. Munro, and A. G. White, *Phys. Rev. A* **64**, 052312 (2001), URL <http://link.aps.org/doi/10.1103/PhysRevA.64.052312>.
- [212] W. K. Wootters, *Phys. Rev. Lett.* **80**, 2245 (1998), URL <http://link.aps.org/doi/10.1103/PhysRevLett.80.2245>.
- [213] L. Gurvits and H. Barnum, *Phys. Rev. A* **66**, 062311 (2002), URL <http://link.aps.org/doi/10.1103/PhysRevA.66.062311>.
- [214] R. Hildebrand, arXiv:quant-ph/0601201 (2006).
- [215] J. Jünemann, A. Cadarso, D. Pérez-García, A. Bermudez, and J. J. García-Ripoll, *Phys. Rev. Lett.* **111**, 230404 (2013), URL <http://link.aps.org/doi/10.1103/PhysRevLett.111.230404>.
- [216] P. Hauke, F. M. Cucchietti, L. Tagliacozzo, I. Deutsch, and M. Lewenstein, *Reports on Progress in Physics* **75**, 082401 (2012), URL <http://stacks.iop.org/0034-4885/75/i=8/a=082401>.

- [217] S. Bose, *Contemporary Physics* **48**, 13 (2007), ISSN 0010-7514, URL <http://dx.doi.org/10.1080/00107510701342313>.
- [218] P. Rebentrost, M. Mohseni, I. Kassal, S. Lloyd, and A. Aspuru-Guzik, *New Journal of Physics* **11**, 033003 (2009), URL <http://stacks.iop.org/1367-2630/11/i=3/a=033003>.
- [219] M. Rigol, V. Dunjko, V. Yurovsky, and M. Olshanii, *Phys. Rev. Lett.* **98**, 050405 (2007), URL <http://link.aps.org/doi/10.1103/PhysRevLett.98.050405>.
- [220] N. Y. Yao, C. R. Laumann, S. Gopalakrishnan, M. Knap, M. Müller, E. A. Demler, and M. D. Lukin, *Phys. Rev. Lett.* **113**, 243002 (2014), URL <http://link.aps.org/doi/10.1103/PhysRevLett.113.243002>.
- [221] J. Schachenmayer, B. P. Lanyon, C. F. Roos, and A. J. Daley, *Phys. Rev. X* **3**, 031015 (2013), URL <http://link.aps.org/doi/10.1103/PhysRevX.3.031015>.
- [222] M. Heyl, *Phys. Rev. Lett.* **115**, 140602 (2015), URL <http://link.aps.org/doi/10.1103/PhysRevLett.115.140602>.
- [223] T.-C. Wei, I. Affleck, and R. Raussendorf, *Phys. Rev. A* **86**, 032328 (2012), URL <http://link.aps.org/doi/10.1103/PhysRevA.86.032328>.
- [224] T.-C. Wei, P. Haghnegahdar, and R. Raussendorf, *Phys. Rev. A* **90**, 042333 (2014), URL <http://link.aps.org/doi/10.1103/PhysRevA.90.042333>.
- [225] P. Walther, K. J. Resch, T. Rudolph, E. Schenck, H. Weinfurter, V. Vedral, M. Aspelmeyer, and A. Zeilinger, *Nature* **434**, 169 (2005), ISSN 0028-0836, URL <http://dx.doi.org/10.1038/nature03347>.
- [226] R. Prevedel, P. Walther, F. Tiefenbacher, P. Bohi, R. Kaltenbaek, T. Jennewein, and A. Zeilinger, *Nature* **445**, 65 (2007), ISSN 0028-0836, URL <http://dx.doi.org/10.1038/nature05346>.
- [227] X.-C. Yao, T.-X. Wang, H.-Z. Chen, W.-B. Gao, A. G. Fowler, R. Raussendorf, Z.-B. Chen, N.-L. Liu, C.-Y. Lu, Y.-J. Deng, et al., *Nature* **482**, 489 (2012), ISSN 0028-0836, URL <http://dx.doi.org/10.1038/nature10770>.
- [228] S. Yokoyama, R. Ukai, S. C. Armstrong, C. Sornphiphatphong, T. Kaji, S. Suzuki, J.-i. Yoshikawa, H. Yonezawa, N. C. Menicucci, and A. Furusawa, *Nat. Photon.* **7**, 982 (2013), ISSN 1749-4885, URL <http://dx.doi.org/10.1038/nphoton.2013.287>.
- [229] O. Mandel, M. Greiner, A. Widera, T. Rom, T. W. Hänsch, and I. Bloch, *Nature* **425**, 937 (2003), ISSN 0028-0836, URL <http://dx.doi.org/10.1038/nature02008>.
- [230] B. P. Lanyon, P. Jurcevic, C. Hempel, M. Gessner, V. Vedral, R. Blatt, and C. F. Roos, *Physical Review Letters* **111**, 100504 (2013).
- [231] K. Chen and H.-K. Lo, *Quantum Information & Computation* **Vol.7**, 689 (2007).

- [232] M. Hein, W. Dür, and H.-J. Briegel, *Phys. Rev. A* **71**, 032350 (2005), URL <http://link.aps.org/doi/10.1103/PhysRevA.71.032350>.
- [233] O. Gühne, G. Tóth, P. Hyllus, and H. J. Briegel, *Phys. Rev. Lett.* **95**, 120405 (2005), URL <http://link.aps.org/doi/10.1103/PhysRevLett.95.120405>.
- [234] B. P. Lanyon, M. Zwerger, P. Jurcevic, C. Hempel, W. Dür, H. J. Briegel, R. Blatt, and C. F. Roos, *Phys. Rev. Lett.* **112**, 100403 (2014), URL <http://link.aps.org/doi/10.1103/PhysRevLett.112.100403>.
- [235] M. Hein, W. Dür, J. Eisert, R. Raussendorf, M. Van den Nest, and H.-J. Briegel, in *Quantum Computers, Algorithms and Chaos* (2006), vol. 6 of *Proceedings of the International School of Physics Enrico Fermi*, pp. 115–218, <http://arxiv.org/abs/quant-ph/0602096>.
- [236] D. E. Browne and H. J. Briegel, arXiv:quant-ph/0603226 (2006).
- [237] D. B. West, *Introduction to Graph Theory* (Prentice Hall, 2001).
- [238] D. Gottesmann, Ph.D. thesis, California Institute of Technology, Pasadena, California (1997).
- [239] H. J. Briegel and R. Raussendorf, *Phys. Rev. Lett.* **86**, 910 (2001), URL <http://link.aps.org/doi/10.1103/PhysRevLett.86.910>.
- [240] M. Van den Nest, A. Miyake, W. Dür, and H. J. Briegel, *Phys. Rev. Lett.* **97**, 150504 (2006), URL <http://link.aps.org/doi/10.1103/PhysRevLett.97.150504>.
- [241] M. V. den Nest, W. Dür, A. Miyake, and H. J. Briegel, *New Journal of Physics* **9**, 204 (2007), URL <http://stacks.iop.org/1367-2630/9/i=6/a=204>.
- [242] R. Raussendorf, J. Harrington, and K. Goyal, *Annals of Physics* **321**, 2242 (2006), ISSN 0003-4916, URL <http://www.sciencedirect.com/science/article/pii/S0003491606000236>.
- [243] R. Raussendorf, J. Harrington, and K. Goyal, *New Journal of Physics* **9**, 199 (2007), URL <http://stacks.iop.org/1367-2630/9/i=6/a=199>.
- [244] T. A. Brun, *Am. J. Phys.* **70**, 719 (2002).
- [245] V. Nebendahl, H. Häffner, and C. F. Roos, *Phys. Rev. A* **79**, 012312 (2009), URL <http://link.aps.org/doi/10.1103/PhysRevA.79.012312>.
- [246] U. Leonhardt, *Physical Review Letters* **74**, 4101 (1995), URL <http://dx.doi.org/10.1103/PhysRevLett.74.4101>.
- [247] M. Ježek, J. Fiurášek, and Z. Hradil, *Physical Review A* **68**, 012305 (2003), URL <http://dx.doi.org/10.1103/PhysRevA.68.012305>.

- [248] C. F. Roos, M. Riebe, H. Häffner, W. Hänsel, J. Benhelm, G. P. T. Lancaster, C. Becher, F. Schmidt-Kaler, and R. Blatt, *Science* **304**, 1478 (2004), ISSN 0036-8075, <http://science.sciencemag.org/content/304/5676/1478.full.pdf>, URL <http://science.sciencemag.org/content/304/5676/1478>.
- [249] G. Tóth and O. Gühne, *Phys. Rev. Lett.* **94**, 060501 (2005), URL <http://link.aps.org/doi/10.1103/PhysRevLett.94.060501>.
- [250] M. Riebe, H. Häffner, C. F. Roos, W. Hansel, J. Benhelm, G. P. T. Lancaster, T. W. Körber, C. Becher, F. Schmidt-Kaler, D. F. V. James, et al., *Nature* **429**, 734 (2004), ISSN 0028-0836, URL <http://dx.doi.org/10.1038/nature02570>.
- [251] M. Riebe, T. Monz, K. Kim, A. S. Villar, P. Schindler, M. Chwalla, M. Hennrich, and R. Blatt, *Nat. Phys.* **4**, 839 (2008), ISSN 1745-2473, URL <http://dx.doi.org/10.1038/nphys1107>.
- [252] V. Coffman, J. Kundu, and W. K. Wootters, *Phys. Rev. A* **61**, 052306 (2000), URL <http://link.aps.org/doi/10.1103/PhysRevA.61.052306>.
- [253] A. M. Steane, *Phys. Rev. Lett.* **77**, 793 (1996), URL <http://link.aps.org/doi/10.1103/PhysRevLett.77.793>.
- [254] A. R. Calderbank and P. W. Shor, *Phys. Rev. A* **54**, 1098 (1996), URL <http://link.aps.org/doi/10.1103/PhysRevA.54.1098>.
- [255] D. A. Lidar and T. A. Brun, eds., *Quantum Error Correction* (Cambridge University Press, New York, 2013).
- [256] D. G. Cory, M. D. Price, W. Maas, E. Knill, R. Laflamme, W. H. Zurek, T. F. Havel, and S. S. Somaroo, *Phys. Rev. Lett.* **81**, 2152 (1998), URL <http://link.aps.org/doi/10.1103/PhysRevLett.81.2152>.
- [257] J. Zhang, R. Laflamme, and D. Suter, *Phys. Rev. Lett.* **109**, 100503 (2012), URL <http://link.aps.org/doi/10.1103/PhysRevLett.109.100503>.
- [258] J. Chiaverini, D. Leibfried, T. Schaetz, M. D. Barrett, R. B. Blakestad, J. Britton, W. M. Itano, J. D. Jost, E. Knill, C. Langer, et al., *Nature* **432**, 602 (2004), ISSN 0028-0836, URL <http://dx.doi.org/10.1038/nature03074>.
- [259] T. B. Pittman, B. C. Jacobs, and J. D. Franson, *Phys. Rev. A* **71**, 052332 (2005), URL <http://link.aps.org/doi/10.1103/PhysRevA.71.052332>.
- [260] M. D. Reed, L. DiCarlo, S. E. Nigg, L. Sun, L. Frunzio, S. M. Girvin, and R. J. Schoelkopf, *Nature* **482**, 382 (2012), ISSN 0028-0836, URL <http://dx.doi.org/10.1038/nature10786>.
- [261] M. Zwerger, H. J. Briegel, and W. Dür, *Scientific Reports* **4**, 5364 (2014), URL <http://dx.doi.org/10.1038/srep05364>.

- [262] A. Aspuru-Guzik, A. D. Dutoi, P. J. Love, and M. Head-Gordon, *Science* **309**, 1704 (2005), ISSN 0036-8075, <http://science.sciencemag.org/content/309/5741/1704.full.pdf>, URL <http://science.sciencemag.org/content/309/5741/1704>.
- [263] M. I. Dyakonov, arXiv:quant-ph/0610117 (2006).
- [264] A. G. Fowler, M. Mariani, J. M. Martinis, and A. N. Cleland, *Phys. Rev. A* **86**, 032324 (2012), URL <http://link.aps.org/doi/10.1103/PhysRevA.86.032324>.
- [265] A. M. Smith, P. Alsing, G. Lott, and M. Fanto, *Journal of Modern Optics* **62**, 1746 (2015), <http://dx.doi.org/10.1080/09500340.2015.1014437>, URL <http://dx.doi.org/10.1080/09500340.2015.1014437>.
- [266] R. Laflamme, D. G. Cory, C. Negrevergne, and L. Viola, *Quant. Inf. Comp* **2**, 166 (2002).
- [267] J. A. Hoyos and G. Rigolin, *Phys. Rev. A* **74**, 062324 (2006), URL <http://link.aps.org/doi/10.1103/PhysRevA.74.062324>.
- [268] T. Werlang and G. Rigolin, *Phys. Rev. A* **81**, 044101 (2010), URL <http://link.aps.org/doi/10.1103/PhysRevA.81.044101>.
- [269] B. P. Lanyon, M. Barbieri, M. P. Almeida, and A. G. White, *Phys. Rev. Lett.* **101**, 200501 (2008), URL <http://link.aps.org/doi/10.1103/PhysRevLett.101.200501>.
- [270] B. Dakic, Y. O. Lipp, X. Ma, M. Ringbauer, S. Kropatschek, S. Barz, T. Paterek, V. Vedral, A. Zeilinger, C. Brukner, et al., *Nat. Phys.* **8**, 666 (2012), ISSN 1745-2473, URL <http://dx.doi.org/10.1038/nphys2377>.
- [271] M. Gu, H. M. Chrzanowski, S. M. Assad, T. Symul, K. Modi, T. C. Ralph, V. Vedral, and P. K. Lam, *Nat. Phys.* **8**, 671 (2012), ISSN 1745-2473, URL <http://dx.doi.org/10.1038/nphys2376>.
- [272] M. Gessner, M. Ramm, T. Pruttivarasin, A. Buchleitner, H.-P. Breuer, and H. Häffner, *Nat. Phys.* **10**, 105 (2014), ISSN 1745-2473, URL <http://dx.doi.org/10.1038/nphys2829>.
- [273] C. E. Shannon and W. Weaver, *The Mathematical Theory of Communication* (University of Illinois Press, 1949).
- [274] T. M. Cover and J. A. Thomas, *Elements of Information Theory* (Wiley, 2006), 2nd ed.
- [275] B. Dakić, V. Vedral, and C. Brukner, *Phys. Rev. Lett.* **105**, 190502 (2010), URL <http://link.aps.org/doi/10.1103/PhysRevLett.105.190502>.
- [276] A. Wehrl, *Rev. Mod. Phys.* **50**, 221 (1978), URL <http://link.aps.org/doi/10.1103/RevModPhys.50.221>.
- [277] A. Streltsov, H. Kampermann, and D. Bruß, *Phys. Rev. Lett.* **106**, 160401 (2011), URL <http://link.aps.org/doi/10.1103/PhysRevLett.106.160401>.

- [278] M. Gessner, E.-M. Laine, H.-P. Breuer, and J. Piilo, *Phys. Rev. A* **85**, 052122 (2012), URL <http://link.aps.org/doi/10.1103/PhysRevA.85.052122>.
- [279] L. Wang, J.-H. Huang, J. P. Dowling, and S.-Y. Zhu, *Quantum Information Processing* **12**, 899 (2012), ISSN 1573-1332, URL <http://dx.doi.org/10.1007/s11128-012-0435-2>.
- [280] Y. Wan, F. Gebert, J. B. Wübbena, N. Scharnhorst, S. Amairi, I. D. Leroux, B. Hemmerling, N. Lörch, K. Hammerer, and P. O. Schmidt, *Nature Communications* **5**, 3096 (2014), URL <http://dx.doi.org/10.1038/ncomms4096>.
- [281] A. Gilchrist, N. K. Langford, and M. A. Nielsen, *Phys. Rev. A* **71**, 062310 (2005), URL <http://link.aps.org/doi/10.1103/PhysRevA.71.062310>.
- [282] E. G. Carnio, A. Buchleitner, and M. Gessner, *Phys. Rev. Lett.* **115**, 010404 (2015), URL <http://link.aps.org/doi/10.1103/PhysRevLett.115.010404>.
- [283] E. G. Carnio, A. Buchleitner, and M. Gessner, arXiv:1602.08973 p. 28 (2016).
- [284] F. Ciccarello and V. Giovannetti, *Phys. Rev. A* **85**, 010102 (2012), URL <http://link.aps.org/doi/10.1103/PhysRevA.85.010102>.
- [285] A. Streltsov, H. Kampermann, and D. Bruß, *Phys. Rev. Lett.* **107**, 170502 (2011), URL <http://link.aps.org/doi/10.1103/PhysRevLett.107.170502>.
- [286] A. Ferraro, L. Aolita, D. Cavalcanti, F. M. Cucchietti, and A. Acín, *Phys. Rev. A* **81**, 052318 (2010), URL <http://link.aps.org/doi/10.1103/PhysRevA.81.052318>.
- [287] A. Datta, *Phys. Rev. A* **81**, 052312 (2010), URL <http://link.aps.org/doi/10.1103/PhysRevA.81.052312>.
- [288] M. Gessner, Ph.D. thesis, Uni Freiburg (2015).
- [289] H. Krauter, C. A. Muschik, K. Jensen, W. Wasilewski, J. M. Petersen, J. I. Cirac, and E. S. Polzik, *Phys. Rev. Lett.* **107**, 080503 (2011), URL <http://link.aps.org/doi/10.1103/PhysRevLett.107.080503>.
- [290] A. I. Solomon, *Journal of Physics: Conference Series* **380**, 012012 (2012), URL <http://stacks.iop.org/1742-6596/380/i=1/a=012012>.
- [291] A. Bermudez, T. Schaetz, and M. B. Plenio, *Phys. Rev. Lett.* **110**, 110502 (2013), URL <http://link.aps.org/doi/10.1103/PhysRevLett.110.110502>.
- [292] J. Hou, K. Słowik, F. Lederer, and C. Rockstuhl, *Phys. Rev. B* **89**, 235413 (2014), URL <http://link.aps.org/doi/10.1103/PhysRevB.89.235413>.
- [293] M. Harlander, Ph.D. thesis, Universität Innsbruck (2012).
- [294] D. Kielpinski, C. Monroe, and D. J. Wineland, *Nature* **417**, 709 (2002), ISSN 0028-0836, URL <http://dx.doi.org/10.1038/nature00784>.

- [295] L. Luo, D. Hayes, T. Manning, D. N. Matsukevich, P. Maunz, S. Olmschenk, J. D. Sterk, and C. Monroe, *Fortschr. Phys.* **57**, 11 (2009).
- [296] J. I. Cirac and P. Zoller, *Nature* **404**, 579 (2000), ISSN 0028-0836, URL <http://dx.doi.org/10.1038/35007021>.
- [297] M. Kumph, Ph.D. thesis, Universität Innsbruck (2015).
- [298] Q. A. Turchette, Kielpinski, B. E. King, D. Leibfried, D. M. Meekhof, C. J. Myatt, M. A. Rowe, C. A. Sackett, C. S. Wood, W. M. Itano, et al., *Physical Review A* **61**, 063418 (2000), URL <http://dx.doi.org/10.1103/PhysRevA.61.063418>.
- [299] L. Deslauriers, S. Olmschenk, D. Stick, W. Hensinger, J. Sterk, and C. R. Monroe, *Physical Review Letters* **97**, 103007 (2006), URL <http://link.aps.org/doi/10.1103/PhysRevLett.97.103007>.
- [300] D. A. Hite, Y. Colombe, A. C. Wilson, K. R. Brown, U. Warring, R. Jördens, J. D. Jost, K. S. McKay, D. P. Pappas, D. Leibfried, et al., *Physical Review Letters* **109**, 103001 (2012), URL <http://dx.doi.org/10.1103/PhysRevLett.109.103001>.
- [301] M. Brownnutt, M. Kumph, P. Rabl, and R. Blatt, *Rev. Mod. Phys.* **87**, 1419 (2015), URL <http://link.aps.org/doi/10.1103/RevModPhys.87.1419>.
- [302] T. Ruster, C. T. Schmiegelow, H. Kaufmann, C. Warschburger, F. Schmidt-Kaler, and U. G. Poschinger, *Applied Physics B* **122**, 1 (2016), ISSN 1432-0649, URL <http://dx.doi.org/10.1007/s00340-016-6527-4>.
- [303] A. L. Fetter and J. D. Walecka, *Quantum Theory of Many-Particle Systems* (McGraw-Hill, New York, 1971).
- [304] N. Majlis, *The Quantum Theory of Magnetism* (World Scientific, Singapore, 2000).
- [305] K. Zyczkowski and I. Bengtsson, *Geometry of Quantum States: An Introduction to Quantum Entanglement* (Cambridge University Press, 2006).
- [306] J. Carl D. Meyer, *SIAM J. Appl. Math.* **25**, 597 (1973).

Danksagung

”Bernhard von Chartres sagte, wir seien gleichsam Zwerge, die auf den Schultern von Riesen sitzen, um mehr und Entfernteres als diese sehen zu können – freilich nicht dank eigener scharfer Sehkraft oder Körpergröße, sondern weil die Größe der Riesen uns emporhebt.”⁴

Dieses Eingangszitat versinnbildlicht eloquent meine Sichtweise auf die Entstehung dieser Doktorarbeit. Es soll zudem all jenen meinen tiefsten Dank zum Ausdruck bringen, die mich die letzten Jahre unterstützt haben und von deren Schultern ich die Welt aus anderen Blickwinkeln erleben durfte.

Meine Reise begann mit einem nicht alltäglichen Glückstreffer: Mir wurde die Chance geboten, Teil eines vollausgestatteten, reibungslos funktionierenden und mit einem kompetenten und dynamischen Team besetzten Experimentes zu sein. Diese wissenschaftliche Umgebung und das Team haben mich massgeblich beeinflusst und meine Denkweise sowohl als Wissenschaftler, als auch als Privatperson, geformt. Für diese einmalige Gelegenheit möchte ich mich bei Rainer Blatt bedanken, der mir ein perfektes Umfeld geboten hat um mich als Wissenschaftler zu entwickeln. Sein Mantra, dass wir Technologie entwickeln müssen, um die Physik zu erforschen (und nicht andersherum), hat mich über die Jahre geprägt.

Der nächste grosse Dank gebührt dem Quantensimulations-Team (ehemals Ca-43), das mich tagtäglich, sowie so manche Nacht, begleitet hat. Hier möchte ich vor allem Christian Roos, Ben Lanyon und Cornelius Hempel danken. Christian hat mit seinem gefühlt unermesslichen Verständnis der Physik viele Stunden damit zugebracht mir Dinge immer und immer wieder zu erklären und hat mir erlaubt ihn ständig mit Fragen zu durchlöchern. Das Verständnis über die Materie, welches ich am Ende dieser Arbeit erlangt habe, habe ich grösstenteils ihm zu verdanken. Auch hat er mein logisches und kritisches Denken mit Gegenfragen und Diskussionen wesentlich beeinflusst. Zu Ben, der während meiner Doktorarbeit als Postdoc am Experiment tätig war, habe ich ein ganz spezielles Verhältnis aufgebaut. Die unzähligen Stunden, Tage, Monate und Jahre zu zweit im Labor liessen uns manchmal wie ein altes Ehepaar wirken (ständiges gegenseitiges Rumgemeckere, um dann nachts beim messen die letzte Mandarine oder Keks zu teilen). Ben war ein unermüdlicher Antriebsmotor (dem scheinbar nie der Kraftstoff ausging), das Experiment und mich stets vorantrieb. Er lehrte mich, sich auf das Wesentliche im Experiment zu fokussieren und, die richtigen Fragen zu stellen. Ben und Christian haben auch massgeblich dazu beigetragen, dass diese Dissertationsarbeit (durch mehrere Korrektur-Runden) in akzeptabler Form verfasst wurde. Cornelius war der ältere Doktorand am Experiment, der jede Schraube, jede Faser und jeden PID Wert auswendig kannte. Er hat sich stets Zeit genommen, um mir das Experiment und

⁴Johannes von Salisbury: Metalogicon 3,4,46-50

den Aufbau im Detail durchzugehen und mir alles zu erklären. Ich möchte ihm nicht nur dafür danken, sondern vor allem auch für seinen steten Drang den Aufbau zu verbessern, sei es QFP, die Adressierung etc., wovon das Experiment und somit auch ich enorm profitieren konnten. Ebenso möchte ich den jüngeren Doktorandinnen, Christine Maier und Tiffany Bridges, für die witzigen und aufgeheiterten Momente im Labor danken. Christine, die zum Zeitpunkt der Entstehung dieser Schrift schon ein alter Hase war, konnte ich das Experiment und mich voll und ganz auf das Schreiben konzentrieren. Tiff hatte die Ausdauer meine Arbeit ganze zwei Mal zu lesen um meine Formulierungen auszubessern und die unzähligen Schreibfehler aufzuspüren. Ich möchte mich auch bei der gesamten Blatt-Gruppe für die vielen Diskussionen, sowie den Ideen- und Wissensaustausch bedanken. Es war ein ganz besonderes Umfeld von dem ich äusserst profitieren konnte.

Des Weiteren möchte ich Stefan Haslwanter, Andreas Strasser und Bernhard Öttl aus der Werkstatt, sowie Gerhard Hendl aus der Elektronik danken, ohne deren Hilfe der Bau und Aufbau eines solchen Experimentes gar nicht möglich gewesen wäre. Ebenso möchte ich der ganzen Administration des IQOQI's dafür danken, dass wir uns nicht mit den ganzen bürokratischen Hürden auseinandersetzen mussten.

Der wichtigste Dank gehört jedoch meiner Familie, allen voran meinem Vater, der mich all die Jahre auf allen erdenkbaren Weisen unterstützt hat. Wir sind gemeinsam durch viele Hochs und Tiefs gegangen und ohne seine Unterstützung wäre ich heute nicht hier wo ich nun stehe. Danke "debeli". Auch möchte ich meiner Freundin Catherine danken, die mir die letzten Jahre ein Anker in so manch rauem Gewässer war. Ohne sie als Ruhepol im hektischen wissenschaftlichen Alltag hätte ich meine Arbeit gewiss deutlich schlechter verrichten können.

Zu guter Letzt möchte ich allen danken, die ich hier namentlich nicht erwähnt habe, die mich jedoch die letzten Jahre im Beruf oder auch privat begleitet haben. Ich hatte eine einzigartige und wundervolle Zeit und sollten Zeitreisen jemals möglich sein, würde ich es nicht anders machen.